

UNIVERSITY OF OKLAHOMA

GRADUATE COLLEGE

SYNOPTIC AND LOCAL INFLUENCES ON A SUMMERTIME,  
LONG-LIVED, MIXED-PHASE CLOUD EVENT OVER SUMMIT,  
GREENLAND

A THESIS

SUBMITTED TO THE GRADUATE FACULTY

in partial fulfillment of the requirements for the

Degree of

MASTER OF SCIENCE IN METEOROLOGY

By

MALLORY PAIGE ROW

Norman, Oklahoma

2016

SYNOPTIC AND LOCAL INFLUENCES ON A SUMMERTIME,  
LONG-LIVED, MIXED-PHASE CLOUD EVENT OVER SUMMIT,  
GREENLAND

A THESIS APPROVED FOR THE  
SCHOOL OF METEOROLOGY

BY

---

Dr. Steven Cavallo, Chair

---

Dr. Dave Turner

---

Dr. Cameron Homeyer





## Acknowledgments

There are far too many people that have helped me get where I am today. Everyone who has come into my life has left an everlasting impact on me, and for that I will be forever grateful. Sparky Anderson said, “Success isn’t something that just happens - success is learned, success is practiced and then it is shared”. I share all my accomplishments and success with those around me for without them I would not be here.

To McFarlin United Methodist Church and YogaLife in Norman, thank you being my escapes from reality.

To the meteorology professors at Valparaiso University, thank you for believing in me and guiding me towards a path I never thought that I could walk down. I have truly found my passion in this life and I could have never found it without your guidance.

To my friends, your support and encouragement has meant the world to me. Regardless of how long our friendship has been, the love, laughs, smiles, and memories I have shared with you all has kept me sane and smiling in the hardest of times.

To Dr. Cameron Homeyer, thank you for undertaking the task of being on my committee, but an even bigger thank you for being a wonderful professor and mentor. I have greatly appreciated your willingness to help me with my research, and all the academic and life chats in your office.

To Dr. Amy Solomon, thank you for all your insight and comments on this research. They truly have made this work better.

To Jimmy Correia, thank you for helping me believe in myself as a researcher. Thank you for all the oreos, scones, venting sessions, and life discussions. I truly would not be here today without your guidance the past 3 years.

To my advisors Dr. Steven Cavallo and Dr. Dave Turner, thank you for this opportunity. It has been the most incredible experience. Thank you for pushing the bar higher than I was comfortable with because I have accomplished more than I ever thought I could. Your patience and encouragement on this journey has meant so much to me. I look up to both of you as scientists and as people. Thank you again for everything.

To my sister, Lindsey, you have been a rock these past 2 years. While we have lived farther apart, I feel it has only brought us closer. Thank you for your advice and support, sharing funny articles and videos, sending me pictures of our cat, and, most of all, thank you for being a wonderful sister.

Finally, to my parents, Ed and Kathy, thank you. I don't know how to even start to say thank you for all you have done. You both have sacrificed so much for me to have this life. You have helped me in so many ways and not once have I heard either of you complain or refuse to help me. Thank you for supporting everything I have ever decided to do and thank you for guiding me in my decisions instead of making them for me.

# Table of Contents

<b>Acknowledgments</b>	<b>iv</b>
<b>List of Tables</b>	<b>ix</b>
<b>List of Figures</b>	<b>x</b>
<b>Abstract</b>	<b>xxi</b>
<b>1 Introduction</b>	<b>1</b>
1.1 Greenland and the Greenland Ice Sheet . . . . .	1
1.1.1 Physical Characteristics and Meteorology . . . . .	1
1.1.2 Past . . . . .	9
1.1.3 Present . . . . .	10
1.1.4 Future . . . . .	13
1.2 Arctic Mixed-Phase Clouds . . . . .	14
1.2.1 History of Arctic Cloud Observational Studies . . . . .	14
1.2.2 Characteristics . . . . .	18
1.2.3 Radiative Impacts . . . . .	19
1.2.4 Formation and Maintenance Processes . . . . .	23
1.3 Importance of Studying Mixed-Phase Clouds	
Over Greenland . . . . .	30
1.4 Thesis Motivations and Hypothesis . . . . .	32
<b>2 Data</b>	<b>35</b>

2.1	Numerical Weather Prediction Models . . . . .	35
2.1.1	Weather Research and Forecasting Model . . . . .	35
2.1.2	Polar Weather Research and Forecasting Model . . . . .	36
2.2	Instrumentation Summit Station, Greenland . . . . .	37
<b>3</b>	<b>Case Description</b>	<b>42</b>
3.1	Synoptic Environment . . . . .	42
3.2	Summit Station, Greenland . . . . .	46
<b>4</b>	<b>Methods and Results</b>	<b>53</b>
4.1	Control Simulation . . . . .	53
4.1.1	Model Version and Forcing Dataset . . . . .	54
4.1.2	Shortwave Radiation Physics . . . . .	58
4.1.3	Domain Size . . . . .	61
4.1.4	Vertical and Horizontal Grid Spacing . . . . .	63
4.1.5	Chosen Control . . . . .	66
4.2	Experimental Simulations . . . . .	85
4.2.1	Synoptic Influence . . . . .	85
4.2.1.1	Fixed Boundary Conditions . . . . .	86
4.2.2	Local Influence . . . . .	97
4.2.2.1	Microphysics: M-PACE Observations . . . . .	97
4.2.2.2	Planetary Boundary Layer Physics Option: Local vs. Non-local . . . . .	105
4.2.2.3	Radiation . . . . .	111
4.3	Results Summary and Discussions . . . . .	133
<b>5</b>	<b>Future Work and Conclusions</b>	<b>139</b>
5.1	Future Work . . . . .	139
5.2	Conclusions . . . . .	140



## List of Tables

4.1	Summary of control simulation settings. . . . .	67
4.2	Summary of experimental model simulations. . . . .	133

## List of Figures

1.1	Modeled Greenland elevation derived from CyroSat-2. Figure 7 from Helm et al. 2014. . . . .	2
1.2	Correlation of the seasonally averaged (a) 500 hPa geopotential height and (b) surface air temperature from the NCEP/NCAR reanalysis with the NAO from January 1981 - December 2010. . . . .	5
1.3	Correlation of the seasonally averaged (a) 500 hPa geopotential height and (b) surface air temperature from the NCEP/NCAR reanalysis with the AO from January 1981 - December 2010. . . . .	6
1.4	500 hPa geopotential height composite anomalies from the NCEP/NCAR reanalysis for a positive Greenland Blocking Index. Images from NOAA Earth Science Research Laboratory Physical Science Division. . . . .	8
1.5	Annual melt extent anomalies from 1978 to 2015 (top) and daily cumulative melt area from 2012 to 2015 (bottom). Images from National Snow and Ice Data Center. Credit: Thomas Mote, University of Georgia . . . . .	11
1.6	Locations of various Arctic field campaigns. Figure is originally from Shupe et al. (2013) . . . . .	16



1.7	Original schematics from Morrison et al. (2012) highlighting their (a) conceptual model illustrating the main processes and simplistic physical structure of persistent Arctic mixed-phase clouds, and (b) hypothesized processes, feedbacks, and interactions linked to Arctic mixed-phase clouds. . . . .	25
2.1	Flow diagram of running the WRF and its different components. . .	36
3.1	July 2012 anomalies (monthly mean - climatology) based from the 1981-2010 climatology of (a) surface air temperature (°C), (b) 500 hPa geopotential height (m), and (c) time series of daily index of NAO (green) and AO (navy). The start and end of the cloud event and 0 index value are marked by the dashed black lines. Data are from the NCEP/NCAR reanalysis and Climate Prediction Center. The location of Summit, Greenland is denoted by ★. . . . .	43
3.2	480 hour backward trajectories from Summit at 20 July 2012 at 00 UTC at 50, 500, and 1000 m above ground level computed using HYPPLIT. Labels along the trajectories are (a) relative humidity (%) and (b) height above ground level (m). Data are from the NCEP/NCAR Reanalysis. The location of Summit, Greenland is denoted by ★. . . . .	44

3.3	(a), (c), (e) Potential temperature ( $^{\circ}\text{K}$ ; color) and winds ( $\text{m s}^{-1}$ ; barbs) on the 2 PVU surface, and (b), (d), (f) total column water vapor ( $\text{kg m}^{-2}$ ; color), mean sea-level pressure (hPa, contour), and surface winds ( $\text{ms}^{-1}$ ; barbs) on (a), (b) 20 July 2012 at 00 UTC, (c), (d) 22 July at 00 UTC, and (e), (f) 24 July at 00 UTC. Wind barbs with a half barb = $2.5 \text{ m s}^{-1}$ , a full barb = $5 \text{ m s}^{-1}$ , and a flag = $25 \text{ m s}^{-1}$ . The 2 PVU surface represents the dynamic tropopause where $1 \text{ PVU} = 10^{-6} \text{ m}^2 \text{ s}^{-1} \text{ kg}^{-1} \text{ }^{\circ}\text{K}$ . Data are from ERA-Interim and the location of Summit, Greenland is denoted by $\star$ . . . . .	45
3.4	Observational-based estimates from the ICECAPS Summit Station, Greenland cloud-atmosphere observatory for (a) the lowest cloud base height (km) detected by ceilometer, (b) liquid water path ( $\text{g m}^{-2}$ ) retrieved from the Microwave Radiometer with 30 (blue) and 0 (black) $\text{g m}^{-2}$ dashed, and time-height cross section of (c) $\log(\text{backscatter})$ from the the MicroPulse Lidar (MPL) and (d) reflectivity (dBZ) from the Doppler 35-GHz Millimeter Cloud Radar (MMCR). . . . .	47
3.5	Images from the Total Sky Imager (TSI) at the ICECAPS Summit Station, Greenland cloud-atmosphere observatory on (a) 20 July 2012, (b) 21 July 2012, (c) 22 July 2012, and (d) 23 July 2012. . . .	48
3.6	Vertical profile of temperature ( $^{\circ}\text{C}$ , red), dewpoint ( $^{\circ}\text{C}$ , green), and winds ( $\text{m s}^{-1}$ ; barbs) from the Summit radiosondes at (a) 20 July 2012 at 00 UTC, (b) 21 July 2012 at 00 UTC, (c) 22 July 2012 at 00 UTC, (d) 23 July 2012 at 00 UTC, and (e) the 24 July 2012 at 00 UTC radiosondes. Wind barbs with a half barb = $2.5 \text{ m s}^{-1}$ , a full barb = $5 \text{ m s}^{-1}$ , and a flag = $25 \text{ m s}^{-1}$ . . . . .	50

3.7	Time series of data from the meteorology tower at Summit from 20-24 July 2012 of the 10-m (a) zonal (red) and meridional (blue) wind ( $\text{m s}^{-1}$ ), (b) 2-m (purple) and 10-m (pink) temperature ( $^{\circ}\text{C}$ ), (c) sea-level pressure (hPa), and (d) relative humidity (%). . . . .	51
4.1	Process for choosing control model simulation. . . . .	53
4.2	Domain for simulations with 150 x 300 grid points in the x and y directions, respectively. The topography of the domain is color filled (km). The location of Summit, Greenland is denoted by $\star$ . . . . .	55
4.3	Time-height cross section through lowest the 1 km AGL of cloud water mixing ratio ( $\text{g kg}^{-1}$ ; colors) and time series of liquid water path ( $\text{g m}^{-2}$ ; purple) from the (a) <i>WRF_GFS</i> , (b) <i>WRF_ERA</i> , (c) <i>PWRF_GFS</i> , and (d) <i>PWRF_ERA</i> simulations. (e) Comparison of liquid water path ( $\text{g m}^{-2}$ ) from MWRRET (gray), <i>WRF_GFS</i> (dark blue), <i>WRF_ERA</i> (dark green), <i>PWRF_GFS</i> (dark purple), and <i>PWRF_ERA</i> (dark red). . . . .	56
4.4	Time-height cross section through lowest the 1 km AGL of relative humidity (%) from the (a) <i>WRF_GFS</i> , (b) <i>WRF_ERA</i> , (c) <i>PWRF_GFS</i> , and (d) <i>PWRF_ERA</i> simulations. . . . .	57
4.5	Time-height cross section through lowest the 1 km AGL of cloud water mixing ratio ( $\text{g kg}^{-1}$ ; colors) and time series of liquid water path ( $\text{g m}^{-2}$ ; purple) from the (a) <i>Dudhia</i> and (b) <i>RRTMG</i> simulations. (c) Comparison of liquid water path ( $\text{g m}^{-2}$ ) from MWRRET (gray), <i>Dudhia</i> (dark purple), and <i>RRTMG</i> (light blue). . . . .	59

4.6	Time-height cross section through the lowest 1 km AGL of temperature ( $^{\circ}\text{C}$ ) from the (a) <i>Dudhia</i> and (b) <i>RRTMG</i> simulations, and (c) AERIoe retrieval. (d) Comparison of 2-m temperature ( $^{\circ}\text{C}$ ) from the Summit meteorology tower (gray), <i>Dudhia</i> (dark purple), and <i>RRTMG</i> (light blue). . . . .	60
4.7	Time-height cross section through the lowest 1 km AGL of water vapor mixing ratio ( $\text{g kg}^{-1}$ ) from the (a) <i>Dudhia</i> and (b) <i>RRTMG</i> simulations, and (c) AERIoe retrieval. . . . .	61
4.8	Domain for simulations with 300 x 300 grid points in the x and y directions, respectively. The topography of the domain is color filled (km). The location of Summit, Greenland is denoted by $\star$ . . . . .	62
4.9	Time-height cross section through lowest the 1 km AGL of cloud water mixing ratio ( $\text{g kg}^{-1}$ ; colors) and time series of liquid water path ( $\text{g m}^{-2}$ ; purple) from the (a) <i>150x300</i> and (b) <i>300x300</i> simulations. (c) Comparison of liquid water path ( $\text{g m}^{-2}$ ) from MWRRET (gray), <i>150x300</i> (light blue), and <i>300x300</i> (dark pink). . . . .	63
4.10	Eta levels at 19 July 2012 at 12 UTC at Summit in the (a) control, (b) <i>51_etalevels</i> , and (c) <i>S16_etalevels</i> simulations. . . . .	64
4.11	Time-height cross section through the lowest 1 km AGL of cloud water mixing ratio ( $\text{g kg}^{-1}$ ; colors) and time series of liquid water path ( $\text{g m}^{-2}$ ; purple) from the (a) <i>40eta,12km</i> , (b) <i>51_etalevels</i> , (c) <i>S16_etalevels</i> , and (d) <i>3km</i> simulations. (e) Comparison of liquid water path ( $\text{g m}^{-2}$ ) from MWRRET (gray), <i>40eta,12km</i> (dark pink), <i>51_etalevels</i> (orange), <i>S16_etalevels</i> (green), and <i>3km</i> (brown). . . .	65

4.12	Time-height cross section through the lowest 1 km AGL of (a) cloud water mixing ratio ( $\text{g kg}^{-1}$ ; colors) and time series of liquid water path ( $\text{g m}^{-2}$ ; purple) with $30 \text{ g m}^{-2}$ dashed, (b) temperature ( $^{\circ}\text{C}$ ), (c) w wind ( $\text{cm s}^{-1}$ ), (d) water vapor mixing ratio ( $\text{g kg}^{-1}$ ), and (e) relative humidity (%). Data are from the control simulation. . . . .	68
4.13	Vertical potential temperature ( $^{\circ}\text{K}$ ; black line) and cloud water mixing ratio ( $\text{g kg}^{-1}$ ; blue dots) profiles in the lowest 2 km AGL at 00 UTC (a,c,e,g,i) and 12 UTC (b,d,f,h) on (a,b) 20, (c,d) 21, (e,f) 22, (g,h) 23, and (i) 24 July 2012. Data are from the control simulation. . . . .	69
4.14	Time series of (a) 2-m (purple) and skin (teal) temperature ( $^{\circ}\text{C}$ ), (b) sensible (brown) and latent (light blue) heat flux ( $\text{W m}^{-2}$ ), and (c) surface net shortwave (gold) and downward longwave (navy) flux ( $\text{W m}^{-2}$ ). Data are from the control simulation. . . . .	70
4.15	Time-height cross section through the lowest 5 km AGL of (a) ice mixing ratio ( $\text{g kg}^{-1}$ ; colors) and ice water path time series ( $\text{g m}^{-2}$ ; purple), (b) temperature ( $^{\circ}\text{C}$ ), (c) meridional wind ( $\text{m s}^{-1}$ ), (d) zonal wind ( $\text{m s}^{-1}$ ), and (e) water vapor mixing ratio ( $\text{g kg}^{-1}$ ). Data are from the control simulation. . . . .	71
4.16	650 hPa relative humidity (%; colors) and winds ( $\text{m s}^{-1}$ ; black arrows) on (a,b) 20, (c,d) 21, (e,f) 22, (g,h) 23, and (i) 24 July 2012 at (a,c,e,g,i) 00 UTC and (b,d,f,h) 12 UTC. Data are from the control simulation, and the location of Summit, Greenland is denoted by $\star$ . 650 hPa is chosen as it is the closest pressure level to the Summit surface. . . . .	73

4.17	10-m zonal wind ( $\text{m s}^{-1}$ ; colors) and smoothed sea-level pressure (hPa; black) on (a,b) 20, (c,d) 21, (e,f) 22, (g,h) 23, and (i) 24 July 2012 at (a,c,e,g,i) 00 UTC and (b,d,f,h) 12 UTC. Data are from the control simulation, and the location of Summit, Greenland is denoted by $\star$ . . . . .	74
4.18	Perceptible water vapor ( $\text{kg m}^{-2}$ ) on (a) 20, (b) 21, and (c) 22 July 2012 at 00 UTC with 1-day backward trajectories for parcels in the lowest 1 km AGL at Summit arriving on (a) 21, (b) 22, and (c) 23 July 2012 at 00 UTC. Data are from the control simulation, and the location of Summit, Greenland is denoted by $\star$ . . . . .	75
4.19	Black line indicates where cross section was taken in Figs. 4.20, 4.21, 4.23, 4.24, 4.35, 4.36, and 4.40. The location of Summit, Greenland is denoted by $\star$ . . . . .	76
4.20	East-west cross section taken through black line in Fig. 4.19 of (a) zonal wind ( $\text{m s}^{-1}$ ), (b) moisture flux convergence ( $\times 10^{-4} \text{ g kg}^{-1} \text{ s}^{-1}$ ), and (c) relative humidity (%) on 23 July 2012 at 00 UTC. Data are from the control simulation, and the location of Summit, Greenland is denoted by $\star$ . . . . .	77
4.21	East-west cross section taken through black line in Fig. 4.19 of ice mixing ratio ( $\text{g kg}^{-1}$ ) at 23 July 2012 at (a) 00 UTC and (b) 03 UTC. Data are from the control simulation, and the location of Summit, Greenland is denoted by $\star$ . . . . .	78
4.22	(a) Time series of Froude number from points plotted in (b). The Froude number is from a height of 2.5 km above sea-level. Data are from the control simulation, and the location of Summit, Greenland is denoted by $\star$ . . . . .	79
4.23	Same as Fig. 4.20, but for 23 July at 12 UTC. . . . .	81

4.24	Same as Fig. 4.20, but for 24 July at 00 UTC. . . . .	82
4.25	Time series of (a) liquid water path ( $\text{g m}^{-2}$ ) retrieved from the Microwave Radiometer (gray) and control simulation (black) with 30 (blue) and 0 (black) $\text{g m}^{-2}$ dashed, 10-m (b) zonal and (c) meridional wind ( $\text{m s}^{-1}$ ), (d) sea-level pressure (hPa), and (e) 2-m temperature ( $^{\circ}\text{C}$ ) from surface tower at Summit (gray) and control simulation (black). . . . .	84
4.26	Time-heights cross section of (a,c) temperature ( $^{\circ}\text{C}$ ) and water va- por ( $\text{g kg}^{-1}$ ) from the (a,b) control simulation and (c,d) AERIoe retrial. . . . .	85
4.27	Same as Fig. 4.12, but data are from <i>fixed_19_12</i> . . . . .	86
4.28	Same as Fig. 4.13, but data are from <i>fixed_19_12</i> . . . . .	87
4.29	Same as Fig. 4.15, but data are from <i>fixed_19_12</i> . . . . .	88
4.30	Same as Fig. 4.14, but data are from <i>fixed_19_12</i> . . . . .	89
4.31	Same as Fig. 4.16, but data are from <i>fixed_19_12</i> . . . . .	91
4.32	Same as Fig. 4.17, but data are from <i>fixed_19_12</i> . . . . .	92
4.33	Same as Fig. 4.18, but data are from <i>fixed_19_12</i> . . . . .	93
4.34	Same as Fig. 4.22, but data are from <i>fixed_19_12</i> . . . . .	93
4.35	Same as Fig. 4.20, but data are from <i>fixed_19_12</i> . . . . .	94
4.36	Same as Fig. 4.21, but data are from <i>fixed_19_12</i> . . . . .	95
4.37	Time series of (a) liquid water path ( $\text{g m}^{-2}$ ) retrieved from the Mir- cowave Radiometer (gray) and control (black) and <i>fixed_19_12</i> (blue) simulations with 30 (blue) and 0 (black) $\text{g m}^{-2}$ dashed, and 10-m (b) zonal and (c) meridional wind ( $\text{m s}^{-1}$ ), (d) sea-level pressure (hPa), and (e) 2-m temperature ( $^{\circ}\text{C}$ ) from surface tower at Summit (gray), and control (black) and <i>fixed_19_12</i> (blue) simulations. . . .	96

4.38	Time series of (a) liquid water path ( $\text{g m}^{-2}$ ), (b) cloud optical depth, and (c) cloud emissivity for MWRRET (gray), and the control (black) and <i>M-PACE</i> (blue) simulations. Time-height cross sections for (d,g) cloud water mixing ratio ( $\text{g kg}^{-1}$ ), (e,h) temperature ( $^{\circ}\text{C}$ ), and (f,i) w wind ( $\text{cm s}^{-1}$ ) for the (d,e,f) control and (g,h,i) <i>M-PACE</i> . . . . .	98
4.39	Same as Fig. 4.13, but data are from <i>M-PACE</i> . . . . .	100
4.40	Same as Fig. 4.21, but data are from <i>M-PACE</i> . . . . .	101
4.41	Same as Fig. 4.15, but data are from <i>M-PACE</i> . . . . .	102
4.42	Same as Fig. 4.14, but data are from <i>M-PACE</i> . . . . .	103
4.43	Same as Fig. 4.37, but for <i>M-PACE</i> . . . . .	104
4.44	Same as Fig. 4.12, but data are from <i>GBM</i> . . . . .	106
4.45	Same as Fig. 4.13, but data are from <i>GBM</i> . . . . .	107
4.46	Same as Fig. 4.15, but data are from <i>GBM</i> . . . . .	108
4.47	Same as Fig. 4.37, but for <i>GBM</i> . . . . .	109
4.48	Same as Fig. 4.14, but data are from the <i>GBM</i> . . . . .	110
4.49	1 day backward trajectories for parcels at Summit arriving on (a) 21, (b) 22, and (c) 23 July 2012 at 00 UTC at heights from 4 to 14 km every 1 km. Parcels at lower heights are darker getting lighter with height. Data are from the control simulation and the location of Summit, Greenland is denoted by $\star$ . . . . .	111
4.50	Same as Fig. 4.49, but for <i>no_CRF</i> . . . . .	112
4.51	Same as Fig. 4.49, but for <i>no_LW_CRF</i> . . . . .	112
4.52	Same as Fig. 4.49, but for <i>no_SW_CRF</i> . . . . .	112



4.53	The area where the cloud radiative forcings are changed is marked by the boxed region; the region extends from gridpoints 136 to 166 in the x-direction and 116 to 166 in the y-direction. The location of Summit, Greenland is denoted by $\star$ . . . . .	114
4.54	Same as Fig. 4.49, but for <i>no_CRF_lim</i> . . . . .	114
4.55	Same as Fig. 4.49, but for <i>no_LW_CRF_lim</i> . . . . .	115
4.56	Same as Fig. 4.49, but for <i>no_SW_CRF_lim</i> . . . . .	115
4.57	Same as Fig. 4.12, but data are from <i>no_CRF_lim</i> . . . . .	116
4.58	Same as Fig. 4.13, but data are from <i>no_CRF_lim</i> . . . . .	117
4.59	Same as Fig. 4.14, but data are from <i>no_CRF_lim</i> . . . . .	118
4.60	Same as Fig. 4.37, but for <i>no_CRF_lim</i> simulation. . . . .	119
4.61	Same as Fig. 4.12, but data are from <i>no_LW_CRF_lim</i> . . . . .	120
4.62	Same as Fig. 4.37, but for <i>no_LW_CRF_lim</i> . . . . .	121
4.63	Same as Fig. 4.12, but data are from the <i>no_SW_CRF_lim</i> . . . . .	122
4.64	Same as Fig. 4.37, but for <i>no_SW_CRF_lim</i> . . . . .	123
4.65	Time series of (a) liquid water path ( $\text{g m}^{-2}$ ), (b) cloud optical depth, and (c) cloud emissivity for MWRRET (gray), and the control (black) and <i>LWP_div10_lim</i> (blue) simulations. The dashed blue line represents the time series of the modified liquid water path in the LW radiation calls. Time-height cross sections for (d,g) cloud water mixing ratio ( $\text{g kg}^{-1}$ ), (e,h) temperature ( $^{\circ}\text{C}$ ), and (f,i) wind ( $\text{cm s}^{-1}$ ) for the (d,e,f) control and (g,h,i) <i>M-PACE</i> . . . . .	125
4.66	Same as Fig. 4.13, but data are from <i>LWP_div10_lim</i> . . . . .	126
4.67	Same as Fig. 4.65, but data are from <i>LWP_div20_lim</i> . . . . .	127
4.68	Same as Fig. 4.13, but data are from <i>LWP_div20_lim</i> . . . . .	128
4.69	Same as Fig. 4.65, but data are from <i>LWP_add30_lim</i> . . . . .	129

4.70	Time series of (a) liquid water path time series ( $\text{g m}^{-2}$ ), (b) cloud optical depth, and (c) cloud emissivity for MWRRET (gray), control (black), and the modified values in the LW radiation calls for <i>LWP_div10_lim</i> (light red), <i>LWP_div20_lim</i> (purple), and <i>LWP_add30_lim</i> (green). . . . .	130
4.71	Same as Fig. 4.65, but data are from <i>dLWP_lim</i> . . . . .	132
5.1	Schematic of the synoptic and local-scale processes involved in the cloud's formation, maintenance, and dissipation. . . . .	142
5.2	Web describing the process for cloud formation and the local feedbacks that lead to its maintenance. . . . .	143

## Abstract

Long-lived, Arctic mixed-phase clouds play a crucial role in modulating the surface energy balance over the Greenland Ice Sheet. However, due to temporally and spatially inconsistent observations, little is known about the mechanisms that cause their longevity. A persistent, single-layer, mixed-phase cloud was observed from 20-24 July 2012 at the “Integrated Characterization of Energy, Clouds, Atmospheric state, and Precipitation at Summit” (ICECAPS) cloud-atmosphere observatory in Summit Station, Greenland. The hypothesis in this study is motivated by Morrison et al. (2012); this study investigates the hypothesis that local processes promote a cloud’s persistent state, while synoptic-scale processes influence the thermodynamic structure of the lower troposphere. This hypothesis is examined on the 20-24 July 2012 ICECAPS cloud event using the Weather Research and Forecasting model with polar modifications (Polar WRF) in a series of controlled experiments.

First, the role of the synoptic-scale processes is examined by fixing the boundary conditions to isolate the influence of the large-scale flow. Westerly winds over western Greenland and easterly winds over eastern Greenland, driven by a surface cyclone off southeastern Greenland, causes flow to converge atop the ice sheet, converse of the usual state due to the katabatic winds. This deeper vertical motion leads to the formation of ice rather than liquid water, leading to cloud dissipation. In the wake of the surface cyclone and moisture boundary, colder, drier air advects over Summit resulting in a very different thermodynamic profile in the boundary layer inhibiting the cloud from reforming.

Second, the role of local-scale processes is examined. An experimental simulation investigating the sensitivity of the cloud to its microphysics shows the cloud liquid water mixing ratio (cloud liquid water content) is sensitive to the ice mixing ratio. For lower ice mixing ratios, the cloud liquid water content is higher as a result of a less effective Wegner-Bergeron-Findeisen process. Another experiment looking at the sensitivity of the simulated cloud to the choice of planetary boundary layer scheme reveals that deeper mixing by larger eddies in the boundary layer is important for cloud maintenance.

Finally, the role of local processes is examined by modifying the cloud radiative forcings. In all simulations, the cloud forms at the surface as a result of strong surface radiative cooling under a surface-based inversion. Once the cloud forms, the radiative regime changes as there is now emission from the liquid water resulting in cloud-top longwave radiative cooling. This drives buoyancy-driven updrafts that elevate the cloud and result in two feedbacks: one, condensation of moist air near the surface maintaining the cloud liquid water and cloud-top longwave radiative cooling and two, a well-mixed layer that couples the cloud with the surface which maintains the cloud through moisture and energy contributions from the surface fluxes. The surface fluxes are also greater in the presence of the cloud as a result of the increased downwelling longwave flux at the surface from the cloud. As the strength of the cloud-top longwave radiative cooling is determined strongly by the cloud liquid water content, there exists a minimum amount of liquid water to drive strong enough cloud-top cooling and induced buoyancy-driven updrafts needed to one, maintain the cloud and two, elevate it from the surface. There is also a point where increasing the liquid water does not strengthen the above described processes. In addition, shortwave radiation does not significantly impact the cloud maintenance. However, there is some impact on the liquid content of the

cloud; this can affect the amount of cloud-top longwave radiative cooling and its induced processes.

# Chapter 1 Introduction

## 1.1 Greenland and the Greenland Ice Sheet

In comparison to other regions around the world, the Arctic, formally defined as the region north of  $66.5^{\circ}\text{N}$  (Serreze and Barry, 2005), is particularly sensitive to climate change. This sensitivity is known as Arctic amplification, where changes in the Arctic temperature trends and variability have the tendency to be larger than those averaged around the Northern Hemisphere and planet (Serreze and Barry, 2011). The Greenland Ice Sheet (GIS) is one of the most dominant features in the Arctic, and thus it exhibits a large influence on the atmospheric and oceanic processes not only in the Arctic, but throughout the globe.

### 1.1.1 Physical Characteristics and Meteorology

Located in the north central Atlantic Ocean, the GIS is the largest permanent snow and ice reservoir in the Northern Hemisphere and the second largest ice sheet in the world (Mernild et al., 2011; Bamber et al., 2001). The island of Greenland covers roughly  $2.1 \times 10^6 \text{ km}^2$  with 80% ( $1.7 \times 10^6 \text{ km}^2$ ) of that being covered by ice comprising the GIS (Serreze and Barry, 2005). The GIS volume is  $2.9 \times 10^6 \text{ km}^3$  (Bamber et al., 2001) containing 12% of the world's glacier ice in volume (Encyclopædia Britannica, 2015). The elevation of the ice sheet inclines toward the center, where the highest elevations of over 3,000 m are found (Fig. 1.1) (Helm et al., 2014).

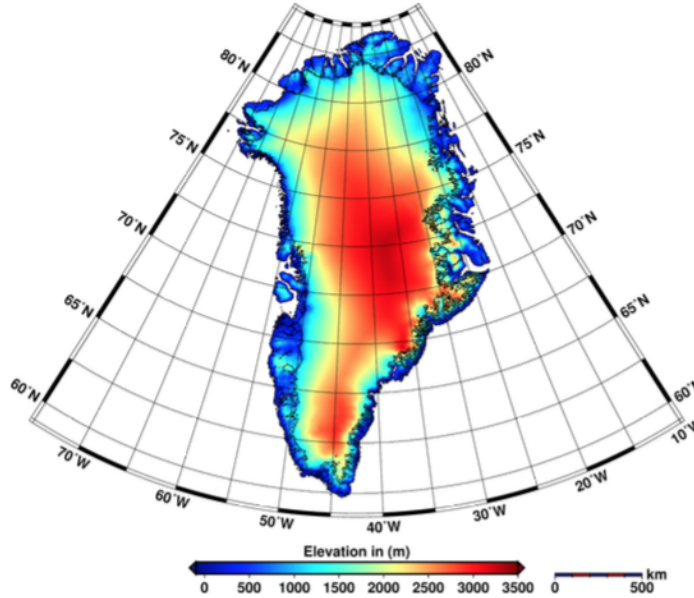


Figure 1.1: Modeled Greenland elevation derived from CyroSat-2. Figure 7 from Helm et al. 2014.

Due to the presence of the GIS, Greenland's stark topography impacts both synoptic-scale and mesoscale flows. The topography acts as a barrier to the synoptic-scale pattern as the flow is predominantly diverted around Greenland rather than over it (Scorer, 1988; Renfrew et al., 2008). This deflection has impacts on features downstream. For example, the Icelandic low is weakened due to the deflection of cold air around Greenland, which weakens cold air advection on the backside of the cyclone, reducing baroclinicity (Kristjánsson and McInnes, 1999).

One of the most well-known and common mesoscale phenomena that occur due to Greenland's topography are the katabatic winds (Scorer, 1988). Air at the top of the GIS is much colder than air at lower elevations. This results in a local-scale pressure gradient force directed towards the lower elevations from the ice sheet center resulting in a downslope flow. The katabatic winds are enhanced overnight

under stable conditions when air at the top of the GIS becomes extremely cold due to strong surface radiative cooling, resulting in a pronounced diurnal cycle of winds near the surface (Heinemann, 1999). Synoptic-scale pressure gradients can enhance this local-scale pressure gradient resulting in stronger katabatic winds (common over western and northwestern Greenland) or can oppose the local-scale pressure gradient and weaken, even reverse, the katabatic winds. The enhancement or weakening of the katabatic winds due to the synoptic-scale pressure gradient is a common occurrence over southeastern Greenland where synoptic-scale cyclones frequently pass (Rasmussen, 1989; Heinemann and Klein, 2002).

Northerly flow along the southeastern coast occurs when cold, stable flow is unable to ascend the GIS resulting in cold air damming. This creates a pressure gradient force directed toward the east that is geostrophically balanced by the Coriolis force resulting in northern winds (Moore and Renfrew, 2005). This phenomenon is known as barrier winds and can frequently exceed  $25 \text{ m s}^{-1}$  during the winter (Moore, 2003). Additionally, the extreme topography of Greenland’s southern tip, known as Cape Farewell, is linked to low-level wind events, occurring primarily during the winter, with winds exceeding  $25 \text{ m s}^{-1}$  (Moore and Renfrew, 2005). The term ‘tip jet’ refers to westerly, low-level jets that occur off the east coast of Cape Farewell and can be understood in terms of the Bernoulli function ( $B$ ) given by

$$B = C_p T + \frac{v^2}{2} + gz \quad (1.1)$$

where  $C_p$  is the specific heat at constant pressure,  $T$  is temperature,  $v$  the is wind speed,  $g$  is Earth’s gravitational constant, and  $z$  is height (Doyle and Shapiro, 1999). Due to the lack of dissipative processes, parcels within the tip jet conserve  $B$  along their trajectories. As a parcel descends over the GIS,  $z$  decreases. Since  $B$  is conserved,  $v$  must increase, for only slight increases in  $T$  (Doyle and Shapiro, 1999). Flow upstream accelerating as it is diverted around Cape Farewell may also



play a role in tip jet formation and strength (Doyle and Shapiro, 1999; Moore and Renfrew, 2005). Converse to the tip jet is the reverse tip jet that is characterized by a more compact, northeasterly, anticyclonically curved low-level jet (Moore, 2003; Moore and Renfrew, 2005). Moore and Renfrew (2005) propose that reverse tip jets are a result of barrier winds reaching the southern most point of Greenland going from a geostrophic to gradient wind balance (balance between the pressure gradient, Coriolis, and centrifugal forces). The flow becomes supergeostrophic and the reverse tip jet takes on an anticyclonic curvature as required by gradient wind balance.

From a large-scale perspective, atmospheric and ice sheet processes over Greenland are strongly influenced by the North Atlantic Oscillation (NAO) (e.g. van Loon and Rogers (1978); Bromwich et al. (1999); Box (2002)). The NAO can be defined as changes in the zonal wind magnitude over the northern Atlantic Ocean due to the pressure difference between the Icelandic, subpolar low and the Azores, subtropical high; the NAO index is calculated from the normalized mean winter pressure anomaly difference between Ponta Delagadas, Azores and Akureyri, Iceland (Rogers, 1984). In a positive phase of the NAO, both the Icelandic low and Azores high are stronger than average resulting in an increased pressure gradient across the northern Atlantic Ocean, and thus stronger zonal winds. Temperatures and precipitation over Greenland tend to be below average due the strong, cold, dry northerly winds on the backside of the Icelandic low (van Loon and Rogers, 1978; Chen et al., 1997; Bromwich et al., 1999). Cyclone activity increases in the Icelandic low region of  $60^{\circ}$  and  $65^{\circ}$ N around southeast Greenland during the positive phase of the NAO (Serreze et al., 1997; Rogers, 1990), and cyclones tend to follow a northeast path through the Atlantic Ocean (Rogers, 1990).

In the negative phase of the NAO, the Icelandic low and Azores high are weaker than normal leading to a decreased pressure gradient across the northern Atlantic

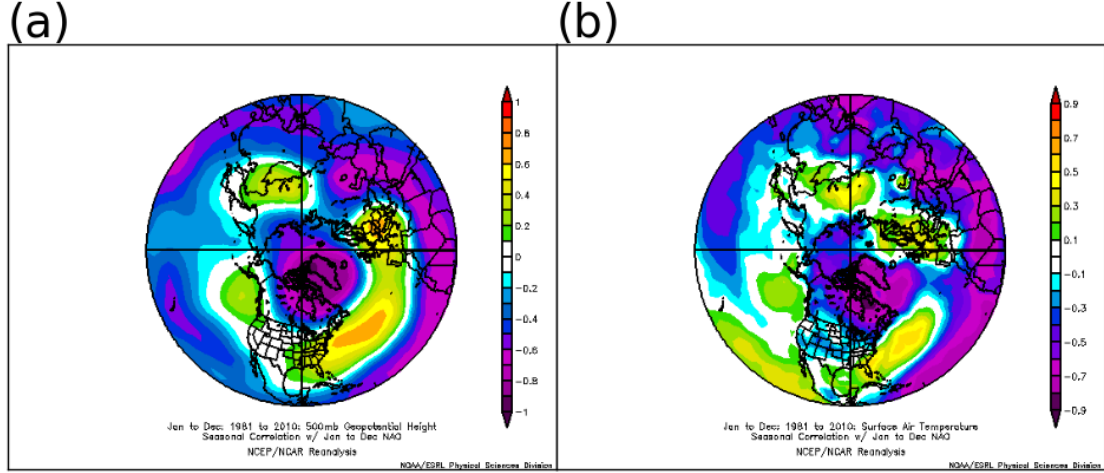


Figure 1.2: Correlation of the seasonally averaged (a) 500 hPa geopotential height and (b) surface air temperature from the NCEP/NCAR reanalysis with the NAO from January 1981 - December 2010.

Ocean and weaker zonal winds (Rogers, 1984). In this case, temperatures and precipitation across Greenland are above average due to warm, moist air advection (van Loon and Rogers, 1978); in the negative NAO phase, the Icelandic low shifts southward between  $50^{\circ}$  and  $60^{\circ}$ N (Serreze et al., 1997; Chen et al., 1997; Bromwich et al., 1999) which allows for the advection of warmer air over Greenland by southerly flow (Bromwich et al., 1999). Cyclone activity decreases in the  $60^{\circ}$  and  $65^{\circ}$ N region near southeast Greenland and increases in the  $40^{\circ}$  and  $60^{\circ}$ N region over the Atlantic Ocean (Serreze et al., 1997). Cyclones in the negative mode of the NAO track eastward in a more zonal track across  $45^{\circ}$ N (Rogers, 1990). High latitude blocking patterns are more frequent in the negative NAO phase (Woollings et al., 2008) helping understand the change in cyclone path and frequency. Correlations of the 500 hPa geopotential heights and surface air temperature from the

National Center for Environmental Prediction (NCEP)/National Center for Atmospheric Research (NCAR) reanalysis (Kalnay et al., 1996) with the NAO from January 1981 - December 2010 are summarized in Fig. 1.2.

The Arctic Oscillation (AO) describes the opposing monthly sea-level pressure anomalies between the Arctic and midlatitudes. The AO is similar to the NAO, but the AO is more centered in the Arctic, poleward of  $20^{\circ}\text{N}$ ; compared to the NAO, the AO patterns are more zonally symmetric (Thompson and Wallace, 1998). The 50 hPa height patterns are strongly correlated to the sea-level pressure pattern at the surface, and so the AO is thought of as the reflection of the stratospheric polar vortex (and its strength) at the surface (Thompson and Wallace, 1998). The daily AO index from the Climate Prediction Center is found by projecting the daily 1000 hPa height anomalies north of  $20^{\circ}\text{N}$  onto the leading mode of Empirical Orthogonal Function of monthly mean 1000 hPa heights from 1979 to 2000.

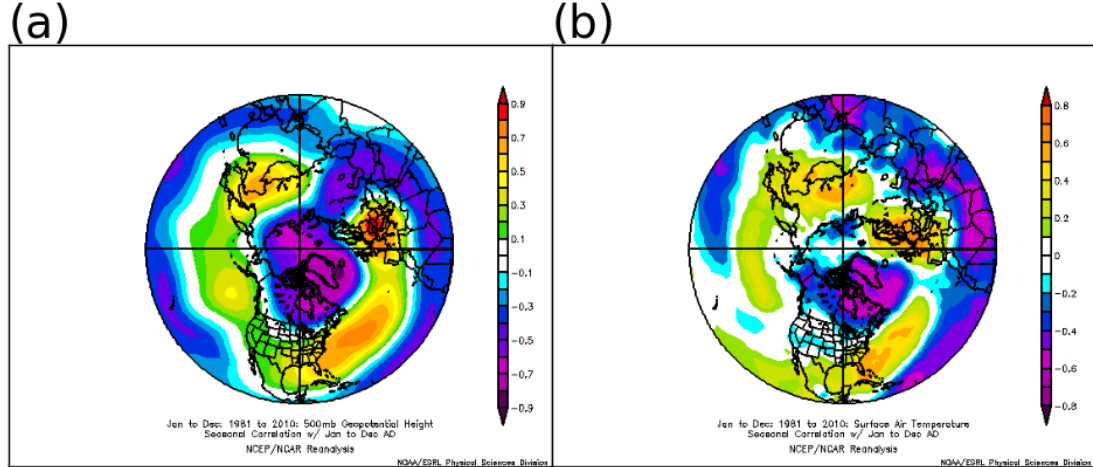


Figure 1.3: Correlation of the seasonally averaged (a) 500 hPa geopotential height and (b) surface air temperature from the NCEP/NCAR reanalysis with the AO from January 1981 - December 2010.

A positive (negative) AO index indicates a stronger (weaker) polar vortex (Thompson and Wallace, 1998). A stronger polar vortex (positive AO) is driven by a stronger pressure gradient force between the Arctic and midlatitudes, thus 500 hPa heights are lower (negative anomaly) and the Northern Hemispheric pattern is more zonal (Ripesi et al., 2012). This zonal pattern traps Arctic air over the region and, as a result, Greenland is typically much colder and drier, while synoptic-scale cyclones track through the northern Atlantic Ocean (Nuttall, 2012). The converse is true for the negative AO. With a more meridional, blocking Northern Hemispheric pattern (Ripesi et al., 2012), synoptic-scale cyclones are driven further south, while warm, moist air is transported north resulting in anomalously warm periods over Greenland. Correlations of the 500 hPa geopotential heights and surface air temperature from the NCEP/NCAR reanalysis (Kalnay et al., 1996) with the AO from January 1981 - December 2010 are summarized in Fig. 1.3.

A phenomenon known as the Greenland block is associated with above average sea-level pressure and 500 hPa heights (anticyclones) near Baffin Bay (Fig. 1.4). This area has a high occurrence of persistent blocking signatures (Knox and Hay, 1985). The Greenland block is related to the NAO, where a high frequency of Greenland blocking events is associated with a stronger, negative NAO phase that is shifted westward and displacement of the jet stream southward (Davini et al., 2012b). The opposite is true for the positive phase of the NAO, in that blocking is infrequent. High latitude blocking is onset by Rossby wave-breaking (RWB), which then increases the chances of more RWB events to maintain blocking (Woollings et al., 2008). The Greenland block is associated with a high frequency of cyclonic RWB events over the region on the poleward side of the jet (Davini et al., 2012a). Cyclonic RWB events are hypothesized to be a mechanism leading to a negative NAO phase, while anticyclonic RWB events lead to a positive phase (Benedict

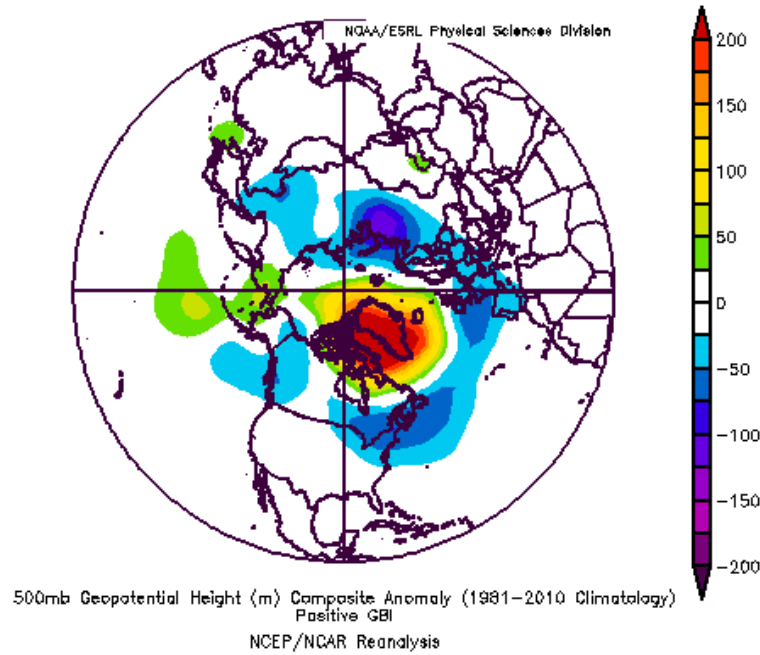


Figure 1.4: 500 hPa geopotential height composite anomalies from the NCEP/NCAR reanalysis for a positive Greenland Blocking Index. Images from NOAA Earth Science Research Laboratory Physical Science Division.

et al., 2004). Thus, it is hypothesized that the Greenland block (and the associated RWB and jet displacement) is a leading mechanism responsible for the NAO (Davini et al., 2012b).

The Greenland block not only has effects on the weather over Greenland, but also across the Northern Hemisphere. The geopotential heights over the Greenland Block Index (GBI) area are correlated with higher summertime temperatures over Greenland and increased GIS surface melt and runoff (Hanna et al., 2013) as this atmospheric pattern favors warm air advection over western Greenland (Fettweis et al., 2013). Blocking around Greenland also strongly influences the track of hurricanes in the northern Atlantic; Hurricane Sandy, for example, turned westward and made landfall over New Jersey due to an anomalously high Greenland blocking pattern (Mattingly et al., 2015).

The atmosphere over the central GIS is unique due to its high elevation. The high elevations result in a compression of the troposphere leading to very dry conditions. In the summer at Summit Station (Summit), Greenland (located in the center of the GIS, 72.6°N, 38.5°W), the air is relatively warmer and more moist with the maximum high temperature for the summer remaining below -10°C and precipitable water vapor (PWV) values exceeding 3 mm. In the winter at Summit, the air is relatively colder and drier with PWV values less than 1.5 mm and temperatures, on average, less than -35°C (Shupe et al., 2013).

Surface-based inversions in temperature and moisture are frequent over the central GIS due to the highly reflective surface from the presence of snow and ice resulting in a high surface albedo (Petty, 2004). Thus, the surface absorbs little incoming solar radiation while strongly emitting longwave radiation (Miller et al., 2013) resulting in a cold surface with the advection of warm, moist air aloft (Curry et al., 1996; Shupe et al., 2013). These inversions create a stable environment decoupling the surface from the atmosphere and limiting vertical mixing. From July 2010 to May 2012, radiosonde observations show surface-based inversions were present 64% of the time at Summit, Greenland (Miller et al., 2013). These inversions were most frequent and strongest during the winter, due to the significant loss of incoming solar radiation, and less frequent and weaker in the summer, due to a warming of the surface from incoming solar radiation, with inversions becoming more elevated (Shupe et al., 2013; Miller et al., 2013).

### **1.1.2 Past**

Ice cores from the center of the GIS have been used to construct temperature and precipitation records dating back thousands of years. During the Eemian interglacial period (nearly 130,000 years ago), the climate was  $8 \pm 4^\circ\text{C}$  warmer than the recent millennial mean and surface melt was frequent across the GIS.

Between 128,000 and 122,000 years ago, the GIS thinned by  $400 \pm 350$  m, and by the end of the period elevations were  $130 \pm 300$  m lower than today (Dahl-Jensen et al., 2013). Over the next 100,000 years, the climate moved toward a colder and drier period known as the Last Glacial Maximum. During the Last Glacial Maximum, around 20,000 years ago, temperatures were  $23 \pm 2^\circ\text{C}$  colder than today with average GIS surface temperatures between  $-55$  and  $-50^\circ\text{C}$  (Dahl-Jensen et al., 1998). Accumulation rates over the GIS were  $5.5$  to  $7 \text{ cm yr}^{-1}$  during the Last Glacial Maximum (Cuffey and Clow, 1997).

The central GIS quickly thickened between the Last Glacial Maximum and a warmer climate state known as the Holocene epoch (Raynaud et al., 1997; Cuffey and Clow, 1997). The transition to a warmer climate led to an increase in precipitation over the GIS before the ice sheet could respond to this warming (i.e., melt; Dahl-Jensen et al. (2013)). Temperatures have steadily increased (Dahl-Jensen et al., 1998) with an average warming of  $15^\circ\text{C}$  since the Last Glacial Maximum (Cuffey and Clow, 1997). Instrumental temperature records from 1873-2001 at Ilulissat/Jakobshaven, Greenland confirm this trend finding statistically significant warming in all seasons (Box, 2002), and coastal weather stations around Greenland have observed an upward temperature trend since the 1990s (Hanna et al., 2008). Ice cores show evidence of a significant thinning of the central GIS from the early Holocene to today (Raynaud et al., 1997), as well as evidence of surface melt across the central GIS in 1889 (Clausen et al., 1988).

### **1.1.3 Present**

In a simulated study of GIS melt, the average spatial extent of melt in 2010 was double that of the early 1970s with increasing melt duration (Mernild et al., 2011). Today, estimates of the total change in mass of the GIS are made by satellites and show a mass change of  $-258 \pm 41 \text{ Gt yr}^{-1}$  from January 2003 to November

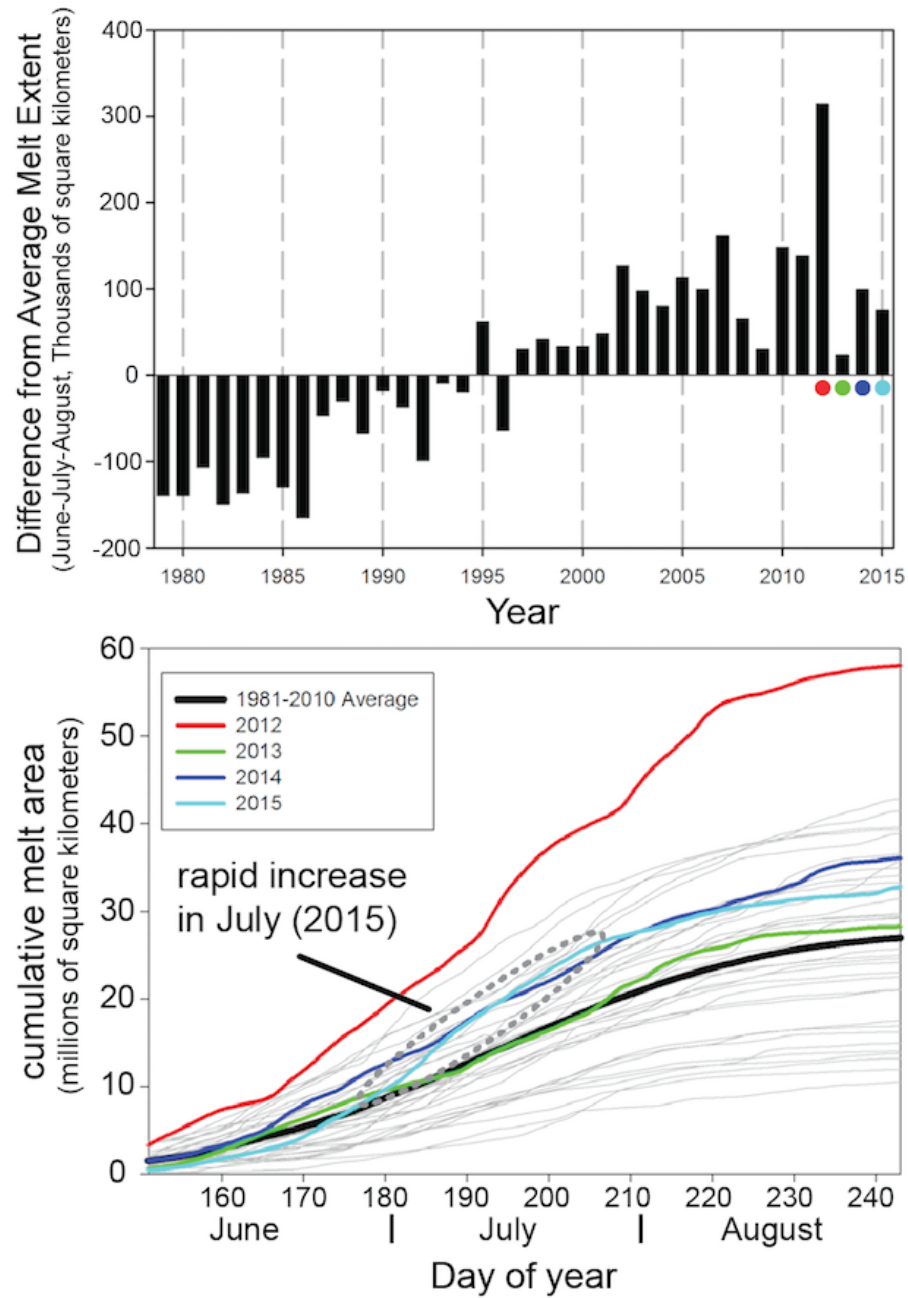


Figure 1.5: Annual melt extent anomalies from 1978 to 2015 (top) and daily cumulative melt area from 2012 to 2015 (bottom). Images from National Snow and Ice Data Center. Credit: Thomas Mote, University of Georgia



2012 (Velicogna and Wahr, 2013). There have been numerous record or near record years of spatial surface melt extent in the 21st century (McGrath et al., 2013), with all years at some point having above average melt (Fig. 1.5, Mote (2015)). These record melt years are driven by atmospheric anomalies that affect heat transport (Graversen et al., 2008), for example, the negative phase of the NAO favoring anticyclones over Greenland leading to warm air advection over the west coast of the GIS (Hanna et al., 2013; Fettweis et al., 2013); these anticyclones have become more frequent since 2000 (Mattingly et al., 2015). The most extreme recent melt event occurred on 12 July 2012 when 98.6% of the GIS experienced surface melt (Nghiem et al., 2012). Even locations in the center of the ice sheet recorded surface melt in the days surrounding this event, which last occurred in 1889.

The annual mean surface temperature from 2010-2012 was 1 to 2°C warmer than the 1950-1980 average (Dahl-Jensen et al., 2013). 6 of the warmest summers since the 1960s have occurred since 2003, and are associated with extreme surface melt years (Hanna et al., 2013). The near-surface air temperature over Summit, Greenland has significantly warmed from 1982 to 2011 with a trend of  $0.09 \pm 0.01^{\circ}\text{C year}^{-1}$ , placing it in the 99th percentile of all global warming trends; the trend from 1992 to 2011 further increased to  $0.12 \pm 0.02^{\circ}\text{C year}^{-1}$  (McGrath et al., 2013). Over western Greenland, the 0°C isotherm, a useful tool for determining if it is warm enough for melt, has been found to be rising in elevation at 35 m  $\text{year}^{-1}$  (McGrath et al., 2013), implying that melt is possible over a larger area of the GIS in recent years. Ice surface temperatures derived from the Moderate-resolution Imaging Spectroradiometer (MODIS) show a  $0.55 \pm 0.44^{\circ}\text{C decade}^{-1}$  warming trend. It is clear that in today's climate Greenland and the GIS are moving toward a warmer state.

#### 1.1.4 Future

In a warmer climate, the GIS could experience greater precipitation, as occurred in the Last Glacial Maximum-Holocene epoch transition and melt runoff (Houghton et al., 2001; Fettweis et al., 2012). By 2025, there is a 50% chance annual melt in the central GIS becomes routine (McGrath et al., 2013). The largest uncertainties lie in how fast the melt of the GIS will occur and how this impacts sea-level. These uncertainties arise from the complex atmospheric and oceanic interactions and their association with the GIS surface mass balance and ice dynamics. Studies have shown a large range in projections of sea-level rise over the next 100 years with as little as  $4 \pm 2$  cm (Fettweis et al., 2012) to as much as 14 cm (Seddik et al., 2012).

On the extreme end, a complete melting of the GIS would lead to a 7 m rise in sea-level (Wallace and Hobbs, 2006; Gregory and Huybrechts, 2006). Many studies have investigated the impacts of various forcings on GIS melt using numerical simulations. Stone et al. (2010) state that atmospheric CO<sub>2</sub> concentrations between 400 and 560 ppmv would lead to the collapse of the GIS; only atmospheric CO<sub>2</sub> concentrations at or below 350 ppmv allow for a stable GIS (Driesschaert et al., 2007). Gregory and Huybrechts (2006) state that a Greenland temperature change of  $4.5 \pm 0.9^\circ\text{C}$  and a global average temperature change of  $3.1 \pm 0.8^\circ\text{C}$  would likely lead to the complete loss of the GIS. A sustained radiative forcing of  $8.5 \text{ W m}^{-2}$  could lead to a complete melting of the GIS as well (Driesschaert et al., 2007). By,

$$\Delta T_{eq} = \lambda \Delta F \tag{1.2}$$

this radiative forcing ( $\Delta F$ ) could change Earth's equilibrium temperature ( $\Delta T_{eq}$ ) by  $5.95^\circ\text{K}$  for a climate sensitivity parameter, that includes feedback effects, ( $\lambda$ ) of  $0.7 \text{ }^\circ\text{K W}^{-1} \text{ m}^2$  (Wallace and Hobbs, 2006). Though these studies have investigated different forcings using numerical simulations, the conclusions are similar;

the complete melting of the GIS is a strong possibility moving forward in today's changing climate.

## 1.2 Arctic Mixed-Phase Clouds

Many meteorological phenomenon that occur in the Arctic are distinct from others across the globe. In particular, Arctic clouds are quite unique (Curry et al., 1996). One example is Arctic mixed-phase clouds (AMPCs), which are low-level stratus clouds composed of supercooled liquid water drops (term used interchangeably with liquid water or cloud liquid water hereafter) and ice crystals that occur frequently across the Arctic (Cesana et al., 2012; Bennartz et al., 2013). Due to a lack of observations, the meteorological understanding of AMPCs is poor; however, these clouds and their feedbacks have been thought to play an important role in Arctic amplification (Curry et al., 1996). This lack of understanding translates to these clouds, and Arctic clouds in general, being poorly simulated in climate and weather models which further leads to large uncertainties in the future state of the rapidly changing Arctic (Gregory and Morris, 1996; Stephens, 2005).

### 1.2.1 History of Arctic Cloud Observational Studies

Studies of Arctic clouds date as far back as the 1930s when a cloud climatology was compiled from the *Maud* expedition (Sverdrup, 1930). This first examination of Arctic clouds demonstrated that it is difficult to visually observe and classify them. Since then, vast improvements in meteorological instrumentation and the advent of remote sensing have lead to a growing knowledge of Arctic clouds.

Satellites make measurements throughout the Arctic; however, there are many issues with these data (Curry et al., 1996). The greatest problem is that the snow and ice surfaces that cover the Arctic are hard to distinguish from clouds due to

both having similar albedos and temperatures. As a result, there are major discrepancies between satellite datasets when it comes to cloud frequency and temperature (Curry et al., 1996; Serreze and Barry, 2005). These datasets, though, still provide crucial information about Arctic clouds. Some of the satellite cloud datasets are as follows: International Satellite Cloud Climatology (ISCCP) (Rossow and Schiffer, 1991), Earth Radiation Budget Experiment (Ramanathan et al., 1989), Advanced Very High Resolution Radiometer (AVHRR) Polar Pathfinder (APP) (Maslanik et al., 1997), Cloud-Aerosol Lidar and Infrared Pathfinder Satellite Observation (CALIPSO) (Winker et al., 2009; Cesana et al., 2012), and Moderate-resolution Imaging Spectroradiometer (MODIS) (Pagano and Durham, 1993; Wang and Key, 2005).

Instrumentation fixed on aircraft in the 1960s provided some of the earliest measurements of Arctic cloud microphysical properties (Dergach et al., 1960) and have been used in more recent field campaigns. One example is the Arctic Stratus Experiment (ASE) (Curry, 1986). Another example is the First ISCCP Regional Experiment (FIRE) Arctic Clouds Experiment (ACE) (FIRE-ACE) that took place from April to June 1998. This experiment used aircraft to collect data over Barrow, Alaska and the Arctic Ocean of clouds and their effects on the radiative transfer between the surface and atmosphere, and the influence of the surface on the clouds (Curry et al., 2000). These datasets are very specific temporally and spatially making it hard to draw general conclusions and climatologies.

In recent decades, cloud-atmosphere observatories have been set up across the Arctic (Uttal et al., 2015) to combat the lack of consistent observations. The Surface Heat Budget of the Arctic Ocean (SHEBA) project placed an observation station on the Arctic Ocean ice pack from 2 October 1997 to 12 October 1998 (Fig. 1.6). The drifting station recorded data of sea-ice characteristics, meteorological conditions, cloud microphysical properties, and oceanic conditions to



Figure 1.6: Locations of various Arctic field campaigns. Figure is originally from Shupe et al. (2013)

help improve model parameterizations (Uttal et al., 2002). The Arctic Summer Cloud Ocean Study (ASCOS) was similar to SHEBA as instrumentation was set on a Swedish icebreaker in the central Arctic from 2 August to 9 September 2008 (Tjernström et al., 2012) (Fig. 1.6). Additionally, the Department of Energy’s Atmospheric Radiation Measurements (ARM) program set up a surface site in Barrow, Alaska, which began taking measurements of clouds and radiation in March 1998 (Stamnes et al., 1999) (Fig. 1.6). The FIRE-ACE, SHEBA, and the ARM Barrow, Alaska site together formed an extensive dataset of Arctic clouds, radiation, and atmospheric structure (Stamnes et al., 1999; Curry et al., 2000; Uttal et al., 2002).

The FIRE-ACE, SHEBA, and the ARM Barrow, Alaska site projects were met with much success and provided data for the initial understanding of Arctic clouds.

These initial datasets revealed the frequent presence of AMPCs. In order to better understand the physical processes of AMPCs, the Mixed-Phase Arctic Cloud Experiment (M-PACE), as a part of the ARM program, ran from 27 September to 22 October 2004 with the objective to collect observations on AMPCs to further understand their microphysical, dynamical, thermodynamical, and radiative properties (Verlinde et al., 2007). Surface stations were set up at Barrow, Atkasuk, Oliktok Point, and Toolik Lake in Alaska and in-cloud measurements were taken by aircraft as well. Using new and advanced remote sensing instruments, M-PACE helped confirm findings from SHEBA, such as the existence of liquid water at temperatures well below the freezing point of water, and added to the in-situ datasets of AMPCs from FIRE-ACE. These in-situ datasets were further built upon by the Indirect and Semi-Direct Aerosol Campaign (ISDAC). ISDAC took place in April 2008 near Barrow, Alaska using ground and aircraft instrumentation to collect observations with the goal to see how aerosol concentration and composition changes affect cloud properties and their radiative forcing (McFarquhar et al., 2011).

The number of Arctic cloud-atmosphere observatories has increased sharply in the 2000s. For example, the “An Integrated Characterization of Energy, Clouds, Atmospheric state, and Precipitation at Summit” (ICECAPS) project has maintained a site since the summer of 2010 in the central GIS at Summit, Greenland (Shupe et al., 2013) (Fig. 1.6). Other sites have been built in countries such as Canada (Fig. 1.6), Russia, Finland, and Svalbard. The International Arctic Systems for Observing the Atmosphere (IASOA) began in 2007 with the goal to coordinate and integrate the data from observing sites to better understand how the Arctic is changing (Uttal et al., 2015). There are currently 10 sites apart of IASOA with 7 countries partaking in the endeavor. With new AMPC datasets, the number of AMPC modeling studies has grown as the simulations can be compared with the observations, further contributing to the understanding of AMPCs.

### 1.2.2 Characteristics

AMPCs are observed in all seasons; SHEBA observations show AMPCs occurring throughout 41% of the year (Shupe et al., 2006). The highest occurrence of AMPCs is in the summer and fall seasons with a minimum in the winter, though the presence of liquid water has been observed to occur 10-20% of the time at various Arctic locations in the winter (Shupe, 2011). At Summit, Greenland, the highest occurrence of liquid-bearing clouds occurs in July (67%), which is not surprising given the increase in moisture and temperature during the summer (Shupe et al., 2013; Miller et al., 2013). AMPCs most frequently occur at temperatures between  $-25$  and  $-5^{\circ}\text{C}$  (Shupe et al., 2006; Verlinde et al., 2007; de Boer et al., 2009), but have been observed as temperatures as low as  $-40^{\circ}\text{C}$  (Shupe et al., 2006).

AMPCs can either be low-level, single-layer stratiform clouds or deeper clouds with multiple layers of supercooled liquid water. In the case of single-layer AMPCs, ice water content (IWC) is greatest at the upper levels (Shupe et al., 2006), while liquid water content (LWC) is greatest just below the top of the cloud (Pinto, 1998). A thin layer of supercooled liquid water resides at the cloud top (Raubert and Tokay, 1991) and is the primary source where ice crystals form (Hobbs and Rangno, 1985; Shupe et al., 2006, 2008a; Solomon et al., 2009) by contact and/or condensation-freezing nucleation (Raubert and Tokay, 1991). As they grow, the ice crystals become heavier and fall out of this layer, as the ice crystals terminal velocity overcomes ascent, toward the middle and lower levels of the cloud and can precipitate out (Raubert and Tokay, 1991; Shupe et al., 2006). SHEBA observations indicate an annual average liquid water path (LWP) of  $61\text{ g m}^{-2}$  and ice water path (IWP) of  $42\text{ g m}^{-2}$  (Shupe et al., 2006). Typical values from M-PACE observations range from 50 to  $300\text{ g m}^{-2}$  for LWP and less than  $100\text{ g m}^{-2}$  for IWP (Shupe et al., 2008a). At Summit, Greenland, the LWP is typically below  $40\text{ g m}^{-2}$  (Miller et al., 2013). Regardless of the exact numbers, it can be concluded that AMPCs

are very much dominated by the liquid water phase as LWPs are much greater than IWPs (Shupe et al., 2015).

Liquid-bearing clouds most frequently reside at heights below 3 km above ground level (AGL) (Shupe, 2011), though they have been observed up to 8 km AGL in Barrow, Alaska (Shupe et al., 2015). Single-layer AMPC bases are typically between 700 and 2100 m AGL and are quite shallow with 200-700 m thicknesses (de Boer et al., 2009). AMPCs can be characterized as long-lived clouds as they persist, on average, for 12 hours with some of the most persistent cases lasting longer than 6 days (Shupe et al., 2006); an AMPC observed during SHEBA lasted 9 days (1 to 10 May 1998) (Zuidema et al., 2005).

It is important to keep in mind that AMPC characteristics are not the same throughout the Arctic; the characteristics vary from location to location (Curry et al., 1996). Additionally, the characteristics at a given location can change from season to season and year to year. For the rest of this thesis when referring to AMPCs, it is in reference to low-level, single-layer AMPCs.

### **1.2.3 Radiative Impacts**

Most clouds throughout the globe have a net cooling effect; that is, the presence of clouds cools the earth (Ramanathan et al., 1989) due to incoming solar radiation being reflected at cloud-top or absorbed by the cloud. However, for a majority of the year, AMPCs have a net warming effect at the surface (Intrieri et al., 2002; Miller et al., 2015) by which their optical properties maximize the surface downwelling longwave (LW) and shortwave (SW) fluxes (Bennartz et al., 2013). This is particularly important to consider in regards to the surface energy balance and ice melt. In order to further understand the radiative impacts of AMPCs on the surface, it is important to first understand what influences their radiative effects, i.e. their optical properties. To do so, it is useful to look at the total surface cloud



radiative forcing (CRF) as well as its SW ( $\text{CRF}_{\text{SW}}$ ) and LW ( $\text{CRF}_{\text{LW}}$ ) components. CRF is given by

$$\text{CRF} = \text{CRF}_{\text{LW}} + \text{CRF}_{\text{SW}} = (F_{\text{LW}}(A_c) - F_{\text{LW}}(A_c = 0)) + (F_{\text{SW}}(A_c) - F_{\text{SW}}(A_c = 0)) \quad (1.3)$$

where  $F_{\text{LW}}$  and  $F_{\text{SW}}$  are the net LW and SW surface fluxes, respectively, and  $A_c$  is the cloud fraction (Ramanathan et al., 1989; Shupe and Intrieri, 2004). Cloud radiative forcing is simply the radiative impact that clouds impart relative to clear skies ( $A_c=0$ ). A positive CRF indicates increased radiation (warming) at the surface, while a negative CRF indicates a reduction in radiation (cooling).

LW emission by a cloud, an atmospheric layer, or surface is given

$$F = \epsilon \sigma_{SB} T^4 \quad (1.4)$$

where  $\epsilon$  is the emissivity,  $\sigma_{SB}$  is the Stefan-Boltzmann constant, and  $T$  is the temperature of the cloud, atmospheric layer, or surface (e.g. Petty (2004)). Cloud LW emission, essentially  $\text{CRF}_{\text{LW}}$ , is determined by the cloud's macrophysical and microphysical properties. Differences in a cloud's temperature will change its LW emission (i.e.  $\text{CRF}_{\text{LW}}$ ); relatively warmer clouds, and thus relatively lower based clouds, have the largest  $\text{CRF}_{\text{LW}}$  (Shupe and Intrieri, 2004).

The only other way to change a cloud's LW emission, and  $\text{CRF}_{\text{LW}}$ , without changing its temperature is to change its emissivity. Cloud emissivity ( $\epsilon_c$ ) is given by

$$\epsilon_c = 1 - e^{-\tau_c} \quad (1.5)$$

where  $\tau_c$  is the cloud optical depth (e.g. Shupe and Intrieri (2004)). The equation for optical depth ( $\tau$ ) is given by

$$\tau(z_1, z_2) = \int_{z_1}^{z_2} \beta_e(z) dz = \int_{z_1}^{z_2} N \sigma_e(z) dz \quad (1.6)$$

where  $z_1$  and  $z_2$  are two heights levels,  $\beta_e$  is the extinction coefficient,  $N$  is the concentration of an atmospheric constituent, and  $\sigma_e$  is the extinction cross-section

(related to area) (e.g. Petty (2004)). In regards to microphysics, the cloud condensation nuclei (CCN) concentration is much higher than the ice-forming nuclei (IN) concentration (Yau and Rogers, 1996). As a result, the concentration of cloud liquid water drops is higher, though the drops are smaller, compared to ice crystals. For the same water content, the concentration of cloud liquid water drops is much higher than for ice crystals (Sun and Shine, 1994). The higher concentration of smaller cloud liquid water drops greatly increases the cloud's optical depth in comparison to the ice crystal concentration ( $N_{liquid}$  is greater than  $N_{ice}$ ). Thus, the radiative impacts of APMCs are strongly determined by the liquid phase rather than the ice phase (Shupe and Intrieri, 2004; Zuidema et al., 2005). As a result, the cloud optical depth is usually characterized as a function of liquid water path (LWP)

$$\tau_c = a_o \text{LWP} \quad (1.7)$$

where  $a_o$  (units are  $\text{m}^2 \text{g}^{-1}$ , thus  $\tau_c$  is a unitless quantity) is the total infrared flux mass absorption coefficient (Stephens, 1978). In the LW, clouds with LWPs greater or equal to  $30 \text{ g m}^{-2}$  emit nearly as blackbodies (Shupe et al., 2006), maximizing their LW emission and, therefore,  $\text{CRF}_{\text{LW}}$ ; for LWPs greater than  $30 \text{ g m}^{-2}$  there is little to no greater impact to  $\text{CRF}_{\text{LW}}$  than if the LWP is  $30 \text{ g m}^{-2}$ .

The transmission of incoming SW radiation through a cloud is a function of its optical depth; the transmittance through a cloud ( $J_c$ ) is defined as

$$J_c = e^{-\tau_c} \quad (1.8)$$

where  $J_c$  ranges from 0 to 1 with a value of 0 meaning no SW radiation makes it through the cloud layer and 1 meaning full transmission through the cloud layer (e.g. Petty (2004)). Since cloud optical depth is a primarily function of LWP, the transmission of incoming SW radiation is greatly effected by changes in LWP. As LWP increases the amount of incoming SW radiation transmitted through the cloud and to the surface decreases. The cloud is either absorbing more radiation or

scattering back more radiation, i.e cloud albedo increases. The weaker transmission of incoming SW radiation due to the increasing LWP results in a greater cooling at the surface,  $\text{CRF}_{\text{SW}}$  is negative (Shupe and Intrieri, 2004). The impact of LWP on SW transmission does not have a “leveling-off” effect or maximum impact that is seen in the  $\text{CRF}_{\text{LW-LWP}}$  relationship (when the LWP greater or equal to 30  $\text{g m}^{-2}$ ).

The  $\text{CRF}_{\text{SW}}$  is influenced also by the solar zenith angle and surface albedo. To include the effects of solar zenith angle, the equation 1.8 is modified by

$$J_c = e^{-\frac{\tau_c}{\cos(\Theta)}} \quad (1.9)$$

where  $\Theta$  is the solar zenith angle (e.g. Petty (2004)). Such that for a greater solar zenith angle the greater optical path the radiation must travel. For an increasing solar zenith angle (sun angle closer to the horizon), the  $\text{CRF}_{\text{SW}}$  approaches 0 as little incoming solar radiation will be getting to the surface regardless if there is a cloudy or clear sky (Shupe and Intrieri, 2004). The surface albedo effects the amount of incoming SW radiation absorbed at the surface effecting the net SW flux,  $F_{\text{SW}}$ , and  $\text{CRF}_{\text{SW}}$ .  $F_{\text{SW}}$  is given by

$$F_{\text{SW}} = F_{\text{SW}}^{\downarrow}(1 - \alpha_{\text{sf}c})J_c \quad (1.10)$$

where  $F_{\text{SW}}^{\downarrow}$  is the downwelling SW flux,  $\alpha_{\text{sf}c}$  is the surface albedo, and  $J_c$  is the cloud transmittance given by 1.9 (e.g. Shupe and Intrieri (2004)). For a decrease in surface albedo the  $\text{CRF}_{\text{SW}}$  becomes more negative as more radiation is absorbed at the surface in the clear-sky scene (Shupe and Intrieri, 2004).

A long-lived (1 to 10 May 1998) AMPC event during SHEBA had an average  $\text{CRF}_{\text{SW}}$  of  $-12 \text{ W m}^{-2}$  and  $\text{CRF}_{\text{LW}}$  of  $53 \text{ W m}^{-2}$  for a total CRF of  $41 \text{ W m}^{-2}$  (Zuidema et al., 2005). The annual mean SHEBA CRF for the LW and SW components for liquid-bearing clouds is 52 and  $-21 \text{ W m}^{-2}$ , respectively, compared to 16 and  $-3 \text{ W m}^{-2}$  for ice clouds (Shupe and Intrieri, 2004). Clouds during

SHEBA warmed the surface through most of the year except for a brief period in the summer due to the effects of a lower surface albedo and weaker transmission of the incoming solar radiation due to clouds (Intrieri et al., 2002). At Summit, Greenland, the average annual CRF is  $33 \text{ W m}^{-2}$  and is positive for all months, resulting in year-round surface warming, with the greatest CRF in July (Miller et al., 2015), which is quite different than findings from SHEBA. This difference is due to the high annual surface albedo at Summit;  $\alpha_{sfc}$  is approximately 1 leaving  $F_{SW}$  and  $\text{CRF}_{SW}$  nearly 0 (Equation 1.10). The CRF at the surface is controlled largely by  $\text{CRF}_{LW}$  as the incoming SW radiation reflected at cloud top or absorbed by the cloud would be reflected anyway due to the high albedo of the GIS surface, so the effects of the  $\text{CRF}_{SW}$  are limited (Miller et al., 2015).

#### 1.2.4 Formation and Maintenance Processes

Theoretical studies of mixed-phase clouds date back to the early 1900s. The Wegener-Bergeron-Findeisen (WBF) mechanism (Wegener, 1911; Bergeron, 1935; Findeisen, 1938) describes the process by which precipitation can form within mixed-phase clouds, i.e. clouds composed of supercooled liquid water drops and ice crystals (Glickman, 2000). At a given temperature below  $0^\circ\text{C}$ , the saturation vapor pressure with respect to ice is less than that with respect to liquid water, which results in a supersaturated environment with respect to ice and subsaturated environment with respect to liquid water. As a result, the liquid water drops evaporate and lose mass, while the ice crystals grow by vapor deposition. This process leads to the glaciation of mixed-phase clouds, which past theoretical studies show for certain conditions can occur in 20-40 minutes (Korolev and Isaac, 2003). AMPCs frequently persist for days; it is not known how these clouds persist for such long periods of time when the WBF theory dictates that they should rapidly convert to a single-phase ice cloud.

There are limitations to the WBF process and certain conditions can render it less effective (Korolev, 2007). If an environment is supersaturated with respect to both liquid water and ice (both saturation vapor pressures are less than the cloud vapor pressure), the WBF process is less efficient and both phases can be maintained. Minimum vertical velocities, anywhere from a few  $\text{cm s}^{-1}$  to  $\text{m s}^{-1}$ , are required for such an environment to occur. These vertical velocities are dependent on temperature, pressure, and concentration and mean radius of ice crystals (Korolev and Mazin, 2003). In such an environment, both ice crystals and supercooled liquid water drops grow at the same time (Korolev, 2007). In order for supercooled liquid water to be produced, not only must the air be supersaturated with respect to water, but the condensate supply rate needs to be greater than the mass diffusional growth rate of ice crystals. These conditions have been shown to exist over a range of temperatures and ice crystal concentrations, even at temperatures colder than  $-30^{\circ}\text{C}$  (e.g. Rauber and Tokay (1991)). At the top of the cloud, ice crystal sizes and concentrations are smaller as larger ice crystals fall toward the bottom of the cloud. The cloud top provides a unique environment for supercooled liquid water drops to exist as the WBF process is less effective there due to smaller and lesser presence of ice crystals.

Case studies done using numerical modeling simulations, observational datasets, as well as theoretical studies help provide insight into at least some of the processes involved in AMPC maintenance. Morrison et al. (2012) describe a framework of processes that are expected contribute to the persistence of AMPCs (Fig. 1.7). These processes are divided into two categories: synoptic-scale and local-scale processes.

The local scales-of-variability of importance for AMPC maintenance are typically on the order of 0.5-10 km, particularly the formation and maintenance is driven by cloud circulations (Shupe et al., 2008a). Local, turbulent updrafts are

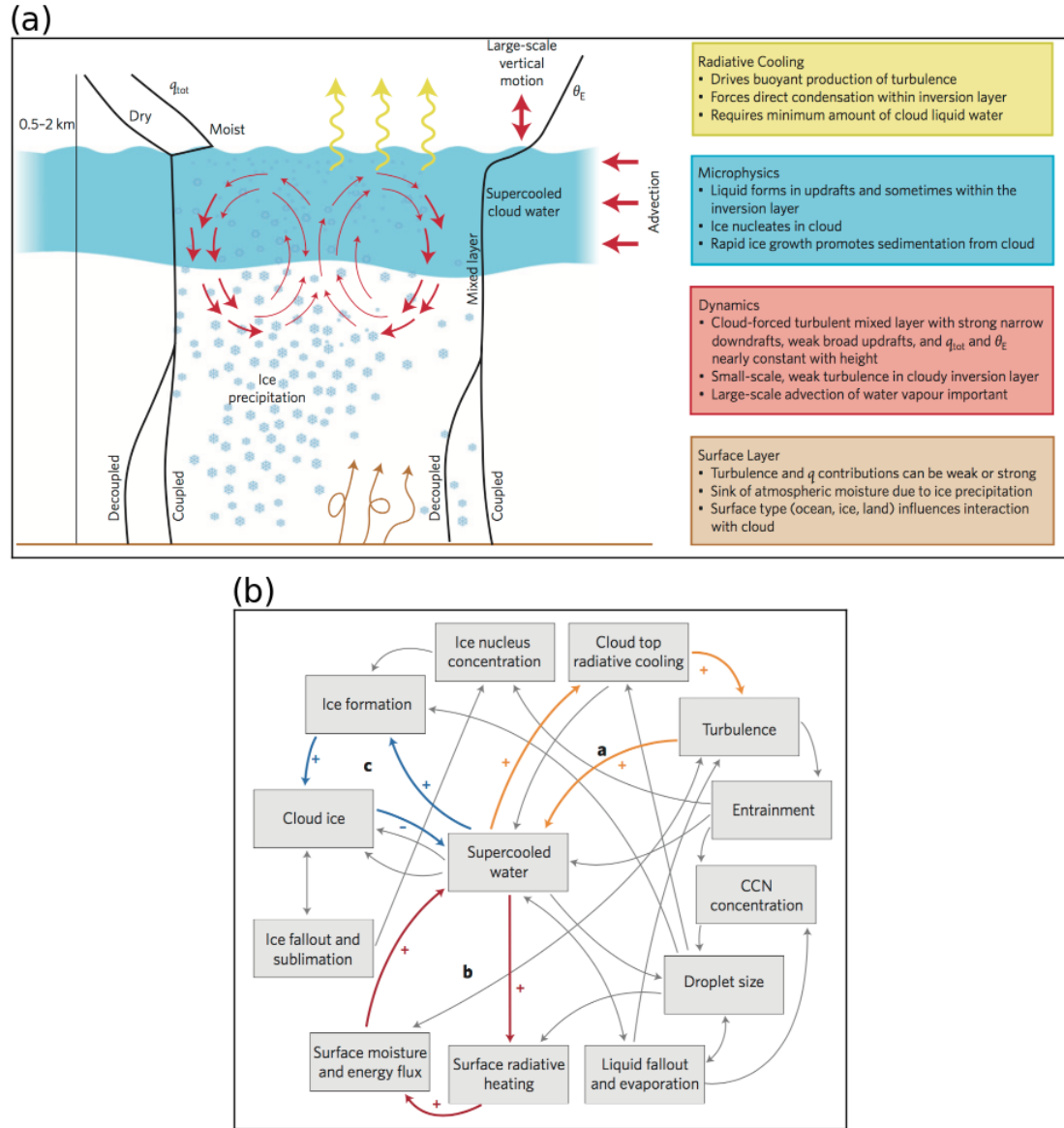


Figure 1.7: Original schematics from Morrison et al. (2012) highlighting their (a) conceptual model illustrating the main processes and simplistic physical structure of persistent Arctic mixed-phase clouds, and (b) hypothesized processes, feedbacks, and interactions linked to Arctic mixed-phase clouds.

critical for the production of supercooled liquid water (Rauber and Tokay, 1991; Shupe et al., 2008a); these updrafts are a means for the production of liquid water as water vapor near the surface is lifted and condensed, maintaining the liquid water supply in the cloud (Morrison et al., 2011, 2012). These cloud liquid water drops are advected upward by the updrafts (Solomon et al., 2009). For liquid water to be produced, a minimum updraft velocity must be reached. This threshold velocity is highly dependent on cloud temperature as well as ice crystal size and concentration; the minimum updraft velocity is greater for colder clouds with larger ice crystals and higher ice crystal concentrations than for warmer clouds with smaller ice crystals and lower ice crystal concentrations (Rauber and Tokay, 1991). For clouds low in ice concentration ( $N_{ice} = 10 \text{ L}^{-1}$ ) with smaller sized ice crystals (diameter of  $100 \mu\text{m}$ ), the threshold updraft velocity is  $0.4 \text{ m s}^{-1}$  for a temperature of  $-32^\circ\text{C}$ ; for  $-10^\circ\text{C}$  with the same ice crystal concentration and size, the minimum updraft velocity is less than  $0.1 \text{ m s}^{-1}$  (Rauber and Tokay, 1991). Increasing  $N_{ice}$  to  $100 \text{ L}^{-1}$  for a temperature  $-10^\circ\text{C}$  requires updraft velocities to be at least  $0.39 \text{ m s}^{-1}$ , while increasing the ice crystal diameter to  $1000 \mu\text{m}$  requires updraft velocities to be at least  $0.61 \text{ m s}^{-1}$  (Rauber and Tokay, 1991). Updrafts associated with AMPCs have been observed to be  $0.4 \text{ m s}^{-1}$  on average (Shupe et al., 2008a).

Cloud-top LW cooling (CTLC) is thought to be a key process in AMPC persistence in that it helps induce the necessary updrafts that lead to condensation (Morrison et al., 2012). One case study of an AMPC during SHEBA observed CTLC rates over  $65 \text{ }^\circ\text{K day}^{-1}$  (Zuidema et al., 2005). Such strong CTLC is due the presence of cloud liquid water (Hogan et al., 2003). The radiative heating rate is defined by

$$\left. \frac{\partial T}{\partial t} \right|_{rad} = -\frac{1}{\rho C_p} \frac{\partial F_{net}(z)}{\partial z} \quad (1.11)$$

where  $\frac{\partial T}{\partial t}_{rad}$  is the temperature change due to radiative effects,  $\rho$  is the air density,  $C_p$  is the specific heat at constant pressure, and  $\frac{\partial F_{net}(z)}{\partial z}$  is the vertical gradient of the net radiative flux with  $F_{net}(z)$  being  $F_{up}(z) - F_{down}(z)$  (e.g. Petty (2004)). The greatest heating or cooling will occur in areas with the greatest vertical change in  $F_{net}$ , which corresponds to the strongest vertical gradient in optical depth. Warming or cooling of a layer can also be thought of in the sense of radiative flux divergence, where radiative flux divergence (convergence) leads to cooling (warming). At cloud-top, there is the strong emission of LW radiation ( $F_{up}$ ), while the atmosphere above the cloud is emitting weakly in the LW ( $F_{down}$ ) in comparison, thus resulting in locally, strong radiative flux divergence and CTLC.

Near the cloud-base, there is also a slight warming associated with latent heat release and LW radiative flux convergence (Pinto, 1998). Strong cooling at cloud-top and weak warming at cloud-base act to destabilize the cloud layer (Curry et al., 1996; Pinto, 1998) enhancing buoyancy-driven turbulent motions (Lilly, 1968; Pinto, 1998; Wang et al., 2001) that further lift and condense air, replenishing the cloud liquid water (Curry, 1986; Morrison et al., 2011; Solomon et al., 2011). A similar mechanism has been proposed in understanding the maintenance of tropical cirrus (destabilization due to radiative effects leads to cloud-scale circulations) (e.g. Ackerman et al. (1988)). Since CTLC cooling rates are much stronger than heating rates at the cloud base (Pinto, 1998), the former is primarily responsible for the driving the turbulence (Wang et al., 2001). There is a minimum CTLC necessary to drive these turbulent motions (Pinto, 1998), which is inherently linked to cloud emission and the LWP. Conversely, the warming due to incoming SW radiation in the cloud reduces LWP and CTLC, leading to weaker turbulent motions (Zuidema et al., 2005; Petters et al., 2012). This is particularly so for clouds with larger sized cloud liquid water drops where the absorption of incoming SW radiation is



greater and the resultant heating can cause cloud droplets to evaporate leading to cloud dissipation (Herman and Goody, 1976).

Single-layer AMPCs have been frequently categorized and observed as boundary layer clouds (e.g. Curry et al. (1988), Curry et al. (1996), Pinto (1998)) as they often reside within or at the top of the atmospheric boundary layer due to their low cloud base heights and relatively thin nature (de Boer et al., 2009; Shupe et al., 2008a; Shupe, 2011). CTLC promotes turbulent mixing resulting in a well-mixed layer below cloud-top (Curry, 1986). This turbulent mixing brings cooler air from the cloud top over a warm surface enhancing the surface sensible and latent heat fluxes (Wang et al., 2001). Additionally, the surface fluxes are greater simply due to the cloud’s warming effect on the surface (Morrison and Pinto, 2006). AMPCs that are coupled with the surface are influenced by the surface fluxes further leading to their persistence (Morrison and Pinto, 2006).

Local microphysical processes also play an important role. Certain aerosols can act as IN or CCN, strongly influencing the microphysics of AMPCs. The persistence of AMPCs is sensitive to the concentration of IN (Jiang et al., 2000; Morrison et al., 2011). Higher concentrations of IN will lead to greater ice crystal nucleation, a more effective WBF process, and cloud glaciation (Morrison et al., 2011), while additionally decreasing the cloud liquid water content, CTLC, and turbulence. Thus, the lifetime of AMPCs is highly dependent on IN concentration (Pinto, 1998; Morrison et al., 2005). Changes in CCN concentration affect the cloud liquid water droplet size and concentration (Morrison et al., 2005) altering the cloud’s LW emission. The higher concentration of CCN increases the cloud liquid water concentration, and thus cloud emissivity and its emission (Garrett and Zhao, 2006). Modeling cases studies have shown the cloud liquid water is dependent not only on ice number concentration, but also on snow number concentration (Solomon et al., 2009).

Synoptic-scale processes can influence AMPC formation and longevity, as well. Large scale rising motion can lead to an increase in the liquid water supply (Zuidema et al., 2005). However, long-lived AMPCs have been observed to occur in both the presence of synoptic-scale rising and sinking motion suggesting that synoptic-scale mechanisms are not solely responsible for their longevity (Pinto, 1998). Transport on the synoptic-scale is important to consider, especially in regard to moisture, temperature, and aerosols. The advection of water vapor is a key component for AMPCs (Pinto, 1998). The advection of warm, moist air aloft results in moisture inversions that occur near cloud top (Curry et al., 1988) and is an important factor in controlling coupling (or lack thereof) between the cloud and the surface (Sedlar et al., 2012; Savre et al., 2015). Entrainment at cloud-top due to cloud-generated turbulence can mix moist air downward from the moisture inversion to maintain the cloud, even in the absence of moist air beneath the cloud (Solomon et al., 2011). AMPCs are insensitive to the moisture source (moisture inversion or moisture near surface air) just so long there is sufficient moisture (Solomon et al., 2014). The transport of aerosols from the midlatitudes into the Arctic is important to consider as there are few local sources for IN over ice pack or the GIS, which greatly impact the cloud microphysics as discussed above (Pinto, 1998). The advection of upper-level ice clouds by the synoptic-scale flow can result in sedimentation falling into a lower-level, mixed-phased cloud leading to the depletion of liquid water in the cloud via cloud glaciation (Zuidema et al., 2005).

The above mentioned processes and their various feedbacks and interactions (summarized in Fig. 1.7) come together to form a distinct, quasi-steady cloud system (Morrison et al., 2012). Observations from SHEBA point toward two states in the Arctic: radiatively clear (clear or radiatively unimportant clouds) and opaquely cloudy (Stramler et al., 2011). These states are long-lived with a rapid transition from one state to the other, indicating that the given state evolves on both fast

and slow timescales (Morrison et al., 2012). From these findings, Morrison et al. (2012) hypothesize that the various local (fast timescale) processes and interactions (Fig. 1.7b) drive the persistence of AMPCs, but significant changes to the synoptic-scale environment (slow timescale) disrupt the balance between the local processes leading to a change in state. The particular meteorological patterns that favor the two states are unknown.

Low-level, single-layer AMPCs over the central GIS differ in some respect from those observed over the open Arctic Ocean or sea-ice. Clouds over the central GIS are more frequently decoupled from the surface compared to those over Beaufort Sea near Barrow, Alaska, for example, due to the frequent presence of a surface-based inversion (Shupe et al., 2013; Miller et al., 2013) making the contributions from surface fluxes negligible. However, during the summer when the inversions become more elevated (Shupe et al., 2013) or CTLC-driven mixing results in a well-mixed layer (Curry, 1986) the influence of surface fluxes is important. Moisture advection is particularly important at Summit as there are no local sources of moisture (Shupe et al., 2006; Morrison et al., 2012). However, the characteristics, structure, and impacts remain similar to those found elsewhere in the Arctic (Shupe et al., 2013).

### 1.3 Importance of Studying Mixed-Phase Clouds Over Greenland

In general, surface net radiative fluxes are sensitive to cloud cover (Walsh and Chapman, 1998; Miller et al., 2013). Using different cloud climatologies and a radiative transfer model, Cawkwell and Bamber (2002) found a maximum difference of  $40 \text{ W m}^{-2}$  in net surface radiative fluxes over the GIS between cloud climatologies. Such dramatic differences in the net surface radiative flux have major

impacts on the surface energy balance. The surface energy balance equation for snowpack is given by

$$M = H_{sen} + H_{lat} + G_s + F_{net} \quad (1.12)$$

where  $M$  is the amount of melt energy,  $H_{sen}$  is the sensible heat flux,  $H_{lat}$  is the latent heat flux,  $G_s$  is the subsurface heat flux, and  $F_{net}$  is the net radiative flux at the surface (Kuipers Munneke et al., 2009).  $F_{net}$  can further be broken down into SW and LW components

$$F_{net} = F_{SW}^{\downarrow} - F_{SW}^{\uparrow} + F_{LW}^{\downarrow} - F_{LW}^{\uparrow} \quad (1.13)$$

where at the surface  $F_{SW}^{\downarrow}$  is the downwelling SW radiation flux,  $F_{SW}^{\uparrow}$  is the upwelling SW radiation flux,  $F_{LW}^{\downarrow}$  is the downwelling LW radiation flux, and  $F_{LW}^{\uparrow}$  is the upwelling LW radiation flux (Bennartz et al., 2013). The direct impacts that clouds have on  $F_{net}$  is through the the transmission of incoming SW radiation to the surface ( $F_{SW}^{\downarrow}$ ) and their LW emission ( $F_{LW}^{\downarrow}$ ), i.e.  $CRF_{SW}$  and  $CRF_{LW}$ , which are influenced by LWP.

As previously stated, AMPCs across the central GIS have a positive net surface radiative flux year around (Miller et al., 2015), which has implications on the surface energy balance and central GIS melt. The historic melt event in July 2012 that occurred across the central GIS, including Summit, is linked to low-level AMPCs (Bennartz et al., 2013). The  $F_{SW}^{\downarrow}$  and  $F_{LW}^{\downarrow}$  CRFs are maximized for clouds with LWPS between 10 and 40 g m<sup>-2</sup>, i.e.  $F_{net}$  is greatest. It is within this range that clouds are optically thin enough to transmit most of the incoming SW radiation, while having substantial LW emission (Bennartz et al., 2013). For greater LWPs, the transmission of SW radiation is weak, and for lesser LWPs LW cloud emission is weak. A modeling study by Solomon et al. (2016) supports the results of Bennartz et al. (2013) in that the melt would have not occurred without the presence of low-level AMPCs. Additionally, the clouds warmed the subsurface of the GIS, which further encouraged surface melt (Solomon et al., 2016). AMPCs

also increase the runoff of GIS meltwater; however, the increase is not directly due to surface warming, but rather due to the hindrance of refreezing from reduced surface radiative cooling. From September 2007 through September 2010, only 45% of meltwater refreezed in the presence of clouds compared to 58% in clear sky conditions (Van Tricht et al., 2016).

Due to their frequent occurrence and radiative impacts to the surface energy balance, it is important to understand not only why AMPCs form, but also why they are so long-lived in order to better represent them and their radiative impacts in climate models. As the Arctic climate is rapidly changing, it is critical to correctly model its state and, more specifically, GIS melt. The melting of the GIS will greatly impact sea-level and, in turn, threaten civilizations at low elevations around the world (Nicholls and Cazenave, 2010).

## 1.4 Thesis Motivations and Hypothesis

The hypothesis proposed by Morrison et al. (2012) provides an interesting framework for why AMPCs could possibly be so long-lived. This research expands upon the Morrison et al. (2012) hypothesis and framework. The hypothesis for this thesis is that local processes lead to the longevity of AMPCs, while synoptic-scale processes are necessary to create a favorable thermodynamic environment. This environment is important in that it ultimately drives the dynamical, local processes (i.e. moisture inversion, surface coupling, etc.). This creates an intimate connection between the synoptic and local scales. The hypothesis will be tested by using a numerical model for case study of an AMPC event that occurred over Summit, Greenland from 20 to 24 July 2012.

Previous modeling studies of AMPCs have used large eddy simulations (LESs) (Morrison et al., 2011; Solomon et al., 2011, 2014; Savre et al., 2015), cloud-resolving models (CRMs) (Klein et al., 2009; Morrison et al., 2009b, 2011; Solomon

et al., 2011), or single-column models (SCMs) (Girard and Curry, 2001; Morrison et al., 2005; Klein et al., 2009; Morrison et al., 2009b), while few have used regional models (Morrison and Pinto, 2006; Solomon et al., 2009, 2016). The Weather Research and Forecasting (WRF) model, a regional model, is used in this research to look at the synoptic and local scale influences on this cloud event.

LESs have a horizontal grid spacing of 50 m or less with domains as large as 100 km and simulation times from a few hours to one day. Due to its fine resolution, LESs can explicitly resolve shallow clouds and boundary layer processes, but there is still a need to parameterize (i.e. simulate processes that are not explicitly resolved) processes such as turbulence and microphysics. CRMs are similar to LESs, but CRMs have different sub-grid scale parametrizations, larger horizontal grid spacing (usually  $\sim 1$  km), and can resolve deeper clouds (Guichard et al., 2004). SCMs simulate a single vertical atmospheric column using the physics parameterizations of a model (Randall and Cripe, 1999).

On the other hand, regional models, such as WRF, have much coarser resolution than LESs, but can more easily be used to perform simulations over longer periods of time and over larger regions; however, due to their coarser representation, regional models often do not resolve convective or boundary layer processes, and therefore, these processes must be parameterized. Regional models are not forced directly with observations, but with state estimates interpolated from gridded global or larger-scale models. The goal of this thesis is to study the processes on both the synoptic and local-scale, thus a regional model is most suitable for diagnosing the important processes on both scales.

Caution must be exercised when performing modeling studies of AMPCs. Numerical simulations of these clouds often struggle to accurately simulate the frequency, persistence, and properties, such as LWP, of these clouds resulting in bias surface radiative fluxes (Girard and Curry, 2001; Morrison et al., 2005; Morrison

and Pinto, 2006; Klein et al., 2009; Morrison et al., 2011). Some errors, for example, are due the microphysical parameterizations as they have been developed for regions that are microphysically and thermodynamically different from the Arctic (Curry et al., 1996; Beesley and Moritz, 1999). However, more complex double moment schemes perform better than single moment schemes and have been shown to better represent observations (Morrison et al., 2005; Morrison and Pinto, 2006; Solomon et al., 2009), lending credence to modeling studies of AMPCs.

## **Chapter 2     Data**

### **2.1   Numerical Weather Prediction Models**

One of the most valuable tools that meteorologists have in understanding the atmosphere are numerical weather prediction models. These models allow for spatially and temporally complete and consistent datasets over a given domain, unlike observations which are for a certain location, inconsistent spatially and temporally, and can often be incomplete.

#### **2.1.1   Weather Research and Forecasting Model**

The Weather Research and Forecasting model (WRF) is one of the most well-established numerical weather prediction models in the field of meteorology. It can be used for operational or research purposes, and is employed by numerous academic, research, and governmental institutions. WRF features two dynamical solvers: the Advanced Research WRF (ARW) (Wang et al., 2007) and the Nonhydrostatic Mesoscale Model (NMM). This research uses the ARW solver (WRF-ARW) version 3.6.1. The ARW solver uses the fully compressible, Euler nonhydrostatic equations. In the horizontal, Arakawa C-grid staggering is used, and in the vertical terrain-following, eta levels are used. Land-surface, planetary boundary layer, atmospheric and surface radiation, microphysics and cumulus convection are parameterized physics with each having several schemes to choose from. WRF-ARW is initialized and the boundary conditions are updated throughout the simulation with other gridded model data.



The WRF Pre-Processing System (WPS) is used prior to running the WRF-ARW. WPS defines the simulation grid, and interpolates the land surface characteristics and meteorological data from the forcing dataset (often alternately stated as the initial and boundary conditions) to the domain. Data for the forcing dataset are often from global models or reanalysis. Once this is complete, the model can be run, and following a successful simulation the output can be post-processed and visualized. A flow chart for running WRF is given in Fig. 2.1.

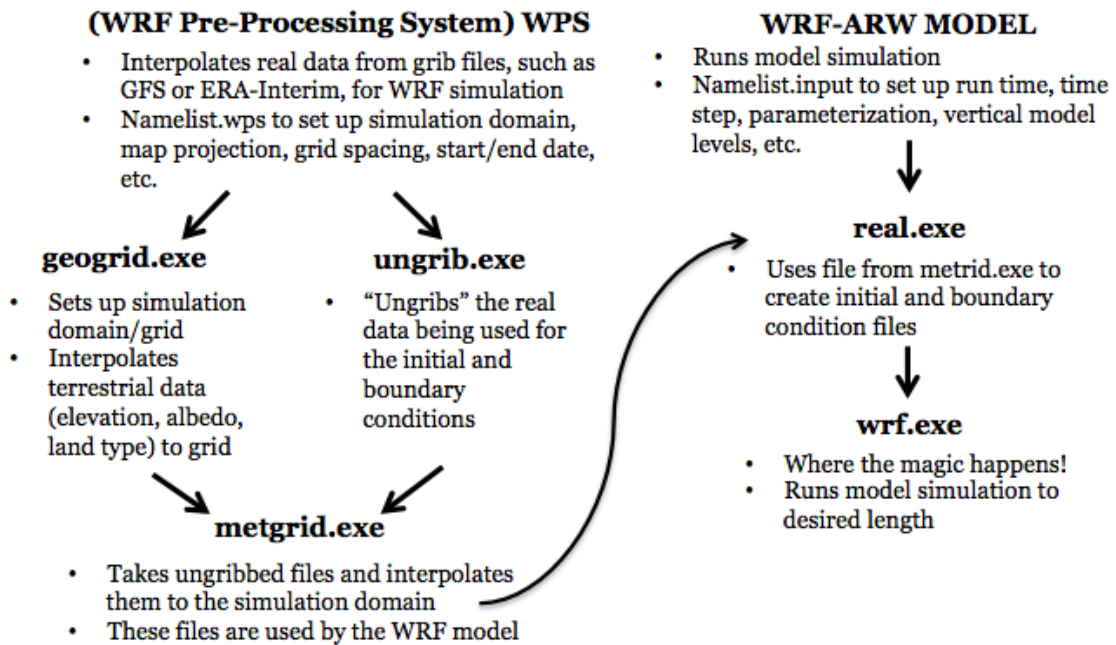


Figure 2.1: Flow diagram of running the WRF and its different components.

### 2.1.2 Polar Weather Research and Forecasting Model

A polar optimized version of WRF-ARW 3.6.1 (PWRF) is maintained by the Byrd Polar Research Center Polar Meteorology Group of The Ohio State University (Hines and Bromwich, 2008). The core of the PWRF code is the same as the WRF

code. A major difference between PWRF and WRF is the ability to specify sea-ice and the associated land-mask, and allowing it to update during the simulation; this is done in WPS. Additionally, changes are made to the Noah land surface model. The snow and ice LW emissivity, and snowpack density, heat capacity and conductivity are changed to reflect values more representative of the Arctic. Thick snowpack is also treated as a part of the prognostic subsurface layers rather than a layer on top of them. PWRF has been tested throughout the Arctic (Hines and Bromwich, 2008; Bromwich et al., 2009; Hines et al., 2011), and is updated to remain consistent with each version of WRF.

## **2.2 Instrumentation Summit Station, Greenland**

The “Integrated Characterization of Energy, Clouds, Atmospheric state, and Precipitation at Summit” (ICECAPS) Project, funded by the Nation Science Foundation, has maintained a cloud-atmosphere observatory at Summit Station, Greenland since the summer of 2010 (Shupe et al., 2013). Summit is located at an elevation of 3,250 m in the center of the GIS, 72.6°N, 38.5°W (Fig. 1.6). The overarching goal of ICECAPS is to further the understanding of the atmospheric and cloud processes that occur over the GIS in order to better understand current and future changes to the ice sheet. The ICECAPS instrumentation suite is modeled after ARM sites, such as the one in Barrow, Alaska, for site-to-site comparison, but also in that the instruments are complementary to each other to provide the best overall description of atmospheric and cloud state. Quick looks of the Summit data are found at <http://www.esrl.noaa.gov/psd/arctic/observatories/summit/browser/>. A full list of the instruments located at Summit are listed in Shupe et al. (2013); however, those most important to this study are described briefly below.

The Microwave Radiometer (MWR) measures microwave radiation at two channels, 23.8 (water vapor dominate emission) and 31.4 (liquid water dominate emission) GHz with temporal resolution of 20 s (Morris, 2006). The primary measurement for the MWR is downwelling brightness temperatures, and has an accuracy of 0.3°K and resolution of 0.25°K (Morris, 2006). MWRs are self-calibrated during clear-sky periods (Liljegren, 2000). Since the MWR measurements at the two channels are sensitive to water vapor and liquid water, PWV and LWP can be retrieved via the MWR Retrieval (MWRRET) algorithm (Turner et al., 2007c). Uncertainties for the retrieved LWP are  $\pm 5$  to  $30 \text{ g m}^{-2}$  (Gaustad et al., 2007; Turner et al., 2007a).

The Atmospheric Emitted Radiance Interferometer (AERI) makes passive spectral downwelling radiance measurements in the infrared ( $3\text{-}19 \text{ }\mu\text{m}$ ,  $530\text{-}3000 \text{ cm}^{-1}$ ) with  $1 \text{ cm}^{-1}$  resolution at a very high temporal resolution (less than 1 minute) (Knuteson et al., 2004a). The AERI is self-calibrated for each observation providing extremely accurate measurements. A radiometric accuracy better than 1% of the ambient radiance is achieved by calibrating against two accurately maintained blackbodies (one at the ambient temperature and one at 60°C) along with corrections for the instrument and accounting for the nonlinearity of the detector (Knuteson et al., 2004b). The AERI’s radiometric uncertainty is derived from the calibration equation, and so the instrument noise is scene-dependent (Knuteson et al., 2004b). For example, at  $11 \text{ }\mu\text{m}$  in the midlatitudes, the AERI radiometric uncertainty is less than  $1 \text{ mW}/(\text{m}^2 \text{ sr cm}^{-1})$  (Turner, 2007b). AERI measurements can be used to determine atmospheric temperature and cloud characteristics in the lowest 2-3 km. AERI retrievals provide vertical profiles of water vapor and temperature, as well as LWP (Turner and Löhnert, 2014). The AERI is very sensitive to LWPs less than  $60 \text{ g m}^{-2}$ ; for retrieved LWPs less  $60 \text{ g m}^{-2}$  the bias is  $2 \text{ g m}^{-2}$  (Turner and Löhnert, 2014). For LWPs greater than  $60 \text{ g m}^{-2}$ , the signal from

the AERI saturates, thus this is a drawback in using solely AERI measurements to retrieve LWP (Turner, 2007b). To further improve LWP retrievals, AERI measurements can be combined with measurements from microwave instrumentation at Summit for a random error of less than 4% for LWPs less than  $50 \text{ g m}^{-2}$  and retrieve LWP values up to  $1000 \text{ g m}^{-2}$  (Turner, 2007b).

A 905 nm wavelength Vaisala Model CT25K ceilometer measures backscatter with a 15 m vertical resolution and 15 s temporal resolution with a backscatter precision of  $1 \times 10^{-4} \text{ km}^{-1} \text{ sr}^{-1}$  (Van Tricht et al., 2014). From this cloud base height can be derived using the standard Vaisala algorithm, which in turn determines cloud presence. Per Vaisala, the ceilometer has a distance accuracy when hitting a hard target of  $\pm 2\%$ . The Total Sky Imager (TSI) takes hourly horizon to horizon pictures of the sky, providing a qualitative picture of cloud cover and type.

The vertically-pointing 35 GHz (Ka band) Millimeter Cloud Radar (MMCR) measures reflectivity, relative backscatter, and Doppler velocity, spectrum width and spectra at a temporal resolution of 2 s with a 45 m vertical resolution (Moran et al., 1998). The MMCR has 4 modes of operation: (1) stratus mode, (2) cirrus mode, (3) general mode, and (4) robust mode. The MMCR has a 0.5 dB uncertainty for reflectivity and  $0.1 \text{ m s}^{-1}$  for mean Doppler velocity and spectrum width (Widener and Johnson, 2005). Cloud phase (Shupe, 2007; Luke et al., 2010) and microphysics (Shupe et al., 2005) along with vertical motion (Shupe et al., 2008b) can all be derived from these measurements. Since radar reflectivity is proportional to the hydrometeor diameter, ice crystals are characterized by higher reflectivity values and cloud liquid water by lower values for particles with equivalent mass. The sensitivity of the reflectivity to diameter is also a hindrance as radar signal has a lower sensitivity to smaller particles in a scanning volume. However, in the

absence of precipitation, the attenuation from MMCR is weak and radar measurements can be taken through the entire atmosphere (Shupe, 2007).

The MicroPulse Lidar (MPL) is a vertically pointing 532 nm wavelength lidar with a 15 m vertical resolution and 5 s temporal resolution (Campbell et al., 2002; Flynn et al., 2007). Measurements are taken of relative backscatter (insight to hydrometeor area) and depolarization ratio (insight to hydrometeor shape). These measurements are useful for determining the phase of the hydrometeor hitting the beam, i.e. cloud water droplets or ice crystals. Welton and Campbell (2002) discuss the algorithm used to determine the relative backscatter uncertainty from the MPL, which is influenced by uncertainties in the raw signal, measured background signal, laser energy, afterpulse (large, false signal from the firing of laser pulse) and overlap (near-field underrepresented signal due to laser pulse not fully being seen in the receiver field of view) corrections. High lidar backscatter values and low depolarization ratio are characteristic of cloud liquid water, and lower lidar backscatter values and higher depolarization ratio are characteristic of ice crystals (Shupe et al., 2013). Other cloud properties can be derived from lidar measurements, as well, such as optical depth (Turner and Eloranta, 2008). Lidar signal is attenuated in the presence of clouds with optical depths greater than or equal to 2 (Sassen, 1974), and therefore in some cases observations in the upper levels of the atmosphere cannot be made.

Radiosondes are launched twice a day at Summit. The radiosondes used at Summit are Vaisala RS-92K and RS-92SGP. They provide information on the vertical structure of temperature, pressure, and relative humidity in the atmosphere with a 1 s temporal resolution. Per Vaisala, the RS-92SGP has a temperature resolution of 0.1 °C and a total uncertainty in the sounding of 0.5°C. The pressure resolution is 0.1 hPa with an uncertainty of 1 hPa from 1080 to 100 hPa. The relative humidity resolution is 1% with a total uncertainty of 5%. RS-92SGP is an

improvement from RS-92K in that the pressure uncertainty in the latter from 1080 to 100 hPa is 1.5 hPa. Furthermore, wind speed and direction for RS-92SGP are found using a code correlating Global Positioning System method, while RS-92K does not measure these variables (RS-92K only measures pressure, temperature and relative humidity). After the summer of 2011, horizontal wind speed and direction measurements from the radiosonde are taken once a day at Summit. The RS-92SGP accuracy of the wind speed is  $0.15 \text{ m s}^{-1}$  and for direction  $2^\circ$ . These measurements are helpful in determining the temperature and moisture structure of the atmosphere and clouds from the surface to the upper troposphere, where some ground-based instrumentation cannot measure.

## Chapter 3 Case Description

### 3.1 Synoptic Environment

July 2012 was an anomalously warm month for Greenland and historic due the spatial extent of GIS surface melt, as previously discussed. The July 2012 monthly mean surface air temperature over the GIS was above the 1981-2010 climatology from the NCEP/NCAR reanalysis (Kalnay et al., 1996) (Fig. 3.1a). Additionally, 500 hPa monthly mean geopotential heights were well above climatology, particularly over southern Greenland (Fig. 3.1b). These patterns are consistent with a negative NAO and AO. The monthly mean NAO index was strongly negative, -1.32, while the AO index was more neutral, 0.17, per the Climate Prediction Center. However, days prior to and during the time of the cloud event (20-24 July, 2012), the daily NAO index transitioned from strongly negative to slightly positive (Fig. 3.1c), while the daily AO index went from positive to negative toward the end of the cloud event and the days following (Fig. 3.1c).

The advection of warm air from a historic heat wave over the United States and water vapor by an atmospheric river over the Atlantic Ocean was hypothesized by Neff et al. (2014) to be important factors in the surface melt that occurred on 11 July 2012 at Summit. Backward trajectories from the Hybrid Single-Particle Lagrangian Integrated Trajectory model (HYSPLIT, (Stein et al., 2015)) calculated from NCEP/NCAR reanalysis data show the air in the lowest 1 km at Summit on 20 July 2012 at 00 UTC originated over the central Atlantic Ocean on 07 July 2012 at 00 UTC (Fig. 3.2). The flow ascended over the southern and western coasts

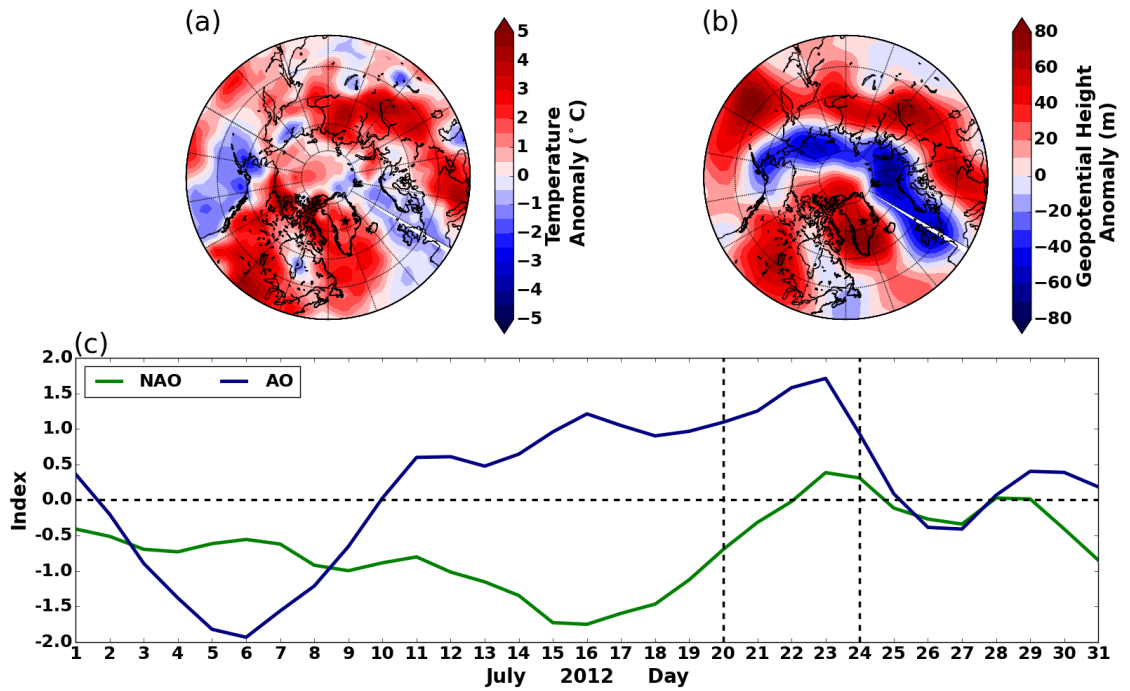


Figure 3.1: July 2012 anomalies (monthly mean - climatology) based from the 1981-2010 climatology of (a) surface air temperature ( $^{\circ}\text{C}$ ), (b) 500 hPa geopotential height (m), and (c) time series of daily index of NAO (green) and AO (navy). The start and end of the cloud event and 0 index value are marked by the dashed black lines. Data are from the NCEP/NCAR reanalysis and Climate Prediction Center. The location of Summit, Greenland is denoted by  $\star$ .



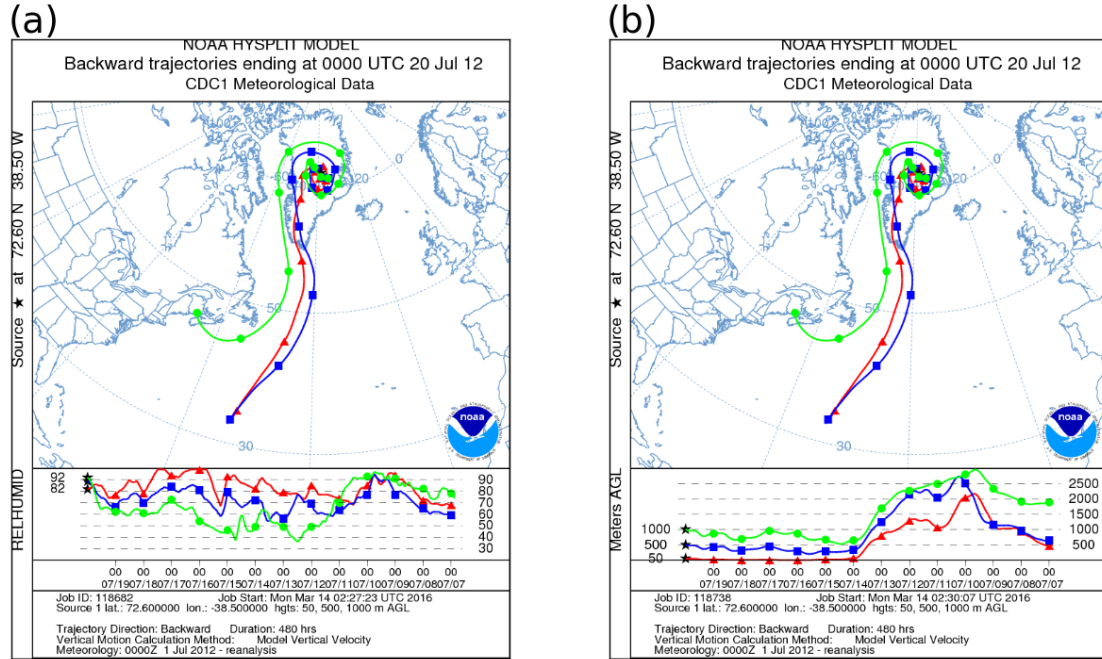


Figure 3.2: 480 hour backward trajectories from Summit at 20 July 2012 at 00 UTC at 50, 500, and 1000 m above ground level computed using HYSPLIT. Labels along the trajectories are (a) relative humidity (%) and (b) height above ground level (m). Data are from the NCEP/NCAR Reanalysis. The location of Summit, Greenland is denoted by ★.

(note the dropping of the heights AGL) from 10 July 2012 at 00 UTC through 14 July 2012 at 00 UTC (Fig. 3.2b). Once at the top of the GIS, the flow circulated anticyclonically around the ice sheet through 20 July 2012 at 00 UTC. Throughout the time period, the relative humidity of the air varied, but upon arrival at Summit the air was quite moist (Fig. 3.2a).

On 20 July 2012 at 00 UTC, there was a ridge of high pressure (as indicated by higher dynamic tropopause potential temperature) over the central United States that extended well into northern Canada (Fig. 3.3a). At the surface, a 988 hPa surface cyclone was located off the southern tip of Greenland. Westerly winds

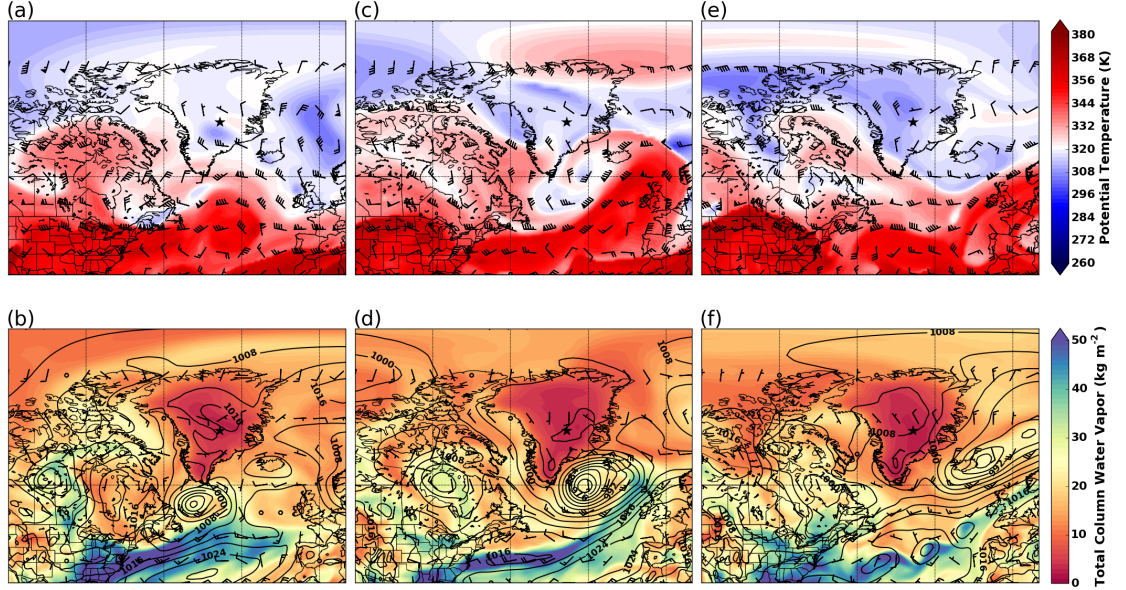


Figure 3.3: (a), (c), (e) Potential temperature ( $^{\circ}\text{K}$ ; color) and winds ( $\text{m s}^{-1}$ ; barbs) on the 2 PVU surface, and (b), (d), (f) total column water vapor ( $\text{kg m}^{-2}$ ; color), mean sea-level pressure (hPa, contour), and surface winds ( $\text{ms}^{-1}$ ; barbs) on (a), (b) 20 July 2012 at 00 UTC, (c), (d) 22 July at 00 UTC, and (e), (f) 24 July at 00 UTC. Wind barbs with a half barb =  $2.5 \text{ m s}^{-1}$ , a full barb =  $5 \text{ m s}^{-1}$ , and a flag =  $25 \text{ m s}^{-1}$ . The 2 PVU surface represents the dynamic tropopause where  $1 \text{ PVU} = 10^{-6} \text{ m}^2 \text{ s}^{-1} \text{ kg}^{-1} \text{ }^{\circ}\text{K}$ . Data are from ERA-Interim and the location of Summit, Greenland is denoted by  $\star$ .

transported moist air across the eastern United States over the Atlantic Ocean (Fig. 3.3b). A cyclonic Rossby wave-breaking event (Thorncroft et al., 1993) took place on 22 July 2012 at 00 UTC southeast of Greenland, noted by the overturning of the isentropes on the dynamic tropopause (Fig. 3.3c). The wave-breaking lead to a positive potential vorticity (PV) anomaly (lower potential temperature values) which induced a cyclonic circulation at the surface. This circulation interacted with the pre-existing surface cyclone, strengthening it to 972 hPa as it moved toward the northeast off the southeastern Greenland coast (Fig. 3.3d); such a cyclone track is consistent with a positive NAO and AO index (Fig. 3.1c). Off the western Greenland coast, a northwest-to-southeast boundary was apparent by the shift in winds from southeasterly ahead to northwesterly behind it. By 24 July 2012 at 00 UTC, a more zonal pattern evolved (Fig. 3.3e) and the surface cyclone weakened as it propagated to the northeast (Fig. 3.3f).

## 3.2 Summit Station, Greenland

Measurements from the instrumentation at Summit Station, Greenland recorded a long-lived AMPC event from 20 July at 00 UTC through 24 July at 00 UTC. The ceilometer observed a cloud base throughout much of the period (Fig. 3.4a). The cloud base height (CBH) rose slowly from 0.25 km AGL on 20 July at 00 UTC to 1.25 km AGL on 22 July at 00 UTC, and remained at this height through 23 July at 00 UTC. The CBH peaked at 1.5 km AGL on 23 July at 06 UTC. After this time, the cloud layer became broken as it started to dissipate through 24 July. Overcast skies were observed through much of the period by the TSI (Fig. 3.5a-c). The cloud started to break at 23 July at 04 UTC with intermittent times of overcast and clear skies (Fig. 3.5d), which compliments the CBH from the ceilometer.

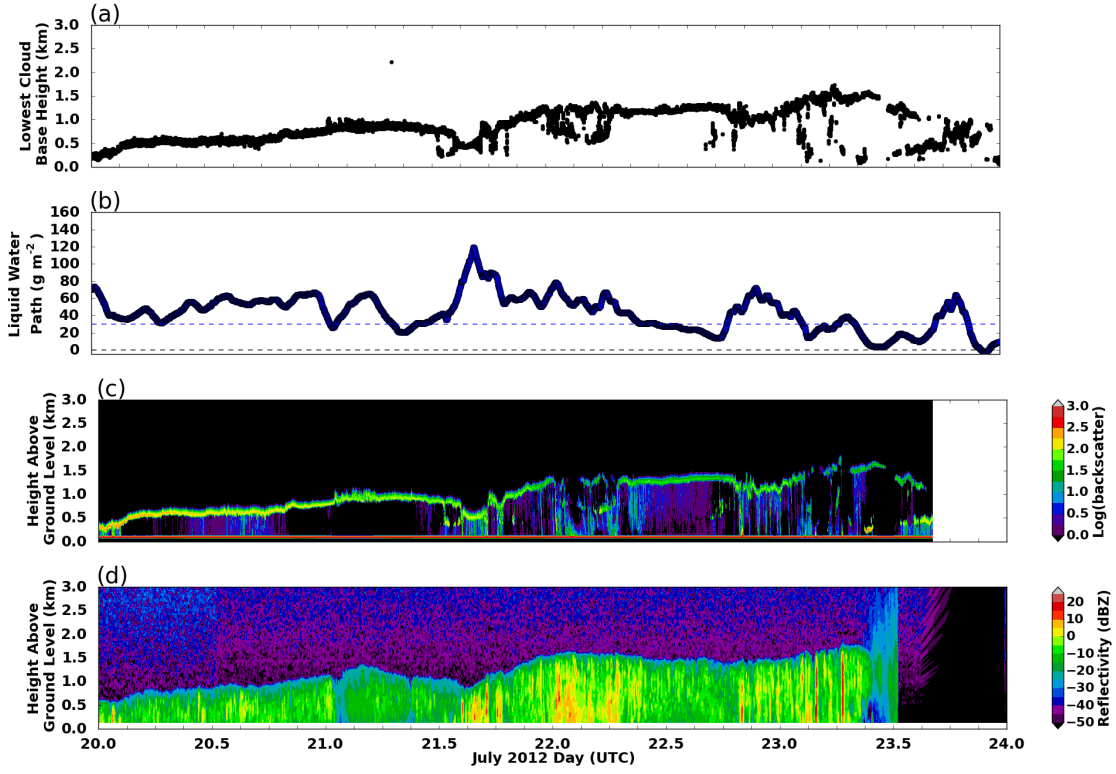


Figure 3.4: Observational-based estimates from the ICECAPS Summit Station, Greenland cloud-atmosphere observatory for (a) the lowest cloud base height (km) detected by ceilometer, (b) liquid water path ( $\text{g m}^{-2}$ ) retrieved from the Microwave Radiometer with 30 (blue) and 0 (black)  $\text{g m}^{-2}$  dashed, and time-height cross section of (c)  $\log(\text{backscatter})$  from the the MicroPulse Lidar (MPL) and (d) reflectivity (dBZ) from the Doppler 35-GHz Millimeter Cloud Radar (MMCR).

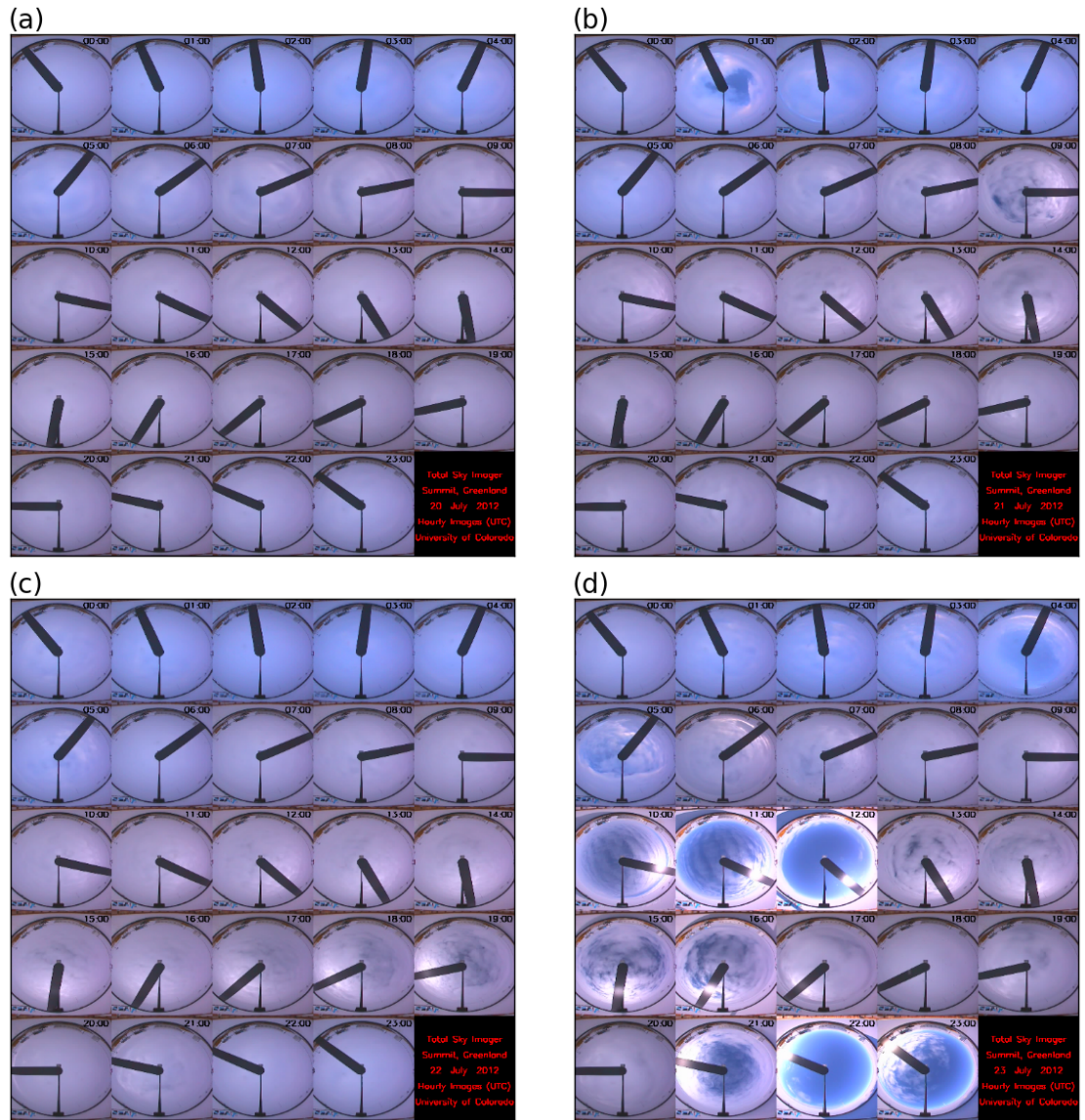


Figure 3.5: Images from the Total Sky Imager (TSI) at the ICECAPS Summit Station, Greenland cloud-atmosphere observatory on (a) 20 July 2012, (b) 21 July 2012, (c) 22 July 2012, and (d) 23 July 2012.



The presence of liquid water is confirmed by non-zero MWRRET LWPs through much of the period (Fig. 3.4b). LWPs were in the range of 40 to 80 g m<sup>-2</sup> through 21 July at 00 UTC and then slowly increased through the day and early into 22 July, where the peak LWP value of 120 g m<sup>-2</sup> was reached. Prior to 22 July at 09 UTC, LWPs were greater than 30 g m<sup>-2</sup>, which is important when considering the LW radiative effects of the cloud. After this time, LWP slowly decreased and became variable with values near or at 0 g m<sup>-2</sup> after 23 July at 06 UTC as the cloud dissipated.

Backscatter from the MPL show a thin layer of higher values (Fig. 3.4c) collocated with lower reflectivity values from the MMCR (Fig. 3.4d) that were coincident with the CBH from the ceilometer (Fig. 3.4a) throughout the period. These measurements indicate there was a thin, elevated, supercooled liquid water layer through the event, as lower reflectivity and higher backscatter values are indicative of liquid water. MMCR reflectivities and MPL backscatter complement the non-zero MWRRET LWPs through much of the event, further confirming the consistent presence of liquid water in the cloud. Beneath this liquid water layer and down to the surface, backscatter values were lower and reflectivity values were higher, indicative of ice crystals (Fig. 3.4c,d). Data from the MPL past 23 July at 15 UTC are missing and reflectivities from the MMCR are very small or negligible past 23 July at 12 UTC. The observations from the ICECAPS instrumentation indicate that a low-level, single-layer, long-lived AMPC was present over Summit from 20 July at 00 UTC through 24 July at 00 UTC.

The radiosonde from 20 July at 00 UTC at Summit measured an elevated moisture and temperature inversion just above 0.5 km AGL (Fig. 3.6a). The CBH was below this inversion (Fig. 3.4a), and the atmosphere was saturated above and below it. Winds throughout the lowest 6 km AGL were predominately easterly. By 21 July at 00 UTC, the inversion rose to just above 1 km AGL with winds

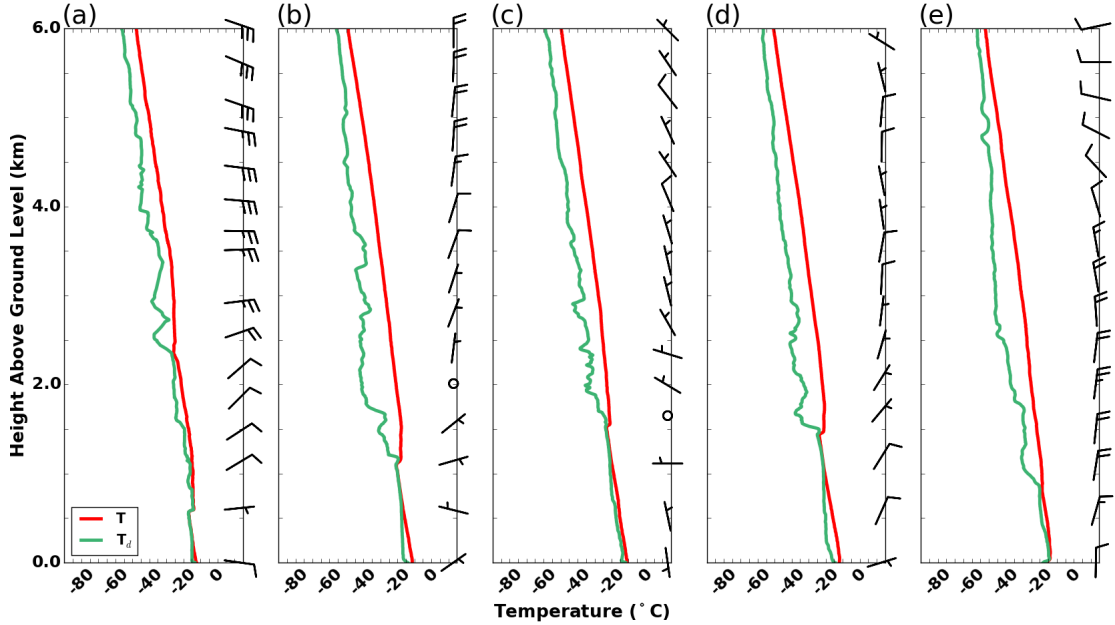


Figure 3.6: Vertical profile of temperature ( $^{\circ}\text{C}$ , red), dewpoint ( $^{\circ}\text{C}$ , green), and winds ( $\text{m s}^{-1}$ ; barbs) from the Summit radiosondes at (a) 20 July 2012 at 00 UTC, (b) 21 July 2012 at 00 UTC, (c) 22 July 2012 at 00 UTC, (d) 23 July 2012 at 00 UTC, and (e) the 24 July 2012 at 00 UTC radiosondes. Wind barbs with a half barb =  $2.5 \text{ m s}^{-1}$ , a full barb =  $5 \text{ m s}^{-1}$ , and a flag =  $25 \text{ m s}^{-1}$ .

varying between easterly and westerly below and to northerly above the inversion (Fig. 3.6b). The air beneath the inversion remained saturated, as the cloud was beneath the inversion, with a drying of air closest to the surface. The vertical wind profile from the 22 July at 00 UTC radiosonde (Fig. 3.6c) was similar to 21 July at 00 UTC, though the winds above the inversion in the former have a more westerly component. The inversion at 22 July at 00 UTC rose to 1.5 km AGL and weakened slightly. On 23 July at 00 UTC, winds began to back through the lowest 6 km AGL, indicative of cold air advection (Fig. 3.6d). The vertical profile of temperature and dewpoint on 23 July at 00 UTC (Fig. 3.6d) changed little from 22 July at 00 UTC with the biggest difference being a drying of the lowest 1 km

at 23 July at 00 UTC. The elevated inversion diminished by 24 July at 00 UTC and a surface-based inversion developed with winds continuing to show a backing vertical profile (Fig. 3.6e).

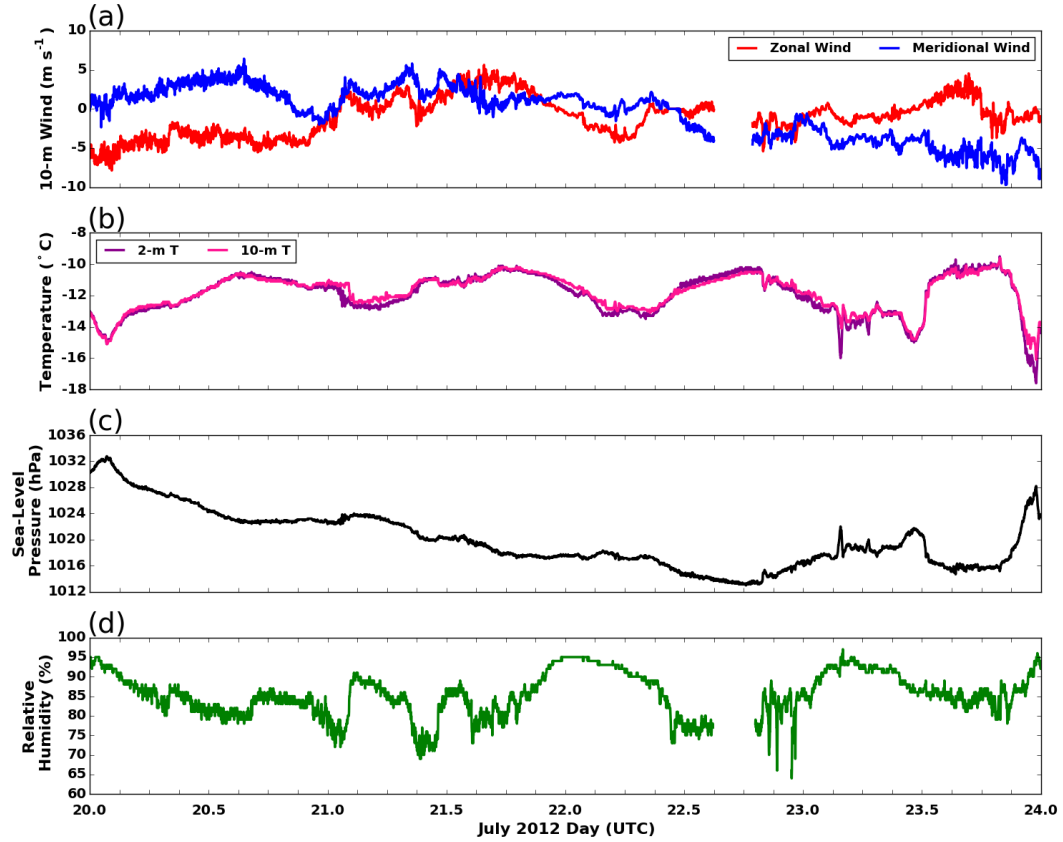


Figure 3.7: Time series of data from the meteorology tower at Summit from 20–24 July 2012 of the 10-m (a) zonal (red) and meridional (blue) wind ( $\text{m s}^{-1}$ ), (b) 2-m (purple) and 10-m (pink) temperature ( $^{\circ}\text{C}$ ), (c) sea-level pressure (hPa), and (d) relative humidity (%).

From surface-based observations, the 10-m wind was primarily easterly early in the period (Fig. 3.7a), consistent with the 20 July at 00 UTC radiosonde (Fig. 3.6a). With time, the 10-m zonal wind shifted from easterly to westerly, while the 10-m meridional wind shifted from southerly to northerly (Fig. 3.7a). A diurnal cycle



of 2 and 10-m temperatures is evident; during the day the 2-m temperature was the same as or slightly warmer than the 10-m, whereas during the night the 2-m temperature was cooler than the 10-m, i.e an inversion (Fig. 3.6b). This overnight inversion was weaker on 20, 21, and 22 July than 23 and 24 July, which is most likely due to surface warming from the cloud. Temperatures late on 23 into 24 July cooled drastically, which was likely due to surface radiative cooling in the absence of a cloud layer (Fig. 3.4). Sea-level pressure slowly declined through 22 July at 18 UTC (Fig. 3.7c), consistent with the nearing surface cyclone (Fig. 3.3b,d), and increased as the cyclone moved away from Greenland (Fig. 3.3f). Relative humidity values show a somewhat less consistent pattern than the other variables; overall, air near the surface was rather saturated with a brief period of dry air between 22 July at 12 UTC and 23 July at 00 UTC (Fig. 3.7d), consistent with the 23 July at 00 UTC radiosonde (Fig. 3.6d).

## Chapter 4 Methods and Results

### 4.1 Control Simulation

In order to do experimental model simulations, a control simulation is needed to compare the experiments against. Numerous simulations were done over several ‘rounds’ using different combinations of numerical model versions, initial and boundary conditions, SW radiation physics options, domain sizes, and vertical and

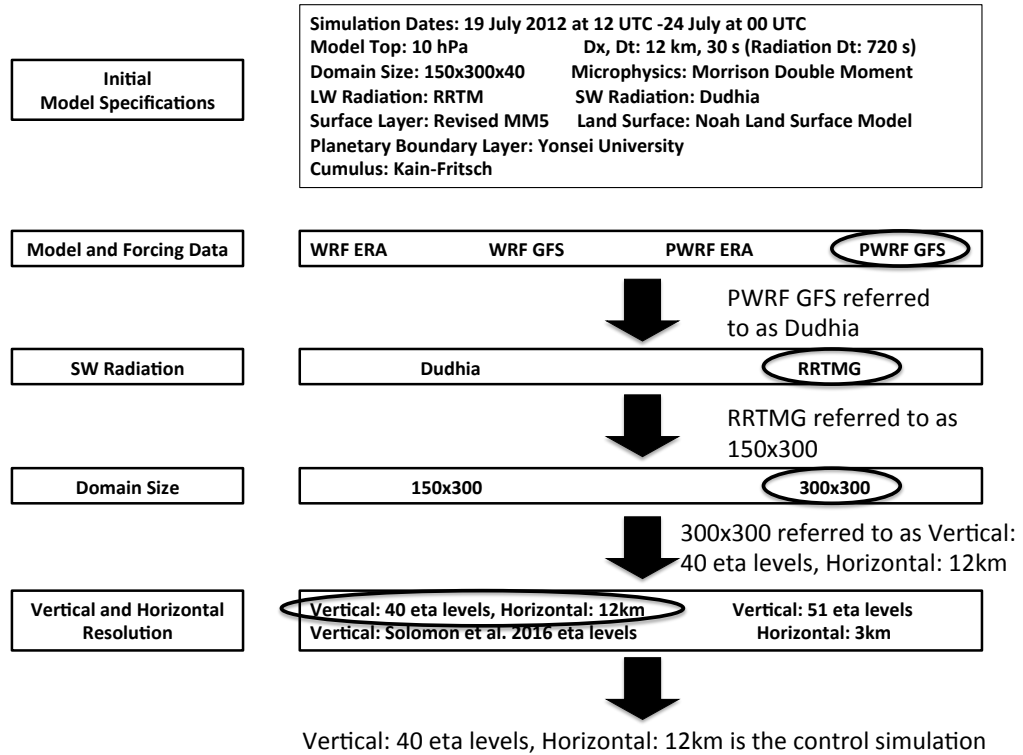


Figure 4.1: Process for choosing control model simulation.

horizontal resolutions. The flow for choosing the control simulation is summarized in Fig. 4.1.

#### 4.1.1 Model Version and Forcing Dataset

The first choice that needed to be made was what model version to use: WRF (section 2.1.1) or PWRF (section 2.1.2). The second decision was what to use for the model initial and boundary conditions: final reanalysis data from the Global Forecast System (GFS) (National Centers for Environmental Prediction, 2000) or the European Centre for Medium-Range Weather Forecasts reanalysis (ERA-Interim) (Dee et al., 2011). In total, there were 4 different test simulations: WRF forced with GFS (*WRF\_GFS*), WRF forced with ERA-Interim (*WRF\_ERA*), PWRF forced with GFS (*PWRF\_GFS*), and PWRF forced with ERA-Interim (*PWRF\_ERA*). The simulation that best compared to the Summit observations was chosen for the next round of control simulation testing.

For all 4 simulations, the model was initialized on 19 July 2012 at 12 UTC and run through 24 July 2012 at 00 UTC. The model top was set to 10 hPa, as recommended by Cavallo et al. (2011) for the choice in LW radiation physics scheme, with 40 eta levels in the vertical. The domain was 150 x 300 gridpoints, in the x and y direction, respectively, with 12 km grid spacing; the size of the domain was 1800 km by 3600 km (Fig. 4.2). A time step of 30 s was used, and the radiation time step was 720 s. The boundary conditions were provided every 6 hours. The physics options used were: Morrison Double Moment for microphysics (Morrison et al., 2009a), rapid radiative transfer model (RRTM) for LW radiation (Mlawer et al., 1997), Dudhia for SW radiation (Dudhia, 1989), revised MM5 for the surface layer (Beljaars, 1995), Noah land surface model for land surface (Tewari et al., 2004), Yonsei University (YSU) for the planetary boundary layer (PBL) (Hong et al., 2006), and Kain-Fritsch for cumulus (convection) (Kain, 2004).

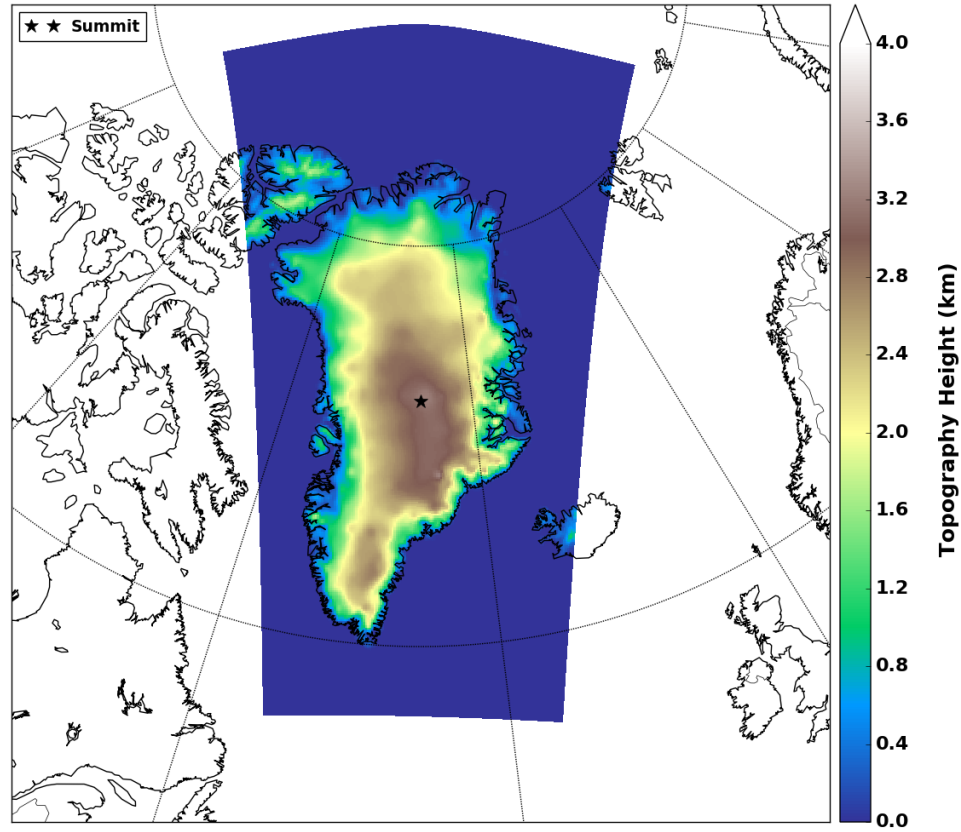


Figure 4.2: Domain for simulations with  $150 \times 300$  grid points in the  $x$  and  $y$  directions, respectively. The topography of the domain is color filled (km). The location of Summit, Greenland is denoted by  $\star$ .

To choose between these 4 simulations, the vertical distribution of cloud water mixing ratio in the lowest 1 km AGL and LWP were compared to the observations. The definition of a cloud used in this research is only concerned with the liquid portion due to its radiative impact. Cloud water mixing ratio provides insight into cloud height and persistence in the model simulation, which can be compared to CBH observations (Fig. 3.4a). LWP calculated from the simulations can be compared to the MWRRET LWP (Fig. 3.4b). None of the simulations produced a cloud layer past 22 July at 15 UTC, and CBHs never ascended above 0.5 km (Fig. 4.3a,b,c,d); these were major differences from the observations. Additionally,

the LWP values from the 4 simulations were much less than the MWRRET LWP (Fig. 4.3e).

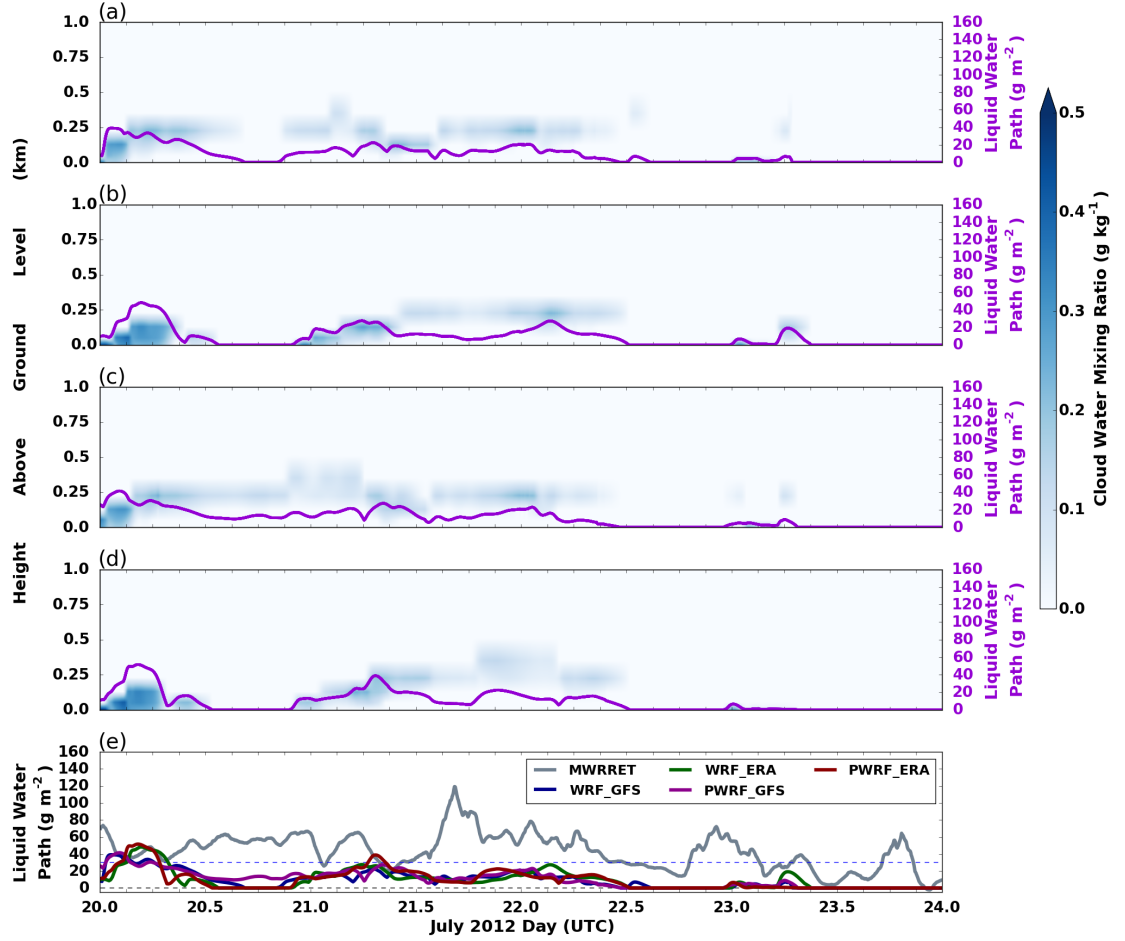


Figure 4.3: Time-height cross section through lowest the 1 km AGL of cloud water mixing ratio ( $\text{g kg}^{-1}$ ; colors) and time series of liquid water path ( $\text{g m}^{-2}$ ; purple) from the (a) *WRF\_GFS*, (b) *WRF\_ERA*, (c) *PWRF\_GFS*, and (d) *PWRF\_ERA* simulations. (e) Comparison of liquid water path ( $\text{g m}^{-2}$ ) from MWRRET (gray), *WRF\_GFS* (dark blue), *WRF\_ERA* (dark green), *PWRF\_GFS* (dark purple), and *PWRF\_ERA* (dark red).

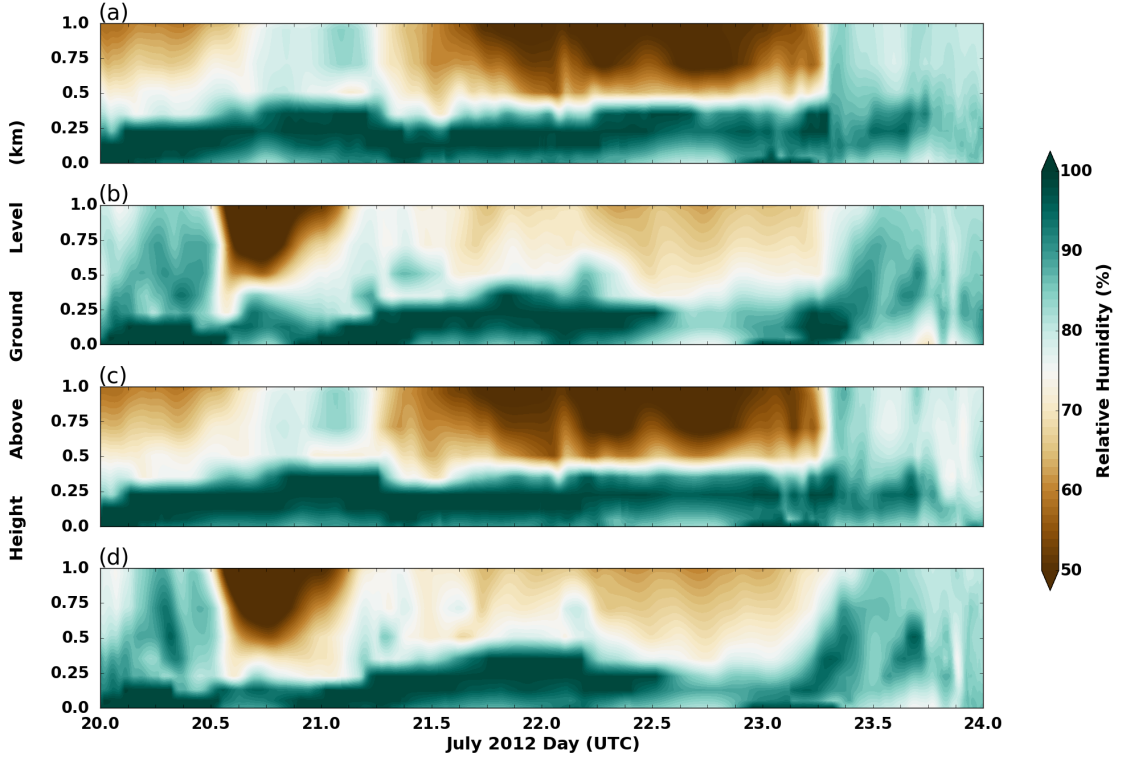


Figure 4.4: Time-height cross section through lowest the 1 km AGL of relative humidity (%) from the (a) *WRF\_GFS*, (b) *WRF\_ERA*, (c) *PWRF\_GFS*, and (d) *PWRF\_ERA* simulations.

The simulated clouds in both the ERA-forced simulations had a break in the cloud layer late on 20 July (Fig. 4.3b,d). This break was simulated in *WRF\_GFS* (Fig. 4.3a), but was shorter in duration than *WRF\_ERA* and *PWRF\_ERA*. This break was not simulated in *PWRF\_GFS* (Fig. 4.3c); *PWRF\_GFS* simulated the most persistent cloud. *WRF\_ERA* and *PWRF\_ERA* simulated the least persistent clouds, though air in the lowest 1 km in the ERA-forced simulations (Fig. 4.4b,d) was initially moister than the GFS-forced simulations (Fig. 4.4a,c). At 20 July at 12 UTC, there was an intrusion of dry air from aloft in both *WRF\_ERA* (Fig. 4.4b) and *PWRF\_ERA* (Fig. 4.4d) which coincides with the break in the cloud. This was not seen in *WRF\_GFS* (Fig. 4.4a) or *PWRF\_GFS* (Fig. 4.4c), and perhaps

explain why the GFS-forced models simulated a more persistent cloud. As for the difference between *WRF\_GFS* and *PWRF\_GFS*, the break in the cloud in *WRF\_GFS* occurred when air near the surface was less saturated (Fig. 4.4a); this was not simulated in *PWRF\_GFS* (Fig. 4.4c). Of the 4 simulations, *PWRF\_GFS* compared best overall to the AMPC observed at Summit, and thus was chosen as the simulation to move on to the next round.

#### 4.1.2 Shortwave Radiation Physics

Another decision to make was which SW radiation parameterization to use. The SW radiation physics option in *PWRF\_GFS* was changed from the Dudhia scheme (*Dudhia*) to the SW RRTM scheme that is used in general circulation models known as RRTMG (*RRTMG*) (Iacono et al., 2008). RRTMG is a more computationally efficient version of RRTM that maintains a minimal loss of accuracy from RRTM. RRTM (and RRTMG) are based on the line-by-line radiative transfer model LBLRTM (Clough et al., 2005), which has been verified against observations (e.g. Brown et al. (1995)). Dudhia, on the other hand, is a more simplistic calculation of the downwelling SW radiation; compared to RRTMG, Dudhia is less computationally expensive. All other model options from the *PWRF\_GFS* simulation remained the same. The best of the 2 simulations that compared to the Summit observations was chosen for the next round of control simulation testing.

The *RRTMG* simulated LWP was higher and more comparable to the MWR-RET LWP than *Dudhia* (Fig. 4.5c). Additionally, *RRTMG* simulated a cloud layer that persisted through 22 July at 15 UTC (Fig. 4.5b), which was longer lived than *Dudhia* (22 July at 09 UTC) (Fig. 4.5a), though there was a slight break in the *RRTMG* simulated cloud between 20 July at 21 UTC and 21 July at 00 UTC. *Dudhia* (Fig. 4.6a) and *RRTMG* (Fig. 4.6b) simulated very different temperature profiles in the lowest 1 km AGL. Overall, *RRTMG* was warmer than

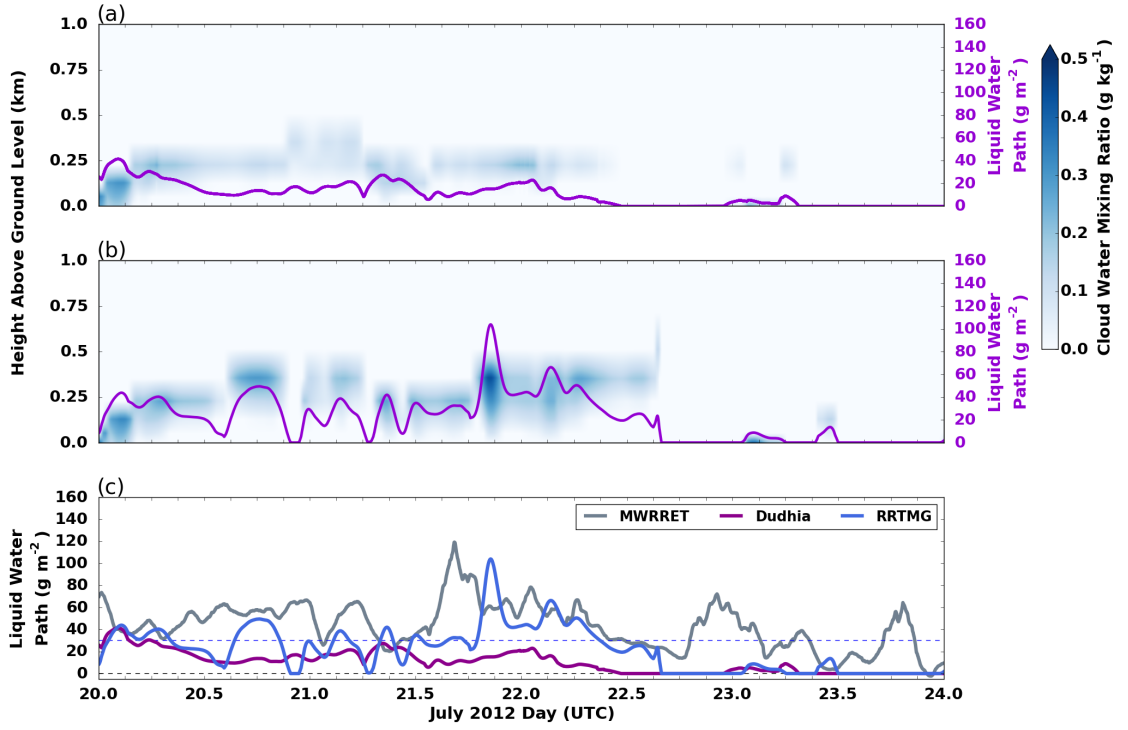


Figure 4.5: Time-height cross section through lowest the 1 km AGL of cloud water mixing ratio ( $\text{g kg}^{-1}$ ; colors) and time series of liquid water path ( $\text{g m}^{-2}$ ; purple) from the (a) *Dudhia* and (b) *RRTMG* simulations. (c) Comparison of liquid water path ( $\text{g m}^{-2}$ ) from MWRRET (gray), *Dudhia* (dark purple), and *RRTMG* (light blue).



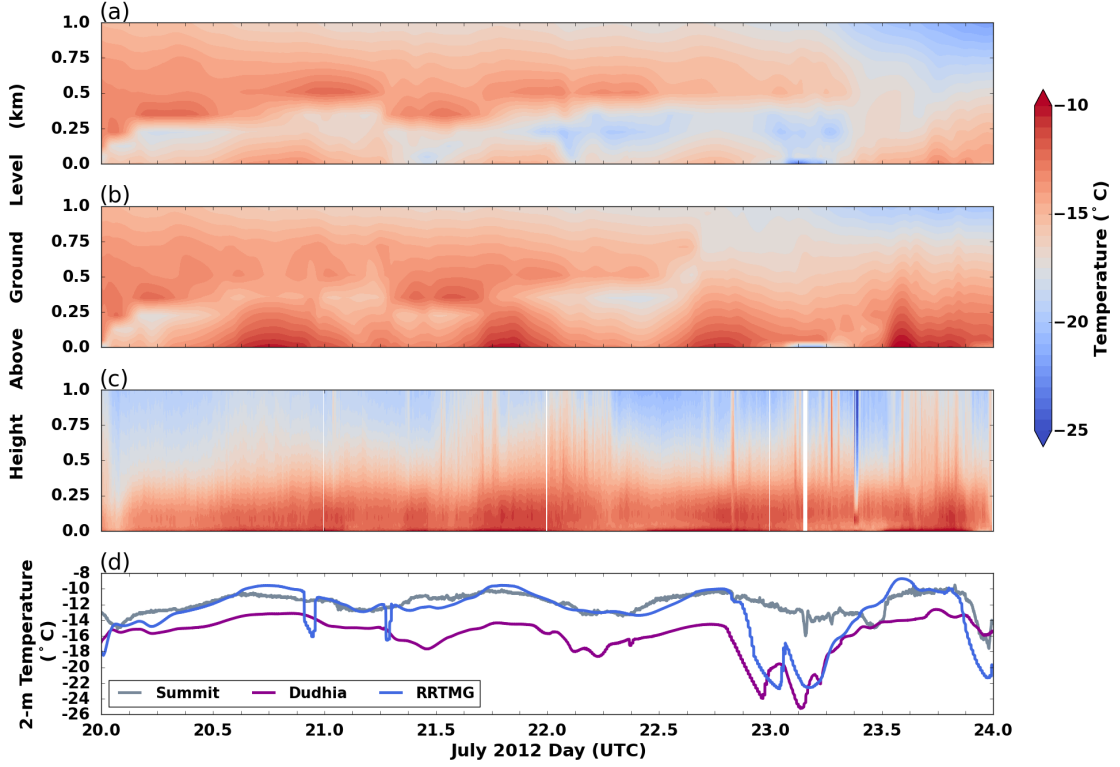


Figure 4.6: Time-height cross section through the lowest 1 km AGL of temperature (°C) from the (a) *Dudhia* and (b) *RRTMG* simulations, and (c) AERI retrieval. (d) Comparison of 2-m temperature (°C) from the Summit meteorology tower (gray), *Dudhia* (dark purple), and *RRTMG* (light blue).

*Dudhia*. This warmer environment was due to the better captured diurnal cycle by *RRMTG*, which better resembled that retrieved from the AERI (Fig. 4.6c). Both simulations were too warm above 0.5 km; however, this may be due to the AERI retrieval falling back to climatology as the observed cloud is too optically thick to glean information from aloft. Moreover, the 2-m temperature from *RRTMG* better resembled the observations than *Dudhia* (Fig. 4.6d).

The environment was also much more moist in *RRTMG* (Fig. 4.7b) than *Dudhia* (Fig. 4.7a). The water vapor mixing ratio profile retrieved from the AERI (Fig. 4.7c) best compared with *RRTMG*, though the low-level water vapor mixing

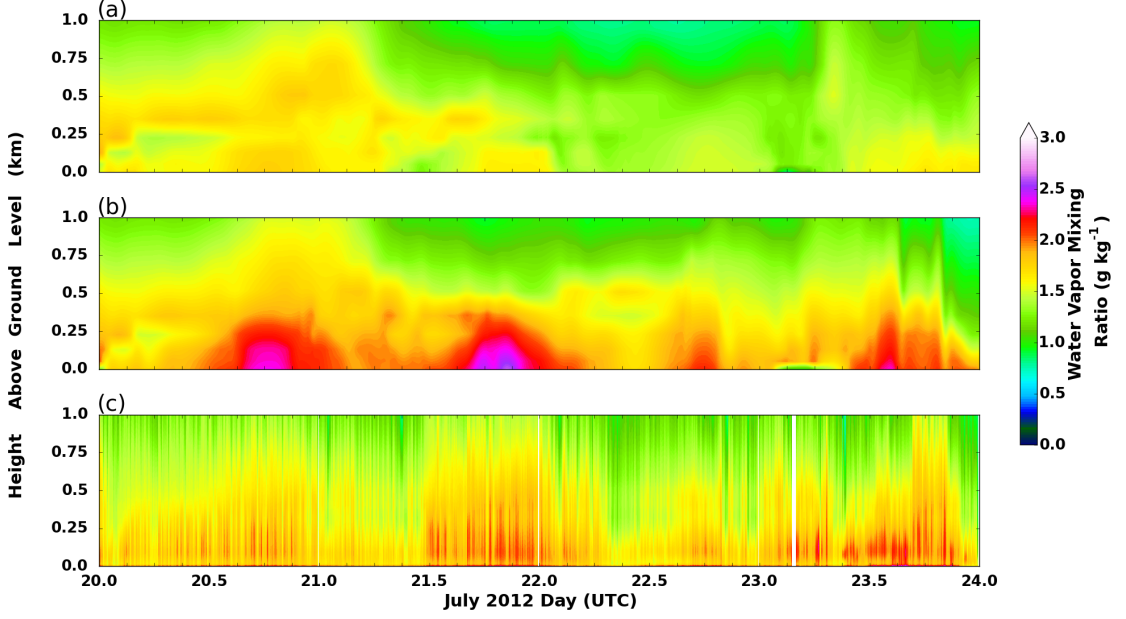


Figure 4.7: Time-height cross section through the lowest 1 km AGL of water vapor mixing ratio ( $\text{g kg}^{-1}$ ) from the (a) *Dudhia* and (b) *RRTMG* simulations, and (c) AERIoe retrieval.

ratios in *RRTMG* were a bit higher early in the period. The warmer and moister boundary layer simulated by *RRTMG* shows why the LWP is greater and the cloud is longer lived than *Dudhia*. *RRTMG* much better represented the observed cloud as well as the boundary layer temperature and moisture profile than *Dudhia* did. Therefore, *RRTMG* was used in the next round of simulations.

#### 4.1.3 Domain Size

The next decision that had to be made was the domain size. The domain from *RRTMG* was changed from 150 gridpoints in the x-direction ( $150 \times 300$ ) to 300 ( $300 \times 300$ ); the size of the domain was changed from 1800 km by 3600 km to 3600 km by 3600 km (Fig. 4.8). By expanding the domain, more of the large-scale flow was resolved by PWRP. All other model options from *RRTMG* remained the same.

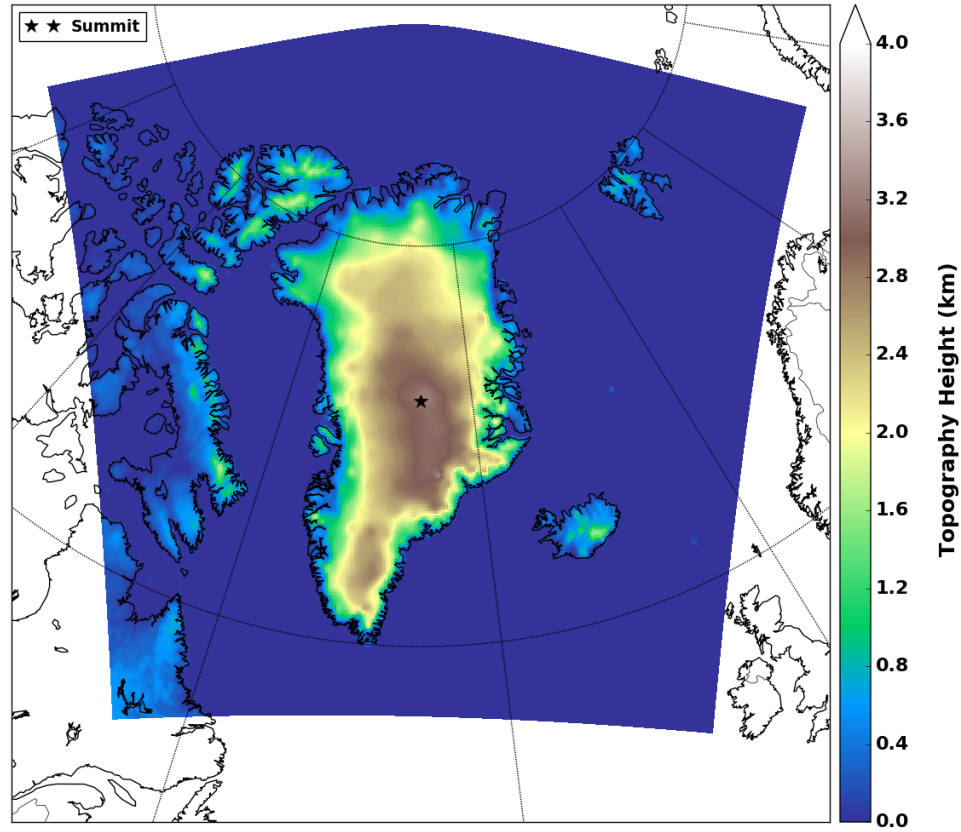


Figure 4.8: Domain for simulations with  $300 \times 300$  grid points in the  $x$  and  $y$  directions, respectively. The topography of the domain is color filled (km). The location of Summit, Greenland is denoted by  $\star$ .

The simulation that compared best to the Summit observations was chosen for the next round of control simulation testing.

Simply expanding the domain in the  $x$ -direction had notable impacts on the cloud. The cloud was longer lived in  $300 \times 300$ , dissipating at 23 July at 00 UTC (Fig. 4.9b) than  $150 \times 300$ , which dissipated at 22 July at 15 UTC (Fig. 4.9a). The LWP from  $150 \times 300$  was much more variable than  $300 \times 300$  (Fig. 4.9c). The LWP variability in  $150 \times 300$  could have been due to the smaller size of the domain. The smaller domain could have resulted in waves reflecting off the boundaries that propagated back to Summit quicker than they would have in the  $300 \times 300$

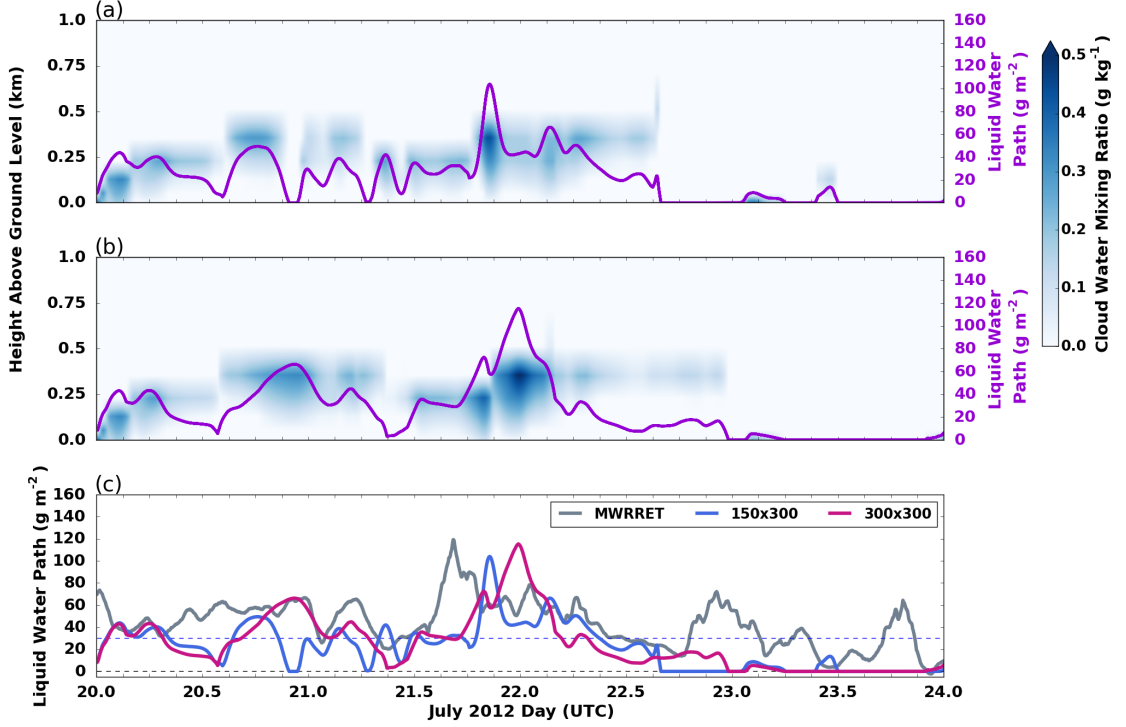


Figure 4.9: Time-height cross section through lowest the 1 km AGL of cloud water mixing ratio ( $\text{g kg}^{-1}$ ; colors) and time series of liquid water path ( $\text{g m}^{-2}$ ; purple) from the (a)  $150 \times 300$  and (b)  $300 \times 300$  simulations. (c) Comparison of liquid water path ( $\text{g m}^{-2}$ ) from MWRRET (gray),  $150 \times 300$  (light blue), and  $300 \times 300$  (dark pink).

domain. Overall,  $300 \times 300$  followed the evolution of the MWRRET LWP better than  $150 \times 300$  (Fig. 4.9c). As  $300 \times 300$  best simulated the observed cloud, this simulation was used in the next round.

#### 4.1.4 Vertical and Horizontal Grid Spacing

The last decisions that needed to be made were in regards to the vertical and horizontal grid spacing. For these simulations, the horizontal and vertical grid spacing from  $300 \times 300$  were changed. For  $300 \times 300$ , the number of eta levels used

was 40 (Fig. 4.10a) and the horizontal grid spacing was 12 km (*40eta,12km*). In one simulation, the number of eta levels from *300x300* was doubled in the lowest 2 km. The eta levels above 2 km and the rest of the model parameters remained unchanged from *300x300*; this resulted in 51 eta levels (*51\_etalevels*, Fig. 4.10b). Next, the eta levels from Solomon et al. (2016) were used in the *300x300* simulation (*S16\_etalevels*); this was a total of 111 eta levels (Fig. 4.10c). All other model options remained the same. Finally, the horizontal grid spacing in *300x300* was changed from 12 km to 3 km (*3km*). In this simulation, the cumulus physics option was turned off as this horizontal grid spacing is sufficient to resolve convective processes, i.e the parameterization of convection is not necessary (e.g. Yu and Lee (2010)). The time step and radiation time step were 7.5 s and 180 s, respectively. All other model options were the same as *300x300*, including the domain size. The simulation out of these that best compared to the Summit observations was chosen as the control.

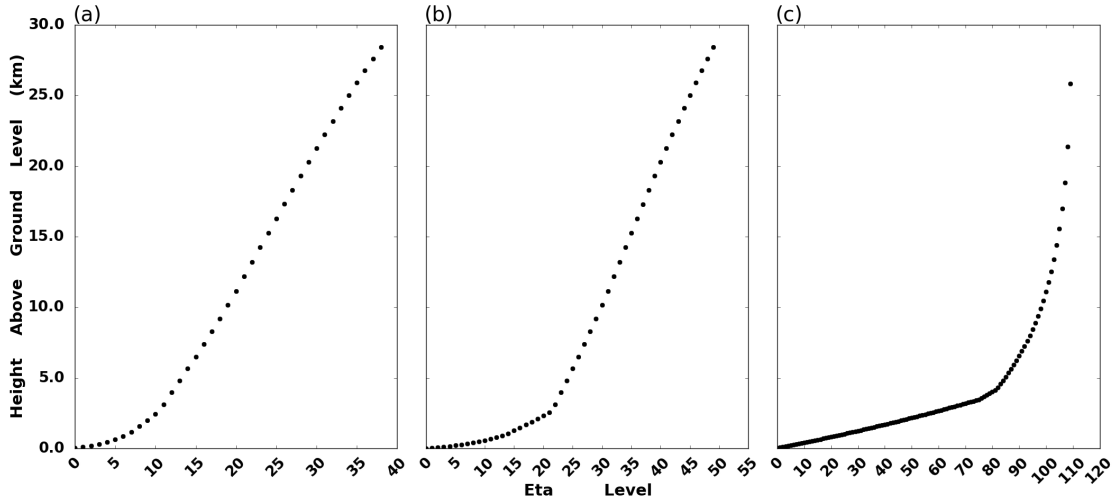


Figure 4.10: Eta levels at 19 July 2012 at 12 UTC at Summit in the (a) control, (b) *51\_etalevels*, and (c) *S16\_etalevels* simulations.

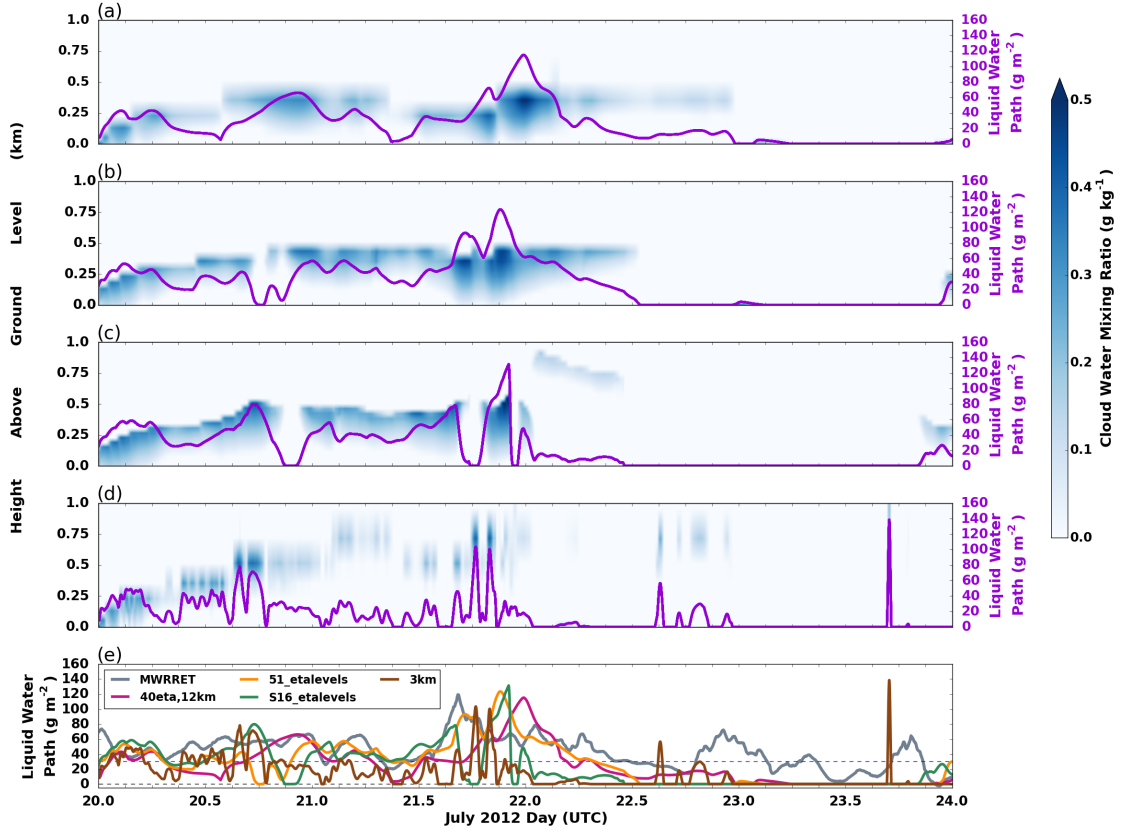


Figure 4.11: Time-height cross section through the lowest 1 km AGL of cloud water mixing ratio ( $\text{g kg}^{-1}$ ; colors) and time series of liquid water path ( $\text{g m}^{-2}$ ; purple) from the (a) *40eta,12km*, (b) *51\_etalevels*, (c) *S16\_etalevels*, and (d) *3km* simulations. (e) Comparison of liquid water path ( $\text{g m}^{-2}$ ) from MWRRET (gray), *40eta,12km* (dark pink), *51\_etalevels* (orange), *S16\_etalevels* (green), and *3km* (brown).

The cloud simulated in *51\_etalevels* (Fig. 4.11b) was comparable to *40eta,12km* (Fig. 4.11a). In *51\_etalevels*, the cloud was better maintained on 21 July from 06 to 12 UTC than *40eta,12km*, but less on 20 July between 18 and 21 UTC. In addition, the cloud was shorter lived in *51\_etalevels*. *S16\_etalevels* simulated a cloud similar to *51\_etalevels*, though the cloud in the former simulation dissipated by 22 July at 00 UTC (Fig. 4.11c). Neither *51\_etalevels* or *S16\_etalevels* vastly improved the simulation in comparison to *40eta,12km*. The increased vertical resolution in the lowest levels, though, provided better clarity in the elevation of the cloud layer through 20 July.

The *3km* CBH best reproduced the observations from the ceilometer (Fig. 3.4a) of any simulation (Fig. 4.11d), but the LWP and cloud lifetime did not compare as well. The LWP is noisier than *40eta,12km* and this is most likely due to the decrease in horizontal grid spacing without adjusting the vertical grid spacing (Lindzen and Fox-Rabinovitz, 1989). Running the simulation with a horizontal grid spacing of 3 km was much more computationally expensive than with 12 km due to the greater number of gridpoints and decreased time step. To capture the large-scale environment as well as having a computationally efficient simulation run time, using a horizontal grid spacing of 3 km was unrealistic to use for a control simulation. Of these 4 simulations, *40eta,12km* best compared with the observations while being computationally efficient (Fig. 4.11e). *40eta,12km* was chosen for the control simulation.

#### 4.1.5 Chosen Control

Based on the previous sections, the model configuration that best simulated the observed cloud at Summit is PWRP 3.6.1 with final GFS reanalysis initial and boundary conditions, RRTMG for the SW radiation physics option, and a 12 km

Model	PWRF 3.6.1
Simulation Dates	19 July 2012 at 12 UTC - 24 July at 00 UTC
Initial and Boundary Conditions	Final Global Forecast System (GFS)
Model Top	10 hPa
$\Delta x, \Delta t$	12 km, 30 s (Radiation $\Delta t$ : 720 s)
Domain Size	300 x 300 x 40
Microphysics	Morrison Double Moment
Longwave Radiation	Rapid Radiative Transfer Model
Shortwave Radiation	Rapid Radiative Transfer Model-G
Surface Layer	Revised MM5
Land Surface	Noah Land Surface Model
Planetary Boundary Layer	Yonsei University
Cumulus	Kain-Fritsch

Table 4.1: Summary of control simulation settings.

horizontal grid spacing on a 300 by 300 (x by y) grid point domain with 40 vertical eta levels. The control is summarized in Table 4.1.

The cloud forms in the control simulation at the surface on 20 July at 00 UTC (Fig. 4.12a). The formation of the cloud is due to the surface radiative cooling under a surface-based inversion leading to the condensation of air near the surface, and thus the birth of the cloud (Fig. 4.13a). The emission from the liquid water changes the ‘radiative regime’ resulting in radiative cooling above the liquid layer (cloudy sky) instead of from the surface (clear sky). Once the cloud forms, the LWP quickly exceeds  $30 \text{ g m}^{-2}$  (above the threshold LWP where a cloud is radiating as approximately as a blackbody) leading to strong CTLC (Fig. 4.12b). This radiative cooling induces weak, narrow, buoyancy-driven updrafts (Fig. 4.12c) lifting the cloud from the surface by 20 July at 12 UTC (Fig. 4.12a, 4.13b).



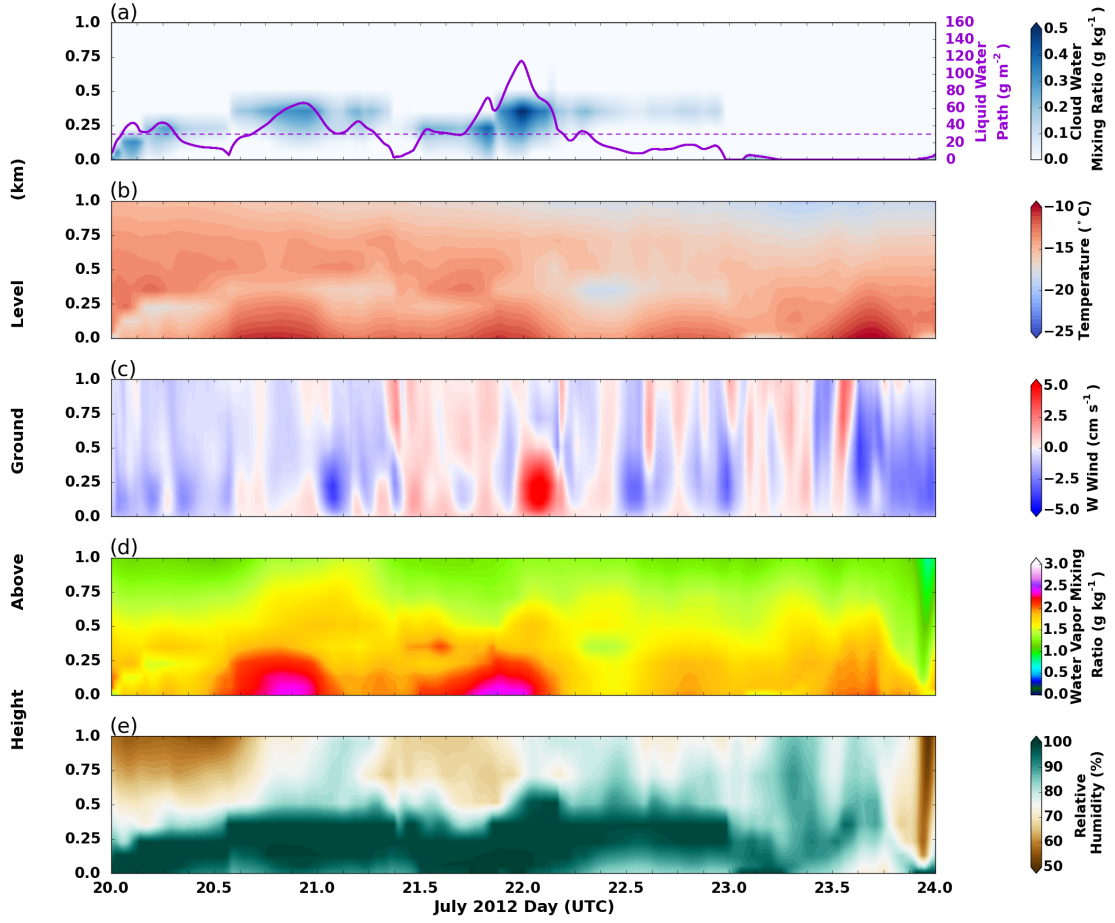


Figure 4.12: Time-height cross section through the lowest 1 km AGL of (a) cloud water mixing ratio ( $\text{g kg}^{-1}$ ; colors) and time series of liquid water path ( $\text{g m}^{-2}$ ; purple) with  $30 \text{ g m}^{-2}$  dashed, (b) temperature ( $^{\circ}\text{C}$ ), (c) w wind ( $\text{cm s}^{-1}$ ), (d) water vapor mixing ratio ( $\text{g kg}^{-1}$ ), and (e) relative humidity (%). Data are from the control simulation.

The buoyancy-driven turbulent mixing results in a well-mixed layer through cloud-top with an inversion above it, as a result of the CTLC, that is maintained through the lifetime of the cloud (Fig. 4.13b-f). During the cloud's lifetime, the air near the surface is saturated, providing a moisture source for cloud maintenance (Fig. 4.12e). The buoyancy-driven updrafts lift and condense this moist air near

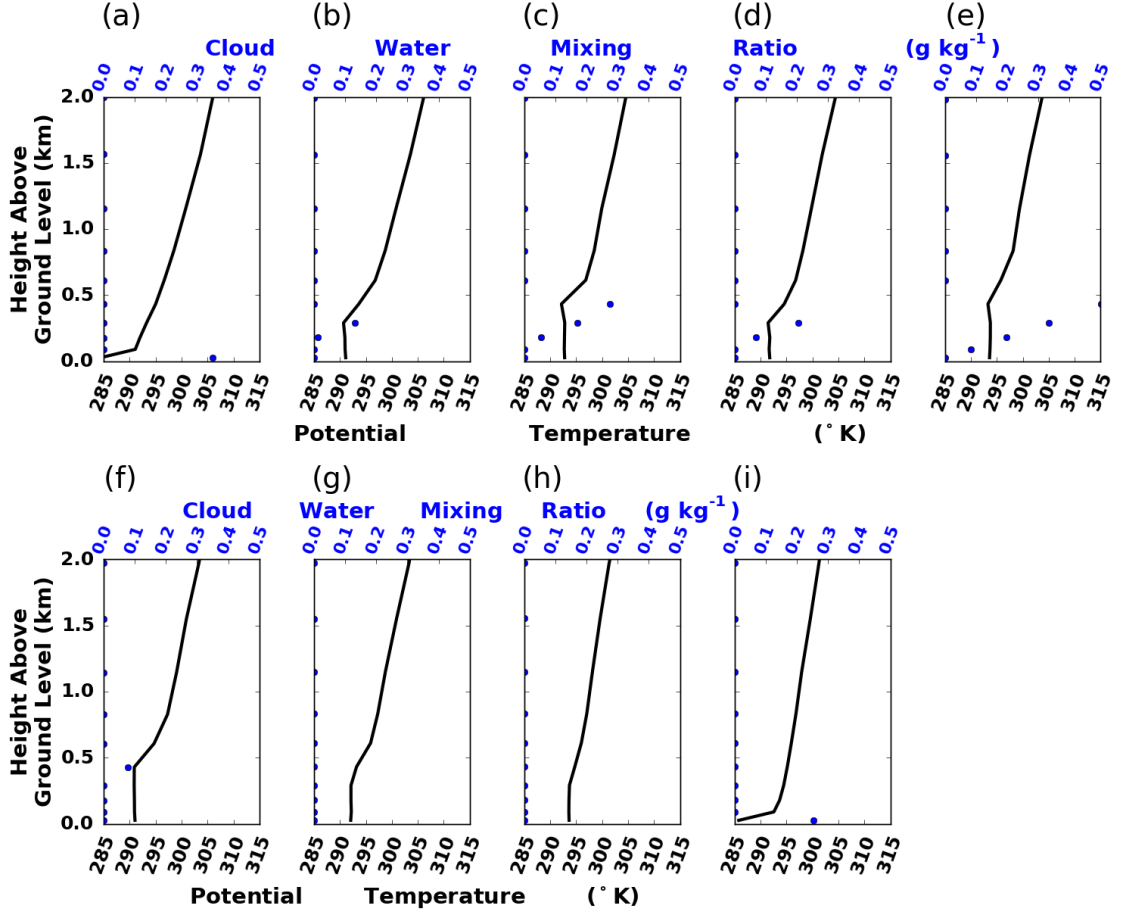


Figure 4.13: Vertical potential temperature ( $^{\circ}\text{K}$ ; black line) and cloud water mixing ratio ( $\text{g kg}^{-1}$ ; blue dots) profiles in the lowest 2 km AGL at 00 UTC (a,c,e,g,i) and 12 UTC (b,d,f,h) on (a,b) 20, (c,d) 21, (e,f) 22, (g,h) 23, and (i) 24 July 2012. Data are from the control simulation.

the surface (Fig. 4.12d) through the cloud-top maintaining the cloud liquid water supply. The average LWP from 20 July at 00 UTC to 22 July at 12 UTC is  $38 \text{ g m}^{-2}$ . The LWP peaks at  $120 \text{ g m}^{-2}$  on 22 July at 00 UTC associated with strong upward motion through the lowest 0.5 km AGL at the time when the well-mixed layer is deeper and the inversion at cloud-top is weaker (Fig. 4.12a,c, 4.13e).

The LWP and the cloud water and water vapor mixing ratios exhibit a diurnal cycle with higher values during the day and lower values at night (Fig. 4.12a,d). With a well-mixed layer below the cloud, there is strong coupling between the surface and the cloud. During the day, the skin temperature is warmer than the 2-m temperature (Fig. 4.14a), driving positive, upward surface sensible heat fluxes (Fig. 4.14b) enhancing the moisture and energy to the cloud, resulting in more liquid within the cloud (Fig. 4.12a). Given the air is near saturation, this results in greater moisture near the surface (Fig. 4.12d,e). During the night, these fluxes are weaker as there is little difference between the two temperatures (due to the

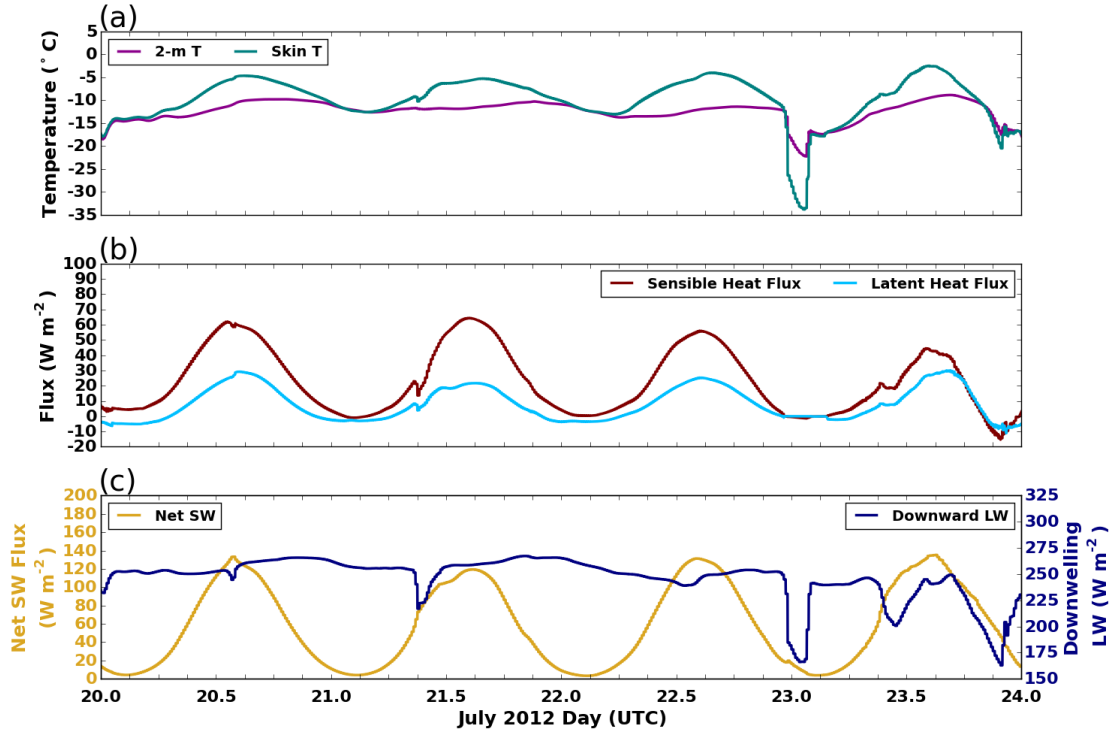


Figure 4.14: Time series of (a) 2-m (purple) and skin (teal) temperature ( $^{\circ}\text{C}$ ), (b) sensible (brown) and latent (light blue) heat flux ( $\text{W m}^{-2}$ ), and (c) surface net shortwave (gold) and downward longwave (navy) flux ( $\text{W m}^{-2}$ ). Data are from the control simulation.

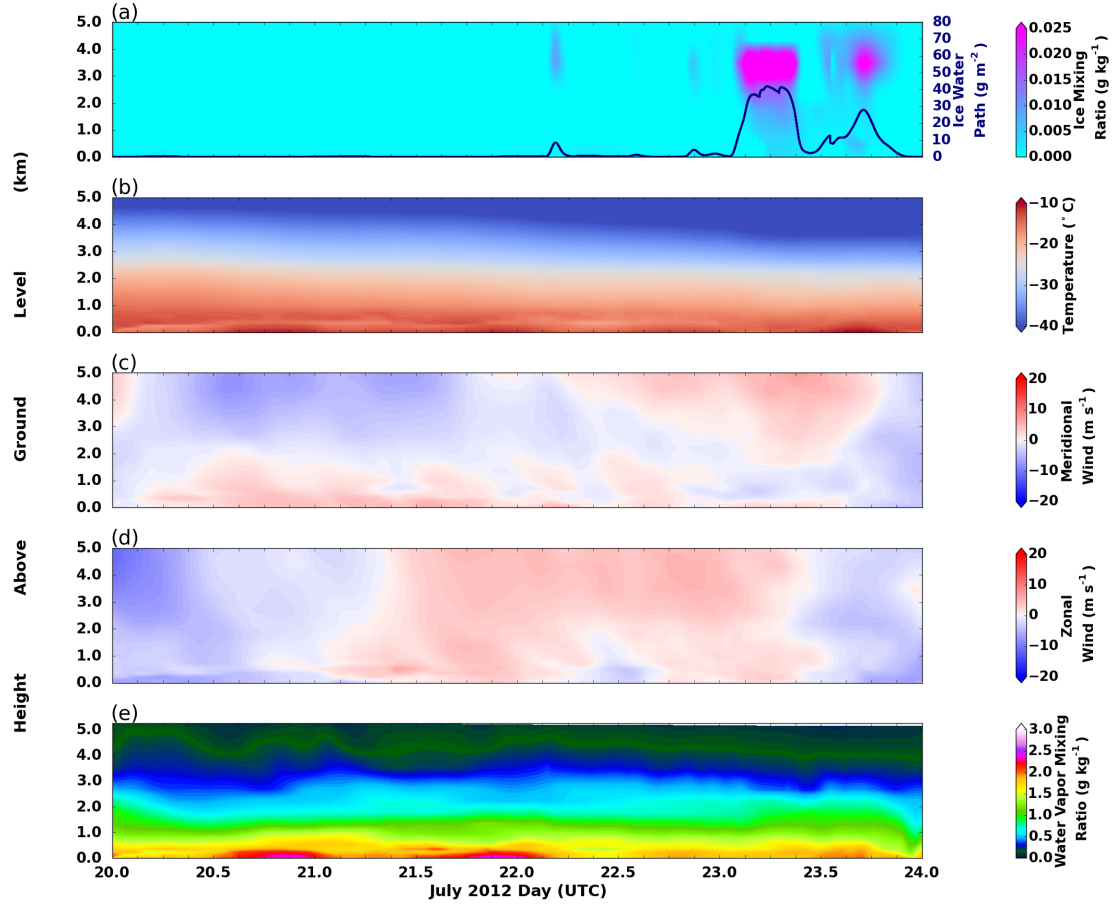


Figure 4.15: Time-height cross section through the lowest 5 km AGL of (a) ice mixing ratio ( $\text{g kg}^{-1}$ ; colors) and ice water path time series ( $\text{g m}^{-2}$ ; purple), (b) temperature ( $^{\circ}\text{C}$ ), (c) meridional wind ( $\text{m s}^{-1}$ ), (d) zonal wind ( $\text{m s}^{-1}$ ), and (e) water vapor mixing ratio ( $\text{g kg}^{-1}$ ). Data are from the control simulation.

loss of incoming SW radiation), and so moisture and energy contributions from the surface fluxes are weaker. This results in less liquid within the cloud at night.

The cloud dissipates on 23 July at 00 UTC (Fig. 4.12a, 4.13g), when there is sinking motion throughout the lowest 1 km AGL (Fig. 4.12c). Without the cloud, the well-mixed layer and the inversion at cloud-top weaken (Fig. 4.13g). The surface downwelling LW flux during cloud lifetime is around  $250 \text{ W m}^{-2}$  with

most of the SW radiation getting through to the surface (Fig 4.14c). Once the cloud dissipates, the surface downwelling LW flux drops from 250 to below 175 W m<sup>-2</sup> and results in the skin and 2-m temperature quickly cooling (Fig 4.14a).

Shortly after cloud dissipation, there is a dramatic increase in ice mixing ratio near 4 km AGL (Fig. 4.15a), colder air descending from aloft (Fig. 4.15b), a shift in the meridional wind from southerly to northerly (Fig. 4.15c) followed by a shift in the zonal wind from westerly to easterly at 23 July at 09 UTC (Fig. 4.15d), and drier air (Fig. 4.12d,e, 4.15e). These factors indicate a change in air mass in the simulation. The well-mixed layer continues to weaken through 23 July at 12 UTC (Fig. 4.13h), and by 24 July at 00 UTC a surface-based inversion develops (Fig. 4.13i). This is a very different thermodynamic profile than the previous 3 days, consistent with conditions of an Arctic ‘clear-sky’ state.

On the synoptic-scale on 20 July at 00 UTC, there is weak, northeasterly flow at 650 hPa over Summit due to an anticyclonic circulation to the north (Fig. 4.16a). There is a high relative humidity air mass across the central GIS with a notably saturated air mass off the northwest coast. A 988 hPa surface cyclone is just off the southern tip of Greenland (Fig. 4.17a). Over western Greenland, the 10-m zonal winds are easterly, while they are westerly over eastern Greenland. This is characteristic of the katabatic winds.

Through 21 July at 00 UTC, the 650 hPa winds over the center of the ice sheet shift to a more southeasterly direction (Fig. 4.16b,c) as the surface cyclone rounds the eastern side of southern Greenland tip (Fig. 4.17b,c). Associated with this southeasterly flow, moister air expands across the central and southeastern GIS (Fig. 4.16b,c). Backward trajectories show parcels in the lowest 1 km AGL arriving at Summit on 21 July at 00 UTC originated from the moist air over southeast Greenland on 20 July at 00 UTC (Fig. 4.18a). The moist air mass that was off the northwestern coast has been advected easterly and elongated meridionally as the

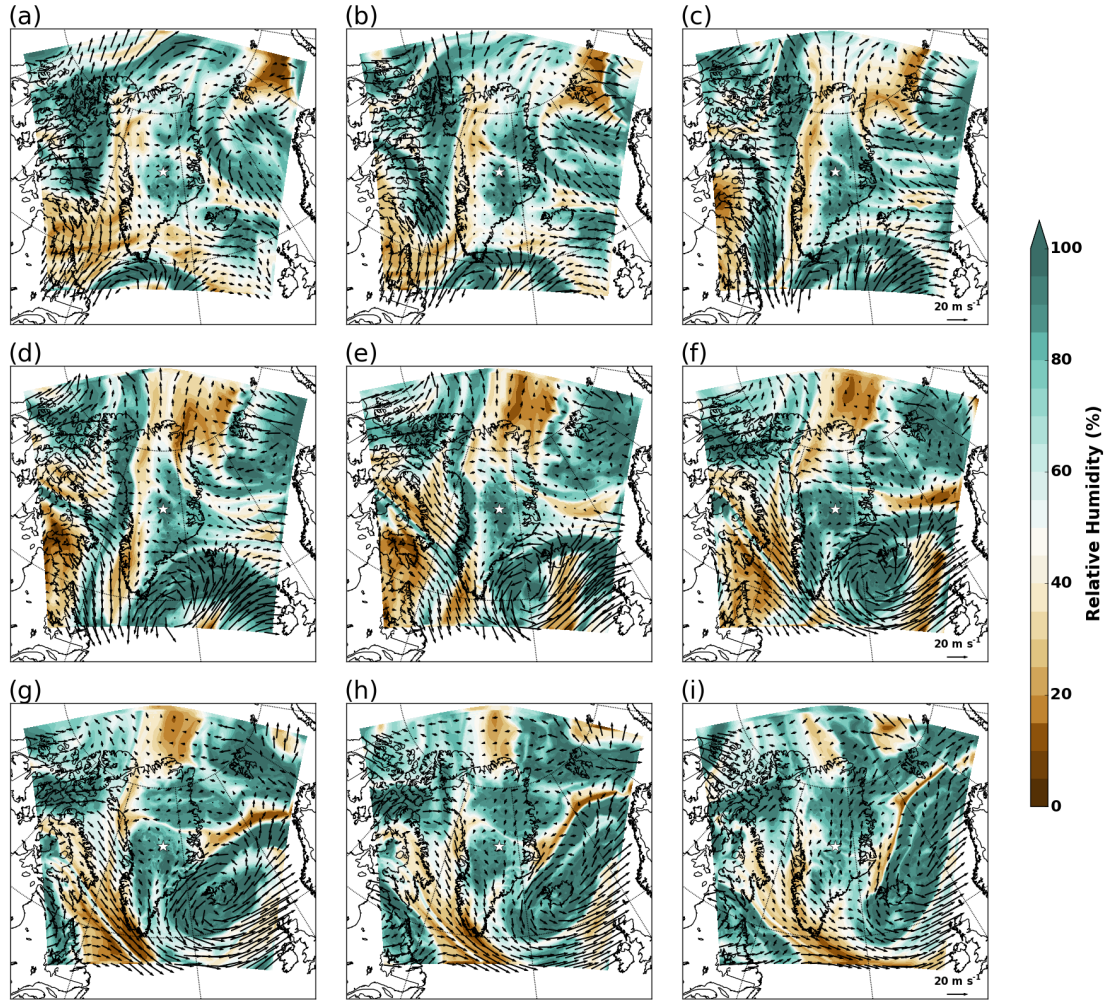


Figure 4.16: 650 hPa relative humidity (%) (colors) and winds ( $\text{m s}^{-1}$ ; black arrows) on (a,b) 20, (c,d) 21, (e,f) 22, (g,h) 23, and (i) 24 July 2012 at (a,c,e,g,i) 00 UTC and (b,d,f,h) 12 UTC. Data are from the control simulation, and the location of Summit, Greenland is denoted by ★. 650 hPa is chosen as it is the closest pressure level to the Summit surface.



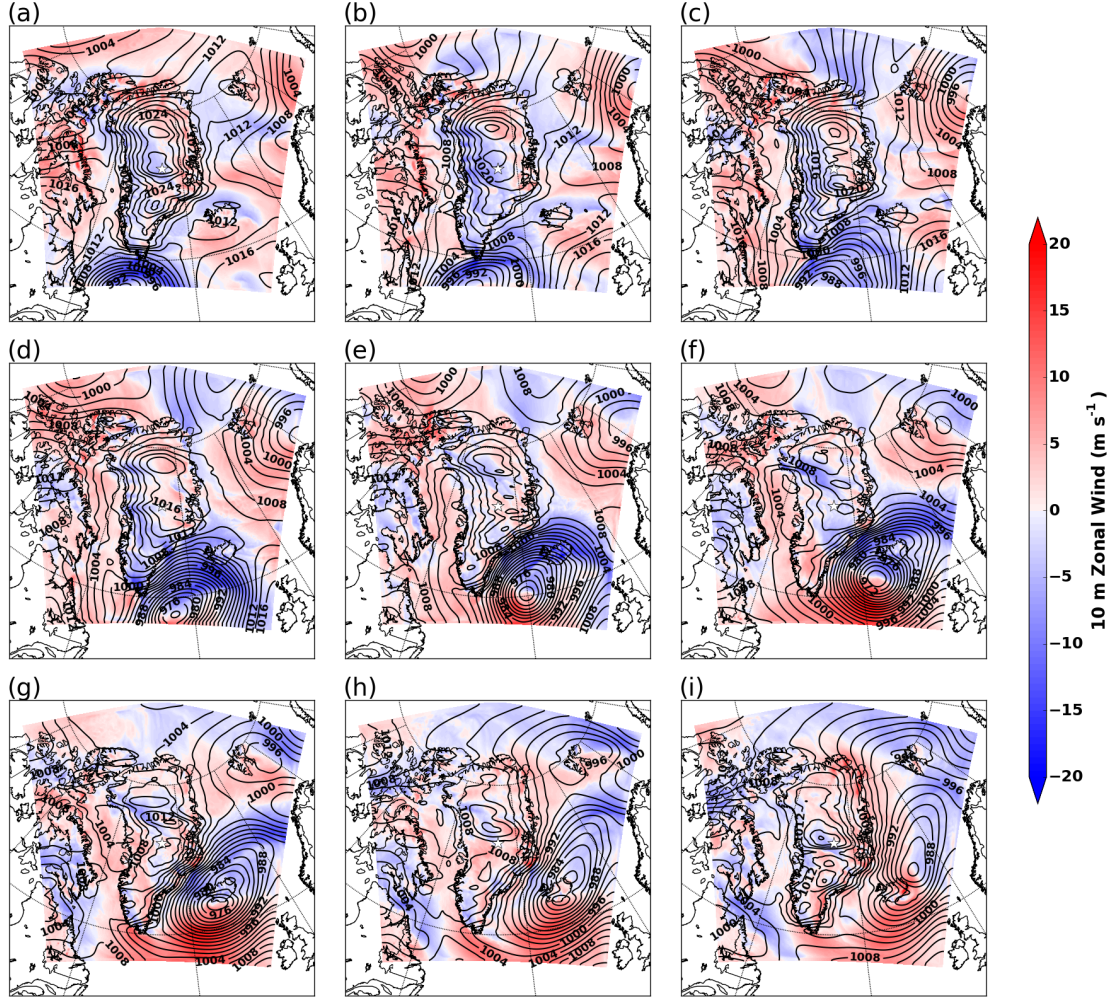


Figure 4.17: 10-m zonal wind ( $\text{m s}^{-1}$ ; colors) and smoothed sea-level pressure (hPa; black) on (a,b) 20, (c,d) 21, (e,f) 22, (g,h) 23, and (i) 24 July 2012 at (a,c,e,g,i) 00 UTC and (b,d,f,h) 12 UTC. Data are from the control simulation, and the location of Summit, Greenland is denoted by ★.

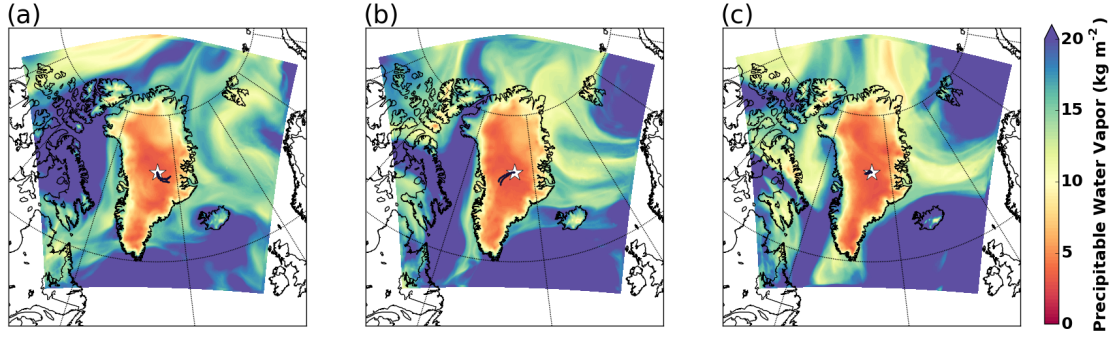


Figure 4.18: Perceptible water vapor ( $\text{kg m}^{-2}$ ) on (a) 20, (b) 21, and (c) 22 July 2012 at 00 UTC with 1-day backward trajectories for parcels in the lowest 1 km AGL at Summit arriving on (a) 21, (b) 22, and (c) 23 July 2012 at 00 UTC. Data are from the control simulation, and the location of Summit, Greenland is denoted by  $\star$ .

flow is diverted north and south around the GIS creating a distinct north-south moisture boundary off the western GIS coast (Fig. 4.16b,c).

By 21 July at 12 UTC, the surface cyclone deepens to 972 hPa as it tracks closer to Greenland (Fig. 4.17d). Westerly flow at 650 hPa across the western portion of the domain has impinged the moisture boundary against the western GIS (Fig. 4.16d). At 650 hPa on 22 July at 00 UTC, there is a ‘bulge’ in the moisture boundary over the western central GIS indicating it is probable that air may be ascending the ice sheet toward Summit due to the strong, dry northwesterly flow behind the boundary (Fig. 4.16e); this flow is driven by the southeast directed pressure gradient force as the surface cyclone deepens to 968 hPa off the southeastern coast (Fig. 4.17e). The location of the surface cyclone in the control is similar to that in the ERA-Interim, but the surface cyclone in the control is slightly stronger than ERA-Interim (cf. Fig. 4.17e to 3.3d). Additionally, backward trajectories show parcels in the lowest 1 km AGL at Summit on 22 July at 00



UTC originated from the west 24 hours prior (Fig. 4.18b). At 22 July at 12 UTC, the 650 hPa flow over the northern and eastern portion of the GIS has taken on a more easterly component (Fig. 4.16f) as the surface cyclone propagates to the northeast paralleling the southeastern coast (Fig. 4.17f). This easterly flow along with drier, northwesterly flow behind the 650 hPa moisture boundary forces the moist air over southern Greenland (Fig. 4.16f).

At the time of cloud dissipation (23 July at 00 UTC), parcels are adiabatically ascending from both the west and east of Summit (Fig. 4.20). Westerly flow over the western GIS and easterly flow over the eastern GIS are meeting atop the ice sheet (Fig. 4.20a), and, as a result, there is low-level moisture flux convergence (Banacos and Schultz, 2005) at Summit (Fig. 4.20b). The moisture boundary at 650 hPa moves slowly over southwestern Greenland (Fig. 4.16g); this boundary is clearly evident in the east-west cross section of relative humidity (Fig. 4.20c). Ahead of the boundary, there is a well-defined ice cloud between 6 and 7 km with

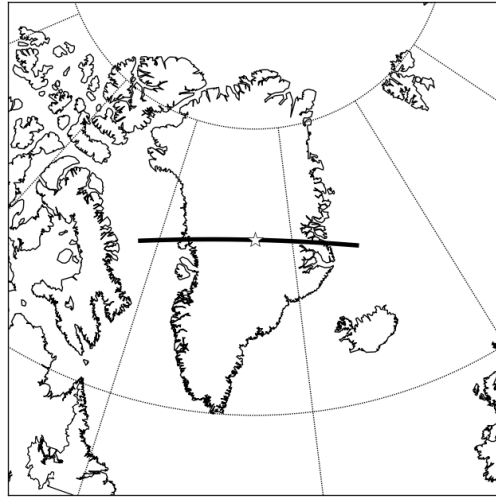


Figure 4.19: Black line indicates where cross section was taken in Figs. 4.20, 4.21, 4.23, 4.24, 4.35, 4.36, and 4.40. The location of Summit, Greenland is denoted by  $\star$ .

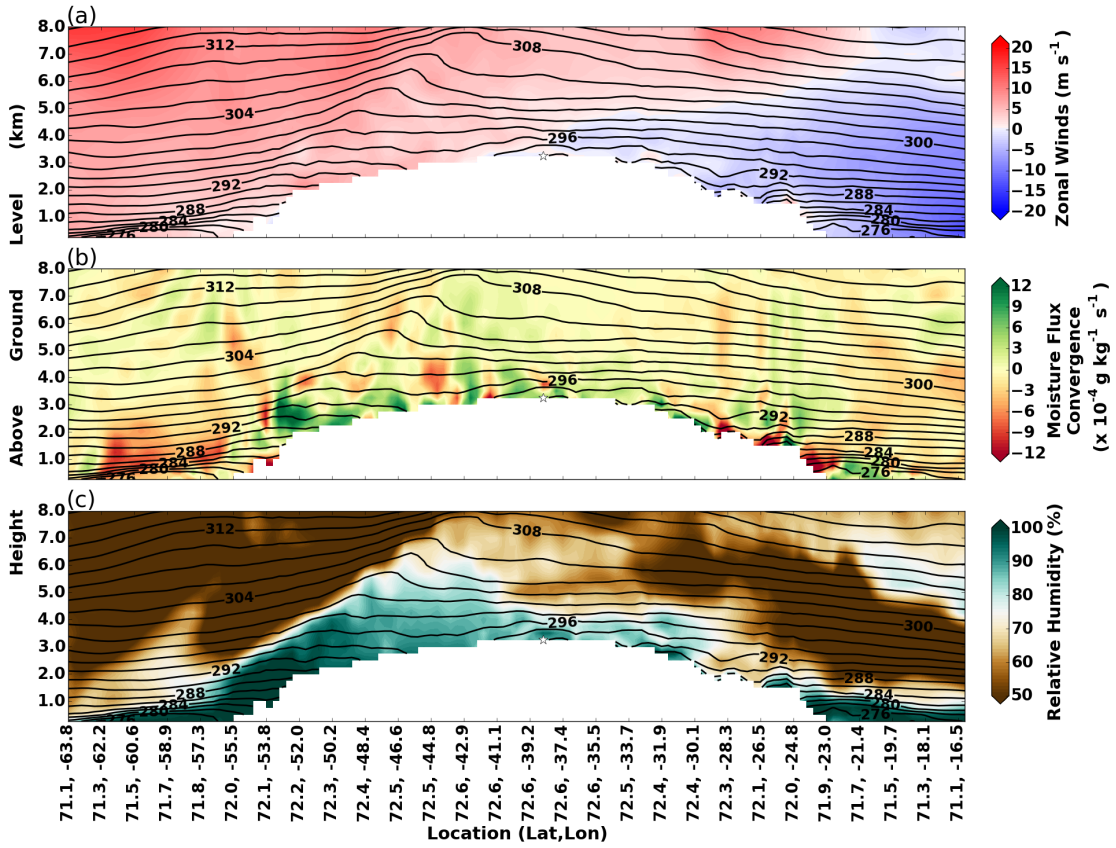


Figure 4.20: East-west cross section taken through black line in Fig. 4.19 of (a) zonal wind ( $\text{m s}^{-1}$ ), (b) moisture flux convergence ( $\times 10^{-4} \text{ g kg}^{-1} \text{ s}^{-1}$ ), and (c) relative humidity (%) on 23 July 2012 at 00 UTC. Data are from the control simulation, and the location of Summit, Greenland is denoted by  $\star$ .

precipitation reaching the surface (Fig. 4.21a). Meanwhile, a ribbon of drier air at 650 hPa extends its way across the ice sheet just north of Summit (Fig. 4.16g).

Due to the dramatic GIS topography, flow ascending to the top of the ice sheet requires a large amount of kinetic energy. The Froude Number ( $F_r$ ) is a diagnostic that quantifies whether flow will ascend over an obstacle (ex. the GIS). Essentially,  $F_r$  is the ratio of kinetic energy, the speed of the flow, to potential energy, atmospheric stability and obstacle height. For low  $F_r$  flow, a value less

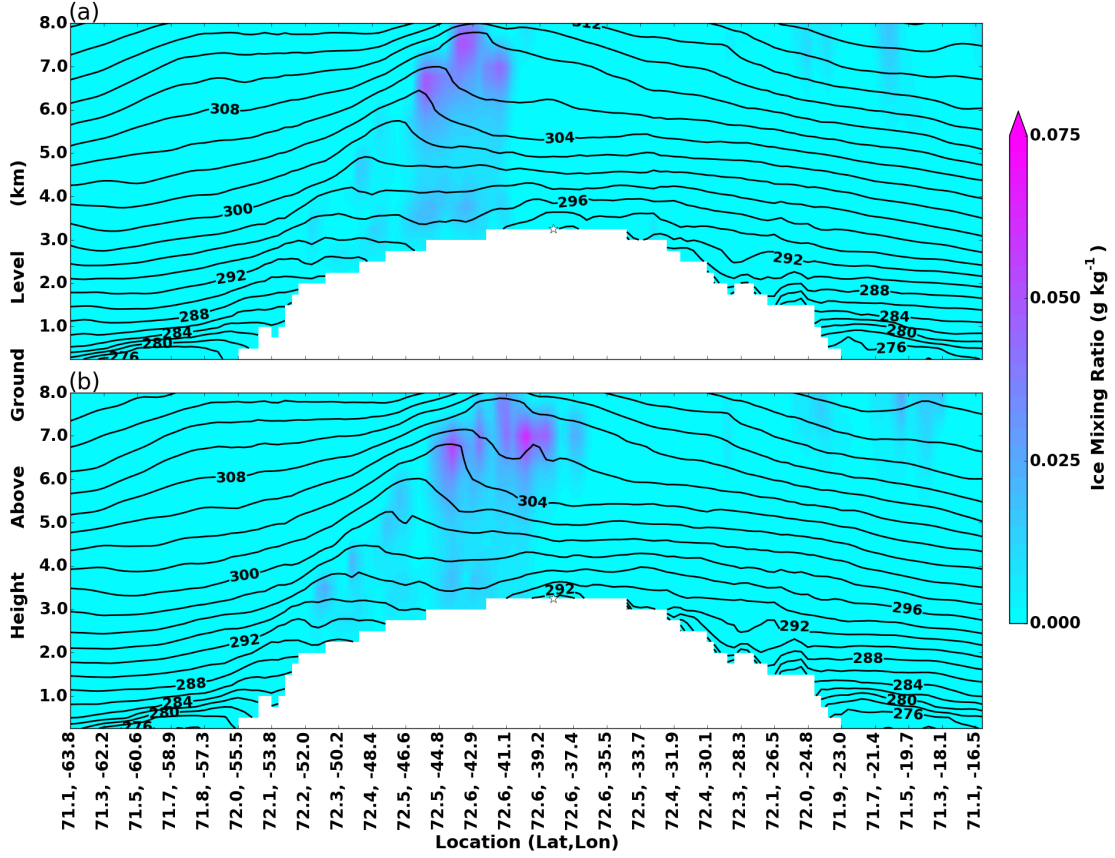


Figure 4.21: East-west cross section taken through black line in Fig. 4.19 of ice mixing ratio ( $\text{g kg}^{-1}$ ) at 23 July 2012 at (a) 00 UTC and (b) 03 UTC. Data are from the control simulation, and the location of Summit, Greenland is denoted by ★.

than 1, the air is blocked or diverted around the obstacle (i.e. kinetic energy is less than potential energy), and high  $F_r$  flow, a value greater than 1, the air ascends over the obstacle (i.e. kinetic energy is greater than potential energy). The equation for  $F_r$  is

$$F_r = \frac{U}{hN} \quad (4.1)$$

where  $U$  is the flow speed perpendicular to the obstacle,  $h$  is the obstacle height, and  $N$  is the Brunt–Väisälä frequency (Bluestein, 1993).  $N$  is the frequency in a

statically stable environment an air parcel will oscillate when vertically displaced (Glickman, 2000) and is given by

$$N = \sqrt{\frac{g}{\theta} \frac{\partial \theta}{\partial z}} \quad (4.2)$$

where  $g$  is Earth's gravitational constant,  $\theta$  is potential temperature, and  $\frac{\partial \theta}{\partial z}$  is the vertical gradient of potential temperature (e.g. Martin (2013)).

The  $F_r$  is calculated for the control simulation at gridpoints across the domain on the model eta levels ( $F_r(t, \eta, x, y)$ ) and then linearly interpolated to height coordinates. As the static stability is non-uniform throughout the domain, the bulk method described in Reinecke and Durran (2008) is used to calculate  $N$ . Thus, equation 4.1 becomes

$$F_r(t, \eta, x, y) = \frac{U(t, \eta, x, y)}{(h - z(t, \eta, x, y)) \sqrt{\frac{g}{\theta(t, \eta, x, y)} \frac{\theta(t, h, x, y) - \theta(t, \eta, x, y)}{h - z(t, \eta, x, y)}}} \quad (4.3)$$

where  $U(t, \eta, x, y)$  is the zonal wind at the gridpoint,  $h$  the elevation of Summit,  $z(t, \eta, x, y)$  is the gridpoint height,  $\theta(t, \eta, x, y)$  is the potential temperature at the gridpoint, and  $\theta(t, h, x, y)$  is the potential temperature at the gridpoint at  $h$ .

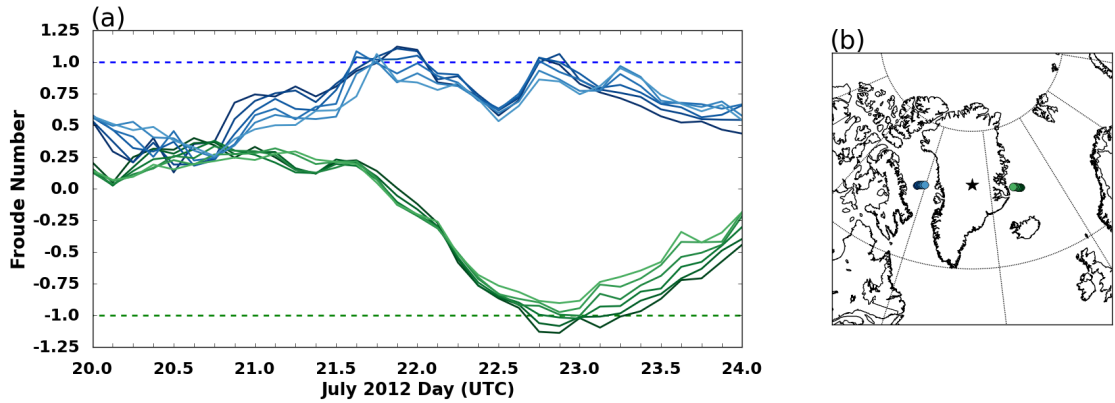


Figure 4.22: (a) Time series of Froude number from points plotted in (b). The Froude number is from a height of 2.5 km above sea-level. Data are from the control simulation, and the location of Summit, Greenland is denoted by  $\star$ .

$F_r$  greater than 1 over western Greenland indicates the ascent of westerly flow, while -1 over eastern Greenland indicates easterly flow ascent. Both instances occur on 22 July at 18 UTC directly to the east and west of Summit for parcels at a height of 2.5 km (Fig. 4.22b); this further confirms the ascent and convergence of flow at Summit a few hours later (Fig. 4.20a,b). This flow pattern is driven by the surface cyclone near Iceland at 23 July at 00 UTC (Fig. 4.17g). Such a positioning of the surface cyclone drives a pressure gradient force with an easterly directed component over western Greenland; backward trajectories for parcels in the lowest 1 km AGL at Summit at 23 July at 00 UTC show the air still originating from the west on 22 July at 00 UTC (Fig. 4.18c). While circulation associated with the surface cyclone results in easterly flow to its north over eastern Greenland. Such converging flow atop the GIS is opposite from the dominant katabatic wind pattern, where there is flow off the ice sheet.

From mass continuity, low-level horizontal convergence requires a response in the vertical motion; the low-level convergence at Summit (Fig. 4.20b) precedes upward motion through the lowest 1 km at 23 July at 03 UTC (Fig. 4.15c). This vertical motion results in the formation of ice (Fig. 4.12a) as a precipitating, upper-level ice cloud advects over Summit (Fig. 4.21b). The precipitating ice falls through the liquid water layer, further leading to the demise of the liquid water. By 23 July at 12 UTC, northerly and easterly flow begins to dominate over Summit and the central GIS (Fig. 4.15c,d, 4.16h, 4.23a) as the surface cyclone continues to move to the northeast (Fig. 4.17h). The moisture boundary slowly moves east across the GIS with low-level moisture and moisture flux convergence ahead of it (Fig. 4.16h, 4.23b,c). At 650 hPa, the thin band of drier air approaches Summit from the northeast (Fig. 4.16h) and is visible in the east-west cross as the drier air in the mid-levels (Fig. 4.23c).

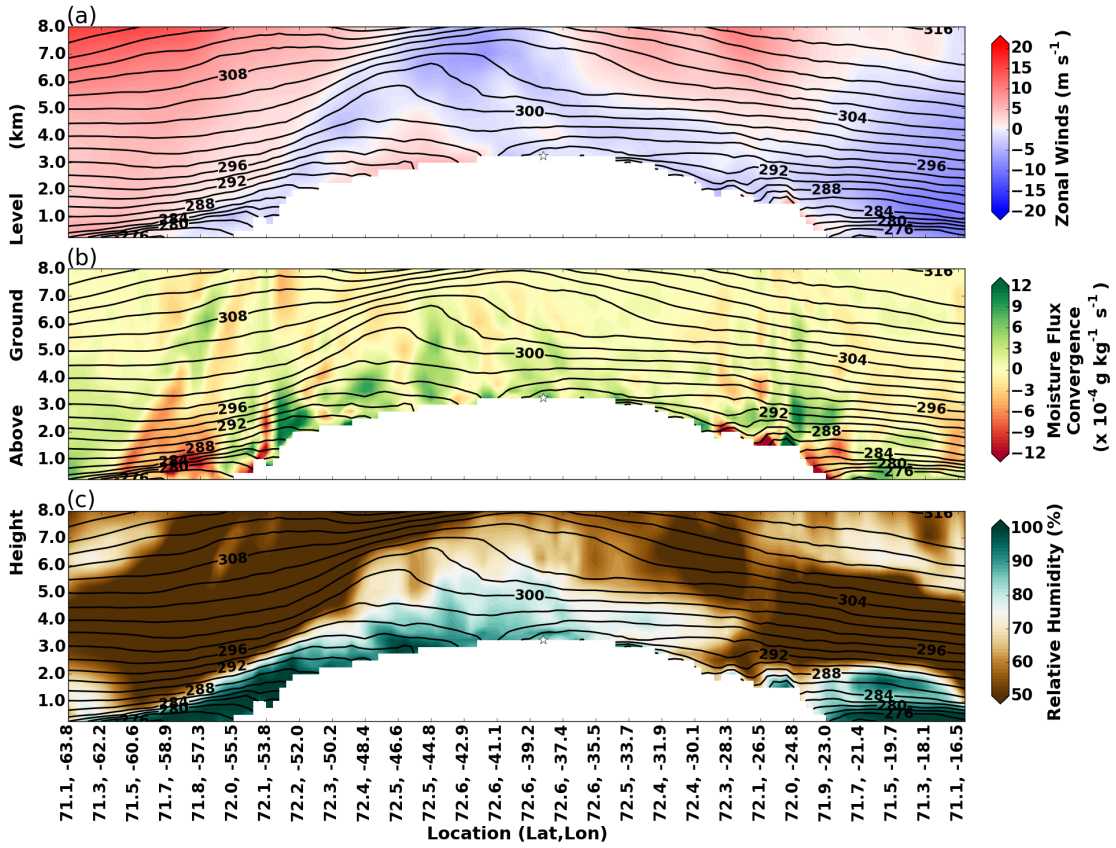


Figure 4.23: Same as Fig. 4.20, but for 23 July at 12 UTC.

By 24 July at 00 UTC, northeasterly flow dominates over Summit and the central GIS (Fig. 4.16i, 4.24a) in the wake of the surface cyclone as it moves north-east away from Greenland (Fig. 4.17i). At Summit, there moisture flux divergence nearest the surface (Fig. 4.24b). The moisture boundary is downstream of Summit, as a dry air mass moves in behind it; the thin band of drier air at 650 hPa reaches Summit by 24 July at 00 UTC (Fig. 4.16i). The moisture profile has significantly dried out, though the low-levels remain decently saturated (Fig. 4.16i, 4.24c). The formation of ice as a result of low-level convergence, the ice cloud ahead of the moisture boundary and its associated sedimentation, along with dramatic change

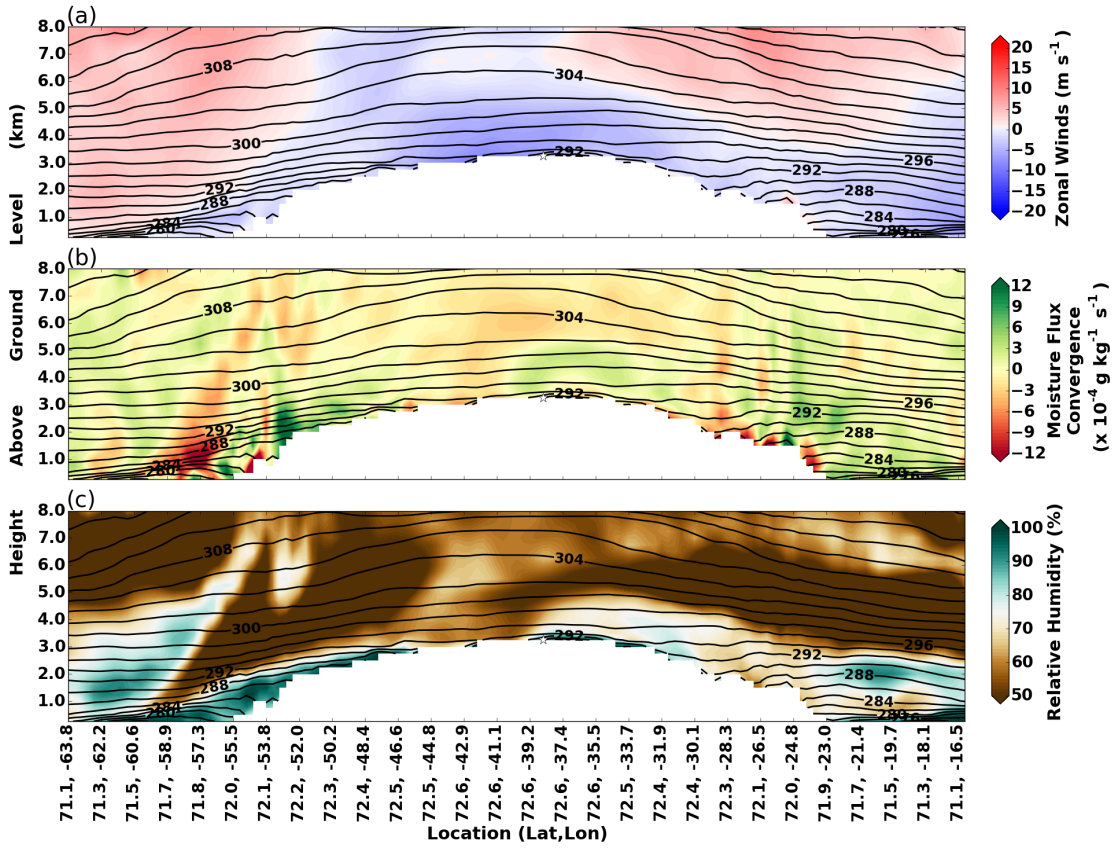


Figure 4.24: Same as Fig. 4.20, but for 24 July at 00 UTC.

in the synoptic environment due the passing of the surface cyclone and moisture boundary (change in air mass) hinder the reformation the low-level AMPC.

The control compares relatively well to the observations from Summit. The control simulated LWP overall follows the peaks and valleys from the MWRRET (Fig. 4.25a). The diurnal cycle of control LWP is not seen as strongly in the MWRRET LWP, but is somewhat apparent on 21 July. Additionally, the peak in the LWP for both are of similar value, though the control simulation peak is about 9 hours after the MWRRET peak. The magnitude of the control 10-m zonal winds at Summit are weaker than the observed, though they mostly follow the same direction (Fig. 4.25b). The same is true for the control meridional winds,



particularly after 22 July at 12 UTC where the observed northerly winds are much stronger than the control simulation (Fig. 4.25c). The sea-level pressure, both observed and simulated (Fig. 4.25d), decline through 23 July at 00 UTC, as the surface cyclone approaches Greenland (Fig. 4.17). On 23 July at 00 UTC, the control simulated sea-level pressure sharply spikes, most likely associated with convergence (Fig. 4.20a,b) and drop in temperature at Summit, while such an increase is not observed (Fig. 4.25e). This perhaps indicates the convergence at the top was overdone or simply the decrease in temperature due to the simulated cloud dissipation was not observed because the cloud was maintained (Fig. 4.25e). Additionally, it appears that the moisture boundary passed over Summit later in the control simulation from the observations. In the observations at 22 July at 12 UTC, the meridional wind shifts from southerly to northerly along the relative humidity quickly dropping (Fig. 3.7a,d); this occurred in the control simulation at 23 July at 00 UTC.

Despite the drop in the control 2-m temperature, the control very nicely captures the observed diurnal cycle in temperature. The control simulation temperature vertical profile (Fig. 4.25a) is much warmer than that retrieved from the AERI (Fig. 4.25c), particularly above 0.5 km. This might be due to the observed cloud being too optically thick and attenuating the signal such that the retrieval falls back on climatology. The water vapor mixing ratio vertical profiles are very comparable; both show a diurnal cycle with higher water vapor mixing ratios during the day than at night. Though, early in the period, the control simulation water vapor mixing ratios (Fig. 4.26b) are higher than the retrieval near the surface (Fig. 4.26d).



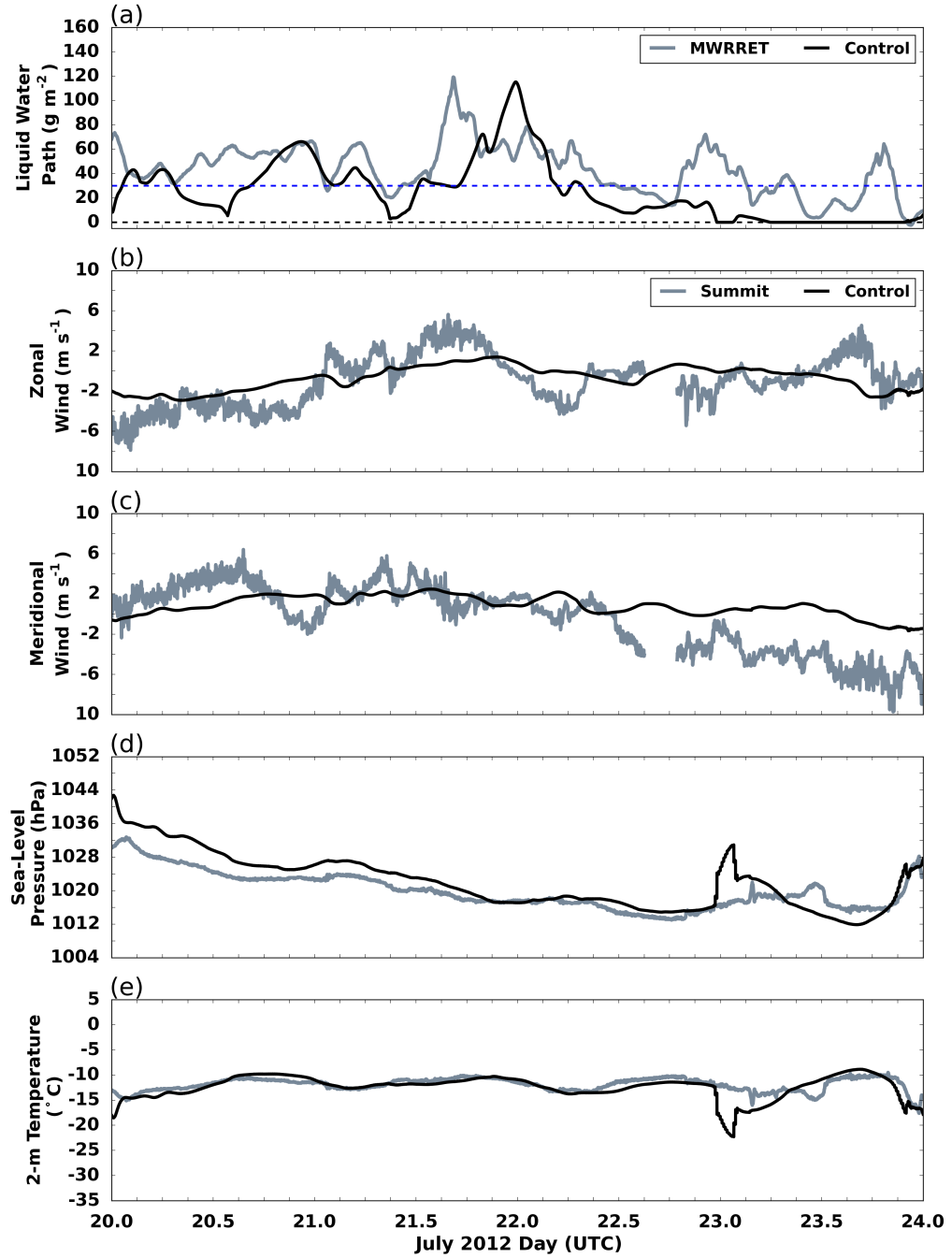


Figure 4.25: Time series of (a) liquid water path ( $\text{g m}^{-2}$ ) retrieved from the Microwave Radiometer (gray) and control simulation (black) with 30 (blue) and 0 (black)  $\text{g m}^{-2}$  dashed, 10-m (b) zonal and (c) meridional wind ( $\text{m s}^{-1}$ ), (d) sea-level pressure (hPa), and (e) 2-m temperature ( $^{\circ}\text{C}$ ) from surface tower at Summit (gray) and control simulation (black).

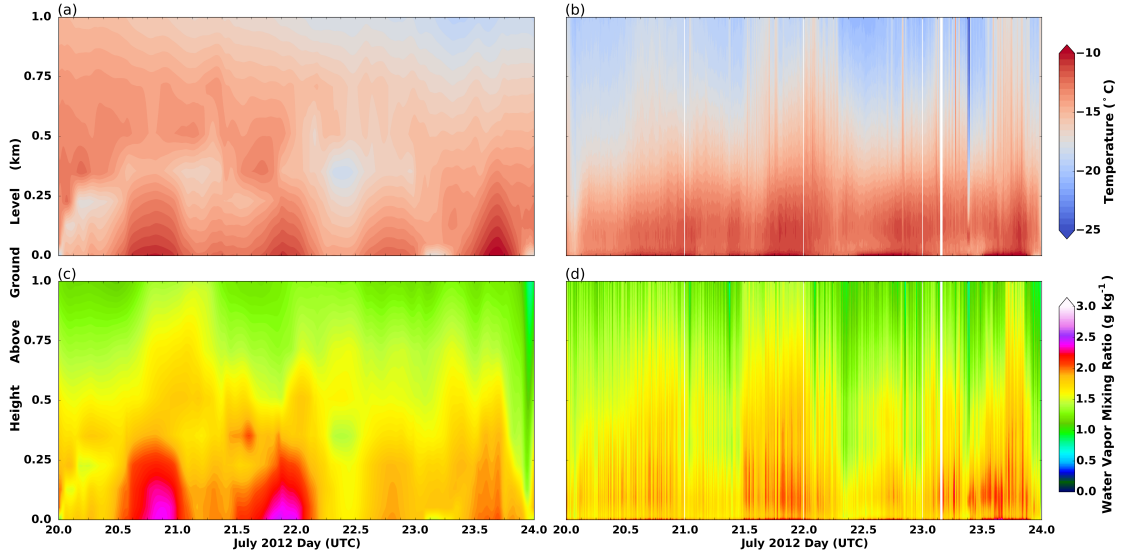


Figure 4.26: Time-heights cross section of (a,c) temperature ( $^{\circ}\text{C}$ ) and water vapor ( $\text{g kg}^{-1}$ ) from the (a,b) control simulation and (c,d) AERIoe retrieval.

## 4.2 Experimental Simulations

The experimental model simulations are broken down into two scale categories to isolate the influences of various forcings on the cloud’s formation and persistence: synoptic and local. These simulations are described below and summarized in Table 4.2 at the end of this section.

### 4.2.1 Synoptic Influence

The effects of the evolution of the synoptic-scale pattern are investigated to understand their effects on the cloud event. Due to Summit’s location at the top of the GIS the air is quite dry, therefore, synoptic-scale moisture advection is likely a critical processes for AMPCs (Morrison et al., 2012).

#### 4.2.1.1 Fixed Boundary Conditions

In order to analyze the influence of the synoptic-scale, an experimental simulation is performed where the boundary conditions (BCs) are fixed at 19 July 2012 at 12 UTC (*fixed\_19\_12*), i.e. the model initialization time. The hypothesis is that if the particular evolution of the synoptic-scale pattern is not important for driving the cloud's persistence, then the cloud evolution will remain largely unchanged from the control simulation, confirming the dominance of local processes on cloud maintenance.

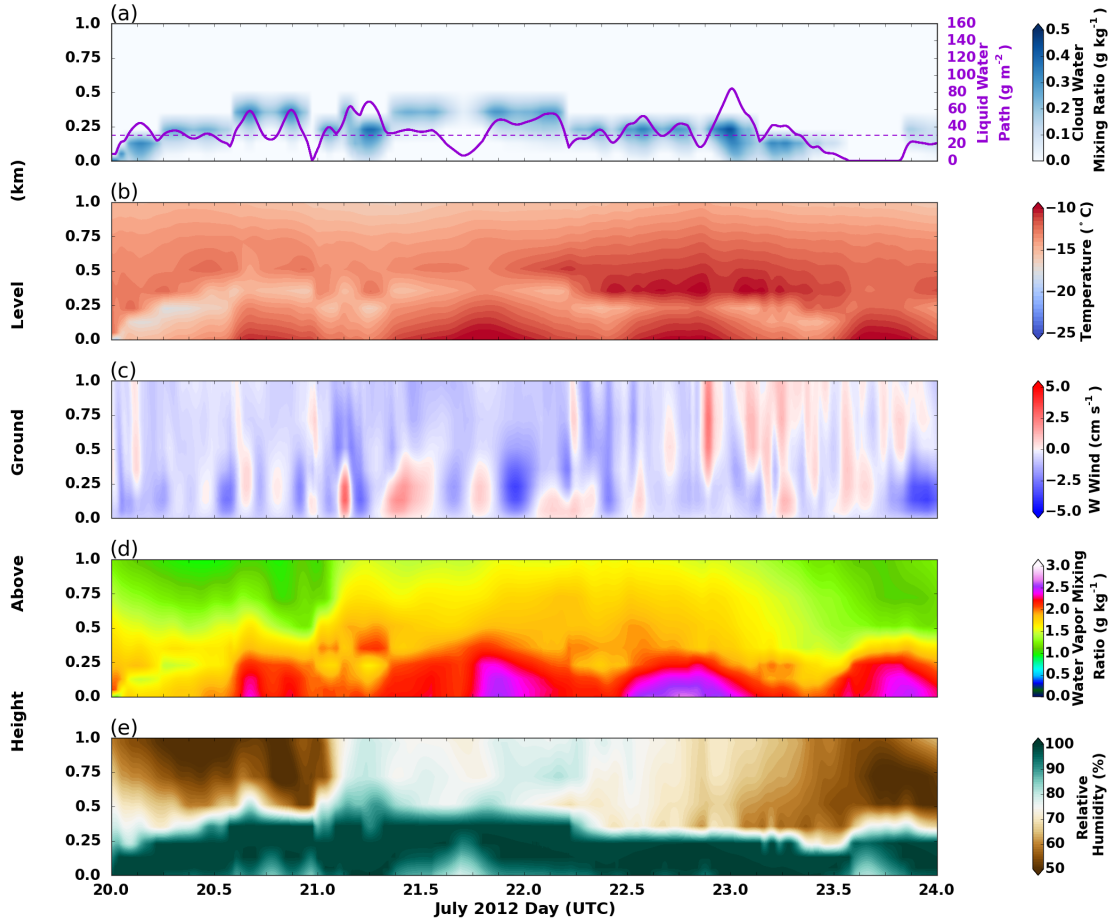


Figure 4.27: Same as Fig. 4.12, but data are from *fixed\_19\_12*.

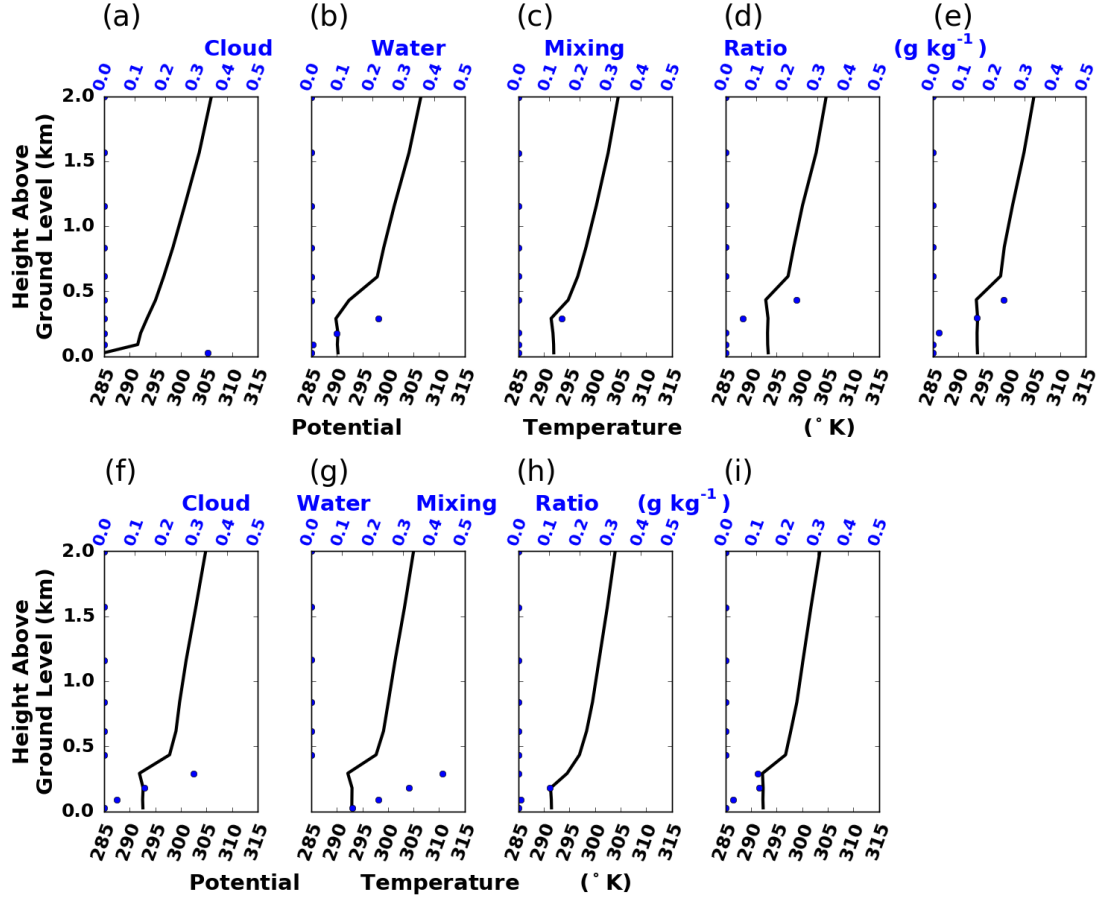


Figure 4.28: Same as Fig. 4.13, but data are from *fixed\_19\_12*.

The evolution of the cloud and thermodynamic profiles at Summit simulated in *fixed\_19\_12* is drastically different than the control. The most notable difference between the simulations is cloud lifetime; the cloud in the *fixed\_19\_12* simulation persists through almost the entire simulation period (Fig. 4.27a), though there is a small break between 23 July at 12 and 21 UTC, whereas in the control the cloud was shorter lived, dissipating at 23 July at 00 UTC (Fig. 4.12a). As in the control, the cloud simulated by *fixed\_19\_12* forms at the surface due to the strong radiative cooling under a surface-based inversion (Fig. 4.28a). Again, the LW radiative cooling due to the liquid water (Fig. 4.27b) drives shallow, weak updrafts at the

surface (Fig. 4.27c) elevating the cloud and creating a well-mixed layer through cloud-top by 20 July at 12 UTC (Fig. 4.28b) that is maintained through cloud lifetime (Fig. 4.28c-i). The CBH never ascends above 0.5 km, similar to the control.

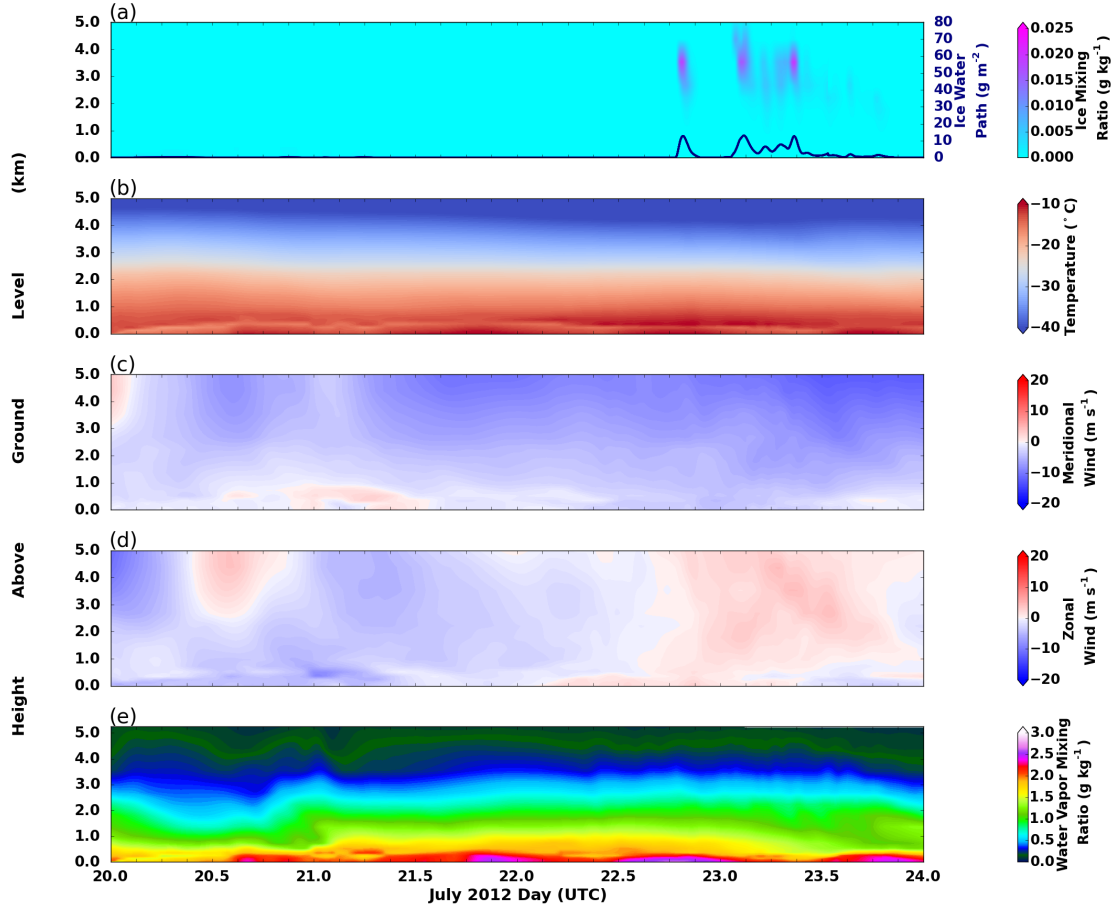


Figure 4.29: Same as Fig. 4.15, but data are from *fixed\_19\_12*.

*Fixed\_19\_12* is substantially warmer (cf. Fig. 4.27b to 4.12b) and moister (cf. Fig. 4.27d,e to 4.12d,e) in the lowest 1 km, especially in the latter half of the period, than the control. The warmer, moister environment in *fixed\_19\_12* helps explain why the cloud is longer lived than the control; reasons the environments are different will be discussed later. Additionally, there is little ice aloft (Fig. 4.29a)

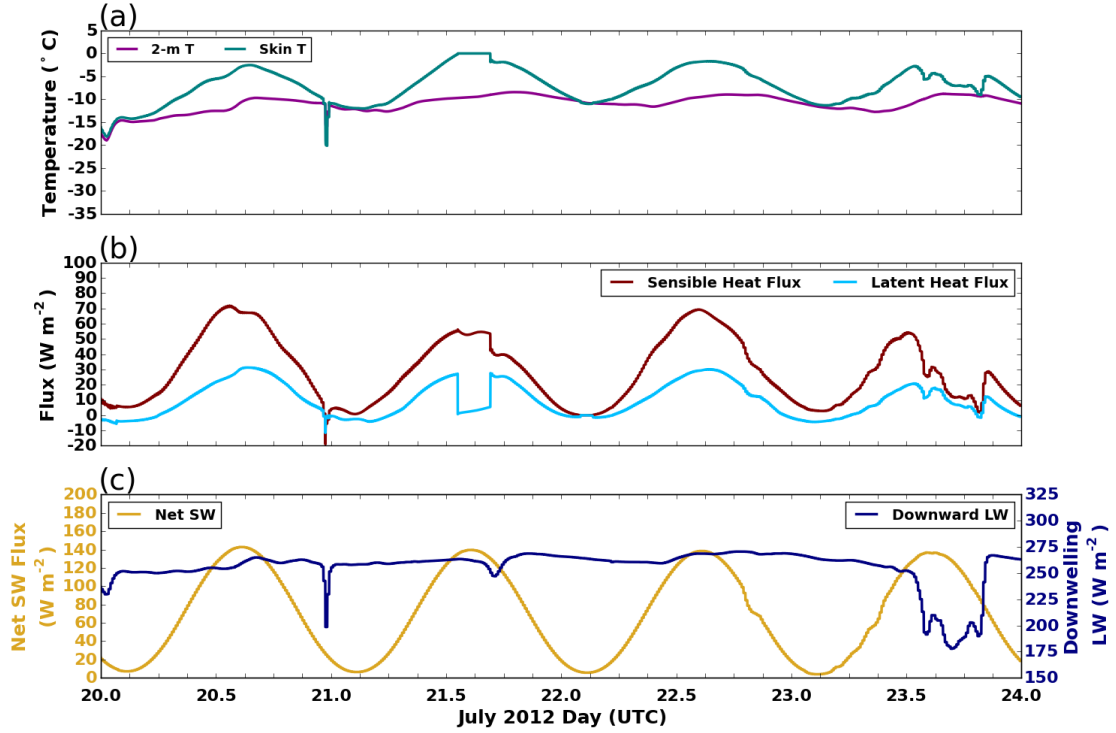


Figure 4.30: Same as Fig. 4.14, but data are from *fixed\_19\_12*.

and little variability in the vertical temperature profile (Fig. 4.29b). The meridional wind at Summit is predominately northerly throughout the simulation (Fig. 4.29c) with a shift in the zonal wind from easterly to westerly after 23 July at 00 UTC (Fig. 4.29d), though this shift in the wind has little impact on the temperature (Fig. 4.29b) and moisture fields (Fig. 4.29e). Thus, there are no indications of a change in air mass as there is in the control simulation (Fig. 4.15).

In this warmer environment simulated by *fixed\_19\_12*, the skin temperature at Summit reached  $0^{\circ}\text{C}$  for about a 3 hour period between 21 July at 13 and 16 UTC (Fig. 4.30a); this did not occur in the control (Fig. 4.14a). There is no evidence of a diurnal cycle in the *fixed\_19\_12* LWP or cloud water mixing ratio (Fig. 4.27a), as there was in the control (Fig. 4.12a), though there is a diurnal cycle in the water vapor mixing ratio field (Fig. 4.27d). This is despite similar surface

coupling and surface fluxes between the control (Fig. 4.13, 4.14b) and *fixed\_19\_12* (Fig. 4.28, 4.30b), suggesting perhaps that there are other processes involved. The vertical motion profile in the *fixed\_19\_12* simulation is dominated much more by sinking motion (Fig. 4.27c) than control (Fig. 4.12c), and perhaps this is hindering the formation of stronger updrafts and condensation.

These differences between the *fixed\_19\_12* and control simulations are due to the different evolution of the synoptic-scale pattern. On 20 July at 00 UTC, the *fixed\_19\_12* synoptic environment (Fig. 4.31a, 4.32a) is not substantially than the control (Fig. 4.16a, 4.17a). The 650 hPa flow in *fixed\_19\_12* is northeasterly at Summit with the moist air mass sitting off the northwestern Greenland coast (Fig. 4.31a). The 10-m zonal wind in *fixed\_19\_12* is characteristic of the katabatic winds on 20 July at 00 UTC (Fig. 4.32a). There is a surface cyclone just to the west of the southern Greenland, while in the far eastern portion of the domain in the Greenland Sea, there is a weak surface cyclone that develops (Fig. 4.32a) that does not develop in the control (Fig. 4.17a).

Due to the fixing of the BCs at 19 July at 12 UTC, there is a continual influx of moisture in the northwestern portion of the domain due to the moist air mass, whereas in the control drier air moves in behind this air mass as the BCs evolved. Through 21 July at 00 UTC at 650 hPa, moisture spreads north and south across the western Greenland coast (Fig. 4.31b,c). Meanwhile, the circulation at 650 hPa associated with the Greenland Sea surface cyclone to the east advects moisture onto the ice sheet (Fig. 4.33a). The southern surface cyclone does not move much remaining south of Greenland (Fig. 4.32b,c).

The 650 hPa moisture from the west continues to expand over the western part of the domain and across the northern GIS through 22 July at 12 UTC (Fig. 4.31d,e,f) due to the northeasterly flow off the Greenland Sea. With northerly flow over Summit and the central GIS, this moisture over the northern GIS is



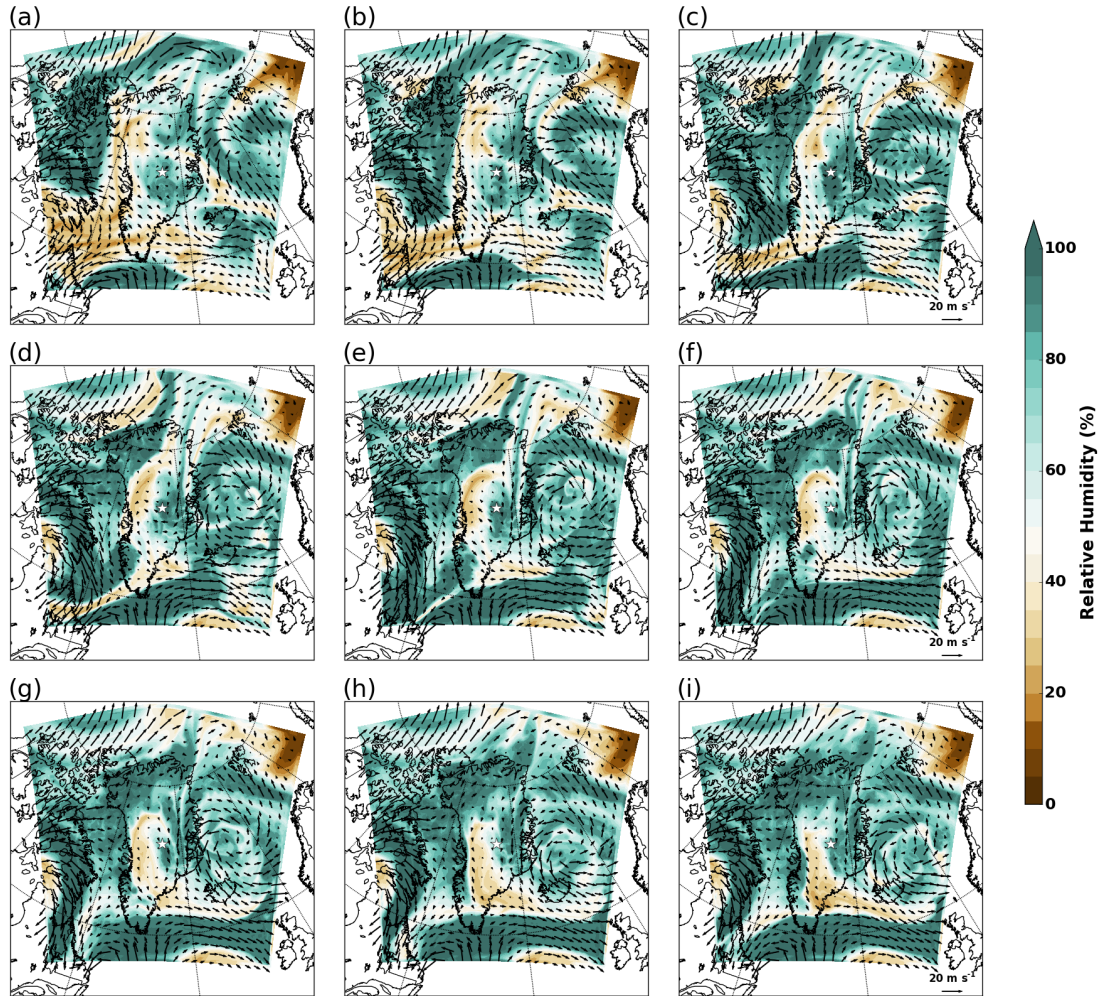


Figure 4.31: Same as Fig. 4.16, but data are from *fixed\_19\_12*.



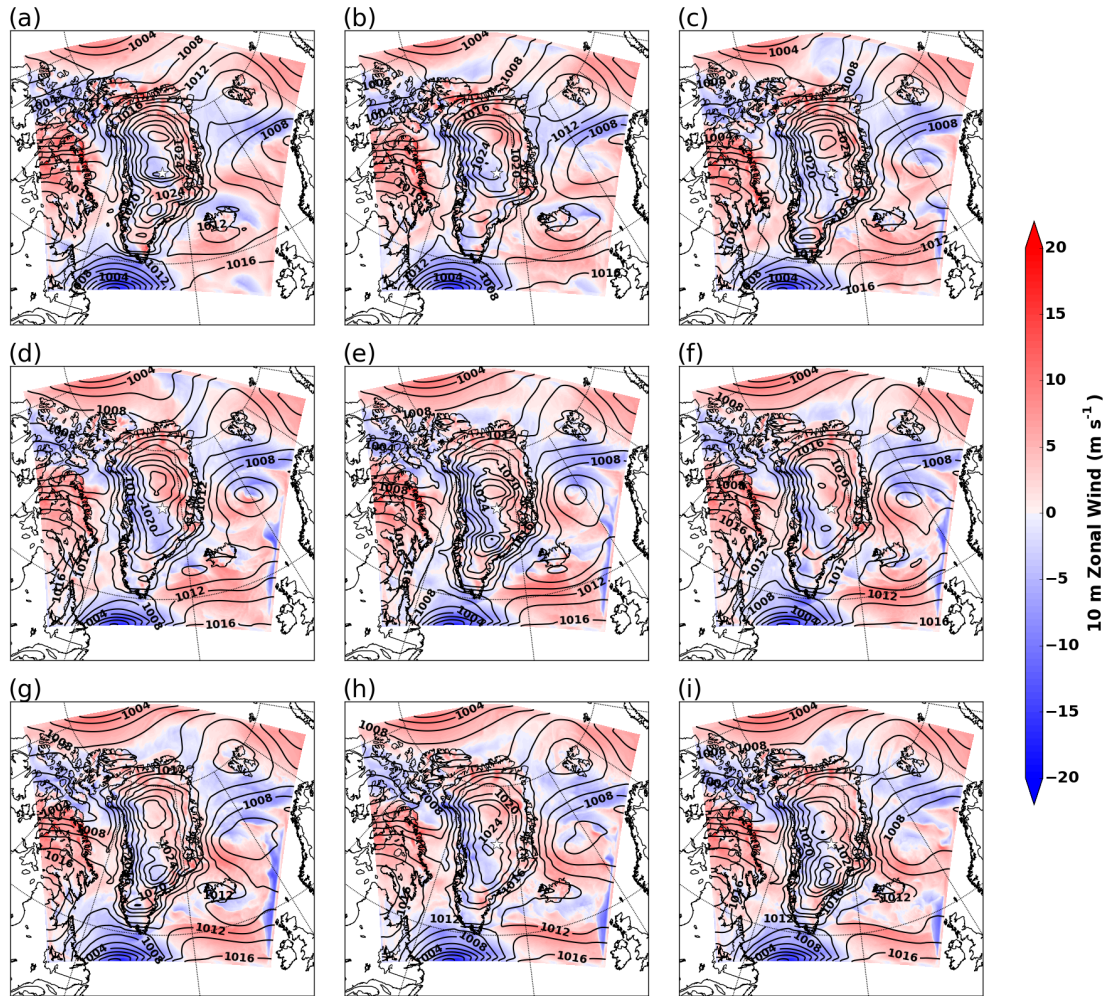


Figure 4.32: Same as Fig. 4.17, but data are from *fixed\_19\_12*.

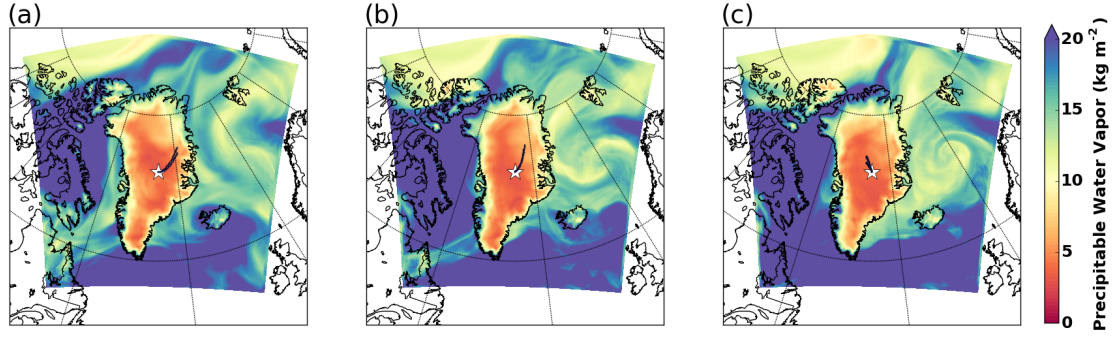


Figure 4.33: Same as Fig. 4.18, but data are from *fixed\_19\_12*.

advected south to Summit (Fig. 4.33b). Both surface cyclones are stationary with the katabatic winds remaining dominate over the ice sheet (Fig. 4.32d,e,f). These processes at 650 hPa and at the surface continue through 24 July at 00 UTC, and by this time, much of the domain is covered in saturated air at 650 hPa (Fig. 4.31g,h,i, 4.32g,h,i, 4.33c).

The differences in the synoptic-scale evolution is consistent with the differences in the low-level environment at Summit between the control (Fig. 4.12) and *fixed\_19\_12* (Fig. 4.27) simulations; the low-level air advected over Summit in the

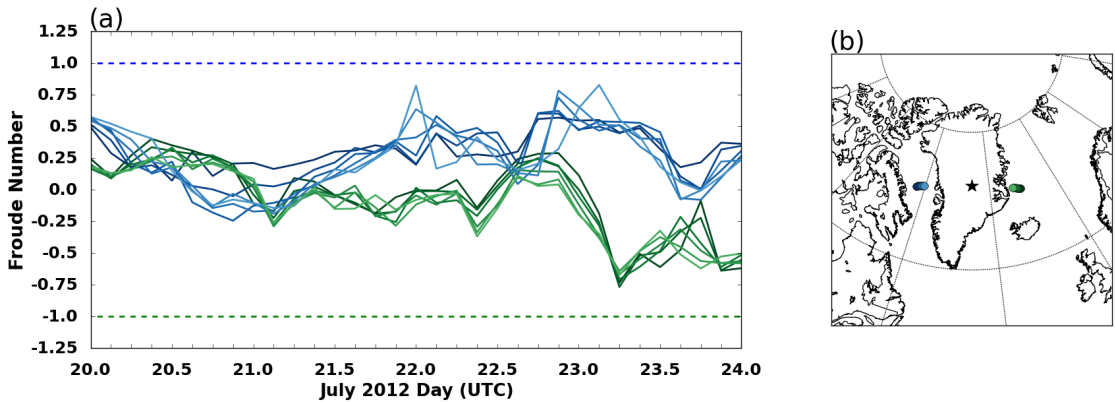


Figure 4.34: Same as Fig. 4.22, but data are from *fixed\_19\_12*.

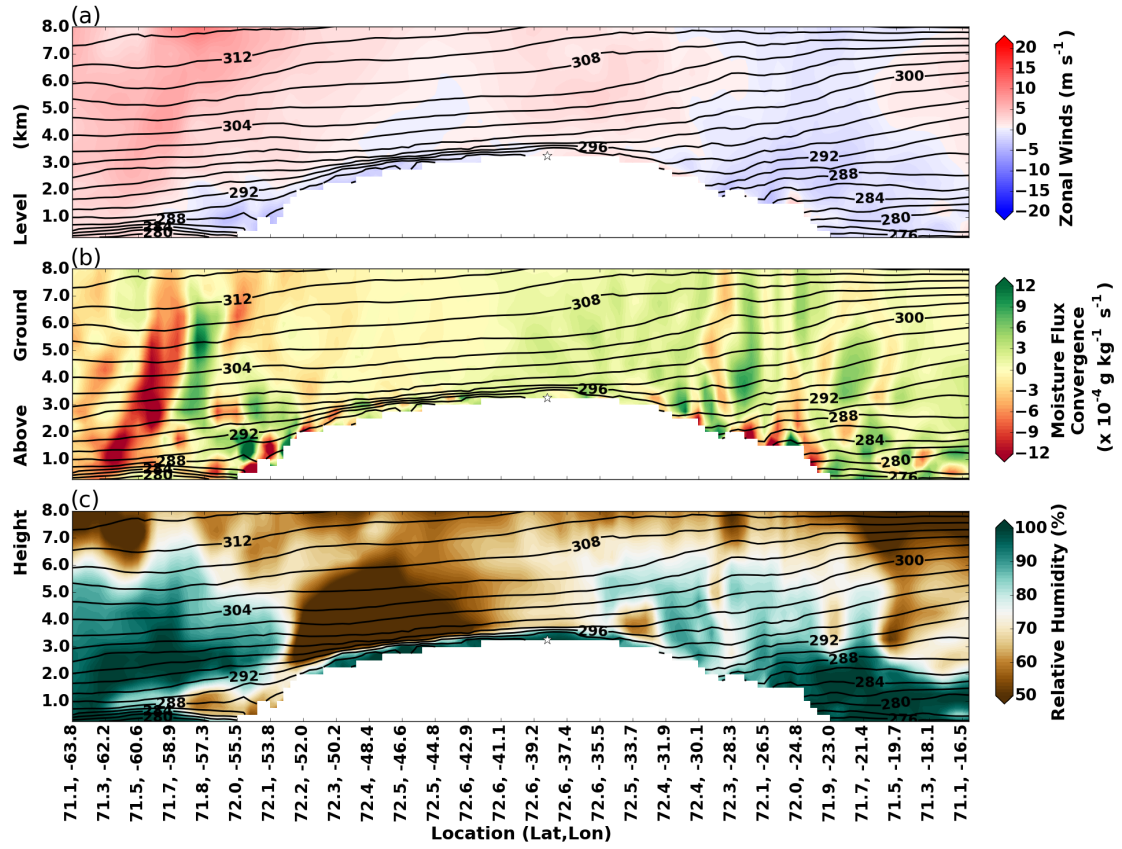


Figure 4.35: Same as Fig. 4.20, but data are from *fixed\_19\_12*.

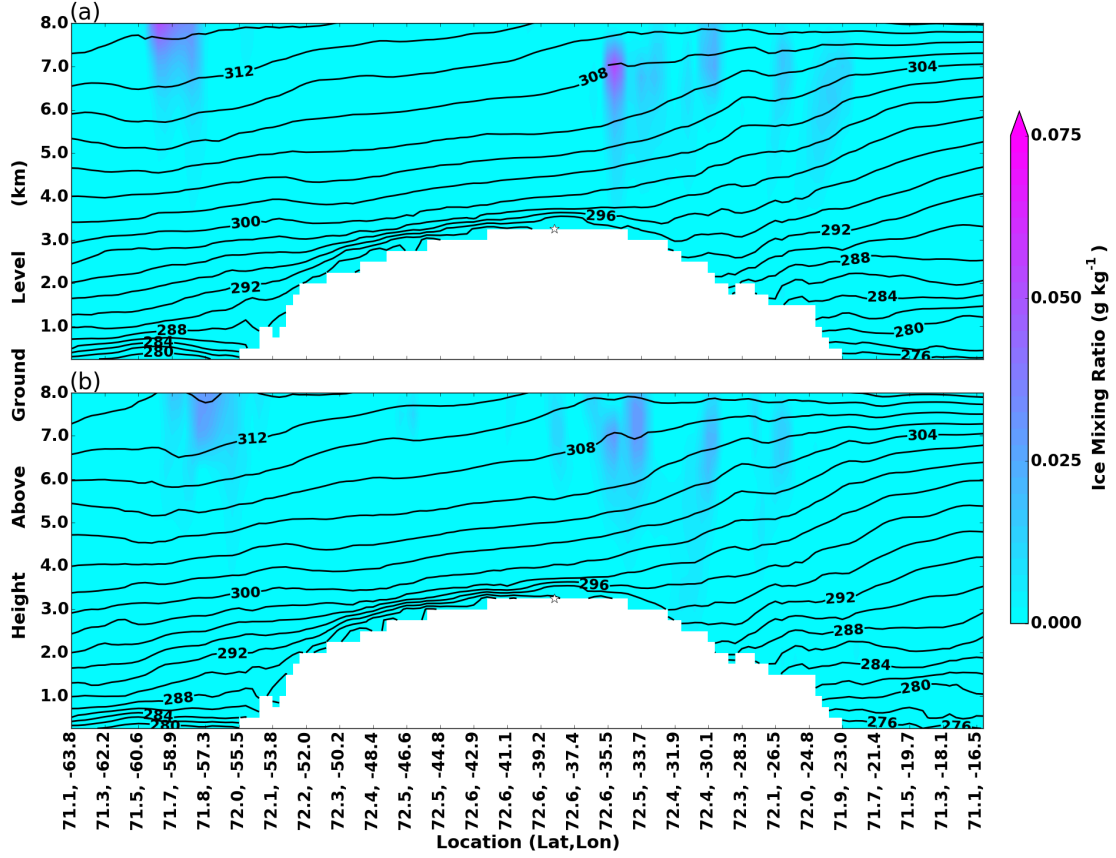


Figure 4.36: Same as Fig. 4.21, but data are from *fixed\_19\_12*.

latter half of the period in *fixed\_19\_12* (Fig. 4.31) is more saturated than in the control (Fig. 4.16). In addition, the surface cyclone that moves past the southeastern coast of Greenland in the control (Fig. 4.17) does not occur in *fixed\_19\_12* due the BCs being held (Fig. 4.32). As a result, there is a weaker pressure gradient, decreasing the probability for flow to ascend to the top of the ice sheet in the second half of the cloud event.  $F_r$  is less (greater) than 1 (-1) on the western (eastern) coast (Fig. 4.34a), thus there is no convergence (Fig. 4.35a,b), and no deep updrafts (Fig. 4.27c) leading to ice production (Fig. 4.29a). Rather, the flow across the GIS is characteristic of the katabatic winds throughout the simulation (Fig. 4.32). Additionally, there is no moisture boundary that passes over

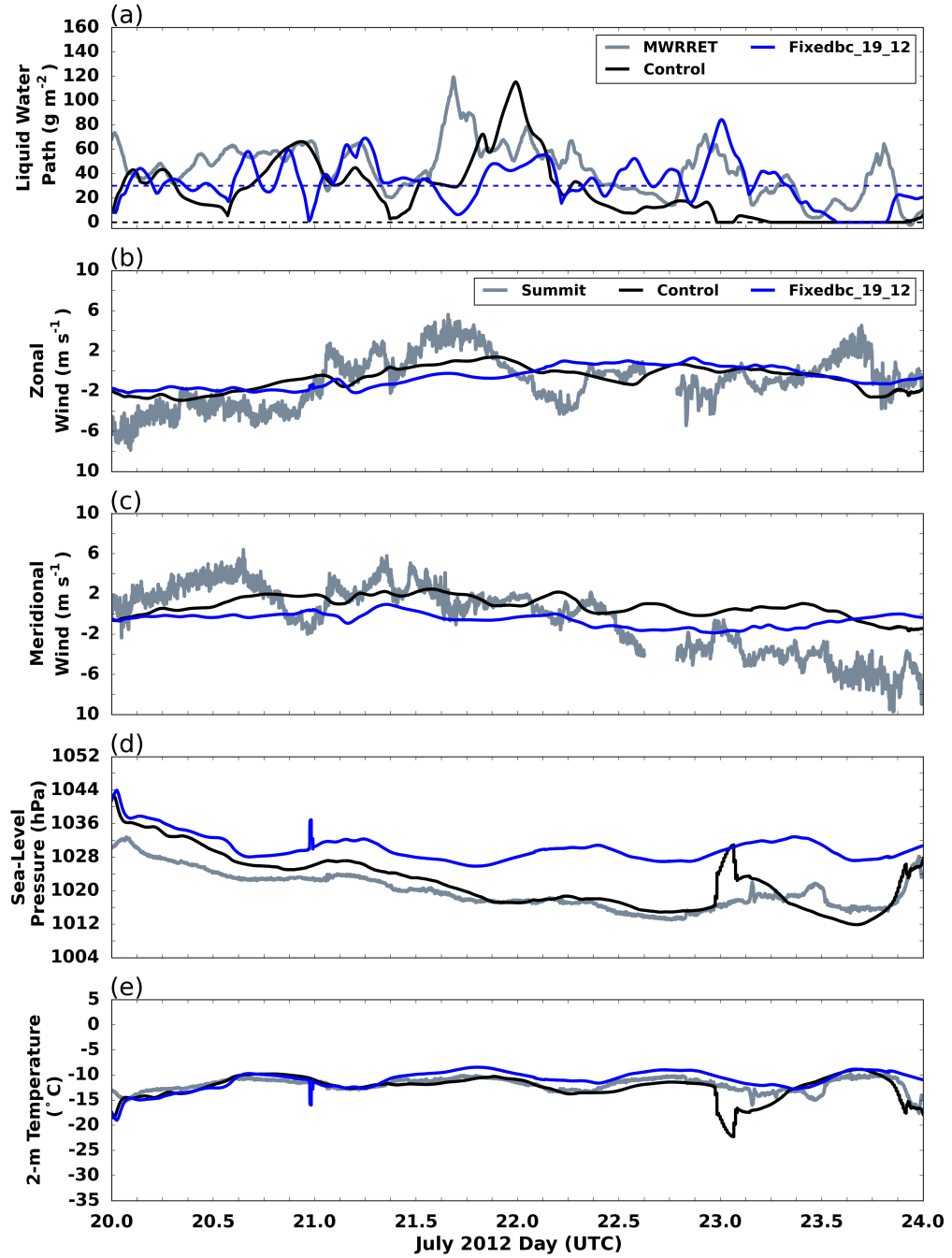


Figure 4.37: Time series of (a) liquid water path ( $\text{g m}^{-2}$ ) retrieved from the Microwave Radiometer (gray) and control (black) and *fixed\_19\_12* (blue) simulations with 30 (blue) and 0 (black)  $\text{g m}^{-2}$  dashed, and 10-m (b) zonal and (c) meridional wind ( $\text{m s}^{-1}$ ), (d) sea-level pressure (hPa), and (e) 2-m temperature ( $^{\circ}\text{C}$ ) from surface tower at Summit (gray), and control (black) and *fixed\_19\_12* (blue) simulations.



the ice sheet (Fig. 4.35c). Thus, there is no advection of an upper-level ice cloud and sedimentation to impact cloud dissipation (Fig. 4.36). With no passing surface cyclone (Fig. 4.37d) or moisture boundary, there is no colder, drier air mass later in the simulation; winds are weak and northeasterly with little change in direction along with a warmer environment in *fixed\_19\_12*, differences from the control (Fig. 4.37b,c,e). Therefore, with a stable, consistent, more moisture rich synoptic-scale pattern, the cloud is longer lived in the *fixed\_19\_12* simulation than the control (Fig. 4.37a). Despite this cloud longevity being closer to that of the observed cloud, it is concluded that this is erroneously the case in this simulation as most other environmental fields are different from the observations.

#### **4.2.2 Local Influence**

Local processes are hypothesized to be important for the persistence of AMPCs (Morrison et al., 2012). Several different types of experimental simulations are done to investigate the effects of local processes on the cloud’s persistence, specifically looking at the influence of microphysics and radiation, as well as looking at the sensitivity to the PBL scheme.

##### **4.2.2.1 Microphysics: M-PACE Observations**

Within the Morrison Double Moment microphysics scheme, there is an option to switch the way the nucleation of cloud ice is simulated within the scheme. By default, the scheme uses the Cooper curve equation (Cooper, 1986) for cloud ice nucleation by deposition and condensation freezing, which is better suited for midlatitude environments. The equation can be changed to use an equation based on M-PACE observations, which are more suited for an Arctic environment; the number concentration of IN in the nucleation equation is changed to a value based on aircraft measurements from M-PACE (Morrison et al., 2008). For the control

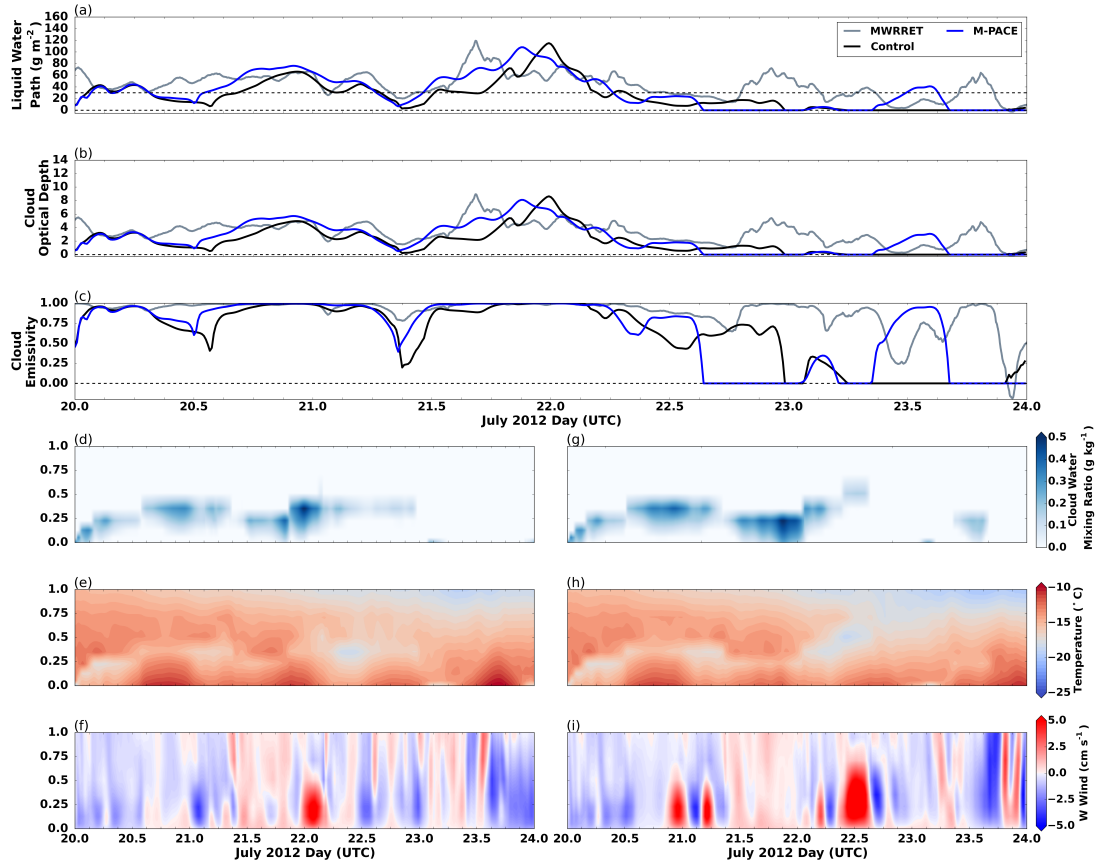


Figure 4.38: Time series of (a) liquid water path ( $\text{g m}^{-2}$ ), (b) cloud optical depth, and (c) cloud emissivity for MWRRET (gray), and the control (black) and *M-PACE* (blue) simulations. Time-height cross sections for (d,g) cloud water mixing ratio ( $\text{g kg}^{-1}$ ), (e,h) temperature ( $^{\circ}\text{C}$ ), and (f,i) w wind ( $\text{cm s}^{-1}$ ) for the (d,e,f) control and (g,h,i) *M-PACE*.

simulation the default is used, but for this experimental simulation the switch is made to use M-PACE based equation in the microphysics scheme *M-PACE*.

Overall, the cloud simulated by *M-PACE* (Fig. 4.38g) is very similar to the control (Fig. 4.38d). The cloud in *M-PACE* dissipates on 22 July at 15 UTC, 9 hours earlier than the control, but towards the end of its lifetime the CBH ascends above 0.5 km due to a strong updraft on 22 July at 09 UTC (Fig. 4.38i). CTLC in *M-PACE* (Fig. 4.38h) is stronger than the control (Fig. 4.38e). This is due to the overall greater LWP (Fig. 4.38a), and in turn greater cloud optical depth (Fig. 4.38b) and emissivity (Fig. 4.38c) in *M-PACE*. The cloud optical depth is calculated by

$$\tau_c = \frac{1}{2} \frac{3\text{LWP}}{2\rho_l r} \quad (4.4)$$

where  $\rho_l$  is the density of liquid water ( $1000 \text{ kg m}^{-3}$ ) and  $r$  is the radius of the cloud droplets, here  $10 \text{ }\mu\text{m}$  is used, and cloud emissivity, which is given by equation 1.5 (e.g. Petty (2004)).

When the cloud forms on 20 July at 00 UTC in *M-PACE*, there is a surface-based inversion present (Fig. 4.39a); again, the CTLC drives mixing beneath cloud-top (Fig. 4.38h,i), resulting in a well-mixed layer with an inversion at cloud-top and elevated cloud by 20 July at 12 UTC (Fig. 4.39b). The well-mixed layer is maintained through the lifetime of the cloud (Fig. 4.39c-f). Without the presence of the AMPC on 23 July at 12 UTC, the well-mixed layer disappears, and instead there is a surface-based inversion (Fig. 4.39g). When there is the brief liquid layer on 23 July at 12 UTC, this again drives a well-mixed layer (Fig. 4.39h) and by 24 July at 00 UTC there is no elevated inversion at all (Fig. 4.39i).

The cloud dissipation at 22 July at 15 UTC coincides with a strong downdraft (Fig. 4.38g,i). This is similar to the control, though it occurs a few hours later on 23 July at 00 UTC (Fig. 4.38d,f). There is only a weak presence of a precipitating



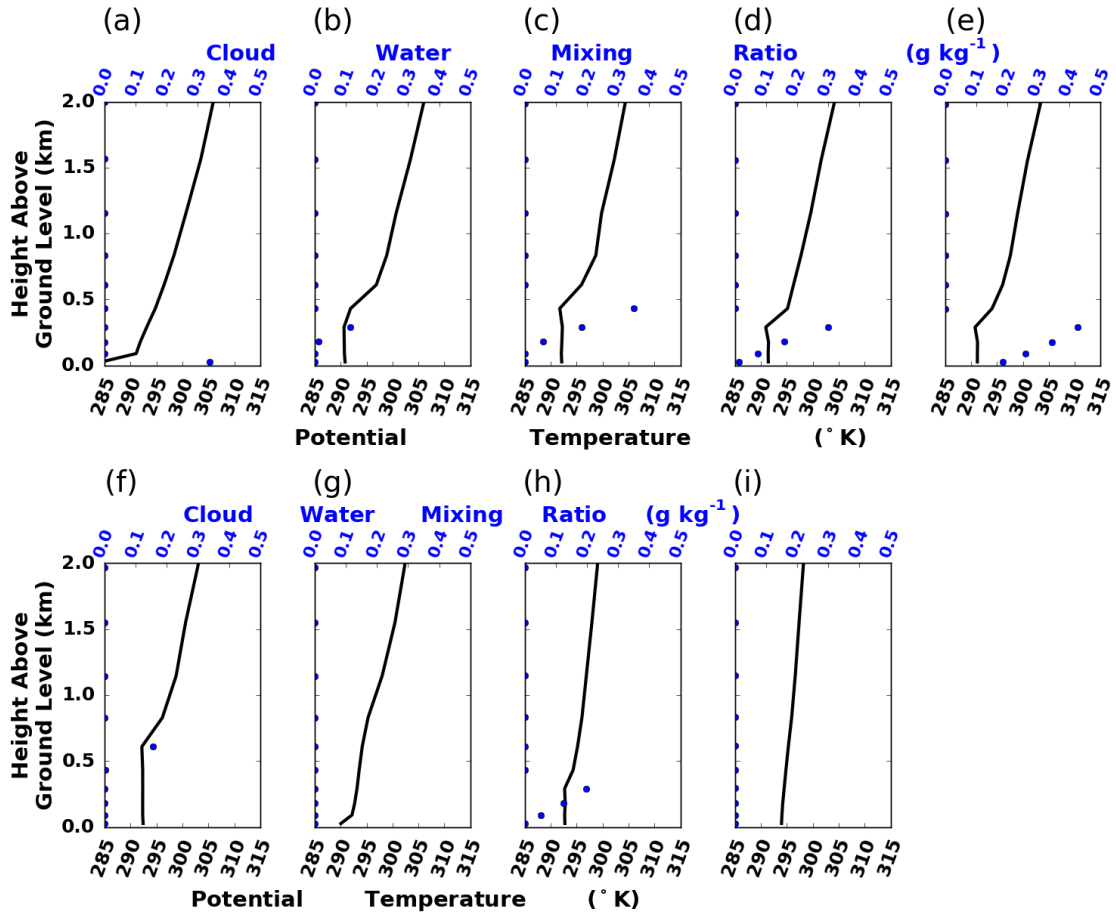


Figure 4.39: Same as Fig. 4.13, but data are from *M-PACE*.

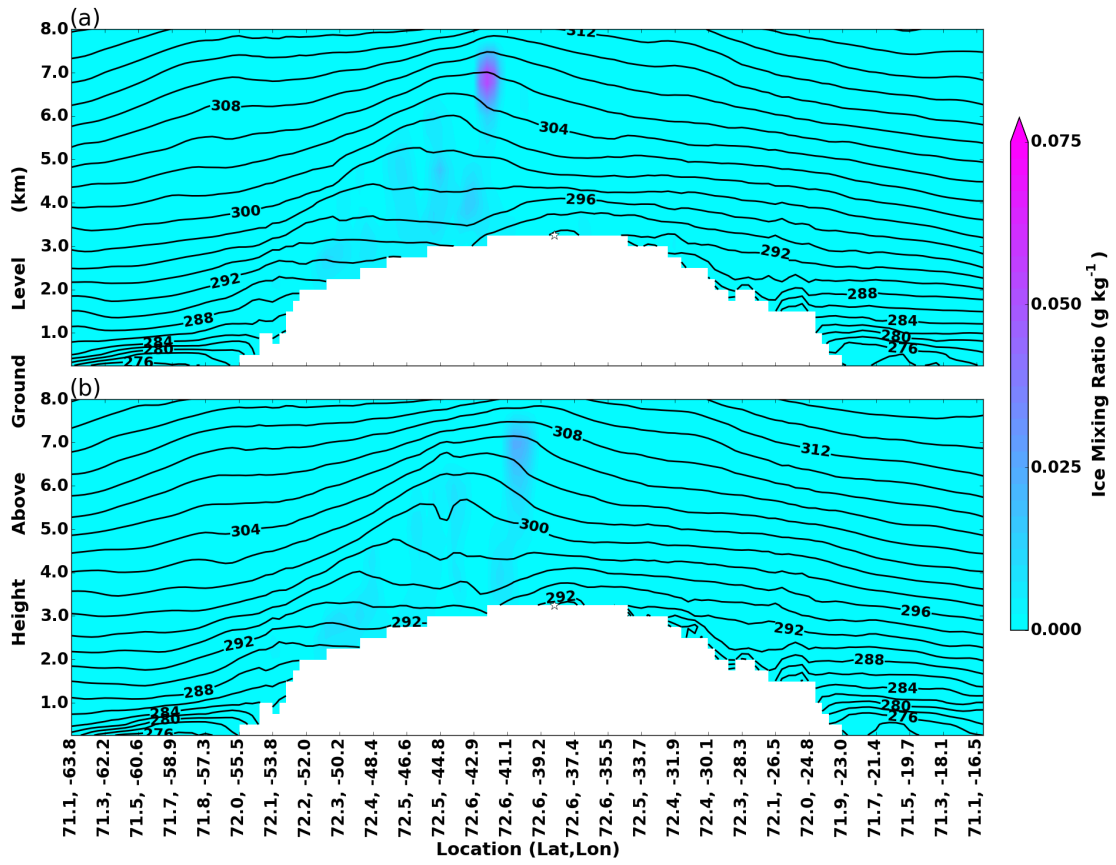


Figure 4.40: Same as Fig. 4.21, but data are from *M-PACE*.

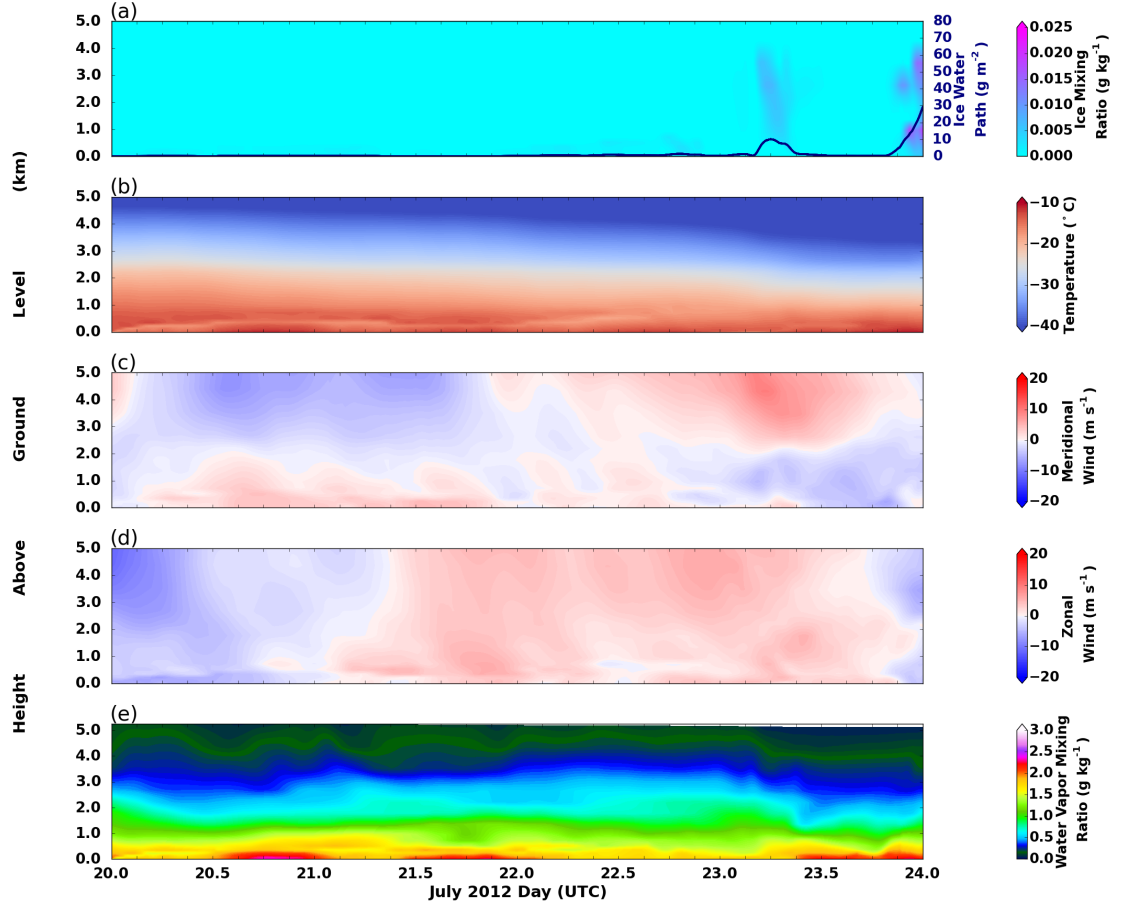


Figure 4.41: Same as Fig. 4.15, but data are from *M-PACE*.

upper-level ice cloud ahead of the boundary (Fig. 4.40), and ice mixing ratio values are lower in the lowest 5 km AGL in *M-PACE* (Fig. 4.41a) than the control (Fig. 4.15a). The shift from southerly to northerly flow in the control is simulated in *M-PACE*, but occurs slightly earlier around 22 July at 15 UTC (Fig. 4.41c), the time of cloud dissipation. There is colder (Fig. 4.41b) and drier (Fig. 4.41e) air sinking down from aloft, as in the control, thus the change in air mass in the control is also seen in *M-PACE*. There is a cooling of the 2-m and skin temperatures (Fig. 4.42a) coinciding with the decrease in the surface downwelling LW flux

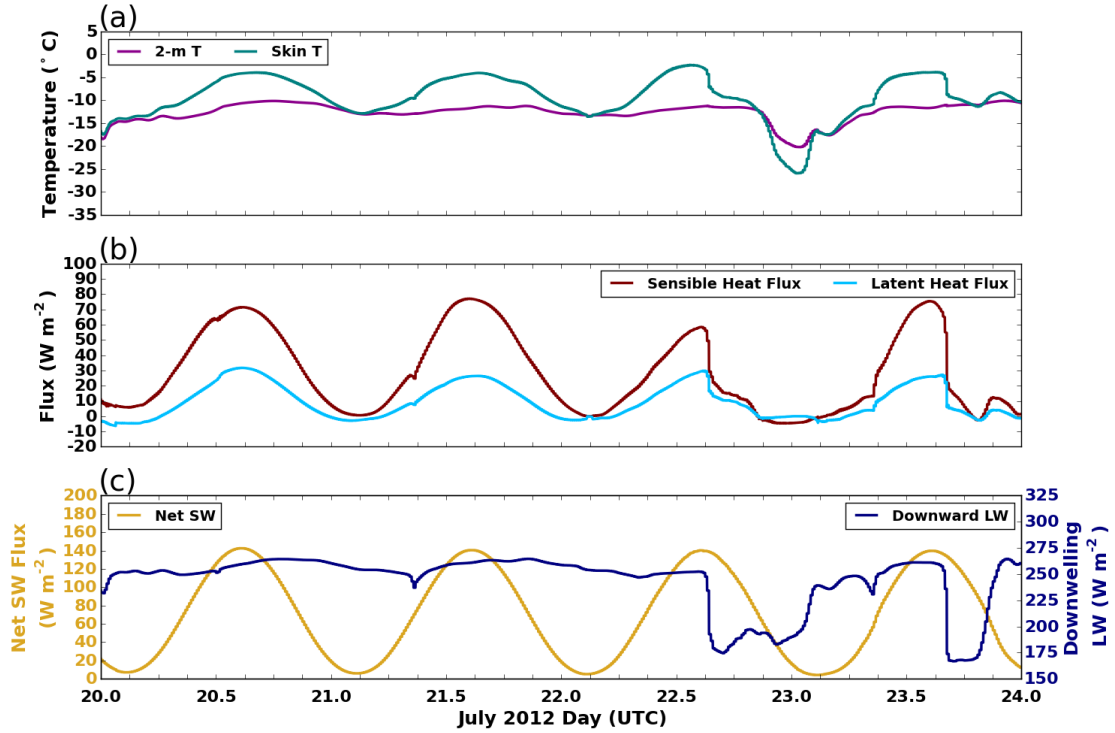


Figure 4.42: Same as Fig. 4.14, but data are from *M-PACE*.

(Fig. 4.42c) due to the dissipation of the cloud. This temperature drop, though, is not as dramatic as the one simulated by the control (Fig. 4.43e).

The LWP simulated in *M-PACE* is greater than the control (Fig. 4.38a, 4.43a); the average LWP from 20 July at 00 UTC to 22 July at 12 UTC is 48 and 38 g m<sup>-2</sup> for *M-PACE* and the control, respectively. The sensible heat fluxes are stronger in *M-PACE* (Fig. 4.42b) than in the control (Fig. 4.14b), which could possibly explain the higher LWPs (Fig. 4.38a, 4.43a). However, the higher *M-PACE* LWPs could additionally be related to the different treatment of ice nucleation in the microphysics. Again, the presence of ice is less in *M-PACE* (Fig. 4.40, 4.41a) than the control (Fig. 4.15a, 4.21); thus, with fewer ice crystals the WBF process is less effective and less liquid water is lost to evaporation allowing the ice crystals to grow by vapor deposition. Other variables such as the zonal (Fig. 4.43b) and meridional

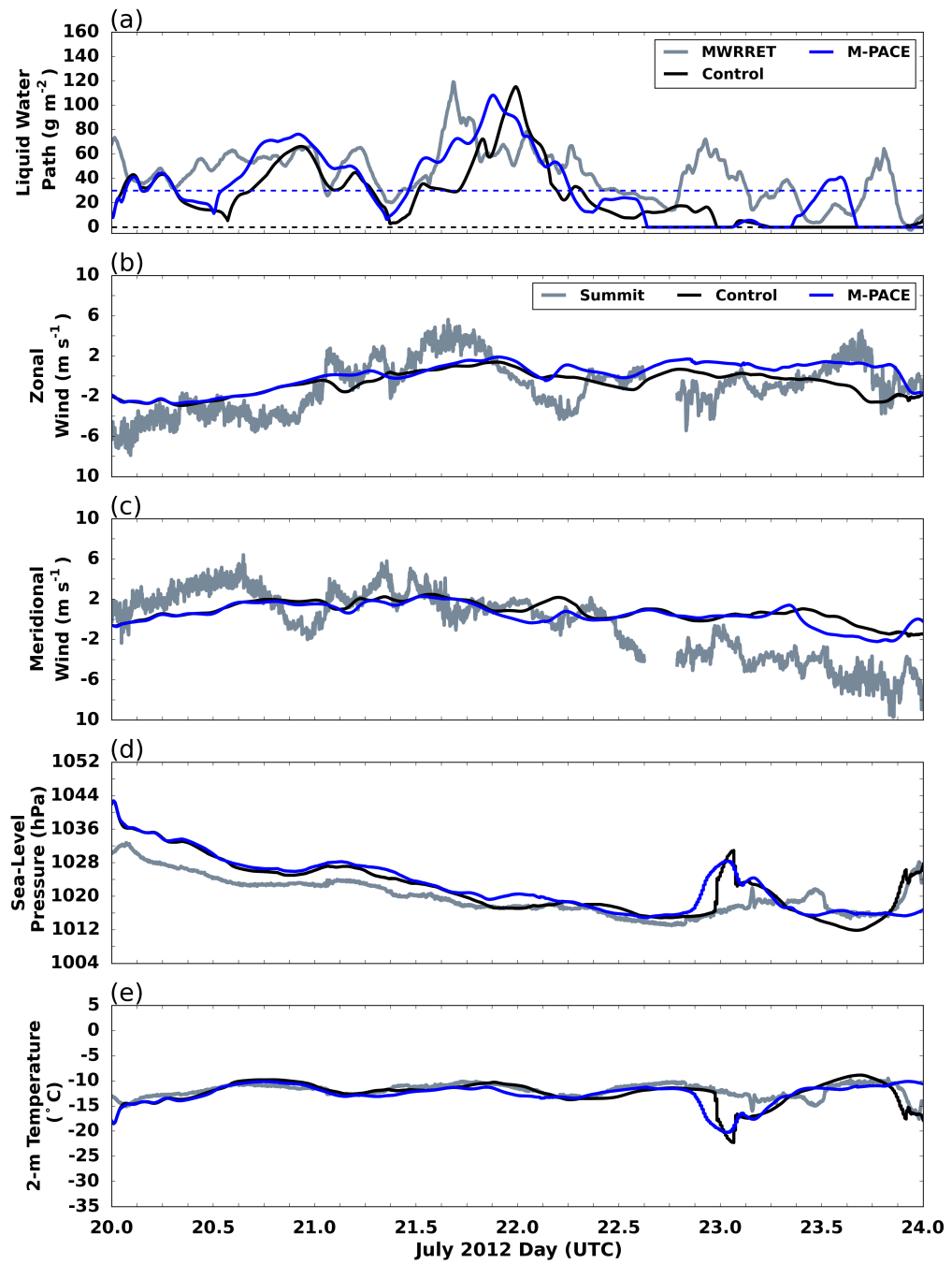


Figure 4.43: Same as Fig. 4.37, but for *M-PACE*.

wind (Fig. 4.43c), and sea-level pressure (Fig. 4.43d) from *M-PACE* follow the control simulation showing that the local microphysics do impact the AMPC. Using the switch for the ice nucleation equation based on M-PACE observations, better representative of Arctic microphysics, than the default mid-latitude equations has an effect on the cloud, particularly in terms of cloud water and ice content which can further affect CTLC.

#### 4.2.2.2 Planetary Boundary Layer Physics Option: Local vs. Non-local

In the control simulation, the PBL physics option used is YSU. This is a non-local scheme, meaning that a given vertical level within the PBL can be influenced by multiple vertical levels above and below it, so long as these levels are within the PBL. Converse to non-local schemes are local schemes. In local schemes, a vertical level is only affected by the levels directly above and below it. Thus, non-local schemes simulate deeper mixing by larger eddies within the PBL than local schemes do. The PBL physics option in the control is changed from non-local, YSU, to local, Grenier-Bretherton-McCaa (GBM) (Grenier and Bretherton, 2001), to test the sensitivity of the simulation to the PBL physics option. GBM is chosen as it has been used in previous modeling studies of AMPCs (Solomon et al., 2016) and is tuned for stratocumulus-topped PBLs. This experimental simulation is referred to as *GBM*.

*GBM* simulates no persistent cloud layer (Fig. 4.44a); instead, a liquid layer forms near the surface and becomes elevated further through the night. This cloud dissipates as the surface warms due to daytime heating (Fig. 4.44b), and this process repeats through the simulation period. The CTLC (Fig. 4.44b) still drives a well-mixed layer (Fig. 4.45a,b,d,f), but without the cloud the well-mixed layer is much shallower, or is diminished and there is a surface-based inversion

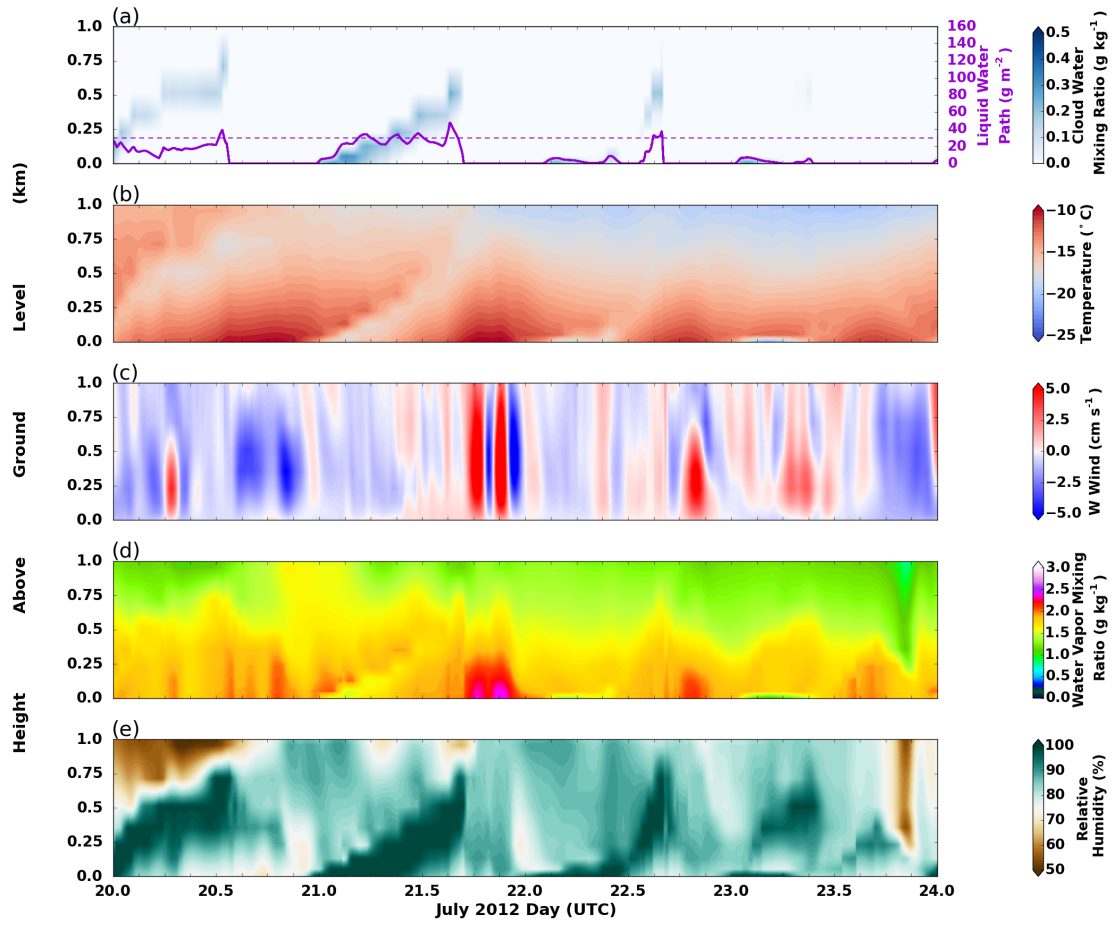


Figure 4.44: Same as Fig. 4.12, but data are from *GBM*.

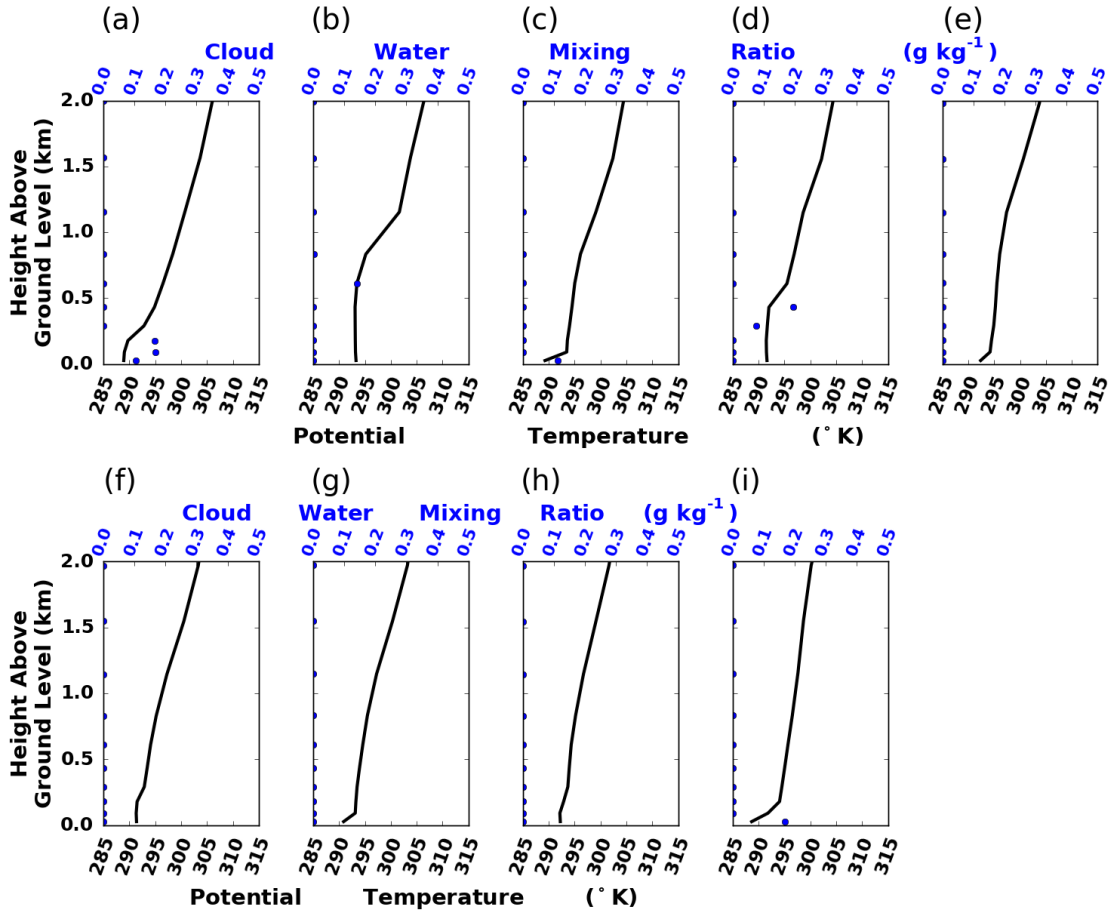


Figure 4.45: Same as Fig. 4.13, but data are from *GBM*.



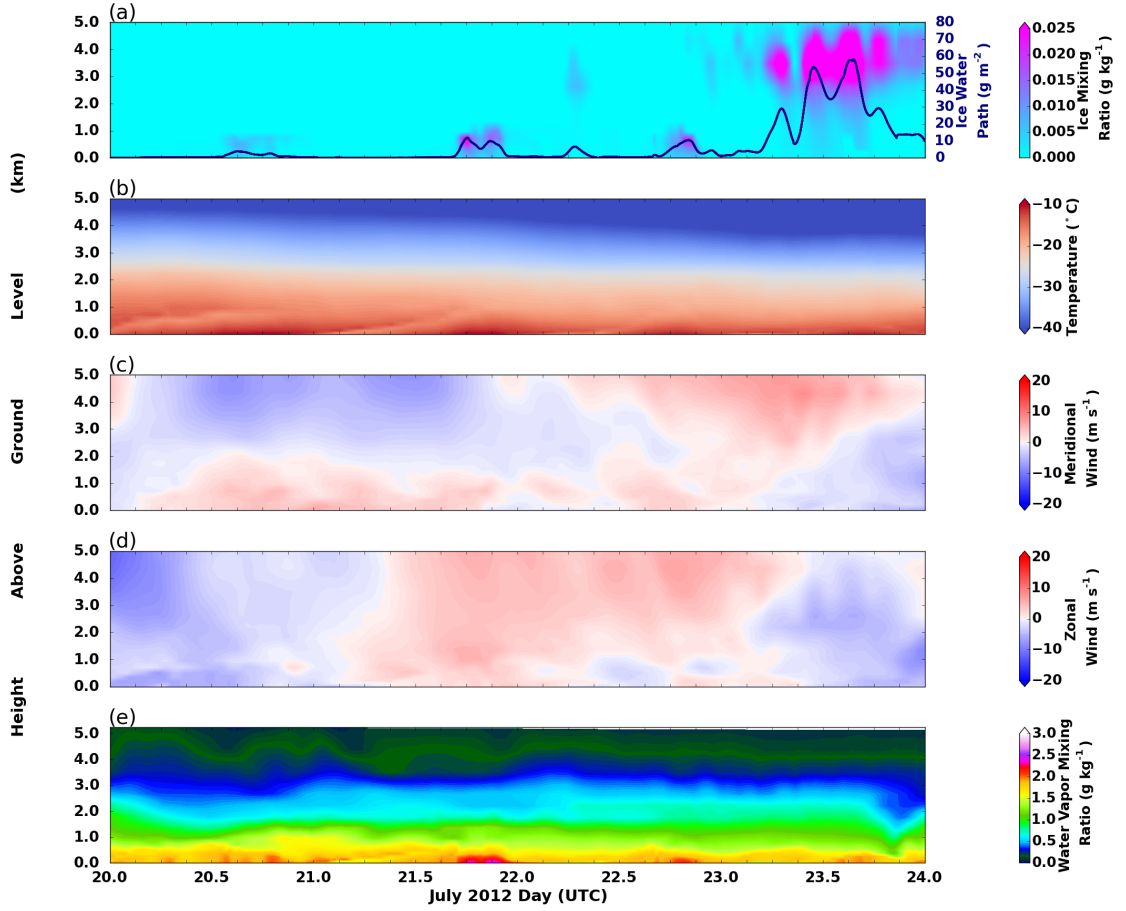


Figure 4.46: Same as Fig. 4.15, but data are from *GBM*.

(Fig. 4.45c,e,g,h,i). The *GBM* vertical motion field is dominated by skinny updrafts (Fig. 4.44c), where in the control the updrafts are a bit wider (Fig. 4.12c). Neglecting the cloud evolution, the *GBM* simulation (Fig. 4.46, 4.47b,c) evolves similar to the control.

Similar to the previously discussed simulations, the *GBM* 2-m and skin temperatures dramatically cool when there is no cloud layer (Fig. 4.48a) as there is no influence of the cloud on the surface downwelling LW flux (Fig. 4.48c). In *GBM*, as there is no persistent cloud layer, the temperatures drop on multiple occasions, which does not occur in the control due the continued presence of the

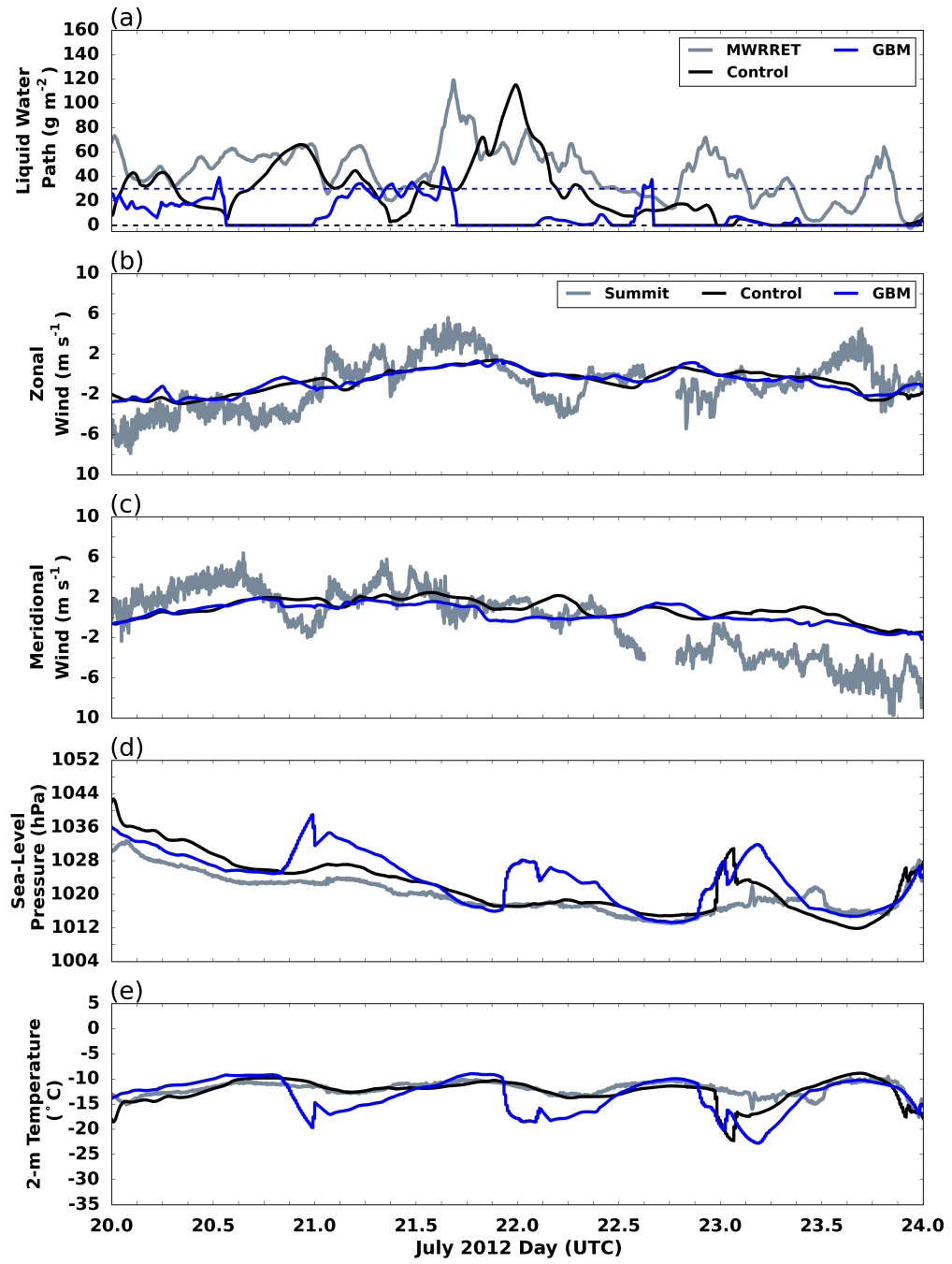


Figure 4.47: Same as Fig. 4.37, but for *GBM*.

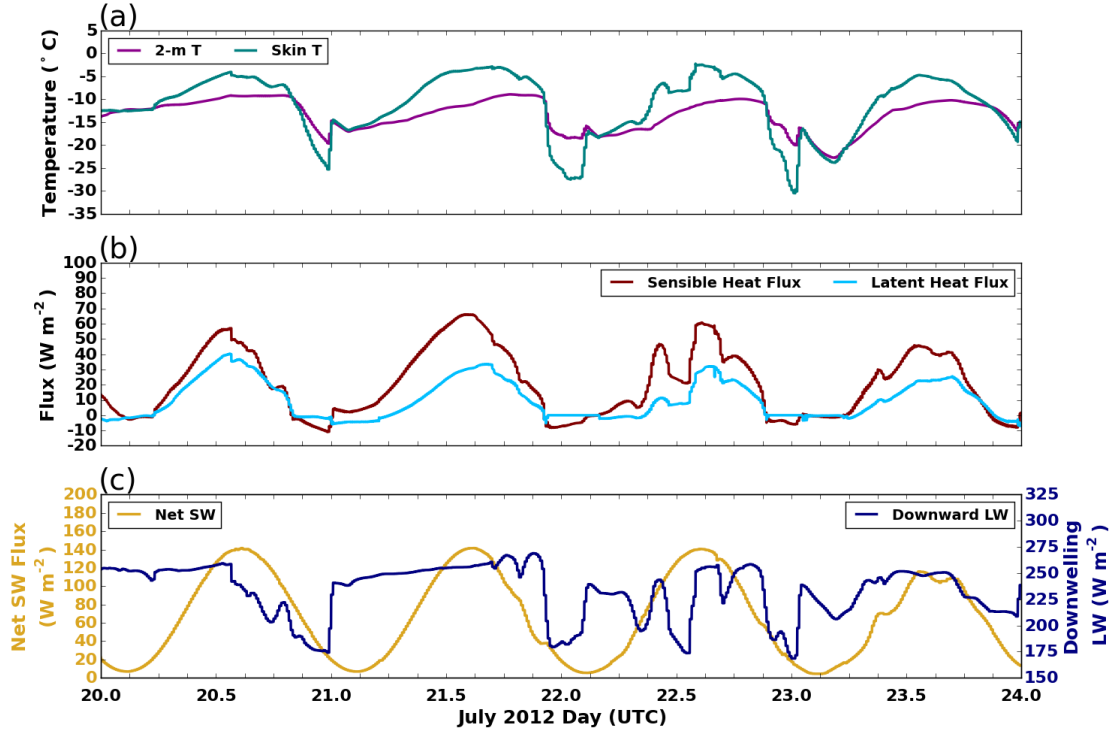


Figure 4.48: Same as Fig. 4.14, but data are from the *GBM*.

cloud (Fig. 4.47a,e). In association with this cooling, the sea-level pressure rises (Fig. 4.47d).

A very different cloud layer is simulated by changing the PBL scheme from a non-local to local scheme. The non-local scheme, i.e. the control, simulated a persistent cloud layer, while the local scheme, i.e. *GBM*, simulated a more broken cloud with a surface-based cloud slowly elevating through the night and dissipating near peak daytime heating. The differences most likely stem from the core difference between the non-local and local schemes; a non-local scheme uses points throughout the PBL to determine the value at a gridpoint, whereas a local scheme uses those adjacent. Non-local schemes, therefore, simulate deeper mixing by larger eddies within the PBL. This deeper mixing through the PBL is important for maintaining the cloud. Additionally, the change in air mass is still simulated at 23 July

at 00 UTC (Fig. 4.44, 4.46). This further supports the change in air mass due to synoptic-scale processes leads to the cloud being diminished.

#### 4.2.2.3 Radiation

As CTLC is an important hypothesized mechanism for AMPC maintenance, the CRFs are altered in the LW and SW radiation calls to test the sensitivity of cloud maintenance to radiation. This is accomplished by accounting for (on) or not accounting for (off) the cloud's optical depth. Cloud optical depth is effectively set to 0 by setting cloud water and ice mixing ratios to 0 only within the radiation parameterizations, similar to Solomon et al. (2016). In the LW, this shuts down the CTLC and ultimately the buoyancy-driven updrafts that impact cloud maintenance. Additionally, there is no absorption by the cloud in the SW.

3 sensitivity tests are performed in which the radiation code is altered for all gridpoints. For the first sensitivity test, there is no CRF in either the LW or SW (*no\_CRF*). The second test accounts for the SW CRF only, while the LW CRF

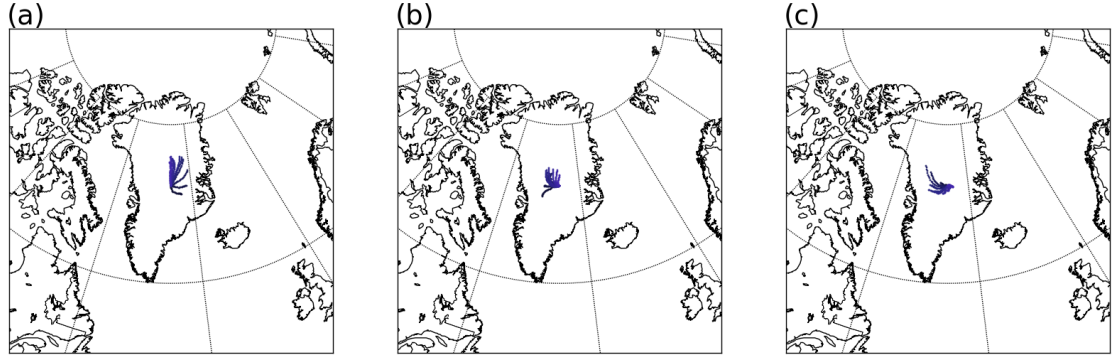


Figure 4.49: 1 day backward trajectories for parcels at Summit arriving on (a) 21, (b) 22, and (c) 23 July 2012 at 00 UTC at heights from 4 to 14 km every 1 km. Parcels at lower heights are darker getting lighter with height. Data are from the control simulation and the location of Summit, Greenland is denoted by  $\star$ .

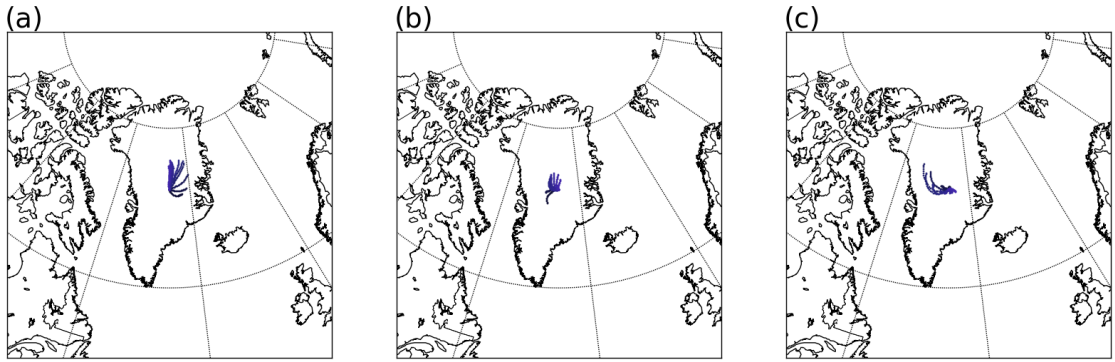


Figure 4.50: Same as Fig. 4.49, but for *no-CRF*.

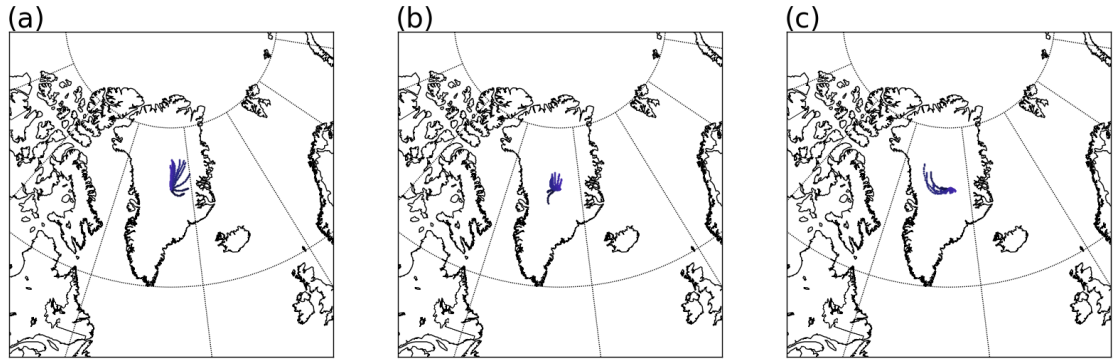


Figure 4.51: Same as Fig. 4.49, but for *no-LW-CRF*.

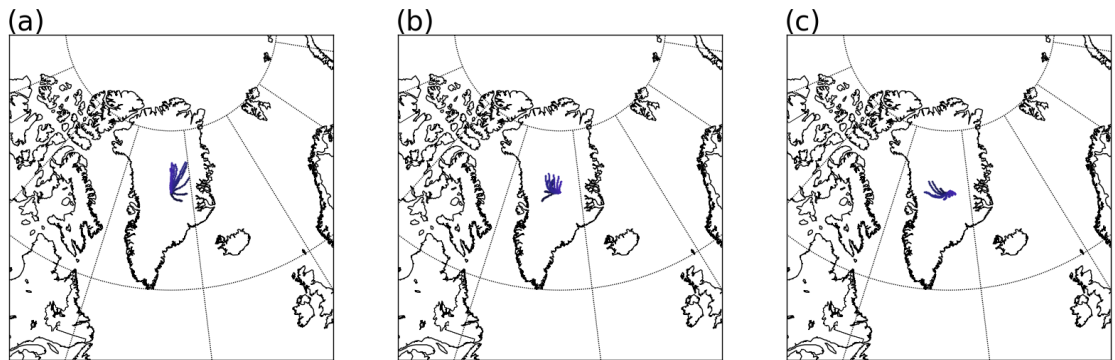


Figure 4.52: Same as Fig. 4.49, but for *no-SW-CRF*.

is turned off (*no\_LW\_CRF*). It is expected that without LW CRF, the cloud will lose a key maintenance mechanism, i.e. CTLC, and, therefore, will not persist. The third sensitivity test accounts for CRF in the LW only, while the SW CRF is turned off (*no\_SW\_CRF*). If the cloud is largely transparent to SW radiation, this experiment should produce a similar result to the control. No changes are made to the radiative effects of the surface or other atmospheric constituents.

First, the 1-day backward parcel trajectories are analyzed to ensure there are no changes from the control's trajectories, which would indicate changes and influences on the synoptic-scale, as the purpose of these experiments is to isolate the local effects of CRF on the cloud only. *no\_CRF* 1-day backwards trajectories for 21 July at 00 UTC (Fig. 4.50a) and 22 July at 00 UTC (Fig. 4.50b) are similar to the control (Fig. 4.49a,b). For 23 July at 00 UTC, the trajectories differ slightly. The 23 July at 00 UTC trajectories for *no\_CRF* in the mid-levels originate further north and west (Fig. 4.50c) than the control (Fig. 4.49c). The same is true for *no\_LW\_CRF* (Fig. 4.51). There are few differences between the control and *no\_SW\_CRF* trajectories, though 23 July at 00 UTC for the *no\_SW\_CRF* trajectories have a more westerly component (Fig. 4.52) than the control (Fig. 4.49).

Since turning on or off the CRF across the domain in the radiation calls influences parcel trajectories, particularly later in simulation period, this indicates influences from the synoptic-scale as a result of altering the CRF across the entire domain. The 3 experimental simulations are repeated, but the CRF changes in the radiation code is limited to a small region within the domain (*no\_CRF\_lim*, *no\_LW\_CRF\_lim*, *no\_SW\_CRF\_lim*). A similar sized region and location to Solomon et al. (2016) is used. On the 300 by 300 gridpoint domain, the CRF changes are done between gridpoints 136 to 166 in the x-direction and 116 to 166 in the y-direction; this region is 372 x 612 km (Fig. 4.53). The trajectories for *no\_CRF\_lim* (Fig. 4.54), *no\_LW\_CRF\_lim* (Fig. 4.55), and *no\_SW\_CRF\_lim*

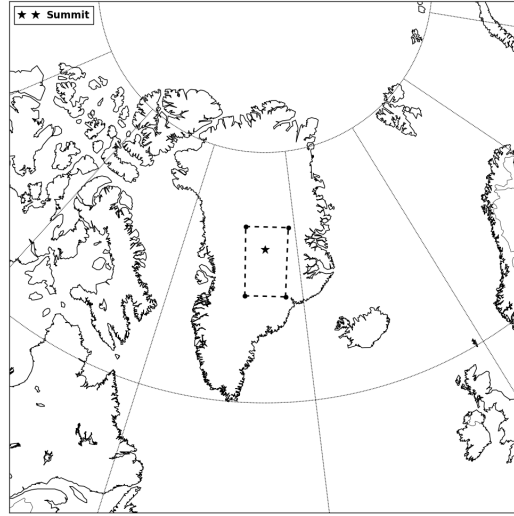


Figure 4.53: The area where the cloud radiative forcings are changed is marked by the boxed region; the region extends from gridpoints 136 to 166 in the x-direction and 116 to 166 in the y-direction. The location of Summit, Greenland is denoted by  $\star$ .

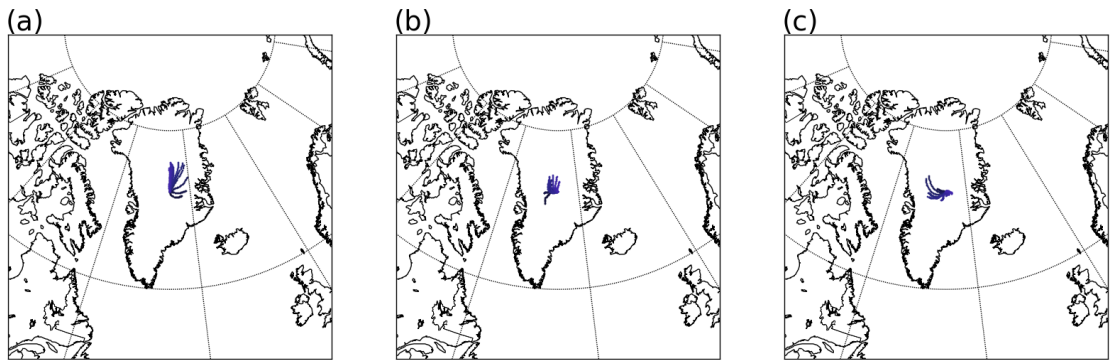


Figure 4.54: Same as Fig. 4.49, but for *no\_CRF\_lim*.

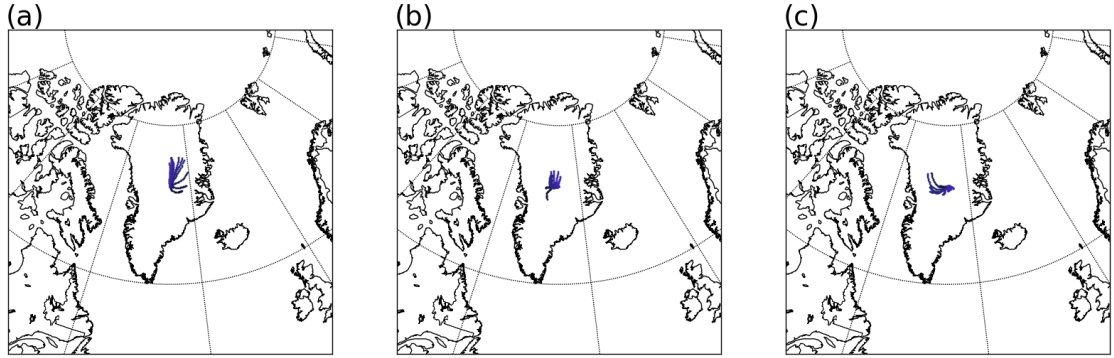


Figure 4.55: Same as Fig. 4.49, but for  $no\_LW\_CRF\_lim$ .

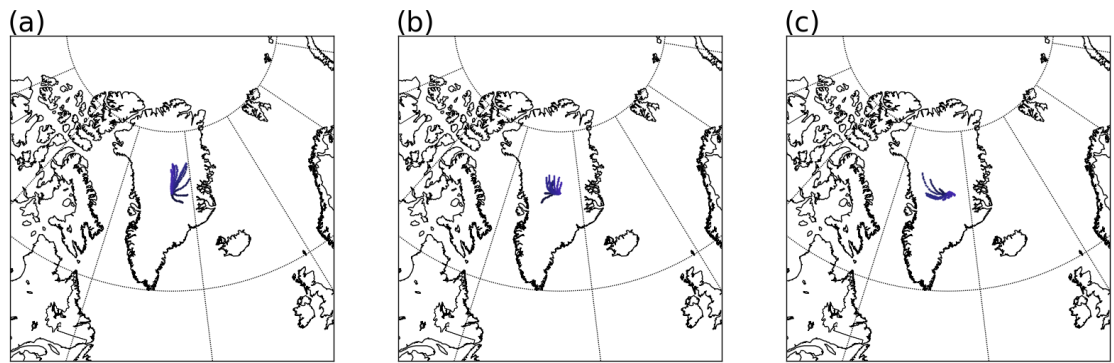


Figure 4.56: Same as Fig. 4.49, but for  $no\_SW\_CRF\_lim$ .



(Fig. 4.56) are comparable to the control trajectories (Fig. 4.49), thus limiting the changes to this region isolates the local CRFs.

In the *no-CRF\_lim*, no elevated cloud layer forms (Fig. 4.57a). Only during the nighttime hours are there higher values of cloud water mixing ratio near the surface and LWP. This is due to the surface radiative cooling (Fig. 4.57b) leading to condensation of the moist near surface air (Fig. 4.57d,e) beneath the surface-based inversion (Fig. 4.58a,c,e,g,i). Without effects of LW emission from the cloud and the resulting CTLC (Fig. 4.57b), no buoyancy-driven updrafts form (Fig. 4.57c).

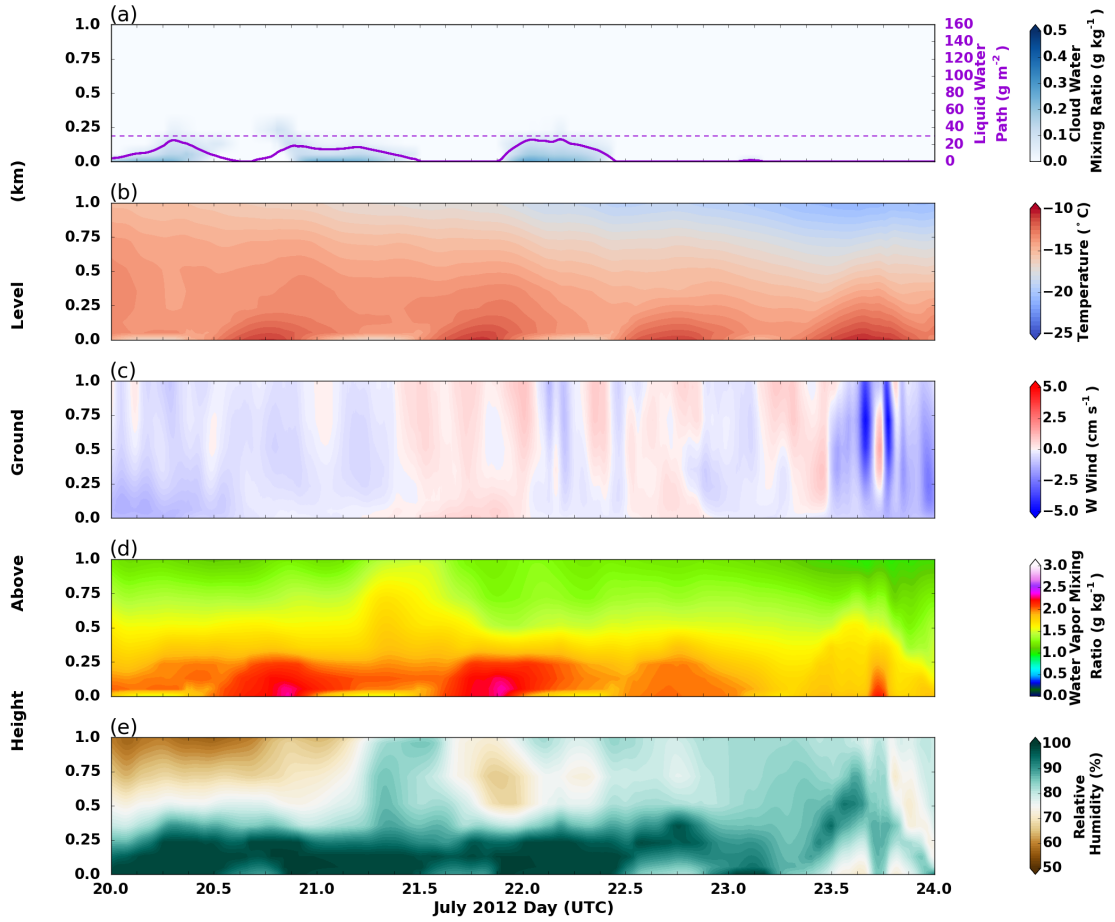


Figure 4.57: Same as Fig. 4.12, but data are from *no-CRF\_lim*.

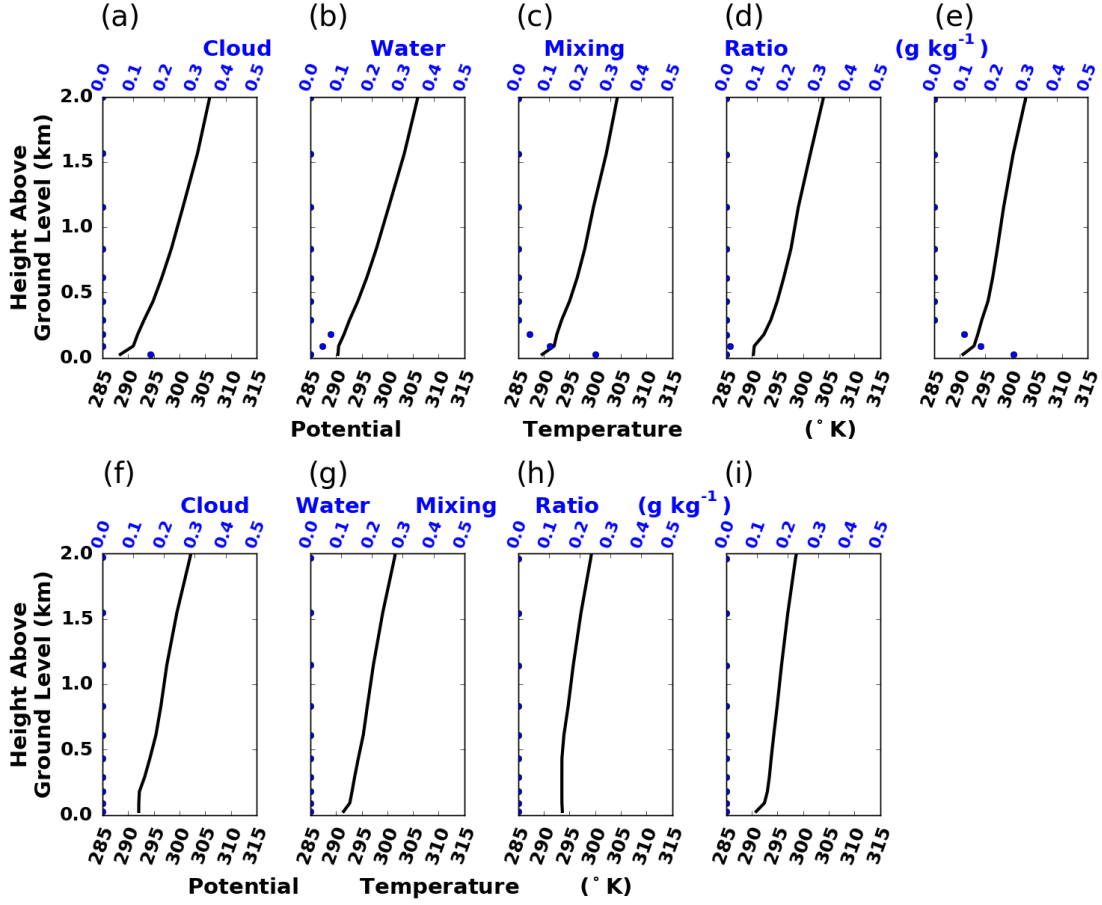


Figure 4.58: Same as Fig. 4.13, but data are from *no\_CRF\_lim*.

As a result, there is no lifting of the cloud from the surface. Without the elevated cloud layer, there is no deeper well-mixed layer that forms (Fig. 4.58b,d,f).

The *no\_CRF\_lim* temperatures show a distinct diurnal cycle (Fig. 4.57b, 4.59a) much more than the control simulation does (Fig. 4.60e). Without the downwelling LW fluxes from the cloud (Fig. 4.59c), the 2-m and skin temperatures are driven by the diurnal cycle from incoming SW radiation and surface radiative cooling. The diurnal cycle in temperature drives a diurnal cycle in sea-level pressure with higher pressure from colder temperatures at night (Fig. 4.60d). The sensible heat

flux (Fig. 4.59b) is also weaker than the control (Fig. 4.14b) due the smaller differences between the 2-m and skin temperatures again due to the lack of downwelling LW fluxes from the cloud. The wind speed and direction and overall decline in sea-level pressure in *no\_CRF\_lim* are all comparable to the control, further confirming the isolation of the local, radiative processes (Fig. 4.60b,c,d).

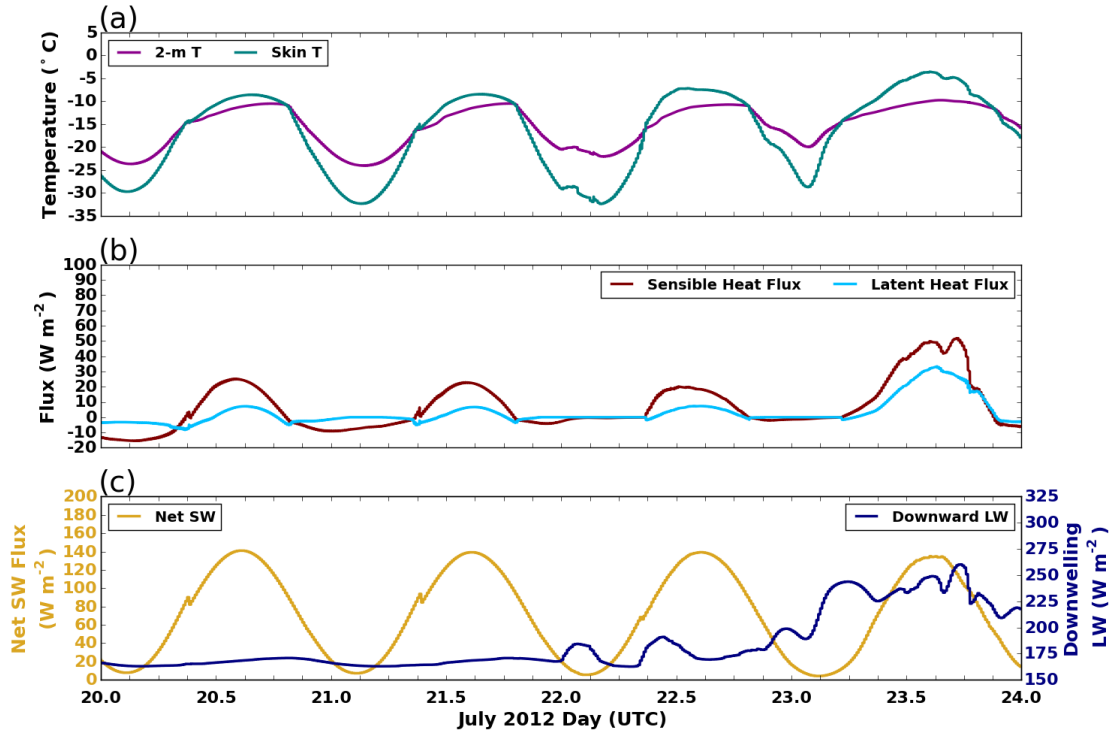


Figure 4.59: Same as Fig. 4.14, but data are from *no\_CRF\_lim*.

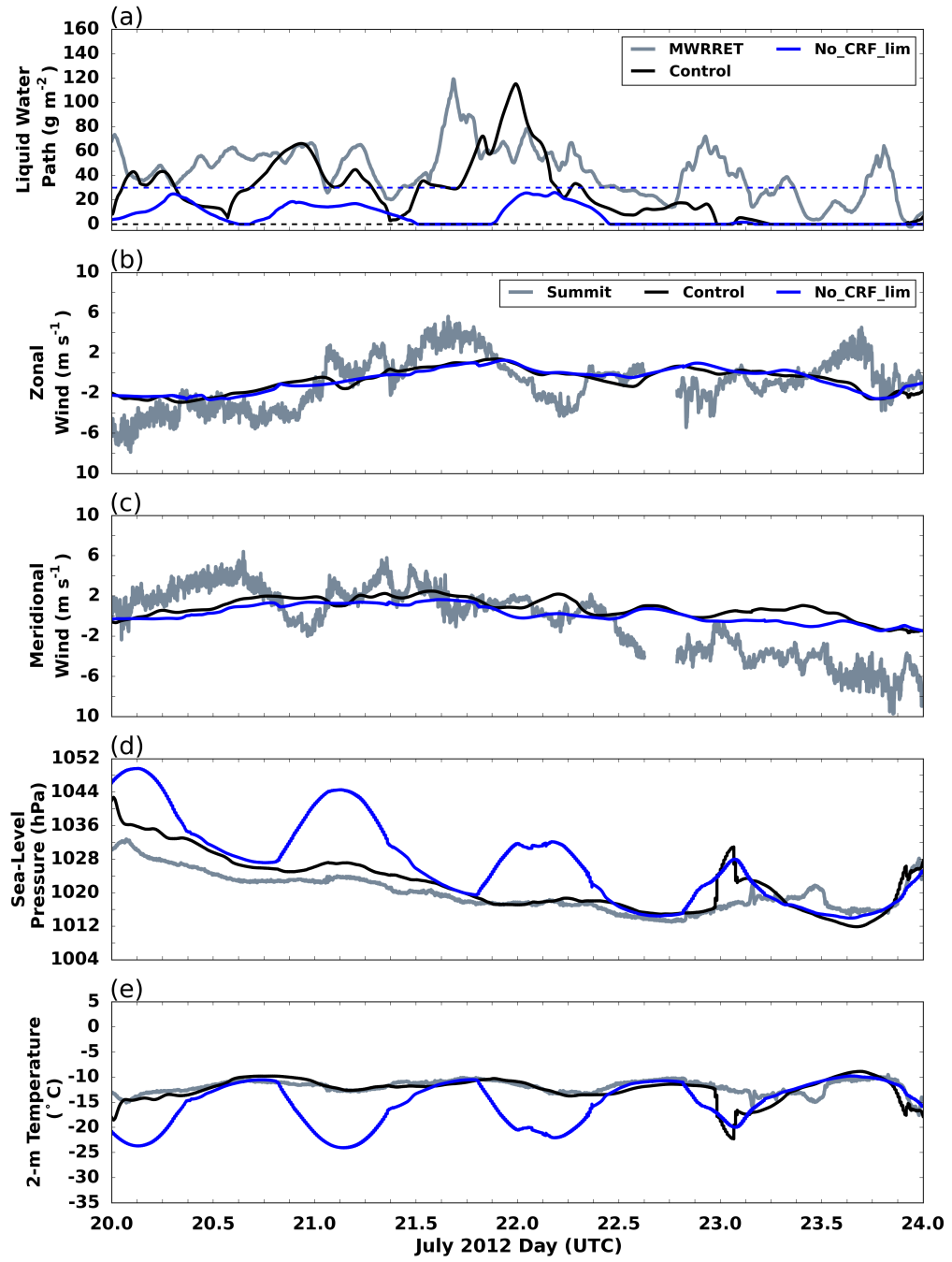


Figure 4.60: Same as Fig. 4.37, but for *no\_CRF\_lim* simulation.

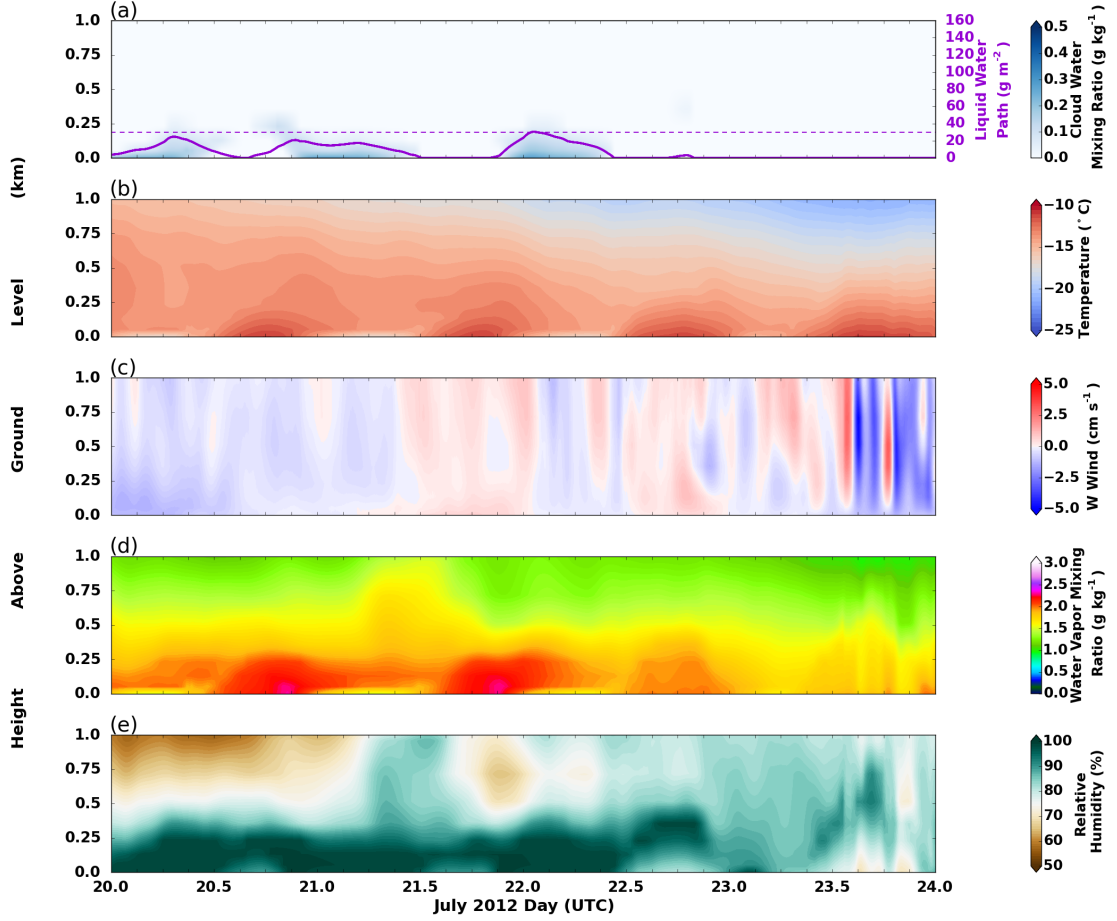


Figure 4.61: Same as Fig. 4.12, but data are from *no\_LW\_CRF\_lim*.

The *no\_LW\_CRF\_lim* simulation yields very similar results to *no\_CRF\_lim*; in *no\_LW\_CRF\_lim*, no elevated cloud layer forms with only condensation taking place at the surface (Fig. 4.61a) due to the surface radiative cooling overnight (Fig. 4.61b). Other meteorological variables from *no\_LW\_CRF\_lim* are similar to the control except for the diurnal cycle of the 2-m temperature and sea-level pressure due to the lack of a persistent cloud (Fig. 4.62).

Between the *no\_CRF\_lim* and *no\_LW\_CRF\_lim* simulations, the importance of cloud-top LW radiative cooling is highlighted, for without this process no turbulent updrafts are induced to elevate or maintain a cloud. This LW ‘clear-sky’

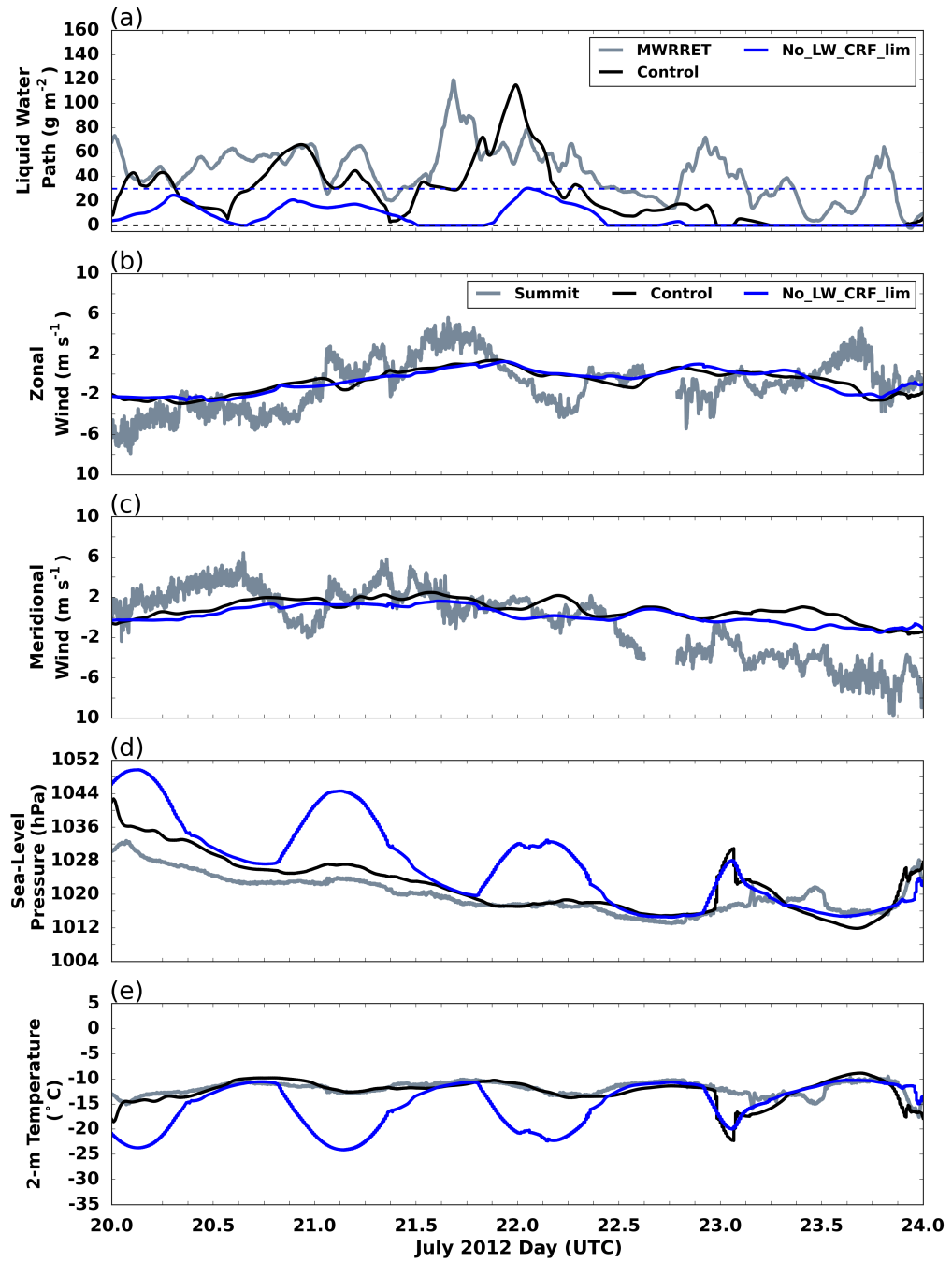


Figure 4.62: Same as Fig. 4.37, but for *no\_LW\_CRF\_lim*.

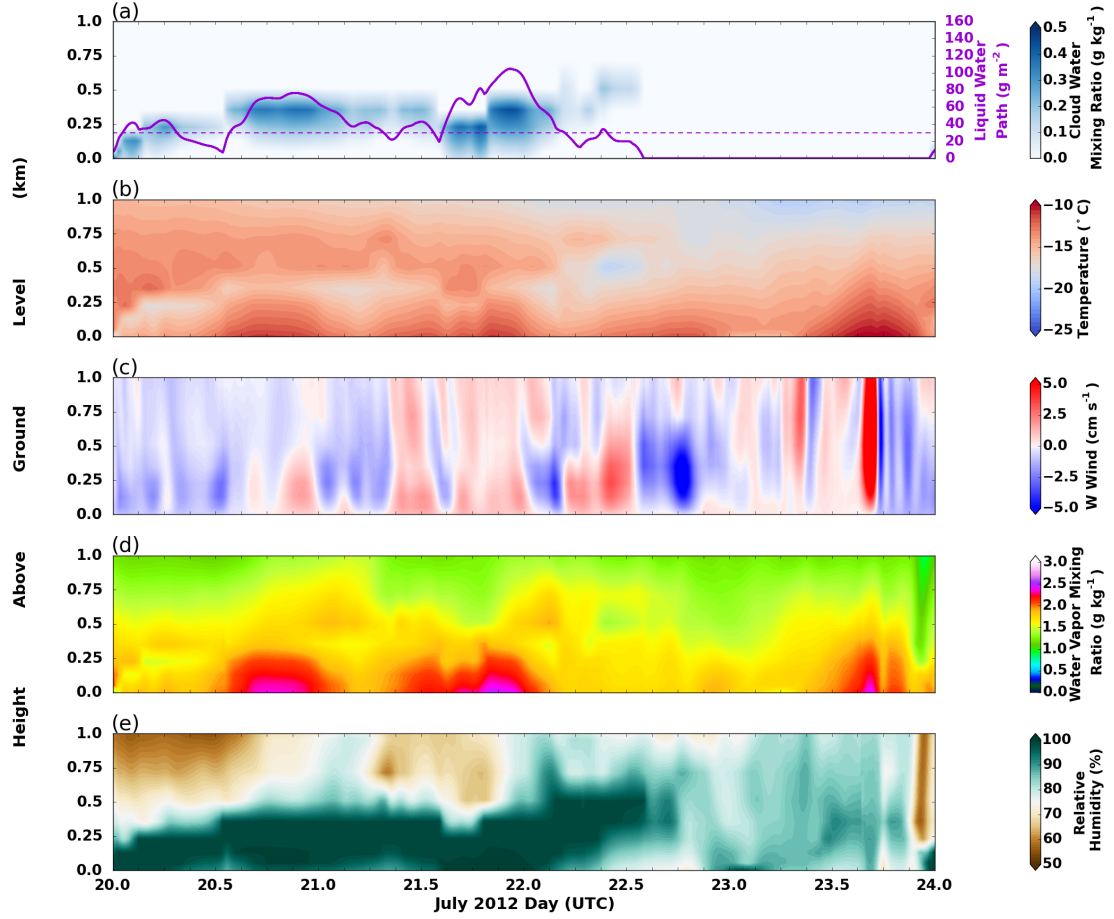


Figure 4.63: Same as Fig. 4.12, but data are from the *no\_SW\_CRF\_lim*.

scene results in near-surface condensation overnight from surface radiative cooling that dissipates during the day from SW radiative heating at the surface. The downwelling LW radiative fluxes from the cloud are lost, as there is no LW CRF, and therefore the 2-m and skin temperatures have a pronounced diurnal cycle. Additionally, the SW CRF has no effect on cloud maintenance.

The cloud simulated by *no\_SW\_CRF\_lim* has a diurnal cycle in LWP (Fig. 4.63a) and cloud water mixing ratio, similar to the control simulation (Fig. 4.64a). The *no\_SW\_CRF\_lim* cloud has more liquid water than the control; the average LWP from 20 July at 00 UTC through 22 July at 12 UTC is 47 g m<sup>-2</sup> compared to 38 g

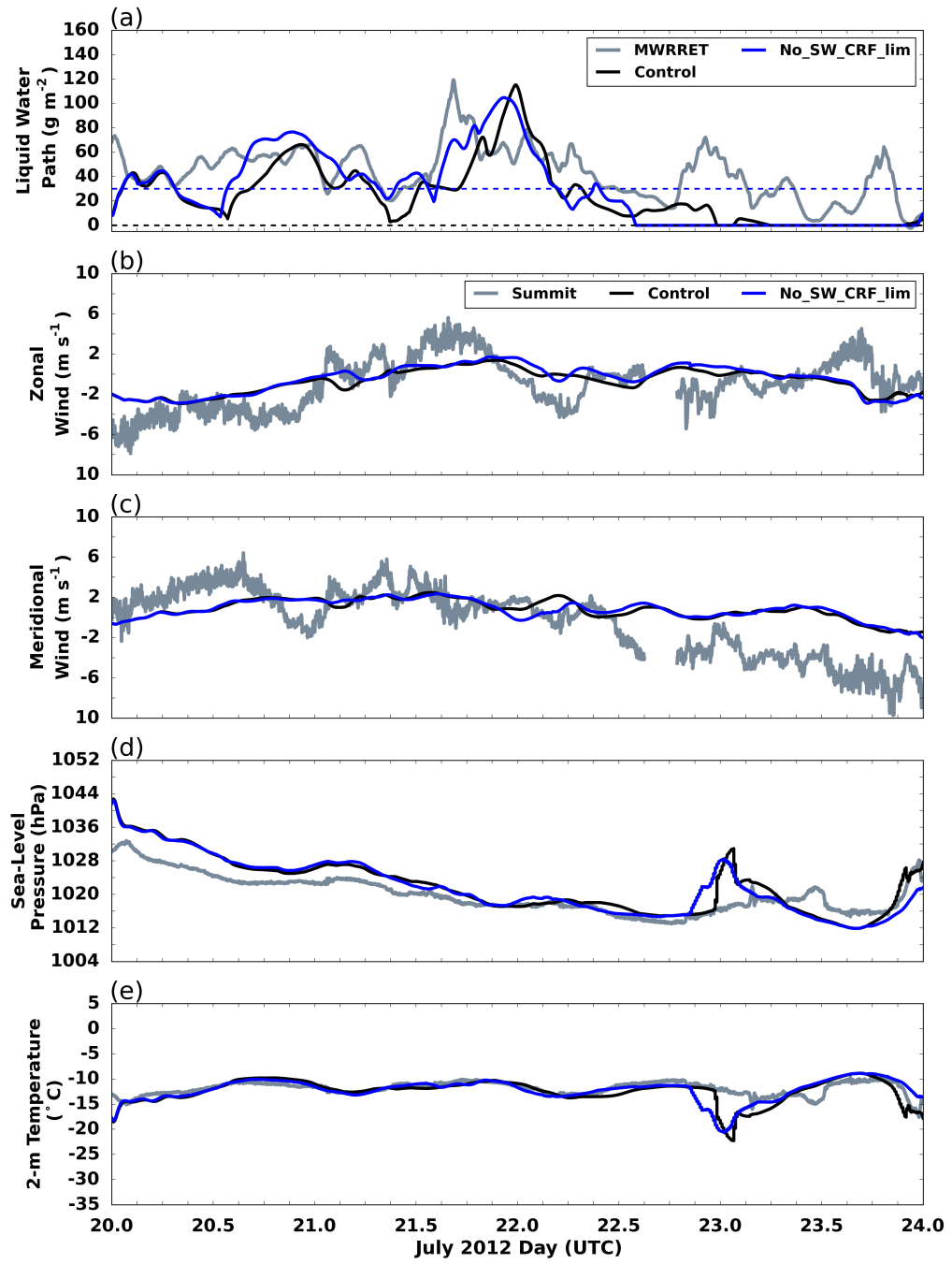


Figure 4.64: Same as Fig. 4.37, but for *no\_SW\_CRF\_lim*.



$\text{m}^{-2}$  from the control. Otherwise, the simulation follows almost identically to the control (Fig. 4.64b-e). This simulation further confirms the importance of cloud-top LW cooling in elevating the cloud and its maintenance. While the incoming SW radiation seems to only effect the cloud liquid water content, presumably from absorption by cloud droplets causing warming and evaporation. This, however, can effect the CTLC and its induced processes.

In addition, over this limited region, 3 more simulations are done in which in the LW radiation calls the model simulated LWP is divided by 10 (*LWP\_div10\_lim*) and 20 (*LWP\_div20\_lim*), and increased by 30 (*LWP\_add30\_lim*). For *LWP\_add30\_lim*, no changes are made to the LWP if the LWP at the time of the radiation call is 0. As LWP is calculated in layers in the radiation code, the addition of  $30 \text{ g m}^{-2}$  to the total LWP is added proportionality into the layers. *LWP\_div10\_lim* and *LWP\_div20\_lim* are a middle ground between *no\_CRF\_lim* and *no\_LW\_CRF\_lim*, and the control in that the cloud radiative effects and optical properties due to the liquid water are not completely ignored, but rather just reduced. *LWP\_add30\_lim* is done to investigate the radiative effects of the cloud if the cloud liquid water were increased. To further understand the impact of these simulations, the cloud optical depth is calculated using equation 4.4 and cloud emissivity using equation 1.5.

The cloud simulated in *LWP\_div10\_lim* forms at the surface on 20 July at 00 UTC (Fig. 4.65g), as the control does (Fig. 4.65d), but the CBH barely elevates from the surface, staying there through 22 July at 12 UTC. Artificially reducing the LWP in the LW radiation calls reduces the CTLC (Fig. 4.65h), in comparison to the control (Fig. 4.65e), and as a result of the decreased LWP, cloud optical depth, and cloud emissivity (Fig. 4.65a,b,c). This significantly reduces the buoyancy-driven updrafts (cf. Fig. 4.65f to i) keeping the cloud from elevating from the surface.

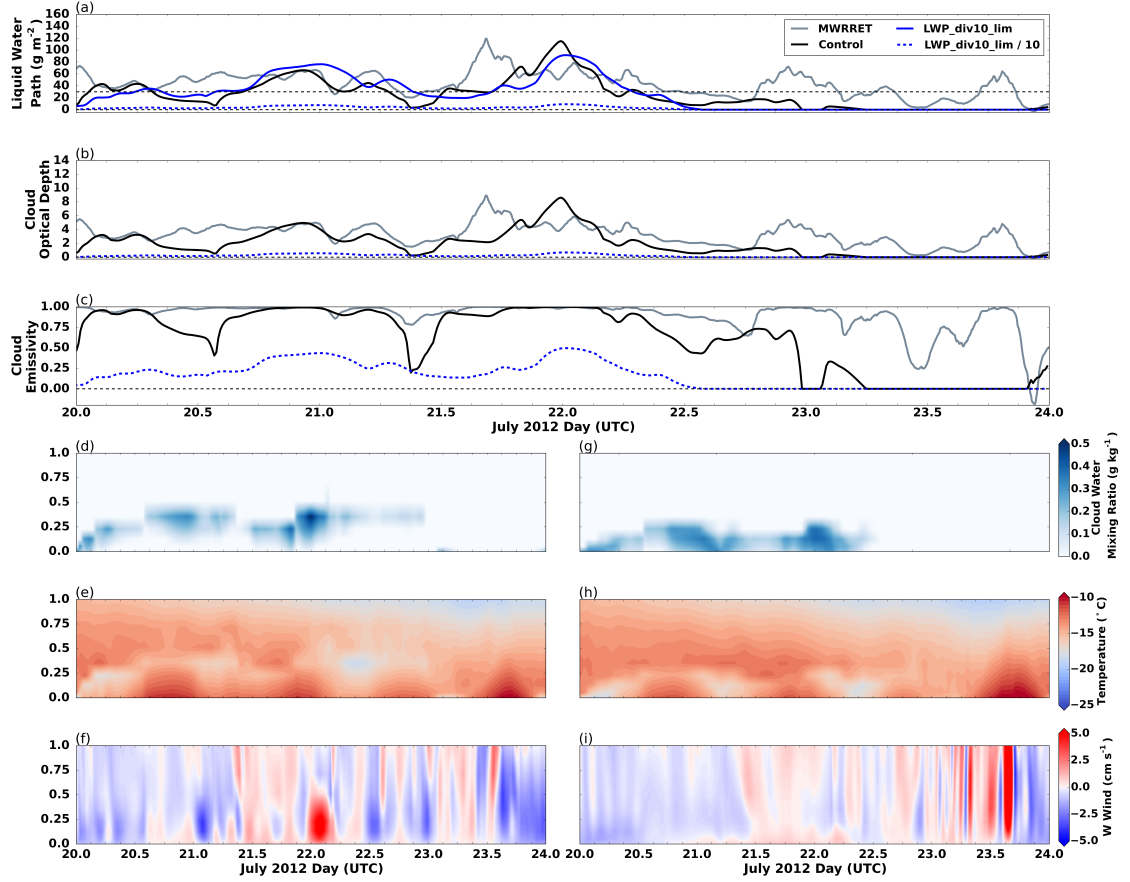


Figure 4.65: Time series of (a) liquid water path ( $\text{g m}^{-2}$ ), (b) cloud optical depth, and (c) cloud emissivity for MWRRET (gray), and the control (black) and *LWP\_div10\_lim* (blue) simulations. The dashed blue line represents the time series of the modified liquid water path in the LW radiation calls. Time-height cross sections for (d,g) cloud water mixing ratio ( $\text{g kg}^{-1}$ ), (e,h) temperature ( $^{\circ}\text{C}$ ), and (f,i) w wind ( $\text{cm s}^{-1}$ ) for the (d,e,f) control and (g,h,i) *M-PACE*.

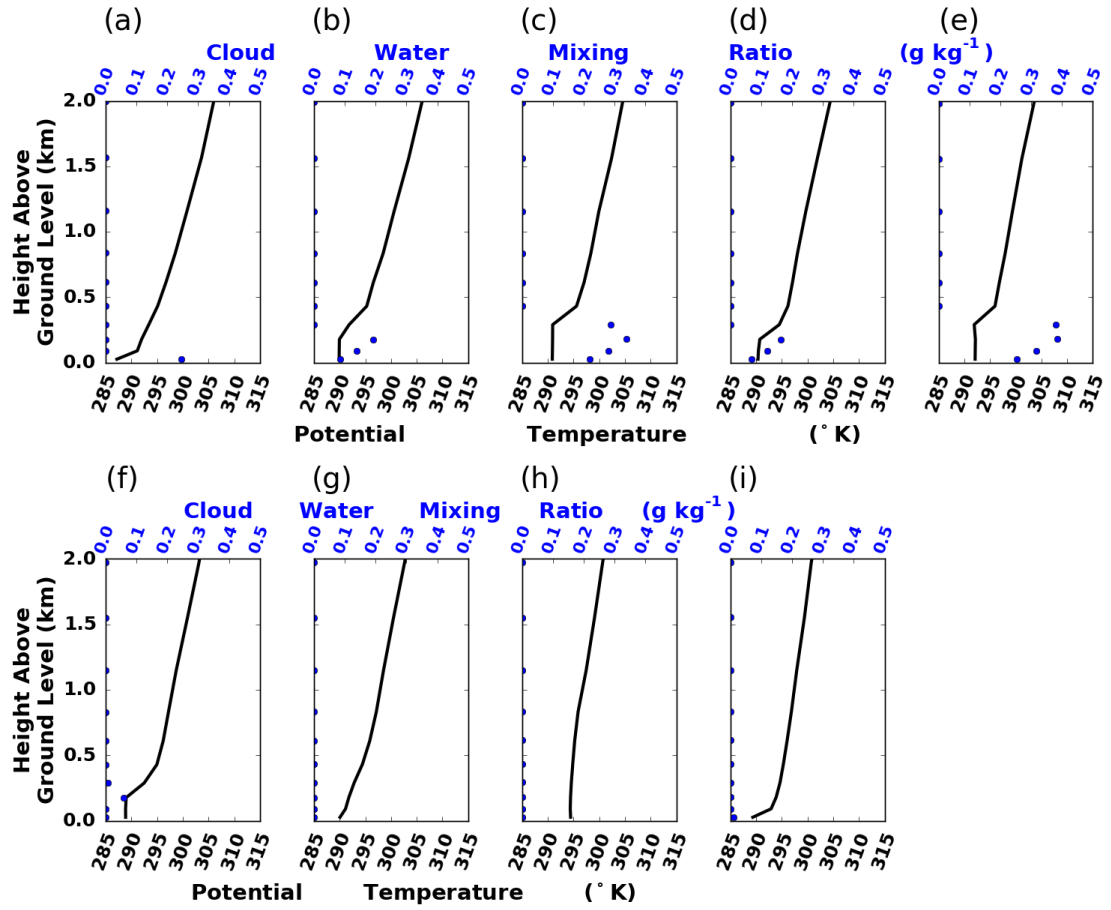


Figure 4.66: Same as Fig. 4.13, but data are from *LWP\_div10\_lim*.

However, these processes are still strong enough to maintain a cloud at the surface and a well-mixed layer through 22 July at 12 UTC (Fig. 4.66b-f).

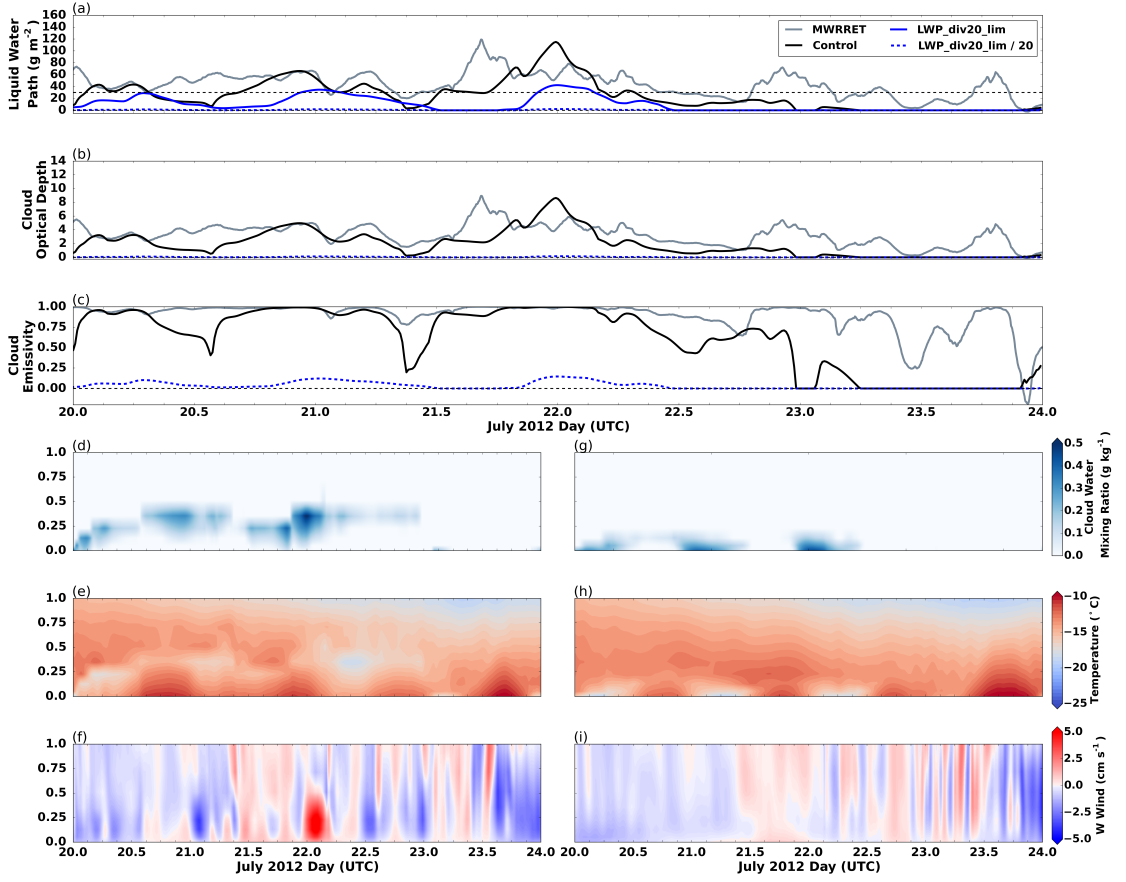


Figure 4.67: Same as Fig. 4.65, but data are from *LWP\_div20\_lim*.

The *LWP\_div20\_lim* simulation produces a cloud (Fig. 4.67g) different from the control (Fig. 4.67d), but similar to *no\_CRF\_lim* (Fig. 4.57a) and *no\_LW\_CRF\_lim* (Fig. 4.61a) in that there is no elevated, long-lived cloud, but instead, liquid forms at the surface due to surface radiative cooling under a surface-based inversion at night (Fig. 4.68). This is a result of the radiative effects of the liquid water being so significantly reduced (Fig. 4.67a,b,c) and is similar to what would be expected if the LW CRF is 0; thus there is essentially no CTLC or induced vertical motion (Fig. 4.67h,i).

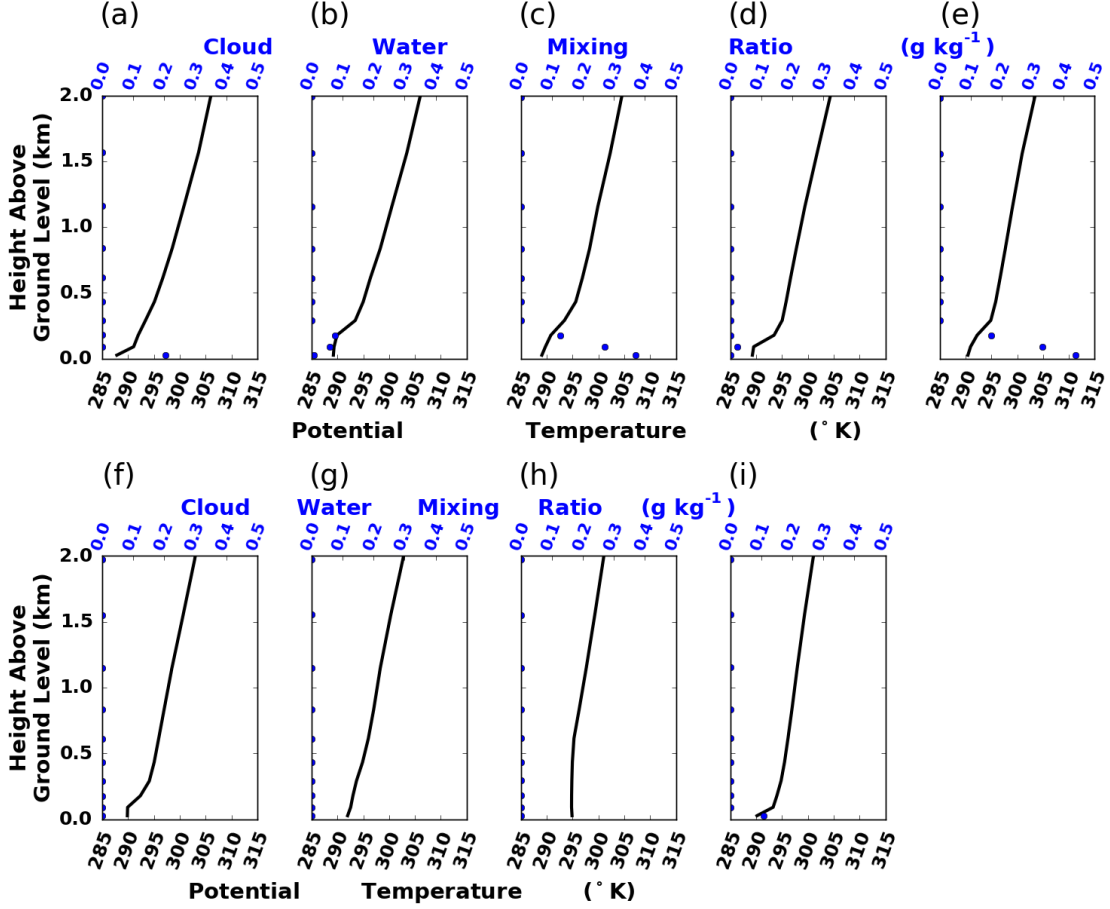


Figure 4.68: Same as Fig. 4.13, but data are from *LWP\_div20\_lim*.

*LWP\_add30\_lim* simulates an elevated cloud (Fig. 4.69g) similar to the control (Fig. 4.69d). Between 21 July at 09 and 12 UTC the cloud in *LWP\_add30\_lim* is better maintained, i.e. higher LWP and cloud water mixing ratio values, than the control. Additionally, in *LWP\_add30\_lim* around 22 July at 09 UTC, towards the end of the cloud's lifetime, the CBH ascends above 0.5 km (Fig. 4.69g). In both instances, the control LWP is below  $30 \text{ g m}^{-2}$ , the point where a cloud emits nearly as a blackbody (Fig. 4.69a). Artificially adding  $30 \text{ g m}^{-2}$  to the LWP in the LW radiation code results in an optically thicker cloud (Fig. 4.69b) and blackbody-like emission from the cloud (Fig. 4.69c), thus resulting in stronger

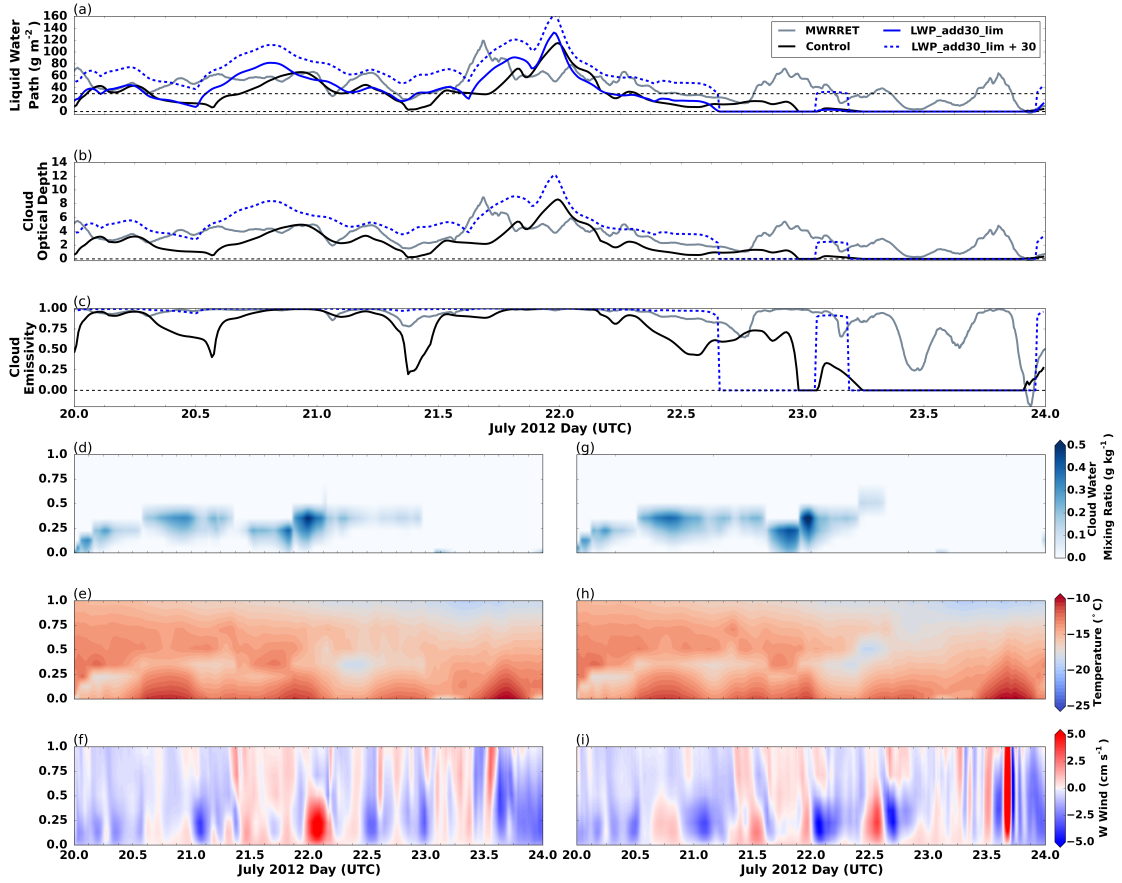


Figure 4.69: Same as Fig. 4.65, but data are from *LWP\_add30\_lim*.

CTLC in *LWP\_add30\_lim* (Fig. 4.69h) than the control (Fig. 4.69e). This greater radiative cooling drives stronger updrafts (Fig. 4.69f,i). Between 21 July at 09 and 12 UTC the greater vertical motion near the surface results in more liquid in the cloud, while at 22 July at 09 UTC this results in the ascent of the cloud, presumably due to the stronger velocity. Despite these instances when the control LWP is less than  $30 \text{ g m}^{-2}$ , the *LWP\_add30\_lim* cloud overall is very similar to the control.

Between these simulations and the control, there appears to be a threshold LWP value, and associated cloud optical depth, emissivity and CTLC, in which (1) a cloud is maintained and (2) strong enough updrafts are induced such that the cloud,

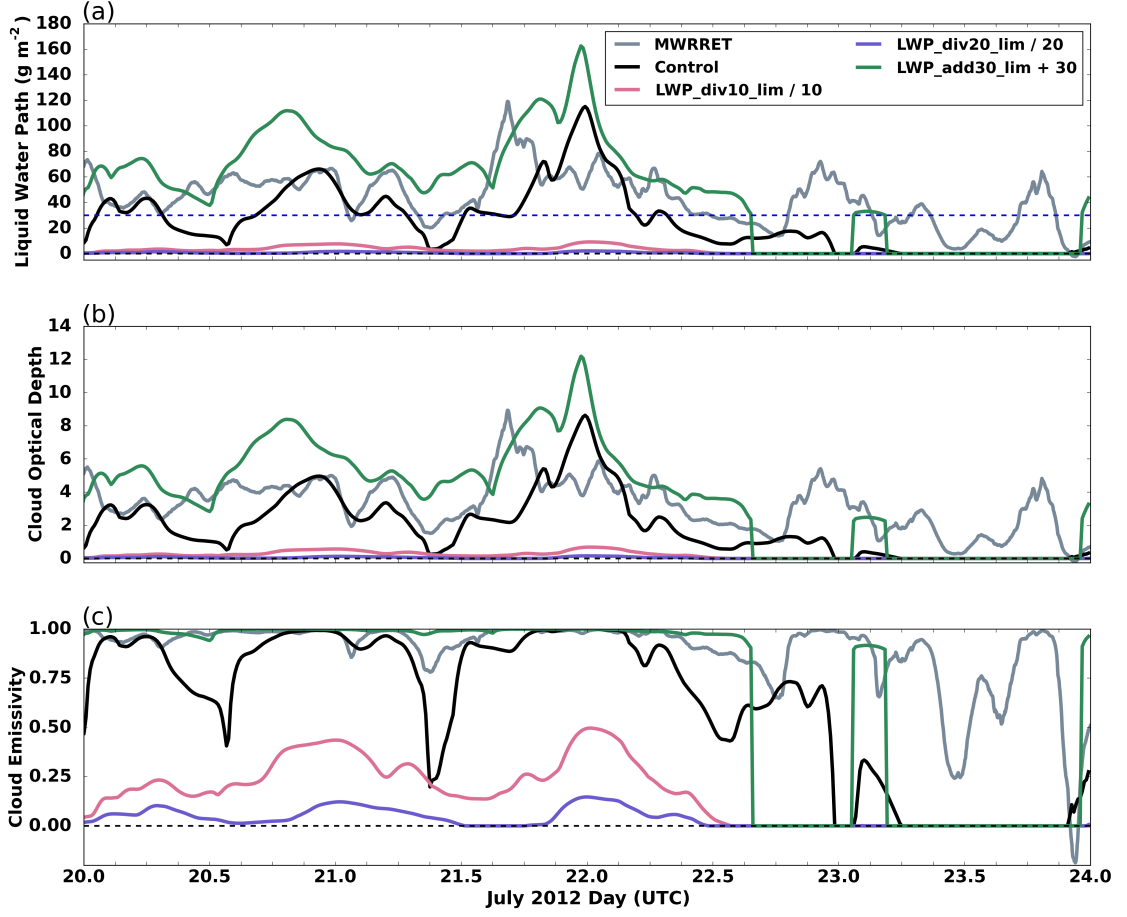


Figure 4.70: Time series of (a) liquid water path time series ( $\text{g m}^{-2}$ ), (b) cloud optical depth, and (c) cloud emissivity for MWRRET (gray), control (black), and the modified values in the LW radiation calls for  $LWP\_div10\_lim$  (light red),  $LWP\_div20\_lim$  (purple), and  $LWP\_add30\_lim$  (green).

which forms at the surface, becomes elevated. Additionally, there is a value of LWP in which any greater value of LWP does not result in any greater CTLC, vertical motion, and more persistent cloud. By artificially decreasing the cloud's LWP by a factor of 10 ( $LWP\_div10\_lim$ ), the LWP is well below the  $30 \text{ g m}^{-2}$  threshold when a cloud emits as nearly a blackbody (Fig. 4.70a), resulting in a lower cloud optical depth (Fig. 4.70b) and emissivity (Fig. 4.70c). The LWP is greater than 0, but

less than  $15 \text{ g m}^{-2}$  and the average cloud emissivity around 0.25. The CTLC is weaker, and strong enough updrafts cannot be generated to lift the cloud from the surface, though they are strong enough to maintain the cloud and well-mixed layer. Artificially decreasing the cloud's LWP by a factor of 20 (*LWP\_div20\_lim*) results in an almost clear-sky scene (Fig. 4.70a,b), resulting in weak emission, and in turn CTLC, from the cloud (Fig. 4.70c); the cloud emissivity is around 0.1. Thus, no cloud or associated well-mixed layer is maintained. Artificially increasing the cloud's LWP by 30 (*LWP\_add30\_lim*) makes little difference in cloud optical depth and emissivity (Fig. 4.70b,c) if the LWP is already above  $30 \text{ g m}^{-2}$  (Fig. 4.70a). It does make a difference for when the LWP is below  $30 \text{ g m}^{-2}$ , resulting in a more optically thick and stronger emitting cloud, and thus strong CTLC and updrafts.

Finally, the layer LWP in the LW radiation code is multiplied by a tuning factor derived from the MWRRET LWP at Summit. First, the model simulated Summit LWP is calculated at the time of the radiation call and then subtracted from the MWRRET LWP. If the difference and the simulated LWP at a gridpoint are greater than zero, then it is added proportionality to the model simulated layer LWP in the LW radiation call, i.e. making the simulation column LWP like the retrieved. If model simulated Summit LWP is 0 or greater than the retrieved LWP, no changes are made at any gridpoint. These changes are done over the limited region in Fig. 4.53 and after 20 July at 12 UTC in the simulation to allow for model spin up (*dLWP\_lim*).

In *dLWP\_lim*, by forcing the column LWP in the LW radiation call to be the MWRRET value (Fig. 4.71a), the simulated cloud has the same optical depth and emissivity as observed (Fig. 4.71b,c). The *dLWP\_lim* simulated cloud shares similarities with the control, while also having clear differences (Fig. 4.71d,g). Through 20 July at 21 UTC, the *dLWP\_lim* follows the control LWP, whereafter the simulations start to diverge, in regards to LWP (Fig. 4.71a). A distinct difference



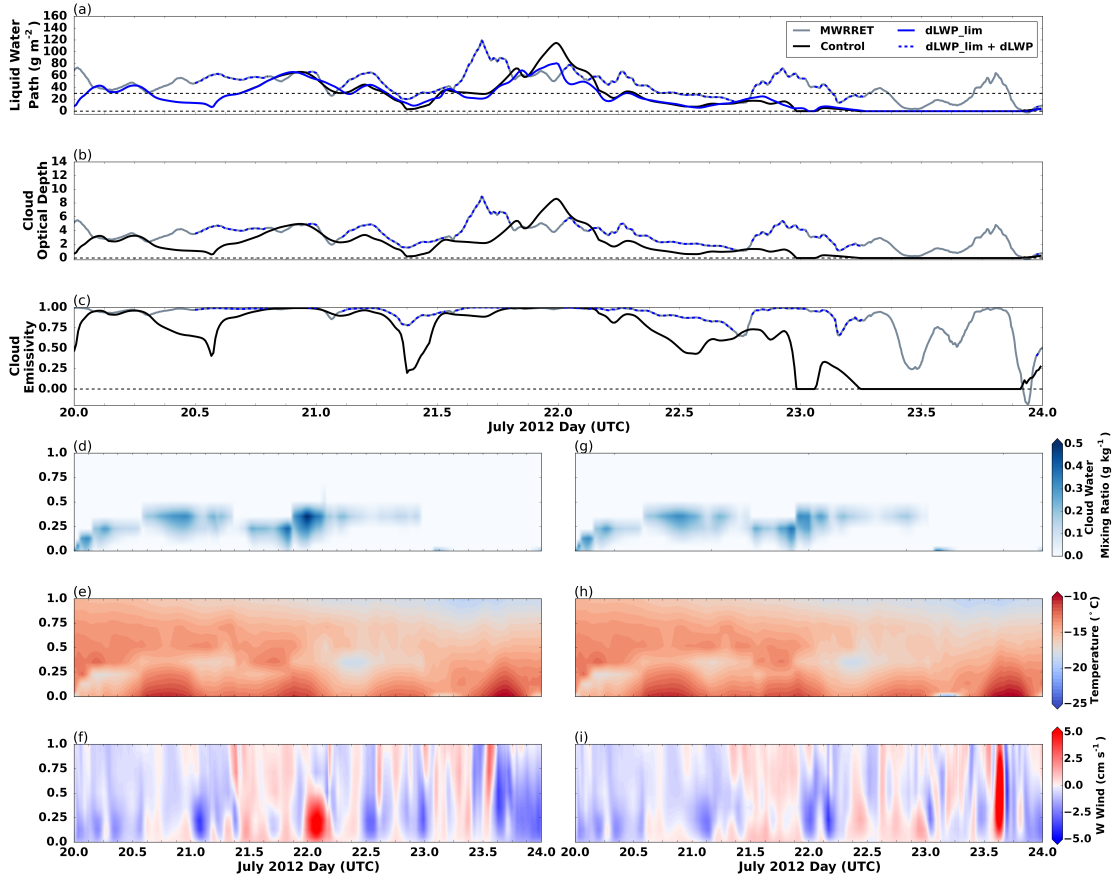


Figure 4.71: Same as Fig. 4.65, but data are from *dLWP\_lim*.

between the two is when the control emissivity is below one, ex. 22 July at 12 UTC to 23 July at 00 UTC (Fig. 4.71c). The CTLC in *dLWP\_lim* is a bit stronger (Fig. 4.71h) than the control (Fig. 4.71e), resulting in more upward vertical motion through cloud-top (cf. Fig. 4.71f to i). Regardless of the LWP being forced to be the MWRRET values in the LW radiation calls, the local processes related to the LW CRF are not enough to persist the cloud past 23 July at 00 UTC as the cloud in *dLWP\_lim* (Fig. 4.71g) and the control (Fig. 4.71d) dissipate at this time; this further supports the cloud dissipation is due to processes on the synoptic-scale.

Simulation	Influence Scale	Description
fixed_19_12	Synoptic	Boundary conditions from forcing dataset from 19 July at 12 UTC only
M-PACE	Local	Ice nucleation equation in microphysics scheme based on M-PACE observations
GBM	Local	PBL physics option changed to local scheme, Grenier-Bretherton-McCaa
no_CRF	Local	Cloud radiative forcing in both the LW and SW radiation calls are turned off
no_LW_CRF	Local	Cloud radiative forcing is turned off in LW radiation calls, but on in the SW
no_SW_CRF	Local	Cloud radiative forcing is turned off in SW radiation calls, but on in the LW
no_CRF_lim	Local	Cloud radiative forcing in both the LW and SW radiation calls are turned off
no_LW_CRF_lim	Local	Cloud radiative forcing is turned off in LW radiation calls, but on in the SW
no_SW_CRF_lim	Local	Cloud radiative forcing is turned off in SW radiation calls, but on in the LW
LWP_div10_lim	Local	LWP in LW radiation calls divided by 10
LWP_div20_lim	Local	LWP in LW radiation calls divided by 20
LWP_add30_lim	Local	LWP in LW radiation calls increased by 30
dLWP_lim	Local	LWP in LW radiation calls tuned to be the MWRRET retrieved values after 20 July at 12 UTC

Table 4.2: Summary of experimental model simulations.

### 4.3 Results Summary and Discussions

The hypothesis for this thesis is that local processes lead to the longevity of AM-PCs, while synoptic-scale processes are necessary to create a favorable thermodynamic environment. This environment is important in that it ultimately drives the dynamical, local processes (i.e. moisture inversion, surface coupling, etc.). This

creates an intimate connection between the synoptic and local scales. The hypothesis was tested by using a numerical model for case study of an AMPC event that occurred over Summit, Greenland from 20 to 24 July 2012. In order to do a series of controlled experiments, a control simulation was chosen over several rounds of different combinations of model versions, initial and boundary conditions, shortwave radiation physics options, domain size, and horizontal and vertical grid spacings. The control simulation was chosen based on what simulation compared best to the observed cloud in terms of cloud lifetime and LWP; the control simulation is summarized in Table 4.1.

The cloud simulated by the control forms at the surface at 20 July at 00 UTC as a result of strong surface radiative cooling under a clear-sky, surface-based inversion leading to condensation; observations of surface-based inversions at Summit confirm that they are conducive for the formation of low-level fog, i.e. liquid water (Miller et al., 2013). The emission due the liquid water results in strong cooling above it resulting in surface-based, buoyancy-driven updrafts that lift the cloud-base (i.e. the point of condensation) from the surface. This formation is similar to that discussed in Herman and Goody (1976) where in a stable atmosphere liquid water first forms at the surface due to radiative cooling, and then elevates from the surface due to the radiative regime change due to the presence of liquid water. Mixing due to the CTLC-induced updrafts additionally creates a well-mixed layer from the surface through cloud-top. A well-mixed layer resulting from the turbulent mixing induced by CTLC is also seen in Morrison and Pinto (2006).

The cloud in the control simulation is maintained by CTLC-induced, surface-base updrafts lifting and condensing moist, saturated air near the surface through cloud-top. This creates a connection between the CTLC, updrafts, and cloud maintenance. The updrafts are induced as a result of the CTLC and these updrafts lead to condensation further maintaining the liquid water supply in the cloud,

which maintains the CTLC. The moist air near the surface is due to southeasterly flow off the Denmark Strait ahead of a surface cyclone near the southern tip of Greenland. This creates a connection between synoptic and local-scale processes by which if there is no moisture source as a result of synoptic-scale moisture advection the cloud cannot be maintained by the locally-driven updrafts.

The cloud is additionally maintained by the surface fluxes as a result of the coupling of the cloud with the surface due to the cloud-driven, well-mixed layer. These surface fluxes exhibit a diurnal cycle (higher during the day than at night) resulting in a diurnal cycle of LWP and cloud water and water vapor mixing ratios. Morrison and Pinto (2006) conclude that moisture supplied to the cloud via the surface fluxes increase cloud lifetime. This creates a positive feedback loop between the CTLC, surface fluxes, and cloud lifetime, where as the CTLC induces turbulent mixing resulting in a well-mixed layer from the cloud-top to the surface. This leads to additional moisture and energy supplied to the cloud to maintain it and the CTLC which further increases the surface fluxes via surface warming and downdrafts bringing colder air over the surface.

As the surface cyclone moves near the southeastern Greenland coast, there is strong easterly flow to its north over eastern Greenland. Over western Greenland, there is strong westerly flow driven by the pressure gradient force due the location of the surface cyclone. At 23 July at 00 UTC, these two flows ascend the GIS and converge at the top of it resulting in a complete reversal of the normal katabatic wind pattern; this is the same time the cloud dissipates. The low-level convergence and the associated deeper, upward motion results in the formation of ice rather than liquid water by 23 July at 03 UTC at Summit, as a precipitating, upper-level ice cloud moves over Summit ahead of a north-south moisture boundary over western Greenland. The presence of ice quickly results in the loss of cloud liquid

water and CTLC, similarly seen in Pinto (1998). Without the cloud, the well-mixed layer weakens, the surface downwelling LW flux drops (Morrison and Pinto, 2006), and the skin and near surface air temperature drops.

As the moisture boundary and surface cyclone move away from Summit after 23 July at 06 UTC, colder, drier air from northeasterly flow dominates over Summit with a surface-based inversion replacing the well-mixed layer resulting in a very different air mass than was in place before, i.e a change in the thermodynamic profile of the lower atmosphere. This colder, drier atmosphere creates an environment unfavorable for a cloud to persist. Such a dramatic change in the synoptic environment at the time of cloud dissipation is consistent with the Morrison et al. (2012) hypothesis.

In a simulation where the BCs from the forcing dataset were fixed to 19 July at 12 UTC, the cloud is longer-lived than the control. This results from the different evolution of the synoptic-scale pattern from the control. In this simulation there is no surface cyclone that passes by the southeast Greenland coast, but rather one develops in the Greenland Sea. This cyclone advects moisture by easterly flow over the central and eastern Greenland. Additionally, there is no moisture boundary that passes over the ice sheet, but instead the fixed BCs result in moisture continually being fed into the western portion of the domain. This air spreads across the western and northern GIS and is advected by northerly flow to Summit. Without these synoptic-scale features, there is no change in air mass, no significant changes in the large-scale pattern, and thus no changes to the thermodynamic profile at Summit. As a result of this more stable pattern, the cloud is much longer lived than the control.

Within the Morrison Double Moment microphysics scheme, changing the equation for ice nucleation based from the default equation to one based on M-PACE

observations results in differences in the cloud liquid water and ice. In the *M-PACE* simulation, the cloud liquid water mixing ratio is greater and ice mixing ratio is less than the control simulation. The lower ice mixing ratios are a result of using the ice nucleation equation based on Arctic observations, i.e. more accurate representation of ice nucleation in the Arctic. The lower ice content renders the WBF process less effective leading to a higher content of cloud liquid water; such results are similarly seen in Morrison and Pinto (2006). Additionally, in a simulation where the PBL scheme is changed from a non-local to local scheme there is no persistent cloud layer. This shows that deeper mixing by larger eddies simulated by the non-local scheme is important for cloud maintenance.

To investigate the sensitivity of cloud maintenance to radiation, the radiative effects of cloud water and ice are turned off in a small region over the center of the GIS. Turning off the LW radiative effects of the cloud results in no elevated, persisting cloud. Rather, in the overnight hours, strong surface radiative cooling under a surface-based inversion results in condensation near the surface, which dissipates during the day due to surface heating from incoming SW radiation. These results are same as those found by Solomon et al. (2016) in a similar experiment. With no CTLC, there are no buoyancy-driven updrafts to elevate or maintain the cloud and well-mixed layer. Similar to Morrison and Pinto (2006), there is a surface-based inversion at night and very shallow well-mixed layer during the day. The effects of incoming SW radiation on the cloud does not effect its maintenance, but instead effects the cloud liquid water mixing ratio. Absorption of the SW radiation by the cloud droplets can cause their evaporation, reducing the amount of liquid water in the cloud potentially effecting its LW radiative effects and maintenance, which is similarly discussed in Petters et al. (2012).

Reducing the LW radiative effects of the cloud in 2 different simulations shows that there appears to be a threshold LWP value in which the cloud optical depth,

emissivity, and the resulting CTLC are enough that first the cloud is maintained (LWP greater than 0 but less than  $5 \text{ g m}^{-2}$  and cloud emissivity around 0.25) and second the cloud is lifted from the surface (LWP greater than  $10 \text{ g m}^{-2}$  and cloud emissivity greater than 0.5). When the LWP is partially reduced (by a factor of 10), the cloud is maintained, but never lifts from the surface. The CTLC is sufficient enough to drive turbulent mixing to maintain a cloud and well-mixed layer, but not enough to drive this mixing deep enough to elevate the cloud. When the LWP is reduced significantly (by a factor of 20), the cloud becomes very optically thin and the CTLC is significantly reduced; the CTLC is almost non-existent and is not strong enough to drive the necessary turbulent mixing to maintain the cloud, and thus looks similar to if there were no LW cloud radiative effects.

In order for the cloud to be maintained the CTLC, the cloud must have a certain LWP and optical depth. Additionally, there is a point where more liquid water in the cloud does not result in any greater cloud LW radiative effects. Nevertheless, the importance of CTLC for cloud maintenance is again highlighted by these simulations. When the LWP is made to be more like the MWRRET LWP in the LW radiation code, there are very subtle differences. The cloud in this simulation and the control dissipate at the same time furthering supporting the cloud dissipation is due to synoptic-scale processes.

## Chapter 5      Future Work and Conclusions

### 5.1      Future Work

This research provides insights into the processes on a variety of scales that aided in the formation, persistence, and dissipation of an AMPC event that took place from 20-24 July 2012 at Summit, Greenland. Although this study considered only a single case, future work will extend the knowledge gained here to variety cases in different seasons, synoptic situations, and different geographical locations throughout the Arctic where observatories exist so that more general conclusions are possible in the future. The building of a strong theoretical framework of Arctic MP clouds, similar to that that exists for midlatitude stratocumulus, will lead to better climate simulations to provide a clearer picture of the future of a rapidly changing Arctic.

Additional numerical simulations using the LES or SCM mode of the WRF-ARW could also be done to provide more insight on this case and other future modeling case studies. These simulations could provide further information on the smaller scale structure and processes occurring in AMPCs.

July 2012 was an anomalously warm month for Greenland with record-breaking GIS surface melt. It would be interesting to perform similar model simulations of a Summit AMPC event that occurred in a more ‘average’ July. Are the same processes that were important on 20-24 July 2012 similar a more typical July for Greenland case? Are the simulated clouds similar in their macro- and microphysical and radiative characteristics? What are the major differences in the synoptic



evolution, and how did this impact the cloud? What about events in the winter, fall, or spring? Additional simulations characterized by the positive and negative phases of various climate indices may provide insight, as well. Positive NAO cases could be particularly interesting as this pattern is associated with colder, drier air over Greenland, but synoptic-scale cyclones more frequently pass southeast of Greenland, which from this research showed advected moisture across the ice sheet. More cases studies of Summit AMPC events would provide further knowledge on their formation and maintenance processes.

Additionally, it would be interesting to compare simulations of Summit AMPC events to those in other areas of the Arctic, such as Barrow, Alaska. Are other processes in cloud maintenance more dominant in one region than another? Are synoptic-scale processes more influential in regions that are at lower elevations than Summit? How do sea-ice or open-water surfaces affect the cloud compared to an ice-sheet surface?

There still remains future work to be done specifically regarding simulations of the 20-24 July, 2012 Summit AMPC event. This research focused primarily on the radiative, local processes and their effect on cloud maintenance, while the effects of cloud microphysics were briefly investigated. This research and other previous studies (e.g. Pinto (1998)) show that AMPC lifetimes are very sensitive to the presence of ice as the effectiveness of the WBF process is very sensitive to this, thus it would be useful to further investigate the effects of the cloud microphysics.

## **5.2 Conclusions**

The Arctic is one of the fastest warming regions on Earth. The Greenland Ice Sheet (GIS) is one of the most dominant features in the Arctic, containing nearly 12% of the world's glacier ice. The GIS affects the synoptic-scale pattern by diverting flow around it and generating unique mesoscale flows, such as the katabatic winds.

In turn, the GIS and its melt are affected by larger scale patterns, such as those associated with a given phase of the NAO and/or AO, as well as smaller scale phenomenon, such as Arctic mixed-phase clouds (AMPCs).

Single-layer AMPCs are low-level stratiform clouds comprised of a thin layer of supercooled liquid water drops at the cloud top with ice forming within this layer and falling toward the bottom and out of the cloud. These clouds occur frequently across the Arctic and are long-lived, persisting for several days, which is peculiar given the Wegner-Bergeron-Findeisen process; they also have a net warming effect on the surface. Due the spatially and temporally inconsistent observations, little is known about the persistence of AMPCs, and as a result, are poorly simulated in weather and climate models. However, the frequency and longevity of AMPCs combined with their warming effect on the surface, it is critical to understand the mechanisms that owe their occurrence and persistence in order to correctly simulate them in climate and weather models to have a clearer picture of the future state of the Arctic. This is particularly true for the Arctic ice surfaces as their melt will greatly impact sea-level.

Morrison et al. (2012) provide a hypothesized framework of processes that lead to the maintenance of AMPCs. The study proposes that various local processes and interactions drive AMPC persistence, but significant changes to the synoptic-scale environment disrupt the balance between the local processes causing the cloud to dissipate. The hypothesis used in this research expands upon Morrison et al. (2012) that the local processes lead to the longevity of AMPCs, while synoptic-scale processes are necessary to create a favorable thermodynamic environment. This environment is important in that it ultimately drives the dynamical local processes creating an inseparable connection between the scales. This hypothesis was investigated by performing a numerically simulated case study of an AMPC that occurred over Summit, Greenland over 20-24 July 2012. The results from the

numerical simulations are compared to the observations from the “Integrated Characterization of Energy, Clouds, Atmospheric state, and Precipitation at Summit” cloud-atmosphere observatory located at Summit.

The control simulation is described in Table 4.1. This simulation decently simulates the observed cloud at Summit, though the cloud in the simulation is lower in base and shorter-lived. The cloud in the simulation forms due to surface radiative cooling under a clear-sky, surface based inversion. This cooling results in condensation near the surface, and the formation of the cloud. The cloud liquid water results in cloud-top longwave radiative cooling (CTLC), which decreases the static stability and drives surface-based, buoyancy-driven updrafts that elevate the cloud from the surface (Fig. 5.1). The air near the surface is moist as a result of synoptic-scale moisture advection ahead of a surface cyclone near southern Greenland. The updrafts lift and condense this air maintaining the cloud liquid water and maintains the CTLC, creating a feedback between the cloud liquid water, updrafts, and CTLC (Fig. 5.2). In addition, the buoyancy-driven updrafts (and downdrafts) lead to a well-mixed layer from the surface to cloud-top; this well-mixed layer is driven by the radiative effects of the cloud. This well-mixed

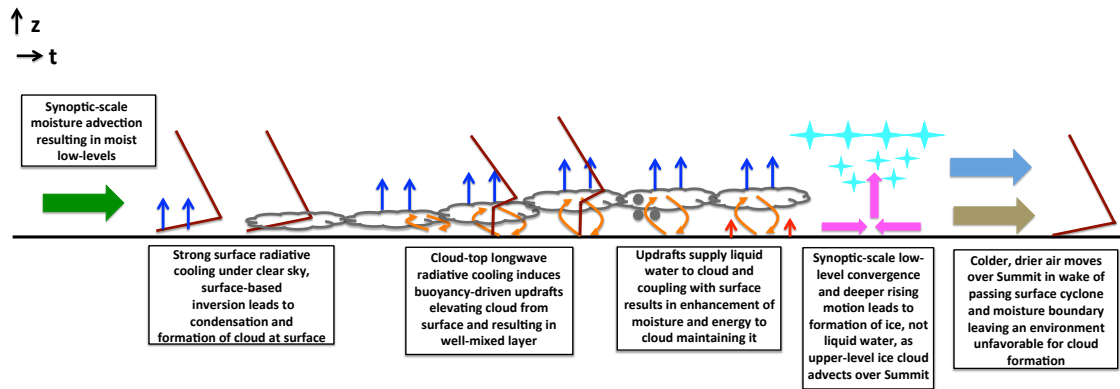


Figure 5.1: Schematic of the synoptic and local-scale processes involved in the cloud's formation, maintenance, and dissipation.

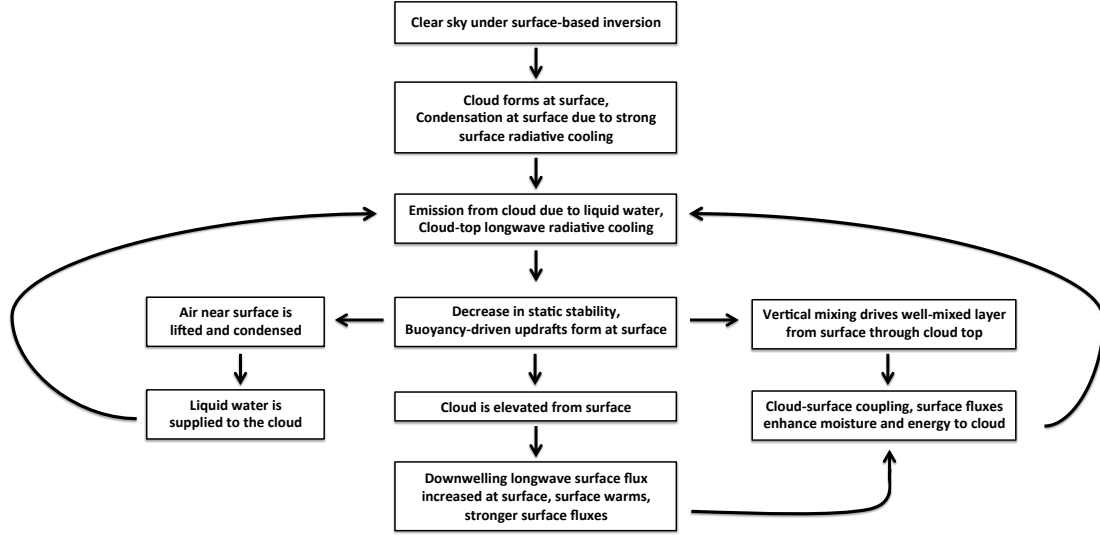


Figure 5.2: Web describing the process for cloud formation and the local feedbacks that lead to its maintenance.

layer couples the cloud to the surface where the surface fluxes provide energy and moisture to the cloud further maintaining the cloud liquid water and CTLC. This creates again another feedback between the CTLC, mixing, and surface fluxes. Moreover, the radiative effects of the cloud increase the downwelling longwave flux at the surface leading to a warmer surface and stronger surface fluxes strengthening the latter discussed feedback (Fig. 5.2).

Thus, CTLC is a very crucial mechanism for the cloud's maintenance. This mechanism is highly dependent on the liquid water path (LWP). Clouds with LWPs greater than  $30 \text{ g m}^{-2}$  emit nearly as blackbodies (cloud emissivity of approximately 1), so LWPs greater than or equal to this value result in the strongest CTLC. Without the cloud radiative effects due to the liquid water (i.e. LWP of or near  $0 \text{ g m}^{-2}$ ), the CTLC and induced above-mentioned processes are not strong enough to maintain a cloud. LWPs less than  $5 \text{ g m}^{-2}$ , but greater than  $0 \text{ g m}^{-2}$

a cloud can be maintain, but the CTLC is not strong enough to drive strong and deep enough updrafts to lift a cloud that has formed at the surface.

These processes maintain the cloud layer; however, the cloud would have not been maintained without synoptic-scale moisture advection (Fig. 5.1). On the other hand, synoptic-scale processes that contribute to the cloud's demise. Flow ascending the eastern and western coasts of Greenland converge at Summit due a surface cyclone off the southeastern Greenland coast; from mass continuity, the atmosphere responds to this low-level convergence through rising motion. The subsequently deeper updrafts result in the formation of ice rather than liquid water, thus killing the AMPC. Additionally, a precipitating, upper-level cloud ahead of a moisture boundary over western Greenland moves over Summit at this time (Fig. 5.1). With a high concentration of ice crystals, the Wegner-Bergeron-Findeisen process is more effective at dissipating the cloud. Not only does this show the maintenance of the cloud is highly dependent on the presence of ice crystals, it further ties the local scale processes, in this case the microphysical ones, to the happenings on the synoptic-scale.

As the surface cyclone moves away from Greenland and the moisture boundary passes over Summit, the atmosphere at Summit is much drier and colder than it was previously. A surface-based inversion replaces the well-mixed layer, which weakened as a result of the cloud dissipation (Fig. 5.1). This profile is not favorable for cloud maintenance or formation. Again, this connects back the synoptic-scale evolution to the processes on the local-scale. In conclusion, local-processes, particularly longwave radiative cooling at cloud-top, maintained the cloud, while synoptic-scale processes created an environment that was either favorable or unfavorable for the cloud to form and be maintained in.

## Bibliography

- Ackerman, T. P., K.-N. Liou, F. P. Valero, and L. Pfister, 1988: Heating rates in tropical anvils. *Journal of the atmospheric sciences*, **45** (10), 1606–1623.
- Bamber, J. L., R. L. Layberry, and S. Gogineni, 2001: A new ice thickness and bed data set for the Greenland ice sheet: 1. Measurement, data reduction, and errors. *Journal of Geophysical Research: Atmospheres*, **106** (D24), 33 773–33 780.
- Banacos, P. C., and D. M. Schultz, 2005: The use of moisture flux convergence in forecasting convective initiation: Historical and operational perspectives. *Weather and Forecasting*, **20** (3), 351–366.
- Beesley, J., and R. Moritz, 1999: Toward an explanation of the annual cycle of cloudiness over the Arctic Ocean. *Journal of Climate*, **12** (2), 395–415.
- Beljaars, A., 1995: The parametrization of surface fluxes in large-scale models under free convection. *Quarterly Journal of the Royal Meteorological Society*, **121** (522), 255–270.
- Benedict, J. J., S. Lee, and S. B. Feldstein, 2004: Synoptic view of the North Atlantic oscillation. *Journal of the Atmospheric Sciences*, **61** (2), 121–144.
- Bennartz, R., and Coauthors, 2013: July 2012 Greenland melt extent enhanced by low-level liquid clouds. *Nature*, **496** (7443), 83–86.
- Bergeron, T., 1935: On the physics of clouds and precipitation. *Proces Verbaux de l'Association de Meteorologie, International Union of Geodesy and Geophysics*, 156–178.
- Bluestein, H. B., 1993: Synoptic-dynamic meteorology in midlatitudes. Volume II. Observations and theory of weather systems.
- Box, J. E., 2002: Survey of Greenland instrumental temperature records: 1873–2001. *International Journal of Climatology*, **22** (15), 1829–1847.
- Bromwich, D. H., Q.-s. Chen, Y. Li, and R. I. Cullather, 1999: Precipitation over Greenland and its relation to the North Atlantic oscillation. *Journal of Geophysical Research: Atmospheres*, **104** (D18), 22 103–22 115.

- Bromwich, D. H., K. M. Hines, and L.-S. Bai, 2009: Development and testing of polar weather research and forecasting model: 2. Arctic Ocean. *Journal of Geophysical Research: Atmospheres*, **114** (D8).
- Brown, P., S. Clough, N. Miller, T. Shippert, D. Turner, R. Knuteson, H. Revercomb, and W. Smith, 1995: Initial analyses of surface spectral radiance between instrument observations and line by line calculations. *Conference on Atmospheric Transmission Models, 6-8 June 1995*, DTIC Document, 84.
- Campbell, J. R., D. L. Hlavka, E. J. Welton, C. J. Flynn, D. D. Turner, J. D. Spinhirne, V. S. Scott III, and I. Hwang, 2002: Full-time, eye-safe cloud and aerosol lidar observation at atmospheric radiation measurement program sites: Instruments and data processing. *Journal of Atmospheric and Oceanic Technology*, **19** (4), 431–442.
- Cavallo, S. M., J. Dudhia, and C. Snyder, 2011: A multilayer upper-boundary condition for longwave radiative flux to correct temperature biases in a mesoscale model. *Monthly Weather Review*, **139** (6), 1952–1959.
- Cawkwell, F., and J. Bamber, 2002: The impact of cloud cover on the net radiation budget of the Greenland ice sheet. *Annals of Glaciology*, **34** (1), 141–149.
- Cesana, G., J. Kay, H. Chepfer, J. English, and G. Boer, 2012: Ubiquitous low-level liquid-containing Arctic clouds: New observations and climate model constraints from CALIPSO-GOCCP. *Geophysical Research Letters*, **39** (20).
- Chen, Q.-s., D. H. Bromwich, and L. Bai, 1997: Precipitation over Greenland retrieved by a dynamic method and its relation to cyclonic activity. *Journal of Climate*, **10** (5), 839–870.
- Clausen, H., N. Gundestrup, S. Johnsen, R. Bindshadler, and J. Zwally, 1988: Glaciological investigations in the Crete area, central Greenland: A search for a new deep-drilling site. *Annals of Glaciology*, **10**, 10–15.
- Clough, S., M. Shephard, E. Mlawer, J. Delamere, M. Iacono, K. Cady-Pereira, S. Boukabara, and P. Brown, 2005: Atmospheric radiative transfer modeling: a summary of the AER codes. *Journal of Quantitative Spectroscopy and Radiative Transfer*, **91** (2), 233–244.
- Cooper, W. A., 1986: Ice initiation in natural clouds. *Precipitation Enhancement—A Scientific Challenge*, Springer, 29–32.
- Cuffey, K. M., and G. D. Clow, 1997: Temperature, accumulation, and ice sheet elevation in central Greenland through the last deglacial transition. *Journal of Geophysical Research: Oceans*, **102** (C12), 26 383–26 396.
- Curry, J. A., 1986: Interactions among turbulence, radiation and microphysics in Arctic stratus clouds. *Journal of the Atmospheric Sciences*, **43** (1), 90–106.

- Curry, J. A., E. Ebert, and G. Herman, 1988: Mean and turbulence structure of the summertime Arctic cloudy boundary layer. *Quarterly Journal of the Royal Meteorological Society*, **114** (481), 715–746.
- Curry, J. A., P. Hobbs, M. King, D. Randall, and Coauthors, 2000: FIRE Artic clouds experiment. *Bulletin of the American Meteorological Society*, **81** (1), 5.
- Curry, J. A., J. L. Schramm, W. B. Rossow, and D. Randall, 1996: Overview of Arctic cloud and radiation characteristics. *Journal of Climate*, **9** (8), 1731–1764.
- Dahl-Jensen, D., K. Mosegaard, N. Gundestrup, G. D. Clow, S. J. Johnsen, A. W. Hansen, and N. Balling, 1998: Past temperatures directly from the Greenland ice sheet. *Science*, **282** (5387), 268–271.
- Dahl-Jensen, D., and Coauthors, 2013: Eemian interglacial reconstructed from a Greenland folded ice core. *Nature*, **493** (7433), 489–494.
- Davini, P., C. Cagnazzo, S. Gualdi, and A. Navarra, 2012a: Bidimensional diagnostics, variability, and trends of Northern Hemisphere blocking. *Journal of Climate*, **25** (19), 6496–6509.
- Davini, P., C. Cagnazzo, R. Neale, and J. Tribbia, 2012b: Coupling between Greenland blocking and the North Atlantic oscillation pattern. *Geophysical Research Letters*, **39** (14).
- de Boer, G., E. W. Eloranta, and M. D. Shupe, 2009: Arctic mixed-phase stratiform cloud properties from multiple years of surface-based measurements at two high-latitude locations. *Journal of the Atmospheric Sciences*, **66** (9), 2874–2887.
- Dee, D., and Coauthors, 2011: The ERA-Interim reanalysis: Configuration and performance of the data assimilation system. *Quarterly Journal of the Royal Meteorological Society*, **137** (656), 553–597.
- Dergach, A., G. Zabrodsii, and V. Morachevskii, 1960: Progress in a complex investigation of St-sc Type Clouds and of Fogs in the Arctic. Tech. rep., DTIC Document.
- Doyle, J. D., and M. A. Shapiro, 1999: Flow response to large-scale topography: The Greenland tip jet. *Tellus A*, **51** (5), 728–748.
- Driesschaert, E., and Coauthors, 2007: Modeling the influence of Greenland ice sheet melting on the Atlantic meridional overturning circulation during the next millennia. *Geophysical Research Letters*, **34** (10).
- Dudhia, J., 1989: Numerical study of convection observed during the winter monsoon experiment using a mesoscale two-dimensional model. *Journal of the Atmospheric Sciences*, **46** (20), 3077–3107.



- Encyclopædia Britannica, ., 2015: Greenland Ice Sheet. URL <http://www.britannica.com/place/Greenland-Ice-Sheet>.
- Fettweis, X., B. Franco, M. Tedesco, J. Van Angelen, J. Lenaerts, M. Van den Broeke, H. Gallée, and Coauthors, 2012: Estimating Greenland ice sheet surface mass balance contribution to future sea level rise using the regional atmospheric climate model MAR. *Cryosphere Discussions*, **6**, 3101–3147.
- Fettweis, X., E. Hanna, C. Lang, A. Belleflamme, M. Erpicum, and H. Gallée, 2013: Important role of the mid-tropospheric atmospheric circulation in the recent surface melt increase over the Greenland ice sheet. *The Cryosphere*, **7**, 241–248.
- Findeisen, W., 1938: Kolloid-meteorologische Vorgänge bei Neiderschlags-bildung. *Meteor. Z*, **55**, 121–133.
- Flynn, C. J., A. Mendoza, Y. Zheng, and S. Mathur, 2007: Novel polarization-sensitive micropulse lidar measurement technique. *Optics Express*, **15** (6), 2785–2790.
- Garrett, T. J., and C. Zhao, 2006: Increased Arctic cloud longwave emissivity associated with pollution from mid-latitudes. *Nature*, **440** (7085), 787–789.
- Gaustad, K., D. D. Turner, and S. McFarlane, 2007: *MWRRET value-added product: the retrieval of liquid water path and precipitable water vapor from microwave radiometer (mwr) datasets*.
- Girard, E., and J. A. Curry, 2001: Simulation of Arctic low-level clouds observed during the FIRE Arctic clouds experiment using a new bulk microphysics scheme. *Journal of Geophysical Research*, **106**, 15.
- Glickman, T., 2000: AMS Glossary of Meteorology. *American Meteorology Society, Boston, USA*,.
- Graversen, R. G., T. Mauritsen, M. Tjernström, E. Källén, and G. Svensson, 2008: Vertical structure of recent Arctic warming. *Nature*, **451** (7174), 53–56.
- Gregory, D., and D. Morris, 1996: The sensitivity of climate simulations to the specification of mixed phase clouds. *Climate Dynamics*, **12** (9), 641–651.
- Gregory, J., and P. Huybrechts, 2006: Ice-sheet contributions to future sea-level change. *Philosophical Transactions of the Royal Society of London A: Mathematical, Physical and Engineering Sciences*, **364** (1844), 1709–1732.
- Grenier, H., and C. S. Bretherton, 2001: A moist PBL parameterization for large-scale models and its application to subtropical cloud-topped marine boundary layers. *Monthly Weather Review*, **129** (3), 357–377.

- Guichard, F., and Coauthors, 2004: Modelling the diurnal cycle of deep precipitating convection over land with cloud-resolving models and single-column models. *Quarterly Journal of the Royal Meteorological Society*, **130** (604), 3139–3172.
- Hanna, E., J. M. Jones, J. Cappelen, S. H. Mernild, L. Wood, K. Steffen, and P. Huybrechts, 2013: The influence of North Atlantic atmospheric and oceanic forcing effects on 1900–2010 Greenland summer climate and ice melt/runoff. *International Journal of Climatology*, **33** (4), 862–880.
- Hanna, E., and Coauthors, 2008: Increased runoff from melt from the Greenland Ice Sheet: a response to global warming. *Journal of Climate*, **21** (2), 331–341.
- Heinemann, G., 1999: The KABEG’97 field experiment: An aircraft-based study of katabatic wind dynamics over the Greenland ice sheet. *Boundary-Layer Meteorology*, **93** (1), 75–116.
- Heinemann, G., and T. Klein, 2002: Modelling and observations of the katabatic flow dynamics over Greenland. *Tellus A*, **54** (5), 542–554.
- Helm, V., A. Humbert, and H. Miller, 2014: Elevation and elevation change of Greenland and Antarctica derived from CryoSat-2. *The Cryosphere*, **8** (4), 1539–1559.
- Herman, G., and R. Goody, 1976: Formation and persistence of summertime Arctic stratus clouds. *Journal of the Atmospheric Sciences*, **33** (8), 1537–1553.
- Hines, K. M., and D. H. Bromwich, 2008: Development and testing of polar weather research and forecasting (WRF) model. Part I: Greenland ice sheet meteorology. *Monthly Weather Review*, **136** (6), 1971–1989.
- Hines, K. M., D. H. Bromwich, L.-S. Bai, M. Barlage, and A. G. Slater, 2011: Development and testing of polar WRF. Part III: Arctic Land. *Journal of Climate*, **24** (1), 26–48.
- Hobbs, P. V., and A. L. Rangno, 1985: Ice particle concentrations in clouds. *Journal of the Atmospheric Sciences*, **42** (23), 2523–2549.
- Hogan, R. J., P. Francis, H. Flentje, A. Illingworth, M. Quante, and J. Pelon, 2003: Characteristics of mixed-phase clouds. I: Lidar, radar and aircraft observations from CLARE’98. *Quarterly Journal of the Royal Meteorological Society*, **129** (592), 2089–2116.
- Hong, S.-Y., Y. Noh, and J. Dudhia, 2006: A new vertical diffusion package with an explicit treatment of entrainment processes. *Monthly Weather Review*, **134** (9), 2318–2341.
- Houghton, J. T., Y. Ding, D. J. Griggs, M. Noguer, P. J. van der Linden, X. Dai, K. Maskell, and C. Johnson, 2001: Climate change 2001: the scientific basis.

- Iacono, M. J., J. S. Delamere, E. J. Mlawer, M. W. Shephard, S. A. Clough, and W. D. Collins, 2008: Radiative forcing by long-lived greenhouse gases: Calculations with the AER radiative transfer models. *Journal of Geophysical Research: Atmospheres*, **113** (D13).
- Intrieri, J., C. Fairall, M. Shupe, P. Persson, E. Andreas, P. Guest, and R. Moritz, 2002: An annual cycle of Arctic surface cloud forcing at SHEBA. *Journal of Geophysical Research: Oceans*, **107** (C10), SHE-13.
- Jiang, H., W. R. Cotton, J. O. Pinto, J. A. Curry, and M. J. Weissbluth, 2000: Cloud resolving simulations of mixed-phase Arctic stratus observed during BASE: Sensitivity to concentration of ice crystals and large-scale heat and moisture advection. *Journal of the Atmospheric Sciences*, **57** (13), 2105–2117.
- Kain, J. S., 2004: The Kain-Fritsch convective parameterization: an update. *Journal of Applied Meteorology*, **43** (1), 170–181.
- Kalnay, E., and Coauthors, 1996: The NCEP/NCAR 40-year reanalysis project. *Bulletin of the American Meteorological Society*, **77** (3), 437–471.
- Klein, S. A., and Coauthors, 2009: Intercomparison of model simulations of mixed-phase clouds observed during the ARM Mixed-Phase Arctic Cloud Experiment. I: Single-layer cloud. *Quarterly Journal of the Royal Meteorological Society*, **135** (641), 979–1002.
- Knox, J. L., and J. E. Hay, 1985: Blocking signatures in the Northern Hemisphere: Frequency distribution and interpretation. *Journal of Climatology*, **5** (1), 1–16.
- Knuteson, R., and Coauthors, 2004a: Atmospheric emitted radiance interferometer. Part I: Instrument design. *Journal of Atmospheric and Oceanic Technology*, **21** (12), 1763–1776.
- Knuteson, R., and Coauthors, 2004b: Atmospheric emitted radiance interferometer. Part II: Instrument performance. *Journal of Atmospheric and Oceanic Technology*, **21** (12), 1777–1789.
- Korolev, A., 2007: Limitations of the Wegener-Bergeron-Findeisen mechanism in the evolution of mixed-phase clouds. *Journal of the Atmospheric Sciences*, **64** (9), 3372–3375.
- Korolev, A., and G. Isaac, 2003: Phase transformation of mixed-phase clouds. *Quarterly Journal of the Royal Meteorological Society*, **129** (587), 19–38.
- Korolev, A. V., and I. P. Mazin, 2003: Supersaturation of water vapor in clouds. *Journal of the Atmospheric Sciences*, **60** (24), 2957–2974.

- Kristjánsson, J., and H. McInnes, 1999: The impact of Greenland on cyclone evolution in the North Atlantic. *Quarterly Journal of the Royal Meteorological Society*, **125** (560), 2819–2834.
- Kuipers Munneke, P., M. Van den Broeke, C. Reijmer, M. Helsen, W. Boot, M. Schneebeli, and K. Steffen, 2009: The role of radiation penetration in the energy budget of the snowpack at Summit, Greenland. *The Cryosphere*, **3** (2), 155–165.
- Liljegren, J. C., 2000: *Automatic self-calibration of ARM microwave radiometers*. VSP Press.
- Lilly, D. K., 1968: Models of cloud-topped mixed layers under a strong inversion. *Quarterly Journal of the Royal Meteorological Society*, **94** (401), 292–309.
- Lindzen, R. S., and M. Fox-Rabinovitz, 1989: Consistent vertical and horizontal resolution. *Monthly Weather Review*, **117** (11), 2575–2583.
- Luke, E. P., P. Kollias, and M. D. Shupe, 2010: Detection of supercooled liquid in mixed-phase clouds using radar Doppler spectra. *Journal of Geophysical Research: Atmospheres*, **115** (D19).
- Martin, J. E., 2013: *Mid-latitude atmospheric dynamics: a first course*. John Wiley & Sons.
- Maslanik, J., C. Fowler, J. Key, T. Scambos, T. Hutchinson, and W. Emery, 1997: AVHRR-based Polar Pathfinder products for modeling applications. *Annals of Glaciology*, **25**, 388–392.
- Mattingly, K. S., J. T. McLeod, J. A. Knox, J. M. Shepherd, and T. L. Mote, 2015: A climatological assessment of Greenland blocking conditions associated with the track of Hurricane Sandy and historical North Atlantic hurricanes. *International Journal of Climatology*, **35** (5), 746–760.
- McFarquhar, G. M., and Coauthors, 2011: Indirect and semi-direct aerosol campaign: The impact of Arctic aerosols on clouds. *Bulletin of the American Meteorological Society*, **92** (2), 183.
- McGrath, D., W. Colgan, N. Bayou, A. Muto, and K. Steffen, 2013: Recent warming at Summit, Greenland: Global context and implications. *Geophysical Research Letters*, **40** (10), 2091–2096.
- Mernild, S. H., T. L. Mote, and G. E. Liston, 2011: Greenland ice sheet surface melt extent and trends: 1960–2010. *Journal of Glaciology*, **57** (204), 621–628.
- Miller, N., D. Turner, R. Bennartz, M. Shupe, M. Kulie, M. Cadetdu, and V. P. Walden, 2013: Surface-based inversions above central Greenland. *Journal of Geophysical Research: Atmospheres*, **118** (2), 495–506.

- Miller, N. B., M. D. Shupe, C. J. Cox, V. P. Walden, D. D. Turner, and K. Steffen, 2015: Cloud radiative forcing at Summit, Greenland. *Journal of Climate*, **28** (15), 6267–6280.
- Mlawer, E. J., S. J. Taubman, P. D. Brown, M. J. Iacono, and S. A. Clough, 1997: Radiative transfer for inhomogeneous atmospheres: RRTM, a validated correlated-k model for the longwave. *Journal of Geophysical Research: Atmospheres*, **102** (D14), 16 663–16 682.
- Moore, G., 2003: Gale force winds over the Irminger Sea to the east of Cape Farewell, Greenland. *Geophysical Research Letters*, **30** (17).
- Moore, G., and I. Renfrew, 2005: Tip jets and barrier winds: A QuikSCAT climatology of high wind speed events around Greenland. *Journal of Climate*, **18** (18), 3713–3725.
- Moran, K. P., B. E. Martner, M. Post, R. A. Kropfli, D. C. Welsh, and K. B. Widener, 1998: An unattended cloud-profiling radar for use in climate research. *Bulletin of the American Meteorological Society*, **79** (3), 443–455.
- Morris, V., 2006: Microwave radiometer (MWR) handbook. *ARM-TR016*.
- Morrison, H., J. Curry, M. Shupe, and P. Zuidema, 2005: A new double-moment microphysics parameterization for application in cloud and climate models. Part II: Single-column modeling of Arctic clouds. *Journal of the Atmospheric Sciences*, **62** (6), 1678–1693.
- Morrison, H., G. de Boer, G. Feingold, J. Harrington, M. D. Shupe, and K. Sulia, 2012: Resilience of persistent Arctic mixed-phase clouds. *Nature Geoscience*, **5** (1), 11–17.
- Morrison, H., and J. Pinto, 2006: Intercomparison of bulk cloud microphysics schemes in mesoscale simulations of springtime Arctic mixed-phase stratiform clouds. *Monthly Weather Review*, **134** (7), 1880–1900.
- Morrison, H., J. O. Pinto, J. A. Curry, and G. M. McFarquhar, 2008: Sensitivity of M-PACE mixed-phase stratocumulus to cloud condensation and ice nuclei in a mesoscale model with two-moment bulk cloud microphysics. *Journal of Geophysical Research*.
- Morrison, H., G. Thompson, and V. Tatarskii, 2009a: Impact of cloud microphysics on the development of trailing stratiform precipitation in a simulated squall line: Comparison of one-and two-moment schemes. *Monthly Weather Review*, **137** (3), 991–1007.

- Morrison, H., and Coauthors, 2009b: Intercomparison of model simulations of mixed-phase clouds observed during the ARM Mixed-Phase Arctic Cloud Experiment. II: Multilayer cloud. *Quarterly Journal of the Royal Meteorological Society*, **135** (641), 1003–1019.
- Morrison, H., and Coauthors, 2011: Intercomparison of cloud model simulations of Arctic mixed-phase boundary layer clouds observed during SHEBA/FIRE-ACE. *Journal of Advances in Modeling Earth Systems*, **3** (2).
- Mote, T., 2015: Greenland Ice Sheet Today. URL <http://nsidc.org/greenland-today/>.
- National Centers for Environmental Prediction, N. U. D. o. C., National Weather Service, 2000: NCEP FNL Operational Model Global Tropospheric Analyses, continuing from July 1999. URL <http://dx.doi.org/10.5065/D6M043C6>.
- Neff, W., G. P. Compo, F. Martin Ralph, and M. D. Shupe, 2014: Continental heat anomalies and the extreme melting of the Greenland ice surface in 2012 and 1889. *Journal of Geophysical Research: Atmospheres*, **119** (11), 6520–6536.
- Nghiem, S., and Coauthors, 2012: The extreme melt across the Greenland ice sheet in 2012. *Geophysical Research Letters*, **39** (20).
- Nicholls, R. J., and A. Cazenave, 2010: Sea-level rise and its impact on coastal zones. *Science*, **328** (5985), 1517–1520.
- Nuttall, M., 2012: *Encyclopedia of the Arctic*. Routledge.
- Pagano, T. S., and R. M. Durham, 1993: Moderate resolution imaging spectroradiometer (MODIS). *Optical Engineering and Photonics in Aerospace Sensing*, International Society for Optics and Photonics, 2–17.
- Petters, J. L., J. Y. Harrington, and E. E. Clothiaux, 2012: Radiative-dynamical feedbacks in low liquid water path stratiform clouds. *Journal of the Atmospheric Sciences*, **69** (5), 1498–1512.
- Petty, G. W., 2004: *A first course in atmospheric radiation*. Sundog.
- Pinto, J. O., 1998: Autumnal mixed-phase cloudy boundary layers in the Arctic. *Journal of the Atmospheric Sciences*, **55** (11), 2016–2038.
- Ramanathan, V., R. Cess, E. Harrison, P. Minnis, B. Barkstrom, E. Ahmad, and D. Hartmann, 1989: Cloud-radiative forcing and climate: Results from the Earth Radiation Budget Experiment. *Science*, **243** (4887), 57–63.
- Randall, D. A., and D. G. Cripe, 1999: Alternative methods for specification of observed forcing in single-column models and cloud system models. *Journal of geophysical research*, **104**, 24.

- Rasmussen, L., 1989: Greenland winds and satellite imagery. *Danish Meteorological Society Vejret*, 32–37.
- Rauber, R. M., and A. Tokay, 1991: An explanation for the existence of supercooled water at the top of cold clouds. *Journal of the Atmospheric Sciences*, **48** (8), 1005–1023.
- Raynaud, D., J. Chappellaz, C. Ritz, and P. Martinerie, 1997: Air content along the Greenland Ice Core Project core: A record of surface climatic parameters and elevation in central Greenland. *Journal of Geophysical Research: Oceans*, **102** (C12), 26 607–26 613.
- Reinecke, P. A., and D. R. Durran, 2008: Estimating topographic blocking using a Froude number when the static stability is nonuniform. *Journal of the Atmospheric Sciences*, **65** (3), 1035–1048.
- Renfrew, I. A., and Coauthors, 2008: The Greenland flow distortion experiment. *Bulletin of the American Meteorological Society*, **89** (9), 1307.
- Ripesi, P., F. Ciciulla, F. Maimone, and V. Pelino, 2012: The February 2010 Arctic Oscillation Index and its stratospheric connection. *Quarterly Journal of the Royal Meteorological Society*, **138** (669), 1961–1969.
- Rogers, J. C., 1984: The association between the North Atlantic Oscillation and the Southern Oscillation in the northern hemisphere. *Monthly Weather Review*, **112** (10), 1999–2015.
- Rogers, J. C., 1990: Patterns of low-frequency monthly sea level pressure variability (1899–1986) and associated wave cyclone frequencies. *Journal of Climate*, **3** (12), 1364–1379.
- Rossow, W. B., and R. A. Schiffer, 1991: ISCCP cloud data products. *Bulletin of the American Meteorological Society*, **72** (1), 2–20.
- Sassen, K., 1974: Depolarization of laser light backscattered by artificial clouds. *Journal of Applied Meteorology*, **13** (8), 923–933.
- Savre, J., A. M. Ekman, G. Svensson, and M. Tjernström, 2015: Large-eddy simulations of an Arctic mixed-phase stratiform cloud observed during ISDAC: sensitivity to moisture aloft, surface fluxes and large-scale forcing. *Quarterly Journal of the Royal Meteorological Society*, **141** (689), 1177–1190.
- Scorer, R., 1988: Sunny Greenland. *Quarterly Journal of the Royal Meteorological Society*, **114** (479), 3–29.
- Seddik, H., R. Greve, T. Zwinger, F. Gillet-Chaulet, and O. Gagliardini, 2012: Simulations of the Greenland ice sheet 100 years into the future with the full Stokes model Elmer/Ice. *Journal of Glaciology*, **58** (209), 427–440.

- Sedlar, J., M. D. Shupe, and M. Tjernström, 2012: On the relationship between thermodynamic structure and cloud top, and its climate significance in the Arctic. *Journal of Climate*, **25** (7), 2374–2393.
- Serreze, M. C., and R. G. Barry, 2005: *The Arctic climate system*, Vol. 22. Cambridge University Press.
- Serreze, M. C., and R. G. Barry, 2011: Processes and impacts of Arctic amplification: A research synthesis. *Global and Planetary Change*, **77** (1), 85–96.
- Serreze, M. C., F. Carse, R. G. Barry, and J. C. Rogers, 1997: Icelandic low cyclone activity: Climatological features, linkages with the NAO, and relationships with recent changes in the Northern Hemisphere circulation. *Journal of Climate*, **10** (3), 453–464.
- Shupe, M. D., 2007: A ground-based multisensor cloud phase classifier. *Geophysical Research Letters*, **34** (22).
- Shupe, M. D., 2011: Clouds at Arctic atmospheric observatories. Part II: Thermodynamic phase characteristics. *Journal of Applied Meteorology and Climatology*, **50** (3), 645–661.
- Shupe, M. D., and J. M. Intrieri, 2004: Cloud radiative forcing of the Arctic surface: The influence of cloud properties, surface albedo, and solar zenith angle. *Journal of Climate*, **17** (3), 616–628.
- Shupe, M. D., P. Kollias, P. O. G. Persson, and G. M. McFarquhar, 2008a: Vertical motions in Arctic mixed-phase stratiform clouds. *Journal of the Atmospheric Sciences*, **65** (4), 1304–1322.
- Shupe, M. D., P. Kollias, M. Poellot, and E. Eloranta, 2008b: On deriving vertical air motions from cloud radar Doppler spectra. *Journal of Atmospheric and Oceanic Technology*, **25** (4), 547–557.
- Shupe, M. D., S. Y. Matrosov, and T. Uttal, 2006: Arctic mixed-phase cloud properties derived from surface-based sensors at SHEBA. *Journal of the Atmospheric Sciences*, **63** (2), 697–711.
- Shupe, M. D., D. D. Turner, A. Zwink, M. M. Thieman, E. J. Mlawer, and T. Shipert, 2015: Deriving Arctic cloud microphysics at Barrow, Alaska: algorithms, results, and radiative closure. *Journal of Applied Meteorology and Climatology*, **54** (7), 1675–1689.
- Shupe, M. D., T. Uttal, and S. Y. Matrosov, 2005: Arctic cloud microphysics retrievals from surface-based remote sensors at SHEBA. *Journal of Applied Meteorology*, **44** (10), 1544–1562.



- Shupe, M. D., and Coauthors, 2013: High and dry: New observations of tropospheric and cloud properties above the Greenland Ice Sheet. *Bulletin of the American Meteorological Society*, **94** (2), 169–186.
- Solomon, A., H. Morrison, O. Persson, M. D. Shupe, and J.-W. Bao, 2009: Investigation of microphysical parameterizations of snow and ice in Arctic clouds during M-PACE through model-observation comparisons. *Monthly Weather Review*, **137** (9), 3110–3128.
- Solomon, A., M. Shupe, P. Persson, and H. Morrison, 2011: Moisture and dynamical interactions maintaining decoupled Arctic mixed-phase stratocumulus in the presence of a humidity inversion. *Atmospheric Chemistry and Physics*, **11** (19), 10 127–10 148.
- Solomon, A., M. D. Shupe, Persson, and N. B. Miller, 2016: Cloud-atmosphere boundary layer-surface interactions on the greenland ice sheet during the july 2012 extreme melt event. *Submitted*.
- Solomon, A., M. D. Shupe, O. Persson, H. Morrison, T. Yamaguchi, P. M. Caldwell, and G. de Boer, 2014: The sensitivity of springtime Arctic mixed-phase stratocumulus clouds to surface-layer and cloud-top inversion-layer moisture sources. *Journal of the Atmospheric Sciences*, **71** (2), 574–595.
- Stammes, K., R. Ellingson, J. Curry, J. Walsh, and B. Zak, 1999: Review of science issues, deployment strategy, and status for the ARM North Slope of Alaska-Adjacent Arctic Ocean climate research site. *Journal of Climate*, **12** (1), 46–63.
- Stein, A., R. Draxler, G. Rolph, B. Stunder, M. Cohen, and F. Ngan, 2015: NOAA’s HYSPLIT atmospheric transport and dispersion modeling system. *Bulletin of the American Meteorological Society*, **96** (12), 2059–2077.
- Stephens, G., 1978: Radiation profiles in extended water clouds. II: Parameterization schemes. *Journal of the Atmospheric Sciences*, **35** (11), 2123–2132.
- Stephens, G. L., 2005: Cloud feedbacks in the climate system: A critical review. *Journal of Climate*, **18** (2), 237–273.
- Stone, E., D. Lunt, I. Rutt, and E. Hanna, 2010: Investigating the sensitivity of numerical model simulations of the modern state of the Greenland ice-sheet and its future response to climate change. *The Cryosphere*, **4** (3), 397–417.
- Stramler, K., A. D. Del Genio, and W. B. Rossow, 2011: Synoptically driven Arctic winter states. *Journal of Climate*, **24** (6), 1747–1762.
- Sun, Z., and K. P. Shine, 1994: Studies of the radiative properties of ice and mixed-phase clouds. *Quarterly Journal of the Royal Meteorological Society*, **120** (515), 111–137.

- Sverdrup, H. U., 1930: *The Norwegian North Polar Expedition with the "Maud" 1918-1925: Scientific Results*, Vol. 3. John Griegs Boktr.
- Tewari, M., and Coauthors, 2004: Implementation and verification of the unified NOAA land surface model in the WRF model. *20th Conference on Weather Analysis and Forecasting/16th conference on Numerical Weather Prediction*, 11–15.
- Thompson, D. W., and J. M. Wallace, 1998: The Arctic Oscillation signature in the wintertime geopotential height and temperature fields. *Geophysical Research Letters*, **25** (9), 1297–1300.
- Thorncroft, C., B. Hoskins, and M. McIntyre, 1993: Two paradigms of baroclinic-wave life-cycle behaviour. *Quarterly Journal of the Royal Meteorological Society*, **119** (509), 17–55.
- Tjernström, M., and Coauthors, 2012: Meteorological conditions in the central Arctic summer during the Arctic Summer Cloud Ocean Study (ASCOS). *Atmospheric Chemistry and Physics*, **12** (15), 6863–6889.
- Turner, D., 2007b: Improved ground-based liquid water path retrievals using a combined infrared and microwave approach. *Journal of Geophysical Research: Atmospheres*, **112** (D15).
- Turner, D., and U. Löhnert, 2014: Information content and uncertainties in thermodynamic profiles and liquid cloud properties retrieved from the ground-based Atmospheric Emitted Radiance Interferometer (AERI). *Journal of Applied Meteorology and Climatology*, **53** (3), 752–771.
- Turner, D. D., S. A. Clough, J. C. Liljegren, E. E. Clothiaux, K. E. Cady-Pereira, and K. L. Gaustad, 2007c: Retrieving Liquid Water Path and Precipitable Water Vapor From the Atmospheric Radiation Measurement (ARM) Microwave Radiometers. *IEEE Transactions on Geoscience and Remote Sensing*, **45** (11), 3680–3690.
- Turner, D. D., and E. W. Eloranta, 2008: Validating mixed-phase cloud optical depth retrieved from infrared observations with high spectral resolution lidar. *IEEE Geoscience and Remote Sensing Letters*, **5** (2), 285–288.
- Turner, D. D., A. Vogelmann, R. T. Austin, J. C. Barnard, and Coauthors, 2007a: Thin liquid water clouds. *Bulletin of the American Meteorological Society*, **88** (2), 177.
- Uttal, T., J. A. Curry, M. G. Mcphee, D. K. Perovich, and Coauthors, 2002: Surface heat budget of the Arctic Ocean. *Bulletin of the American Meteorological Society*, **83** (2), 255.

- Uttal, T., and Coauthors, 2015: International Arctic Systems for Observing the Atmosphere (IASOA): An International Polar Year Legacy Consortium. *Bulletin of the American Meteorological Society*, **(2015)**.
- van Loon, H., and J. C. Rogers, 1978: The seesaw in winter temperatures between Greenland and northern Europe. Part I: General description. *Monthly Weather Review*, **106 (3)**, 296–310.
- Van Tricht, K., I. Gorodetskaya, S. Lhermitte, D. Turner, J. Schween, and N. Van Lipzig, 2014: An improved algorithm for polar cloud-base detection by ceilometer over the ice sheets. *Atmospheric Measurement Techniques*, **7 (5)**, 1153–1167.
- Van Tricht, K., and Coauthors, 2016: Clouds enhance Greenland ice sheet melt-water runoff. *Nature Communications*, **7**.
- Velicogna, I., and J. Wahr, 2013: Time-variable gravity observations of ice sheet mass balance: Precision and limitations of the GRACE satellite data. *Geophysical Research Letters*, **40 (12)**, 3055–3063.
- Verlinde, J., J. Y. Harrington, G. McFarquhar, V. Yannuzzi, and Coauthors, 2007: The mixed-phase Arctic cloud experiment. *Bulletin of the American Meteorological Society*, **88 (2)**, 205.
- Wallace, J. M., and P. V. Hobbs, 2006: *Atmospheric science: an introductory survey*, Vol. 92. Academic Press.
- Walsh, J. E., and W. L. Chapman, 1998: Arctic cloud-radiation-temperature associations in observational data and atmospheric reanalyses. *Journal of Climate*, **11 (11)**, 3030–3045.
- Wang, S., Q. Wang, R. E. Jordan, and P. Persson, 2001: Interactions among long-wave radiation of clouds, turbulence, and snow surface temperature in the Arctic: A model sensitivity study. *Journal of Geophysical Research: Atmospheres*, **106 (D14)**, 15 323–15 333.
- Wang, W., D. Barker, J. Bray, C. Bruyere, M. Duda, J. Dudhia, D. Gill, and J. Michalakes, 2007: User’s Guide for Advanced Research WRF (ARW) Modeling System Version 3. *Mesoscale and Microscale Meteorology Division–National Center for Atmospheric Research (MMM-NCAR)*.
- Wang, X., and J. R. Key, 2005: Arctic surface, cloud, and radiation properties based on the AVHRR Polar Pathfinder dataset. Part I: Spatial and temporal characteristics. *Journal of Climate*, **18 (14)**, 2558–2574.
- Wegener, A., 1911: *Thermodynamik der atmosphäre*. JA Barth.

- Welton, E. J., and J. R. Campbell, 2002: Micropulse lidar signals: Uncertainty analysis. *Journal of Atmospheric and Oceanic Technology*, **19** (**12**), 2089–2094.
- Widener, K., and K. Johnson, 2005: Millimeter wave cloud radar (MMCR) handbook.
- Winker, D. M., M. A. Vaughan, A. Omar, Y. Hu, K. A. Powell, Z. Liu, W. H. Hunt, and S. A. Young, 2009: Overview of the CALIPSO mission and CALIOP data processing algorithms. *Journal of Atmospheric and Oceanic Technology*, **26** (**11**), 2310–2323.
- Woollings, T., B. Hoskins, M. Blackburn, and P. Berrisford, 2008: A new Rossby wave-breaking interpretation of the North Atlantic Oscillation. *Journal of the Atmospheric Sciences*, **65** (**2**), 609–626.
- Yau, M. K., and R. Rogers, 1996: *A short course in cloud physics*. Elsevier.
- Yu, X., and T.-Y. Lee, 2010: Role of convective parameterization in simulations of a convection band at grey-zone resolutions. *Tellus A*, **62** (**5**), 617–632.
- Zuidema, P., and Coauthors, 2005: An Arctic springtime mixed-phase cloudy boundary layer observed during SHEBA. *Journal of the Atmospheric Sciences*, **62** (**1**), 160–176.